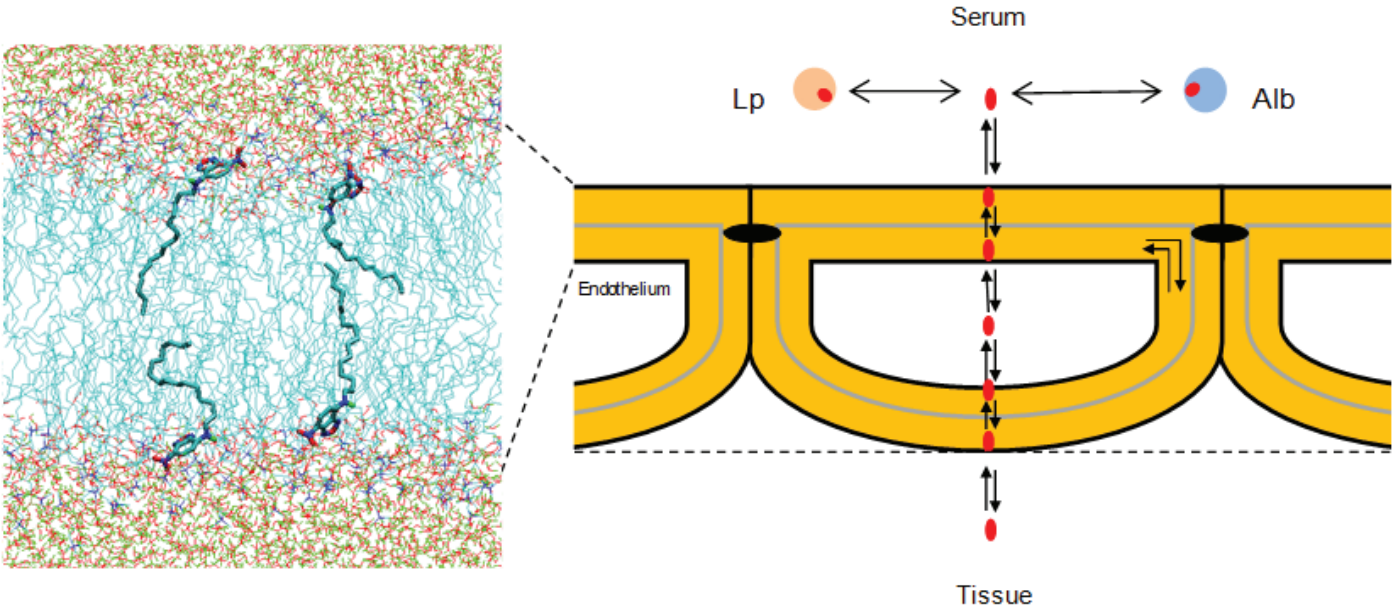

Hugo Alexandre Louro Filipe

FOLLOWING AMPHIPHILIC MOLECULES ON THEIR WAY THROUGH LIPID MEMBRANES: DEVELOPMENT OF A KINETIC MODEL OF PASSIVE PERMEATION THROUGH THE BLOOD-BRAIN BARRIER

Tese de Doutoramento em Química, ramo de Química Biológica, orientada pela Professora Doutora Maria João Pedrosa Ferreira Moreno Silvestre e pelo Professor Doutor Luís Miguel Santos Loura e apresentada à Faculdade de Ciências e Tecnologia da Universidade de Coimbra

Coimbra, 2014

· U C ·

Universidade de Coimbra

Faculdade de Ciências e Tecnologia da Universidade de Coimbra

Departamento de Química

Hugo Alexandre Louro Filipe

Following Amphiphilic Molecules on Their Way through Lipid Membranes: Development of a Kinetic Model of Passive Permeation through the Blood-Brain Barrier

Tese de Doutoramento em Química, ramo de Química Biológica, orientada pela Professora Doutora Maria João Pedrosa Ferreira Moreno Silvestre e pelo Professor Doutor Luís Miguel Santos Loura e apresentada à Faculdade de Ciências e Tecnologia da Universidade de Coimbra.

2014

Coimbra

Agradecimentos

Esta tese é o culminar de um período de dedicação à investigação científica em que considero ter evoluído bastante, profissionalmente como químico, mas também como pessoa. No entanto, este é o resultado de um trabalho de interacção com um conjunto de pessoas e instituições que, de uma forma ou de outra, deram o seu valioso contributo. Assim, gostaria de deixar aqui uma palavra de agradecimento a todos aqueles, sem os quais este resultado não teria sido possível.

Gostaria de agradecer ao Departamento de Química da Universidade de Coimbra por disponibilizar as suas instalações, e ao Centro de Química da Universidade de Coimbra, enquanto instituição de acolhimento. Agradeço à Fundação para a Ciência e Tecnologia (FCT), pelo financiamento através da bolsa com a referência SFRH/BD/65375/2009, sem o qual este percurso teria sido muito mais difícil. Ao Laboratório de Computação Avançada da Universidade de Coimbra, ao CSC-IT Center for Science, na Finlândia e ao programa DECI do PRACE pela disponibilização dos seus computadores, fornecendo as horas de computação que permitiram um extenso estudo usando a técnica de dinâmica molecular.

À Professora Doutora Maria João Moreno gostaria de agradecer pela sua amizade e pela oportunidade de realizar este trabalho. Agradeço pela sua orientação crítica e dedicada, pela motivação, paciência, e por promover um debate de ideias sempre muito produtivo.

Ao Professor Doutor Luís Loura, que abriu as portas do seu gabinete de uma forma invulgar e me introduziu no mundo da dinâmica molecular. Agradeço toda a sua disponibilidade e prontidão a quando do aparecimento de um novo desafio.

Ao Doutor Armindo Salvador, agradeço pela sua disponibilidade, pelo entusiasmo em diversas discussões e pelo apoio no desenvolvimento dos modelos cinéticos.

Ao Professor Doutor Winchil Vaz, pelas diversas conversas, sempre muito interessantes, por todas as valiosas sugestões, e pela motivação em relação à investigação científica.

Ao Professor Doutor Ilpo Vattulainen, agradeço por me ter recebido no Biological Physics Group, em Tampere, na Finlândia, pelas discussões críticas e pragmáticas, proporcionando uma experiencia muito enriquecedora tanto no plano profissional como pessoal.

Aos colegas do grupo de Química Biológica - Biomembrane Structure and Function, Renato Cardoso, Filipe Gomes e Patrícia Martins, agradeço pela amizade, por todas as discussões científicas e não científicas, pelo apoio apresentado sempre que necessário e pelo ambiente saudável e de alegria que tornou todo o trabalho mais fácil. Agradeço também aos colegas do Computational and Systems Biology Group por toda a boa disposição na partilha do "local de trabalho".

A todos os meus amigos, especialmente aos do Espinheiro o aos de "Coimbra", por todo o apoio e pela partilha de experiências pessoais e pelo convívio. Ao pessoal do Espinheiro, espero conseguir dedicar-vos mais tempo.

À Ana, por me aturar durante todo este percurso, o que acredito ter sido por vezes bastante difícil, e por toda a sua motivação especialmente nos momentos de menor entusiasmo.

Ao meu irmão, Luís, à Sandra e à pequena Maria, que partilham comigo os fins-de-semana quando vou ao Espinheiro, e me fazem lembrar das coisas importantes da vida.

Aos meus tios Néu e Maria Custódia, e aos meus pais, Amélia e Manuel Filipe, por todo o incentivo e por estarem sempre presentes, por todos os ensinamentos e por me transmitirem os valores, que espero continuar a receber, e pelos quais espero continuar a guiar-me.

Table of Contents

Agradecimentos ..... **I**

Table of Contents ..... **III**

Resumo ..... **IX**

Abstract ..... **XI**

List of Abbreviations ..... **XIII**

List of Figures ..... **XVII**

List of Tables ..... **XXVII**

Chapter I Objectives and Outline **1**

Objectives 3

Outline 4

Chapter II Literature Review **7**

II.1 – Biological Membranes 9

II.1.1 – Historical Perspective 9

II.1.2 – Structure and Composition of Biological Membranes 10

II.1.2.1 – Membrane Density Profile 14

II.1.2.2 – Membrane Lateral Pressure 15

II.1.2.3 – Electrical Properties 16

II.1.3 – Dynamics and Organization of Biological Membranes 18

II.1.4 – Membrane Asymmetry 23

II.2 – The role of Cholesterol in Lipid Membranes 25

II.3 – Membrane Permeation 28

II.3.1 – Potential of Mean Force (PMF) Profiles through Lipid Bilayers 31

II.3.2 – Quantitative Evaluation of Permeation of the Amphiphiles through Lipid Bilayers – the Inhomogeneous Solubility-Diffusion Model 33

II.4 – Delivery of Drugs through the Tight Endothelium of the Blood-Brain Barrier 35

II.4.1 – The Blood-Brain Barrier 36

II.4.1.1 – Routes for Drug Delivery through the BBB 38

II.4.1.2 – Model Systems for the BBB 40

II.4.2 – Blood Composition 41

II.4.2.1 – Serum Albumin 42

II.4.2.2 – Lipoproteins 43
II.4.2.3 – Erythrocytes 43
II.5 – Models to Predict the Permeation of Molecules through Cell Monolayers 44
Chapter III Methods 49
III.1 – Molecular Dynamics Simulation of Biological Systems 51
III.1.1 – The Molecular Dynamics Method 52
III.1.2 – Force fields, Constraints and Topologies 54
III.1.3 – Ensembles and Boundary Conditions 57
III.1.4 – Temperature and Pressure Control 58
III.1.5 – Electrostatic Interactions and Cutoffs 60
III.1.6 – Output and Analysis 60
III.2 – Method Details of the MD Simulations Performed on Chapters IV to VII 61
III.2.1 – Simulation Details for the Study of the Interaction of NBD-Labeled Fatty Amines with Lipid Bilayers 61
III.2.2 – Simulation Details for the Calculation of Free Energy Profiles of Long Amphiphiles Interacting with Lipid Membranes 63
III.2.2.1 – Umbrella Sampling Simulations in Pure POPC Bilayers 64
III.2.2.2 – Umbrella Sampling Simulations in Cholesterol-Containing Bilayers 65
III.2.2.3 – Convergence of Free Energy Profiles 66
III.3 – Simulation Details for the Kinetic Modeling of the Passive Distribution of Free Cholesterol in the Blood 66
III.4 – Simulation Details for the Quantitative Modeling of the Passive Permeation through a Cell Monolayer 68
Chapter IV Interaction of NBD-Labeled Fatty Amines with POPC Bilayers: A Molecular Dynamics Study 73
IV.1 – Introduction 75
IV.2 – Results and Discussion 77
IV.2.1 – Area per Lipid 77
IV.2.2 – Bilayer Thickness and Position of Different Atoms 78
IV.2.3 – Orientation of the NBD Fluorophore 85
IV.2.4 – Hydrogen Bonding 86
IV.2.5 – Order of the NBD-C_n and POPC Acyl Chains 88

IV.2.6 – Electrostatic Potential 90
IV.2.7 – Mass Density Profiles 91
IV.2.8 – Lateral Diffusion 92
IV.3 – Concluding Remarks 94
Chapter V Interaction of NBD-Labeled Fatty Amines with POPC:Chol and SpM:Chol Bilayers: A Molecular Dynamics Study 97
V.1 – Introduction 99
V.2 – Results and Discussion 102
V.2.1 – Area per Lipid 102
V.2.2 – Bilayer Thickness and Position of Different Atoms 104
V.2.3 – Orientation of the NBD Fluorophore 110
V.2.4 – Hydrogen Bonding 111
V.2.5 – Order of the NBD-C_n, POPC and SpM Acyl Chains 113
V.2.6 – Electrostatic Potential 114
V.2.7 – Mass Density Profiles 116
V.2.8 – Lateral Diffusion 117
V.3 – Concluding Remarks 118
Chapter VI How to Tackle the Issues in Free Energy Simulations of Long Amphiphiles Interacting with Lipid Membranes: Convergence and Local Membrane Deformations 121
VI .1 – Introduction 123
VI.2 – Results and Discussion 126
VI.2.1 – Convergence of PMF should not be Taken for Granted with Complex Long Molecules 126
VI.2.2 – How to Deal with Local Membrane Deformations During PMF Calculations: PMFs for the NBD-C_n Homologous Series 131
VI.2.3 – Membrane Deformations Characterized by Bilayer Thickness 134
VI.2.4 – Conformation of the Amphiphile Markedly Depends on its Location and Sheds Light on the Cause of the Sampling Problem at the Membrane-Water Interface 135
VI.3 – Concluding Remarks 137
Chapter VII Free Energy of Interaction of a Homologous Series of NBD-Labeled Fatty Amines with Lipid Bilayers 139

VII.1 – Introduction 141
VII.2 – Results and Discussion 144
VII.2.1 – Characterization of the Lipid Membranes 144
VII.2.2 – PMF Profiles for the NBD-Cn Homologous Series through Lipid Membranes 145
VII.2.3 – Time Relaxation of the Amphiphiles from the Transition States to the Equilibrium Position: Distance of the NBD Group to the Bilayer Center. 149
VII.2.4 – Analysis of Several System Properties During the Permeation Process154
VII.2.4.1 – Membrane Deformations Characterized by Bilayer Thickness 154
VII.2.4.2 – Distance between N1 and Cter Atoms 155
VII.2.4.3 – Hydrogen Bonding 158
VII.2.4.4 – Orientation of the NBD Group 160
VII.2.5 – Quantitative Evaluation of Permeation of the Amphiphiles through the Lipid Bilayers – Application of the Inhomogeneous Solubility-Diffusion Model162
VII.3 – Concluding Remarks 167
Chapter VIII Homeostasis of Free Cholesterol in the Blood: a Preliminary Evaluation and Modeling of its Passive Transport 169
VIII.1 – Introduction 171
VIII.2 – Results and Discussion 173
VIII.2.1 – Modeling the Distribution of Free Cholesterol in the Blood 173
VIII.2.2 – Kinetics of Free Cholesterol Distribution among the Blood Compartments, Modeled as DHE 177
VIII.2.3 – Kinetics of Free Sterol Distribution among the Blood Compartments - Cholesterol *vs* DHE 179
VIII.2.4 – Steady State Distribution of Cholesterol among the Blood Compartments – LCAT effect 181
VIII.2.5 – Cholesterol Homeostasis in the Blood – Passive *vs* Active Transport. 183
VIII.2.6 – Limitations of This Study 185
VIII.3 – Concluding Remarks 185
Chapter IX Beyond Overton's rule - Quantitative Modeling of Passive Permeation through a Cell Monolayer 187
IX.1 – Introduction 189
IX.2 – Results and Discussion 191

IX.2.1 – Kinetic Model for the Permeation through the Cell Monolayer 191

IX.2.2 – Simple Analysis from the Experimentally Obtained Values..... 194

IX.2.3 – Permeation of the Amphiphiles through the Cell Monolayer 195

IX.2.4 – Drug Sequestration by Serum Components 199

IX.2.5 – Rate Limiting Steps in the Permeation Process 201

IX.2.6 – Effect of Reversibility in the Solute Transfer and Presence of Sequestrators in the Acceptor Compartment..... 205

IX.2.7 – Analytical Solutions to Predict the Rate of Permeation through the Cell Monolayer..... 207

IX.3 – Concluding Remarks..... 210

Chapter X General Concluding Remarks..... 213

Appendix 221

References..... 253

Resumo

O transporte passivo é a principal via para a permeação de fármacos e xenobióticos através de monocamadas de células, como as que constituem o endotélio da barreira hemato-encefálica. A caracterização da velocidade de permeação passiva de um dado fármaco através de bicamadas lipídicas é, por conseguinte, um passo muito importante na previsão da sua farmacocinética. Neste trabalho realizámos um estudo detalhado, em escalas espaciais e temporais diversas, da permeação de moléculas anfifílicas através de membranas lipídicas, e sua distribuição entre diversos compartimentos biológicos. Neste sentido foram realizadas e analisadas simulações de dinâmica molecular com o detalhe atómico dos sistemas, e também simulações com modelos cinéticos usando dados experimentais e informações ao nível macroscópico dos sistemas biológicos. Na sequência do trabalho desenvolvido nos últimos anos por este grupo de investigação, caracterizou-se com detalhe atómico a interação da série homóloga de aminas gordas, NBD-Cn, com bicamadas lipídicas de diferentes composições. As composições lipídicas escolhidas foram POPC, o principal constituinte das membranas biológicas eucarióticas e, POPC:Chol (1:1) e SpM:Chol (6:4), que permitem a representação dos folhetos interno e externo, respectivamente, dos eritrócitos e da membrana plasmática de células endoteliais. A série homóloga escolhida permite o estudo sistemático dos efeitos da estrutura molecular, neste caso, o número de átomos de carbono da cadeia apolar das anfifilas, em várias propriedades da interacção com as bicamadas lipídicas e na permeação através de monocamadas de células. A descrição atomística destes sistemas através de simulações de dinâmica molecular tem dado uma contribuição considerável para a interpretação dos resultados experimentais obtidos pelo grupo de investigação. Em bicamadas de POPC, e para todas as anfifilas, o grupo NBD localiza-se próximo do grupo glicerol do lípido. Em bicamadas de POPC:Chol (1:1) e SpM:Chol (6:4), o grupo NBD localiza-se na interface, numa posição mais externa do que nas bicamadas de POPC puro. Além disso, a técnica de "umbrella sampling" foi aplicada com o objectivo de obter e comparar barreiras de energia livre calculadas com barreiras de energia livre determinadas experimentalmente para os processos de inserção/dessorção e translocação das anfifilas em bicamadas lipídicas. Alguns problemas presentes em cálculos de energia livre em bicamadas lipídicas foram identificados. Verificámos que a região mais problemática para os cálculos de energia livre, com moléculas anfifílicas de cadeia longa é a interface membrana-água. Para todas as bicamadas estudadas, os perfis de

Potential of Mean Force (PMF) têm um valor mínimo quando NBD está localizado na região das cabeças dos lípidos, numa posição mais externa em membranas contendo colesterol, de acordo com outras simulações e resultados experimentais. A comparação quantitativa entre os dados revelou-se muito complicada, impedindo a determinação de constantes de velocidade destes processos para sistemas que não tenham sido experimentalmente caracterizados. No entanto, a descrição qualitativa da interação das anfifilas em diferentes profundidades da bicamada foi realizada. Esta informação fornece uma ilustração esclarecedora do caminho de moléculas anfifilas durante o processo de permeação através de membranas lipídicas.

Numa maior escala temporal e espacial, a homeostase e distribuição de colesterol no sangue foram modeladas usando dados experimentais para a interação do desidroergosterol (DHE) e do colesterol com os principais compartimentos do sangue, ou seja, bicamadas lipídicas que imitam a membrana do eritrócito, lipoproteínas e albumina. O DHE parece ser um bom análogo do colesterol em relação à sua distribuição de equilíbrio. No entanto, a sua cinética de interacção com compartimentos biológicos é significativamente mais rápida. Os resultados mostram a importância da via passiva na homeostase do colesterol no sangue. Além disso, os resultados mostram que a aplicação de dados experimentais para a interacção de moléculas anfifílicas com compartimentos biológicos podem ser usados para avaliar a sua permeação passiva através de barreiras biológicas. Esta metodologia foi aplicada para construir um modelo cinético capaz de simular a permeação passiva de moléculas anfifílicas, como fármacos, através de uma monocamada de células, análoga ao endotélio da barreira hemato-encefálica. Este estudo permitiu a obtenção de regras para a permeação de drogas através da barreira hemato-encefálica. Para alguns derivados da série homóloga NBD-Cn, um aumento na hidrofobicidade leva a uma diminuição na velocidade de acumulação nos tecidos, em oposição ao previsto pelo modelo de partição-difusão. Verificou-se que o passo limitante da velocidade para a permeação através do endotélio depende das características moleculares das anfifilas. Para cadeias longas, é a interacção (constante da velocidade de dessorção) com a membrana do endotélio, enquanto que para cadeias curtas é translocação entre monocamadas. Para comprimentos de cadeia intermédios nenhum passo limitante da velocidade pode ser definido. Verificou-se igualmente que a sequestração do soluto por agentes no compartimento dador reduz substancialmente a velocidade de permeação.

Abstract

Passive transport is the major route for the permeation of drugs and xenobiotics through tight cell monolayers such as the tight endothelia of the blood-brain barrier (BBB). The characterization of the rate of passive permeation through lipid bilayers for a given drug is therefore a critical step in the prediction of its pharmacokinetics. In this work we have performed a detailed study, at different time and length scales, of the permeation of amphiphiles through lipid membranes, and their distribution among biologic compartments. In this regard, we performed and analyzed detailed atomistic Molecular Dynamics (MD) simulations, and also kinetic modeling simulations comprising experimental data and macroscopic information of biological systems. Following the work developed in the last years by this research group, we characterized at atomic detail the interaction of the homologous series of fatty amines, NBD-Cn, with lipid bilayers of different compositions. The chosen lipid compositions are POPC, the major constituent of eukaryotic biomembranes, and POPC:Chol (1:1) and SpM:Chol (6:4), which mimic the inner and outer leaflets, respectively, of erythrocytes and plasma membrane of endothelial cells. The chosen homologous series allows the systematic study of the effect of molecular structure, namely the number of carbons of the alkyl chain of the amphiphiles, on several properties regarding the interaction with lipid bilayers, and the permeation through cell monolayers. The atomistic description of these systems using unrestrained MD simulations has been a considerable contribution for the interpretation of experimental results obtained by the research group. In POPC bilayers, the NBD fluorophore locates near the glycerol backbone/carbonyl region of the lipid, for all amphiphiles. In POPC:Chol (1:1) and SpM:Chol (6:4) bilayers, the NBD group locates at the interface, in a more external position than observed in pure POPC bilayers. Further, the umbrella sampling technique was applied in order to compare calculated and experimental free energies for the insertion/desorption and translocation steps of the amphiphiles' interaction with lipid bilayers. Some pitfalls in free energy calculations were identified. We found that the most challenging environment for free energy computations with long amphiphiles is the membrane-water interface. For all studied bilayers the Potential of Mean Force (PMF) profiles have a minimum value when NBD is located at the head group region, which is more external in cholesterol-containing bilayers in agreement with other simulations and experimental results. A quantitative comparison between calculated and experimental data proved

very complicated, precluding the determination of rate constants for systems that were not experimentally characterized. However, the qualitative description of the interaction of the amphiphiles with the lipids, at different bilayer depths was performed. This gives an enlightened illustration of the path of the amphiphiles during the permeation process through lipid membranes.

At larger time and length scales the blood homeostasis and distribution of cholesterol were modeled using experimental data for the interaction of dehydroergosterol (DHE) and cholesterol with major blood compartments, namely lipid bilayers mimicking the erythrocyte membrane, lipoproteins, and albumin. DHE seems to be an adequate surrogate of cholesterol concerning its equilibrium distribution. However, its kinetics of interaction with biological compartments is significantly faster. The results show the importance of the passive pathway in free cholesterol homeostasis in the blood. Further, the results show that the application of experimental data for the interaction of amphiphilic molecules with biologic compartments can be used to assess their passive permeation through biological barriers. This methodology was applied to build a kinetic model for the passive permeation of amphiphilic molecules, like drugs, through a cell monolayer such as the tight endothelium of the BBB. This allowed the obtention of rules for the BBB permeation of drugs. For some derivatives of the NBD-Cn homologous series, an increase in hydrophobicity leads to a decrease in the characteristic rate of accumulation in the tissue, in opposition to that predicted by the solubility-diffusion model. The rate limiting step for overall permeation through the endothelium was found to depend upon molecular characteristics of the amphiphile. For long chains it is the interaction (desorption rate constant) with the membrane of the endothelium, whereas for short chains it is translocation between bilayer leaflets. For intermediate chain lengths no single rate-limiting step can be defined. It was also found that solute sequestration by binding agents in the donor compartment substantially reduces the rate of overall permeation.

List of Abbreviations

LATIN ALPHABET

Alb – albumin

BB – [brain]/[blood]

BBB – blood-brain barrier

BSA – bovine serum albumin

C_6-NBD-PC – 1-palmitoyl-2-[6-(7-nitrobenz-2-oxa-1,3-diazol-4-yl)aminohexanoyl]-*sn*-glycero-3-phosphocholine

C_{12}-NBD-PC – 1-palmitoyl-2-[12-(7-nitrobenz-2-oxa-1,3-diazol-4-yl)aminododecanoyl]-*sn*-glycero-3-phosphocholine

CAC – critical aggregation concentration

CMC – critical micelle concentration

Chol – cholesterol

CNS – central nervous system

COM – center of mass

CPP – critical packing parameter

CW – pulling direction, from the center of the membrane to bulk water

D – diffusion coefficient

DAPC – 1,2-diarachidoyl-*sn*-glycero-3-phosphocholine

DHE – ergosta-5,7,9(11),22-tetraen-3β-ol (dehydroergosterol)

DOPC – 1,2-dioleoyl-*sn*-glycero-3-phosphocholine

DPPC – 1,2-dipalmitoyl-*sn*-glycero-3-phosphocholine

Ery – erythrocyte

FAC – force autocorrelation

GPI – glycosylphosphatidylinositol

HDL – high density lipoprotein

IAM – immobilized artificial membrane chromatography

K – equilibrium association constant

K_P – equilibrium Partition Coefficient

k_+ – insertion rate constant

k_- – desorption rate constant

k_f – translocation rate constant

K_P^{Ery} – partition coefficient between the aqueous phase and the erythrocyte membrane

$\kappa_+^{Ery^o}$ – rate constant for insertion into the outer leaflet of erythrocyte membrane

$\kappa_-^{Ery^o}$ – rate constant for desorption from the outer leaflet of erythrocyte membrane

$\kappa_{+}^{a^{o}}$ – rate constant for insertion into the outer leaflet of the apical side

$\kappa_{-}^{a^{o}}$ – rate constant for desorption from the outer leaflet of the apical side

$k_{f\,a}^{o\to i}$ – rate constant for translocation into the inner leaflet of the apical side

$k_{f\,a}^{i\to o}$ – rate constant for translocation into the outer leaflet of the apical side

$\kappa_{-}^{a^{i}}$ – rate constant for desorption from inner leaflet of the apical side

$\kappa_{+}^{a^{i}}$ – rate constant for insertion into the inner leaflet of the apical side

$\kappa_{+}^{b^{i}}$ – rate constant for insertion into the inner leaflet of the basolateral side

$k_{f\,b}^{i\to o}$ – rate constant for translocation into the outer leaflet of the basolateral side

$k_{f\,b}^{o\to i}$ – rate constant for translocation into the inner leaflet of the basolateral side

$\kappa_{-}^{b^{o}}$ – rate constant for desorption from outer leaflet of the basolateral side

$\kappa_{+}^{b^{o}}$ – rate constant for insertion into outer leaflet of the basolateral side

LCAT – lecithin-cholesterol-O-acyl transferase

LDL – low density lipoprotein

logP – logarithm of the partition coefficient

Lp – lipoprotein

LUV – large unilamellar vesicles

MD – molecular dynamics

MSD – two-dimensional mean square displacement

NBD – 7-nitrobenz-2-oxa-1,3-diazol-4-yl

NBD-Cn – homologous series of NBD substituted with an alkyl chain of varying length (n)

NBD-DMPE – NBD- 1,2 dimyristoyl-*sn*-glycero-3-phosphoethanolamine

P – permeability coefficient

P-P$_{dist}$ – distance between P atoms in opposing bilayer leaflets

PAMPA – parallel artificial membrane permeation assay

PD – pharmacodynamics

P-gp – P-glycoprotein

PGC – pull geometry cylinder

PGD – pull geometry distance

PK – pharmacokinetics

pKa – negative logarithm of the acid dissociation constant (ionization constant)

PMF – potential of mean force

POPC – 1-palmitoyl, 2-oleoyl-*sn*-glycero-3-phosphocholine

POPC:Chol – POPC:Chol (1:1)

PC – phosphatidylcholine

PE – phosphatidylethanolamine

PS – phosphatidylserine

PSA – polar surface area

PI – phosphatidylinositol

r – fluorescence anisotropy

$\mathbf{S_{CD}}$ – deuterium order parameter

SM – sphingomyelin

SpM – palmitoylated sphingomyelin

SpM:Chol – SpM:Chol (6:4)

TJ – tight junction

TST – transition state theory

US – umbrella sampling

VLDL – very low density lipoproteins

WC – pulling direction, from bulk water to the center of the membrane

WHAM – weighted histogram analysis method

z – position along the bilayer normal

Greek Alphabet

$\boldsymbol{\beta}$ – exchange rate constant

ξ – friction coefficient

$\mathbf{\Phi_F}$ – fluorescence quantum yield

τ – average fluorescence life time

List of Figures

Figure II.1: Illustration of a biological membrane. Adapted from http://www.cmns.leeds.ac.uk/SSbiomemb.htm. 9

Figure II.2 – Illustration of a glycerophospholipid structure, showing the structure of POPC. 11

Figure II.3: Free volume distribution (left) and electron density profile (right) along the bilayer normal. Adapted from [37]. 15

Figure II.4: Lateral pressure profile of a lipid bilayer. Schematic illustration of a cross section through a symmetric lipid bilayer with an indication of the forces that act within the layer (left) and the resulting pressure or stress profile (right). Adapted from [39]. . 16

Figure II.5 - Lipid motions in biomembranes and their approximate characteristic times. Adapted from [52]. 19

Figure II.6 – Order parameter magnitude $|S_{CH}|$ vs. carbon segment number for the *sn*-1 (A) and *sn*-2 (B) acyl chains of POPC. Adapted from [64]. Black dots and red dots refer to experimental data and MD simulations from [64]. Blue triangles refer to data from references therein. 21

Figure II.7 – Illustration of the distribution of major phospholipids, sphingomyelin (SM), phosphatidylcholine (PC), phosphatidylethanolamine (PE); phosphatidylserine (PS) and phosphatidylinositol (PI), between the outer and cytoplasmic leaflets of the human erythrocyte membrane. Adapted from [96] 24

Figure II.8 – Schematic drawing of the blood-brain barrier, showing endothelium, basement membrane, pericytes, astrocytes and tight junctions. Adapted from [176]. ... 37

Figure II.9 – Pathways across the blood–brain barrier. The main routes for molecular traffic across the BBB are shown: a) cell migration, b) passive diffusion, c) carrier mediated efflux, d) carrier mediated influx, e) receptor-mediated transcytosis (RMT), f) adsorptive mediated transcytosis (AMT), g) tight junction modulation. Adapted from [180]. 38

Figure II.10 – Illustration of several blood components. a) X-ray crystallographic Structure of Human Serum Albumin (HSA), adapted from http://www2.hawaii.edu/~chungeun/; b) Schematic illustration of a Lipoprotein, adapted from http://lipidlibrary.aocs.org/Lipids/lipoprot/index.htm; c) A micrograph of Erythrocytes, adapted from http://en.wikipedia.org/wiki/Red_blood_cell. 42

Figure III.1 – Potential energy function for molecular interactions in the molecular mechanics approximation. Adapted from [229] 53

Figure III.2 – Atoms along an alkane chain. 56

Figure III.3 – Periodic boundary conditions in two dimensions with the primary cell surrounded by its image cells. 58

Figure IV.1 – Structures of POPC (left) and NBD-C_{16} (right), showing the atom numbering as used throughout the text. 76

Figure IV.2 – Average transverse position <z> of specific atoms in the POPC/NBD-C_n systems. See Figure IV.1 for atom numbering. Cter represents the methyl group at the end of the fatty amine chain. 79

Figure IV.3 – Variation of the transverse distance between N1 and the terminal methyl group of the amphiphiles (Cter). The line is the best linear fit to the $n \leq 10$ points, with a slope equal to 0.091 nm/CH_2. 80

Figure IV.4 – (A): Comparison between the average transverse positions <*z*> of C13 of POPC (black diamonds) and N6 of NBD-C_n (white squares). Also shown is the steady state fluorescence anisotropy (*r*) measured for $n \geq 8$ (white triangles) [5]. (B): Comparison between average transverse positions of C24 of POPC (carbon 9 of the *sn*-2 chain) and the chain end methyl group (Cter) of NBD-C_n. The two dotted lines represent the average transverse location of the acyl chains' end methyl group in the two bilayer leaflets. 81

Figure IV.5 – Left: typical snapshot of a POPC bilayer containing 4 NBD-C_{16} molecules, one of which displays clear interdigitation behavior. Right: zoomed snapshot of this interdigitating NBD-C_{16} and a nearby POPC molecule, showing NBD N1 – NBD H14 – POPC O14 hydrogen bonding. CH_n groups (n=0–3), O atoms, N atoms, P atoms and polar H atoms are displayed in cyan, red, blue, tan and green, respectively. 82

Figure IV.6 – Fraction of interdigitated conformations (*f*) as a function of the amphiphile chain length *n*. The points are the values obtained from simulation, whereas the line was calculated assuming linear variation of <*z*>(Cter) and normal distribution of *z*(Cter) (see text for details). 83

Figure IV.7 – (A) Definition of long and short axes of the NBD fluorophore. (B–D) Probability density functions $P(\theta)$ of the angles between the long axis (B), the short axis (C), and the normal to the NBD plane (defined as the vector product of the short and long axes; D), relative to the bilayer normal. 86

Figure IV.8 – NBD N1-H14-POPC or water acceptor atom (A) and water donor-NBD acceptor atom (B) H-bond fractional frequencies (*f*). 88

Figure IV.9 – Deuterium order parameter of the NBD amphiphiles. (A) – a perspective of the order of each amphiphile as a function of the carbon segment. (B) – a perspective of the order of each carbon segment as a function of the number of total carbons of the alkyl chain. 90

Figure IV.10 – Electrostatic potential in the center of the bilayer (relative to the water region) as function of the total number of carbons of the NBD-C_n alkyl chains. 91

Figure IV.11 – Mass density distributions of POPC (black) and water (red), both recovered from pure POPC bilayers, and NBD-C_6 (blue), -C_{10} (green) and –C_{16}

(magenta), recovered from the respective 4 NBD-C_n/POPC systems. The profiles of the NBD amphiphiles were multiplied by 32 for better visualization. 92

Figure IV.12 – Diffusion coefficients of POPC (A) and NBD-C_n (B) for all studied systems. 93

Figure V.1 – Structures of POPC, SpM, Chol and NBD-C_{16} (from left to right, respectively), showing the atom numbering as used throughout the text. 102

Figure V.2 – Average transverse position <*z*> of specific atoms in the POPC:Chol:NBD-C_n (top) and SpM:Chol:NBD-C_n (bottom) systems. Error bars represent standard deviations calculated over molecules and frames. See Figure V.1 for atom numbering. Cter represents the methyl group at the end of the fatty amine chain. For each atom of the POPC, SpM and Chol, the first (black) bar concerns the system without NBD-Cn. Following this bar, the order is that of increasing amphiphile chain length (from 4 to 16). The same applies to NBD-Cn atoms (which, however, lack the black bar). 105

Figure V.3 – Variation of the transverse distance between N1 and the terminal methyl (Cter) group of the amphiphiles in POPC:Chol:NBD-C_n and SpM:Chol:NBD-C_n systems. The lines are the best linear fits to the $6 \leq n \leq 14$ points, with a slope equal to 0.111 nm/CH_2 and $8 \leq n \leq 14$ points, with a slope equal to 0.110 nm/CH_2 for, POPC:Chol:NBD and SpM:Chol:NBD, respectively. Data obtained for POPC:NBD-Cn systems are added for comparison. 106

Figure V.4 – Comparison between the average transverse positions <*z*> of some relevant atoms in POPC (A), POPC:Chol:NBD-C_n (B) and SpM:Chol:NBD-C_n (C) systems. In plot (A) and (B) the host lipid atoms represented are P8 (black squares), C13 (black triangles) C24 (black circles) and average Cter of POPC (black diamonds) while in plot (C) they are P8 (black squares), C13 (black triangles) and average Cter of SpM (black diamonds). In all plots the amphiphiles are represented by N1 (green), N6 (blue), NBD COM (red) and Cter (orange). 108

Figure V.5 – Experimental parameters of the NBD-C_n homologous series in POPC (blue) [5] and POPC:Chol (1:1) (red) (unpublished results). (A) fluorescence quantum yield (Φ_F), (B) negative logarithm of the ionization constant (pKa), (C) fluorescence anisotropy (*r*) and (D) average fluorescence life time (τ). 109

Figure V.6 – Fraction of interdigitated conformations (*f*) as a function of the amphiphile chain length *n* for NBD-Cn amphiphiles in POPC (black squares), POPC:Chol (red triangles) and SpM:Chol (green circles). The fraction of interdigitated frames of the phospholipid is also shown for POPC (black line), POPC:Chol (red line) and SpM:Chol (green line). 110

Figure V.7 – Orientation of the NBD group in POPC:Chol:NBD (A, B, C) and SpM:Chol:NBD (D, E, F) bilayers. Probability density functions $P(\theta)$ of the angles between the long axis (A, D), the short axis (B, E), and the normal to the NBD plane

(defined as the vector product of the short and long axes; C, F), relative to the bilayer normal. The amphiphiles shown are NBD-C_4 (blue), NBD-C_8 (green) and NBD-C_{16} (violet). 111

Figure V.8 – H-bond fractional frequencies (*f*) of the amphiphiles in POPC:Chol:NBD (A, B) and in SpM:Chol:NBD (C, D, E) bilayers: (A) H_2O as donor for NBD acceptor atoms, (B) NBD as donor for H_2O, POPC and Chol acceptor atoms, (C) H_2O as donor for NBD acceptor atoms, (D) NBD as donor for H_2O, SpM and Chol acceptor atoms, (E) NH-SpM as donor for NBD acceptor atoms. 113

Figure V.9 – NBD-Cn alkyl chain deuterium order parameter profiles (S_{CD}) in POPC:Chol:NBD (A) and in SpM:Chol:NBD bilayers (B). Order parameter profiles of POPC *sn*-1 and SpM sphingosine chains in amphiphile free systems are also included in the plots A and B, respectively. 114

Figure V.10 – Electrostatic potential in the center of the bilayer (relative to the water region) as function of the total number of carbons of the NBD-C_n alkyl chains in POPC:Chol:NBD and SpM:Chol:NBD bilayers. 115

Figure V.11 – Mass density distributions of some selected POPC:Chol:NBD (A) and SpM:Chol:NBD (B) systems. Mass density distributions of POPC:Chol or SpM:Chol (black) and water (blue), both recovered from pure bilayers, and NBD-C_{12} (cyan), -C_{14} (orange) and –C_{16} (violet), recovered from the respective lipid:4-NBD-C_n systems, are shown. The profiles of the NBD amphiphiles were multiplied by 18 (POPC:Chol) or 23 (SpM:Chol) for better visualization. 116

Figure V.12 – Diffusion coefficients (cm^2/s) of (A) POPC (black), Chol (blue) and NBD-C_n (red) for POPC:Chol:NBD and (B) SpM (black), Chol (blue) and NBD-C_n (red) for SpM:Chol:NBD bilayers. 118

Figure VI.1 – Convergence of the PMF of NBD-C_{16} calculated from PGD simulations in the CW case: (A) Increasing the total simulation time by 5 ns intervals until the maximum of 110 ns. The arrows indicate the evolution of the PMF profiles (black line stands for a 5 ns simulation, red being 10 ns, etc.). (B) Discarding successive 5 ns intervals from the simulation data (for equilibration) with a maximum simulation time of 110 ns. (C) Data analyzed over 20 ns intervals (see inset). The time dependence of the free energy barriers for translocation/flip-flop (black) and desorption (red) are shown as insets in each plot. In the middle panel, $\Delta^{\ddagger}G_t^{o}$ and $\Delta^{\ddagger}G_d^{o}$ indicate the free energy barriers for the translocation and desorption processes, respectively. 128

Figure VI.2 – Convergence of the PMF calculated from PGD simulations for WC: (A, B) increasing the total simulation time by 5 ns intervals until the maximum simulation time of 130 ns; (C, D) discarding successive 5 ns intervals for equilibration with a maximum simulation time of 130 ns. The profiles shown in panels (A, C), and (B, D), have the reference position defined to be at the center of the bilayer and in the water region, respectively. The arrows show how the PMF profile evolves. The time

dependence of the free energy barriers for translocation (black) and desorption (red) are shown as insets in panels (A, C). 129

Figure VI.3 – PMF profiles of NBD-C_{16} calculated from PGD simulations with the CW (black) and WC (red) schemes. In CW, the data used for analysis covered a period from 20 ns to 110 ns, and in WC a period from 120 ns until the end of the simulation. In (A) the PMF is defined to be zero in the center of the bilayer, and in (B) the PMF is defined to be zero in the water region. 130

Figure VI.4 – (A) PMF profiles of the NBD-C_n molecules calculated with the PGD method in the CW case. (B) PMF profiles of the NBD-C_n molecules calculated with the PGC method using the CW scheme. PMFs of NBD-C_4, -C_8, -C_{12}, and -C_{16} are depicted as blue, red, green, and black lines, respectively. (C) Density profile for the unperturbed bilayer taken from the system with NBD-C_4 at a distance of 4 nm from the bilayer center. The blue, cyan, and black lines refer to POPC, water, and the whole system, respectively. Grey areas show the region where the free energy is at RT (kJ/mol) from the minimum, using PGC. 132

Figure VI.5 – Experimental [6] and calculated (PGD and PGC) free energies $\Delta^{\ddagger}G^{o}$ for the translocation and desorption processes of the amphiphiles in the POPC bilayer... 133

Figure VI.6 – Average membrane thickness in terms of the P-P distance computed over all the lipids in the membrane. Results are given as a function of distance from the center of mass of the NBD moiety to membrane center: (A) NBD-C_4; (B) NBD-C_8; (C) NBD-C_{12}; and (D) NBD-C_{16}. Results are given for the PGD (gray) and PGC (black) schemes. The length of each bar represents the standard deviation of the calculated P-P distance. 135

Figure VI.7 – Average distance (along the membrane normal direction) between the N1 and Cter units (see Figure IV.1) of each amphiphile, $< z >_{N1\text{-}Cter}$, for varying distance z to the bilayer's center. Here, the membrane-water interface is approximately at 2.5 nm. The distance to center used here corresponds to the distance from the COM of the NBD unit to the local COM of the bilayer (PGC), or to the center of the whole membrane (PGD). 136

Figure VII.1 – Order parameter of the POPC (A) and SpM (B) chains in the symmetric POPC (blue), POPC:Chol (1:1) (red) and SpM:Chol (6:4) (green) and of the asymmetric SpM:Chol (6:4)/POPC:Chol (1:1) (black) lipid bilayers. Solid lines refer to POPC *sn*-1 and SpM acyl chains, while dashed curves refer to POPC *sn*-2 acyl chain and SpM sphingosine. 145

Figure VII.2 – PMF of NBD-C_4 (blue), NBD-C_8 (red), NBD-C_{12} (green) and NBD-C_{16} (black) in POPC (A), POPC:Chol (1:1) (B) and SpM:Chol (6:4) (C) bilayers. 147

Figure VII.3 – Energy barriers ($\Delta^{\ddagger}G^{0}$) for the processes of translocation (black) and desorption (red) of each amphiphile in POPC (A), POPC:Chol (1:1) (B) and SpM:Chol (6:4) (C) bilayers. 148

Figure VII.4 – Comparison between the PMF profiles obtained for the POPC:Chol (1:1) (red) and SpM:Chol (6:4) (green) and the PMF profiles obtained for the asymmetric bilayer (black). Data is shown for NBD-C_8 (A), NBD-C_{12} (B) and NBD-C_{16} (C). 149

Figure VII.5 – Transfer of the amphiphiles from the center of the bilayer to the equilibrium position evaluated as the *z*(t) distance from the NBD COM to the bilayer center, in POPC bilayers: (A) NBD-C_4, (B) NBD-C_8, (C) NBD-C_{12}, (D) NBD-C_{16}. NBD equilibrium positions determined from unrestrained simulations (blue) and from PMF minima (green) are shown for comparison. 152

Figure VII.6 – Frequency factor for the transfer of the NBD group from the center of the bilayer to its equilibrium position as function of the number of carbons of the alkyl chain (○), and conversion factors for the deactivation of the transition state of desorption/translocation (□/○) of the amphiphiles, calculated from the ratio between the experimental desorption/translocation rate constant and the energetic component of the absolute rate theory, applying equation (VII.6). 153

Figure VII.7 – Relaxation of the amphiphiles, NBD-C_4 (A), NBD-C_8 (B), NBD-C_{12} (C) and NBD-C_{16} (D), from the desorption transition state until the equilibrium position in POPC bilayers. The average data of several simulations (black) was fitted with a biexponential function (red). Reference for P atoms (orange), and NBD equilibrium positions determined from unrestrained simulations (blue) and from PMF minima (green) are shown for comparison. 154

Figure VII.8 – Effect in the bilayer thickness induced by the NBD-Cn amphiphiles, -C_4 (blue), -C_8 (red), -C_{12} (green) and -C_{16} (black), when located at different depths in the bilayer. Data for POPC (A), POPC:Chol (1:1) (B), SpM:Chol (6:4) (C) bilayers and for the asymmetric bilayer (lightened curves in B and C). 155

Figure VII.9 – Distance, $\langle d \rangle_{N1\text{-}Cter}$ (A, B, C) and projection in the z axis, $\langle z \rangle_{N1\text{-}Cter}$ (D, E, F) between the atom N1 and the atom Cter of alkyl chain of the amphiphiles, NBD-C_4 (blue), -C_8 (red), -C_{12} (green) and -C_{16} (black), as a function of the restrained position of the NBD group in POPC (A, D), POPC:Chol (1:1) (B, E) and SpM:Chol (6:4) (C, F). 157

Figure VII.10 – Chain dihedrals in POPC bilayers. (A) distribution of the chain dihedrals of NBD-C_{16}, and (B) fraction of *trans* dihedrals of the alkyl chains of the NBD-C_n amphiphiles, as function of the distance of the NBD to the bilayer center. Gray bar indicates the equilibrium position of the NBD group. 158

Figure VII.11 – Average fraction of hydrogen bonds over the simulation time. For each amphiphile, NBD-C_4 (A, B, C), NBD-C_8 (D, E, F), NBD-C_{12} (G, H, I), NBD-C_{16} (J, K, L), data is shown for the simulation in POPC (black), POPC:Chol (1:1) (red) and SpM:Chol (6:4) (green). Hydrogen bonds are evaluated between the NBD and the lipid

(A, D, G, J) and between the NBD and the water oxygens (B, E, H, K) or water hydrogens (C, F, I, L). 160

Figure VII.12 – Orientation of the NBD group at different bilayer depths in POPC bilayers for NBD-C_4 (A), NBD-C_8 (B), NBD-C_{12} (C) and NBD-C_{16} (D). 162

Figure VII.13 – Free energy (A, B, C, D), local diffusion coefficient (E, F, G, H) and local resistance (I, J, K, L) profiles for the amphiphiles NBD-C_4 (A, E, I), NBD-C_8 (B, F, J), NBD-C_{12} (C, G, K) and NBD-C_{16} (D, H, L) in POPC (black), POPC:Chol (1:1) (red) and SpM:Chol (6:4) (green) bilayers. 164

Figure VII.14 – Integration of the profile of the local resistances across the lipid bilayer of POPC (black), POPC:Chol (1:1) (red) and SpM:Chol (6:4) (green), for NBD-C_4 (A), NBD-C_8 (B), NBD-C_{12} (C) and NBD-C_{16} (D). 165

Figure VII.15 – Comparison of permeability coefficients of NBD-Cn, calculated from MD simulations using the inhomogeneous solubility-diffusion model, for POPC (black), POPC:Chol (1:1) (red) and SpM:Chol (6:4) (green), and calculated from the integration of the kinetic rate constants through a cell monolayer mimicked by POPC (Chapter IX) (orange). The application of the inhomogeneous solubility-diffusion model considers the origin of the PMF profiles in the water (A) or in the energy minimum of the system (B). 167

Figure VIII.1 – Equilibrium distribution of unesterified cholesterol in the various blood compartments considered in the model. Reference values in vivo (light grey bar) and equilibrium values predicted from the model using equation (VIII.3) and the parameters obtained in this work for DHE (black bar). Left panel – whole blood (a logarithm scale was used to allow comparison for all blood compartments, dominated by the erythrocytes if a linear scale was used); Right panel – lipoprotein fraction..... 177

Figure VIII.2 – Simulation results for the kinetics of cholesterol redistribution in the blood at 37 ^{o}C after a bolus of 10% total unesterified cholesterol in the aqueous compartment. The rate constants used in the kinetic model were those obtained in this work for DHE (A) or taken from literature for cholesterol [385, 394] (B). Time evolution of the concentration of unesterified cholesterol in the distinct blood compartments: aqueous phase (light blue, □), HDL_3 (green, □), HDL_2 (pink, □), Alb (blue, □), LDL (light green, □), VLDL (dark blue, □) and Erythrocytes (red, □). The *y* axis is the concentration at time *t* , $C_{(t)}$, divided by the equilibrium concentration before the bolus, $C_{(0)}$. The insets show the results obtained at longer simulation times, with the transfer of cholesterol from the lipoproteins to the erythrocytes..... 179

Figure VIII.3 – Distribution of unesterified cholesterol in the various blood compartments considered in the model. Reference values *in vivo* (light grey) and steady state values predicted from the model using equations (VIII.5) for cholesterol in the aqueous phase and in HDL, and equations in (VIII.4) for the remaining compartments, considering the rate constants obtained in this work for DHE (grey) and those taken

from literature for cholesterol [385, 394] (black). The results for the whole blood are shown in the left panel and the distribution of cholesterol among the lipoproteins is given in the right panel. The steady-state distribution in the lipoproteins obtained from the kinetic data of Chol deviate less than 1% from those measured experimentally (lower panel) or calculated from DHE rate constants (upper panel). The steady state is attained with v_+=7.5×10^{-6} M s^{-1}, k_{LCAT}=1.3×10^{-2} s^{-1} and v_+=9.9×10^{-7} M s^{-1}, k_{LCAT} =1.8×10^{-3} s^{-1}, when the dissociation rate constants of DHE and cholesterol are used, respectively. 182

Figure VIII.4 – Simulation of the homeostasis of unesterified cholesterol in the blood at 37 ^{o}C due to passive processes. The rate constants obtained in this work for DHE are used in plot A and B, while desorption rate constants taken from literature for cholesterol [385, 394] are used in plot C and D. The concentrations of unesterified cholesterol in the distinct pools were obtained from the steady state solution of the kinetic scheme developed in this work, equations (VIII.4) and (VIII.5) for a rate of cholesterol entry in the blood equal to 1.1×10^{-8} M s^{-1}. At t=0 the unesterified cholesterol in the HDL fraction was replaced by Chα and that in LDL *and* VLDL fractions was replaced by Chβ. The relative enrichment in Chα (plot A and C) and Chβ (plot B and D) in the distinct blood compartments was followed over time for HDL (black, □), LDL and VLDL (grey, □) and the erythrocytes (light grey, □)..... 184

Figure IX.1 – Scheme describing the passive permeation through tight endothelia with the inclusion of the rate and equilibrium constants as well as structural data of the compartments considered. K_{B} and $K_{\mathrm{L_p}}$ are equilibrium binding constants to serum albumin (Alb) and Lipoproteins (L_P), respectively. The rate constants of insertion, desorption, translocation and diffusion are represented by $\kappa_+^{p^{\mathrm{q}}}$, $\kappa_-^{p^{\mathrm{q}}}$, $k_{\mathrm{f}\,x}^{q}$ and k_{ld}^{p}, where p represents the membrane compartment (apical, a, or basolateral, b); $a \rightarrow b$ indicating the direction from the apical to the basolateral membrane, and q the respective leaflet (inner, i, or outer, o); $o \rightarrow i$ indicating the direction from the outer to the inner leaflet. The surface areas of the cell membrane compartments are represented by A^{p^q}, the volumes of the lipid compartments by $V_L^{p^q}$ and the volumes of the aqueous compartments by V_{w}^{r}, where p and q are defined as above and r represents the donor (D), the cytoplasm (e) and the acceptor (A) compartments. 192

Figure IX.2 – Rate constants of insertion (□), desorption (○) and translocation (Δ) (A), and affinities of the amphiphiles for cell membranes (Δ), albumin (○) and all lipoproteins (□) (B), predicted from the parameters obtained for interaction with POPC LUVs, BSA and lipoproteins [5, 6] at 25 ^{o}C. The bimolecular steps, insertion and equilibrium association, were converted into pseudo-unimolecular steps multiplying the

respective kinetic or equilibrium parameter by the amount of binding agent available ($k_{+}^{\mathrm{Lv}} \times [\mathrm{Lv}]$, $K_{\mathrm{L}} \times [\mathrm{Lv}]$, $K_{\mathrm{B}} \times [\mathrm{Alb}]$ and $K_{\mathrm{L_p}} \times [\mathrm{L_p}]$)..... 194

Figure IX.3 – A) Irreversible accumulation in the tissue for a total amount of 5×10^{-6} mol of amphiphile (see color code). The results obtained for NBD-C_8 are shown as a dashed line to permit the visualization of both -C_8 and -C_2, which show a very similar rate of accumulation in the tissue. B) Fractional deviation from the conditions at infinite time, equation IX.2, for the systems represented in the left plot: accumulation in the tissue (solid), and disappearance from the serum (dashed). Note that the logarithmic representation of the solute disappearance/accumulation is essentially linear as expected for a mono-exponential function. 196

Figure IX.4 – Dependence of the characteristic rate constant for transfer, β, and permeability coefficient calculated from equation (IX.4), P_β, with the number of carbons for the NBD-C_n homologous series, for model M1 with (□) and without (○) binding agents in the donor compartment. 197

Figure IX.5 – Plot A - Effect of the total elimination of serum albumin, lipoproteins and serum albumin *plus* lipoproteins, in the characteristic transfer rate constant (β) (and consequently in the permeability coefficient (P)) for the irreversible transfer (M1) of amphiphiles from the serum to the tissue. Plot B – Sensitivity analysis ($\beta/\beta_{\mathrm{M1}}$) with respect to the concentration of lipoproteins (main plot) or albumin (inset) in the donor compartment (see color code). The concentration of lipoproteins and albumin was varied through the multiplication of its reference value (Table A.5 in the Appendix) by a factor (*mf*). The axes in the inset of plot B are the same as in the main plot..... 200

Figure IX.6 – Relative variation of β with the values of the rate constants for the lateral diffusion in the membrane (A), translocation across the bilayer leaflets (B), desorption from (C) and insertion into (D) the cell membranes, and variation of both desorption and insertion (inset of plot D), for the model considering irreversible transfer (M1). The axes in the inset of plot D are the same as in the main plot. Gray lines represent the reference values for the rate constants ($k/k_{\mathrm{ref}} = mf$. equal to 1). Due to the kinetic details of the system, the maximal sensitivity expected with respect to each parameter is 1. In the log-log representation of the characteristic rate constant for transfer vs. a parameter, a line segment with slope 1 indicates that the parameter in point is the rate limiting step on the overall permeation over that range of parameter values. In turn, segments with slope 0 indicate that the parameter does not influence the overall permeation over that range of parameter values, as verified for the rate constants of the steps that are in fast equilibrium. 202

Figure IX.7 – Amount of amphiphile accumulated in the acceptor compartment (A), and permeability coefficient calculated from equation (IX.3) (B), for the transfer of the NBD-C_n homologous series from the serum to the tissue considering model M1 (black squares), M2 (white circles), M3 (light grey triangles), M4 (grey inverted triangles), and

M4 with the amount of binding agents in the acceptor compartment decreased by a factor of 10^3 (white inverted triangles). 206

Figure IX.8 – Prediction of the accumulation of solute in the tissue according to the analytical solutions obtained from equation (IX.6) (solid black) or from equation (IX.7) (dashed black) and results obtained by integration of the complete kinetic scheme, equations (IX.1) (solid grey), for model M2. Plot A shows the results obtained for NBD-C_{16} (similar to NBD-C_{14}) and Plot B for NBD-C_8 (similar to NBD-C_n with n = 2, 4, 6). Note that in plot A the gray line is coincident with the predictions from equation (IX.6). 208

Figure IX.9 – Prediction of the accumulation of solute in the tissue according to the analytical solutions obtained from equation (IX.6) (solid black) or from equation (IX.7) (dashed black) and results obtained by integration of the complete kinetic scheme, equations (IX.1) (solid grey), for model M1. Plot A shows the results obtained for NBD-C_{16} (similar to NBD-C_{14}) and Plot B for NBD-C_8 (similar to NBD-Cn with n = 2, 4, 6). Note that in plot A the gray line is coincident with the predictions from equation (IX.6). 210

List of Tables

Table II.1 – Structures of the most common glycerophospholipids, sphingolipids and sterol in eukaryotic cells. R, R1, R2 and R3 represent the fatty acid acyl chains, and the glycerol backbone is highlighted in green. The structures at pH=7 are shown. 13

Table IV.1– Average area per lipid and average P-P distance obtained from MD simulation. 78

Table V.1 – Structures of lipid modifications found on intracellular proteins. Adapted from [330] 100

Table V.2 – Average area per lipid and average P-P distance obtained from MD simulation. Data for the pure POPC bilayer were taken from [326] (Chapter IV), and are shown for comparison. 104

Table VII.1 – Areas per lipid of the components of the bilayers. 145

Chapter I

Objectives and Outline

Objectives

Biophysical studies regarding the characterization of membrane structure and dynamics are often carried by fluorescence studies which imply the incorporation of fluorescent dyes in the membranes. In these studies, the fluorescent membrane probe is a foreign molecule inserted in the lipid bilayer. Thus, perturbation of bilayer structure with consequences on the dynamics and thermotropic behavior of the membrane is expected to happen, and it is important to know its extention. Another concern regarding fluorescence probes is the uncertainty regarding the location of the fluorophore in the bilayer, as well as the dynamics of the bilayer-inserted probe. In this situation, the utility of the fluorescence measurement may be compromised, as there are doubts regarding the bilayer region being characterized, as well as whether the membrane probe used is a good model for the host lipid component it is supposed to emulate. In this regard, Molecular Dynamics (MD) simulations have been established as a powerful methodology to analyze both the location and dynamics of the inserted probe and its effect on the host lipid bilayer. A number of experimental observables, such as area per lipid, bilayer thickness, membrane conformational order, electrostatic potential and lateral diffusion can be characterized in probe-free and probe-loaded simulations, which is also useful to validate the methodology.

In addition to the membrane characterization, the attachment of fluorescent dyes to other solutes is useful to study the equilibrium and kinetics of the interaction of drug-like molecules with membranes, which is a topic of interest to several research groups, including ours. In the last years our research group has been studying the structure and dynamics of phospholipid bilayers, and more recently we have been studying the detailed kinetics and thermodynamics of the interaction of amphiphilic molecules with lipid bilayers in different phases [1-7], with proteins [5, 8] and lipoproteins [9, 10]. These work led to the determination of equilibrium constants such as binding constants to Large Unilamellar Vesicles (LUVs) with different compositions, K_L; binding constants to serum proteins, K_B; binding constants to lipoproteins, K_{LP}; and kinetic parameters such as insertion of the amphiphiles into (k_+) and desorption of the amphiphiles from the vesicles (k_-), and translocation from one monolayer to the other (k_f). The free energies obtained from the determined equilibrium and kinetic rate constants may be compared with values calculated using MD simulations. MD

simulations of drugs in membranes can also help to rationalize the experimental permeation process in terms of detailed intermolecular interactions.

Pharmacological agents are often not substrates for active mechanisms but rather permeate the BBB by passive transport. It is therefore of extreme pharmaceutical and medical importance to quantitatively understand the mechanisms of passive transport of these agents across the BBB. For passive permeation across a cell monolayer, such as a tight endothelium, the permeating molecule must first interact with the plasma membrane and permeate the apical domain exposed to the blood, then cross the cytoplasm of the cell and finally interact again with the plasma membrane and permeate the basolateral domain before entering the target tissue. Therefore, conjugating the equilibrium and kinetic parameters available in the literature, it is possible to build a mechanistic scheme to predict the permeation rate of molecules through biological barriers and their accumulation profiles in each of the system compartments.

One of the great challenges in the development of new and more efficient pharmaceuticals, targeted to brain pathologies, is to find means to foster the transport of active drugs across complex membrane structures, such as the tight endothelium of the BBB. Therefore, the prediction of the permeation rate of new drugs through biological barriers is certainly valued by the characterization and by the establishment of rules for the interaction of solutes with lipid membranes. Regarding membrane biophysics, the ability to understand and describe, at high spacial and temporal resolution, how molecules interact and follow their way through lipid membranes is also of fundamental importance. To increase the current knowledge in the field, this work intend to perform three main tasks: i) the atomistic characterization of the interaction of the fluorescent molecules of the 7-nitrobenz-2-oxa-1,3-diazol-4-yl (NBD)-Cn homologous series, with lipid membranes; ii) the atomistic characterization of the permeation process through lipid bilayers with the focus on the energetics of the process, and finally; iii) compile all the simulation and experimental data available to build a mechanistic model to simulate and predict the permeation rate of those molecules through lipid barriers.

Outline

This dissertation is organized in 10 main chapters. In this Chapter, the objectives and outline of the dissertation are exposed. Chapter II consists of a literature review

covering all the important topics addressed in the dissertation. Chapter III is dedicated to the description of the methodologies used. First, a general introduction to MD is given. Then the methods and approximations used in further Chapters are described. In Chapters IV and V the equilibrium interaction of the homologous series of NBD-labeled fatty amines with cholesterol-free and cholesterol-containing lipid bilayers, respectively, is characterized using MD simulations. Chapter VI describes an MD study with methodological focus on how to obtain the free energy of interaction of the NBD-Cn homologous series with lipid bilayers. Then, Chapter VII presents the free energy of interaction of the homologous series with cholesterol-free and cholesterol-containing lipid bilayers, and with an asymmetric lipid bilayer, where the permeation process is characterized with atomic detail. Chapter VIII assesses the importance of passive transport in blood cholesterol homeostasis using kinetic modulation with experimental parameters, and in Chapter IX the importance of the kinetics of the interaction of drugs with lipid bilayers is assessed by the quantitative modeling of passive permeation through a cell monolayer. Finally, in Chapter X, all information is summarized in a general concluding chapter, which is followed by an appendix section and references.

Chapter II

Literature Review

II.1 – Biological Membranes

II.1.1 – Historical Perspective

The relationship between hydrophilic aqueous medium and hydrophobic fatlike molecules has intrigued scientists since the 1770s. [11] In the 1890s, Overton measured the rate of absorption of several compounds into cells. He also measured their olive oil-water partition coefficients, and found that lipophilic compounds readily entered the cell, whereas hydrophilic compounds did not [12]. This lead him to conclude that the cell membrane must be oil-like. In 1925, Gorter and Grendel [13] proposed a model where membrane lipids are arranged in a bilayer configuration, in which parallel sheets of phospholipids have polar or charged headgroups oriented toward the aqueous environment and acyl chains interacting within the hydrophobic membrane core. In the following years, models for the cell biological membrane appeared, such as that of Danielli and Davson in 1935 [14]. The latter, which included a lipid bilayer covered by a layer of protein on both sides, was the first membrane model to be widely accepted. In 1972, Singer and Nicolson proposed the fluid-mosaic model [15], which took into consideration the dynamic nature of lipid-protein interactions, describing the biological membrane as a fluid-like phospholipid bilayer, in which freely diffusing globular proteins are embedded. This model, illustrated in Figure II.1, became the framework and benchmark for our current understanding of membrane bilayers and their physiological function.

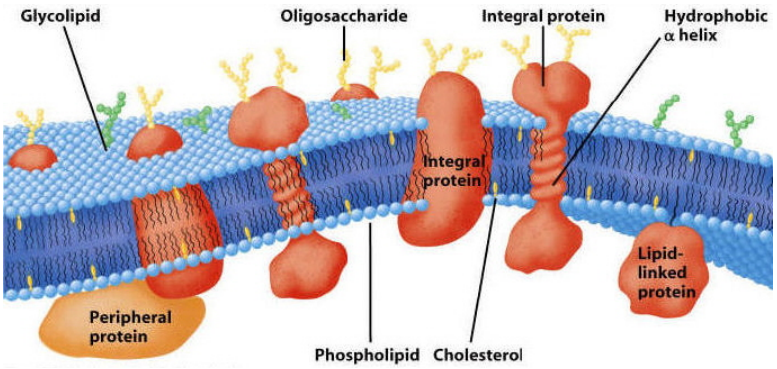

Figure II.1: Illustration of a biological membrane. Adapted from http://www.cmns.leeds.ac.uk/SSbiomemb.htm.

The assumed homogeneous nature of membrane lipid bilayers was called into question still in the 1970s [16], including in the work of Singer and Nicholson. A heterogeneous distribution of lipids and proteins is observed within spatially separated regions of the same membrane of Golgi or apical and basolateral plasma membranes of polarized cells [17]. During the past two decades, the organization of lipid and membrane proteins has focused on localized regions within the membrane, known as membrane microdomains [18] or membrane rafts [19]. The current view of biomembranes is more like a ‘‘dynamically structured mosaic model’’, accounting for the formation of small-scale clusters at the molecular level and large-scale clusters (or groups of clusters) at the submicrometer level [20], that induce some restrictions to the diffusion of membrane components.

The rapid development of computing power during the last decade has made molecular simulations of lipid bilayers feasible for many research groups, and computer simulations have become a well established tool for modern investigations on molecular structure. The first attempts of computer simulations of model bilayers composed of amphiphilic molecules with atomistic resolution were made in 80s, [21, 22] which were later followed by simulations of fully hydrated bilayers built by lipids typical of biological membranes [23-25]. Despite their limitations, computer simulations are currently, in close collaboration with the experiments, a strong technique for the characterization of lipid bilayers of increasing complexity. [26, 27]

II.1.2 – Structure and Composition of Biological Membranes

Biological membranes play an important role on the function of all cells, both prokaryotic and eukaryotic, plant and animal, defining the borders of different biological compartments like cells or cell organelles, and presenting support for different types of biological functions. Membrane lipids are amphiphilic molecules that contain two main parts with different water solubility: the hydrophobic nonpolar tails, with higher affinity to nonpolar solvents and the hydrophilic head group, with higher affinity to polar solvents, such as water. Glycerophospholipids, the most abundant lipids in biological membranes, have a hydrophilic head group and two hydrophobic alkyl chains connected by a glycerol backbone as shown in Figure II.2.

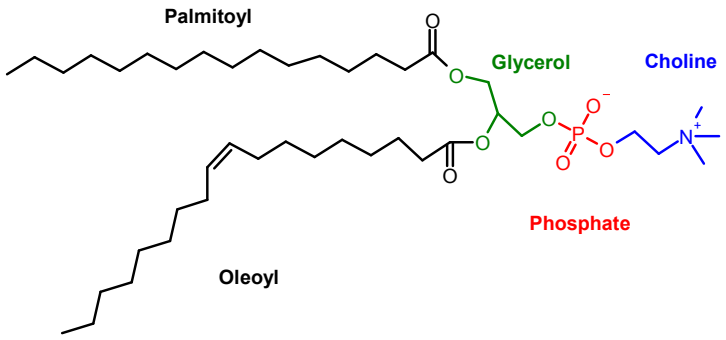

Figure II.2 – Illustration of a glycerophospholipid structure, showing the structure of POPC.

In aqueous solutions, amphiphiles spontaneously aggregate in an arrangement that allows each part of the molecule to interact with its favored environment**,** such as, micelles, microemulsions and vesicles. The main force behind this self-aggregation phenomenon is the hydrophobic effect. Due to the energetically unfavourable exposition of the hydrophobic chains to the aqueous environment, lipids will aggregate to minimize the free energy of the system. The formation of these self-assembled structures only occurs above a certain concentration called Critical Aggregation Concentration (CAC), or Critical Micelle Concentration (CMC) if micelles are formed. The structure that a lipidic aggregate will adopt in aqueous solution is the one that minimizes the free energy of the system, and can be predicted considering three molecular parameters. The "Critical Packing Parameter" (CPP) relates the polar and nonpolar parts of an amphiphilic molecule, through the optimal area occupied by the polar interface (S_0), the maximum length (l) and the molecular volume of the apolar portion of the amphiphile (v). [28, 29]

$$CPP = \frac{v}{l.S_0} \qquad \text{(II.1)}$$

Systems with CPP < 1/3 tend to form normal micelles (with positive curvature), systems with CPP = 1 tend to form bilayer structures and if CPP > 1 the system will form reverse micelles (with negative curvature). The two acyl chains of most biological phospholipids and their large polar head group results in a CPP ≈ 1, forming a bilayer.

In biological membranes the lipid bilayer provides a barrier with selective permeability that restricts the movement of hydrophilic molecules and macromolecules in and out of the compartment. The different types of proteins present on the two faces of the bilayer contribute to the distinct functions of each compartment's interior and exterior, and

control the movement of selected hydrophilic molecules and macromolecules across the bilayer.

The major lipid classes present in biological membranes are: Glycerophospholipids, such as phosphatidylcholine (PC), phosphatidylethanolamine (PE), phosphatidylserine (PS), phosphatidylinositol (PI) and phosphatidic acid (PA), where one of the glycerol hydroxyls is linked to a polar phosphate-containing group, and the other two hydroxyls are linked to hydrophobic acyl groups; Phosphosphingolipids, such as sphingomyelin, with the same head group as glycerophospholipids, but where the hydrophobic group is constituted by ceramide; Glycoglycerolipids, such as monogalactosyldiacylglycerol, where the *sn*-3 position of glycerol forms a glycosidic link to a carbohydrate; Glycosphingolipids, such as monoglycosyl ceramides, with a glycosidic linkage to the terminal hydroxyl of ceramide; and sterols like cholesterol. Structures of the most common glycerophospholipids, sphingolipids and sterols in eukaryotic cells are summarized in Table II.1. Glycerophospholipids may account for nearly 70% of the total lipid content in mammalian cells, while the remaining 30% consists of cholesterol, sphingomyelin and glycosphingolipids. [30] PC (40-50%) and PE are the most prevailing glycerophospholipids (20-45%), PS, PI and PA being present in smaller amounts (10%). [31] Although these classes of lipids are the most common, any single membrane can contain well over 100 unique lipid species, permitting specific lipid combinations in order to reach the best performance for a determined function. [32] The most common fatty-acid chains (saturated or unsaturated) in glycerophospholipids include myristate, palmitate, stearate, oleate, linoleate, and arachidonate. These fatty acids differ in carbon atom number by multiples of 2 because they are elongated by the addition of 2 carbon units through Acetyl-CoA. [33]

Table II.1 – Structures of the most common glycerophospholipids, sphingolipids and sterol in eukaryotic cells. R, R1, R2 and R3 represent the fatty acid acyl chains, and the glycerol backbone is highlighted in green. The structures at pH=7 are shown.

<table>
<tr><td rowspan="2">Glycerophospholipids</td><td>Triacylglycerol</td><td> 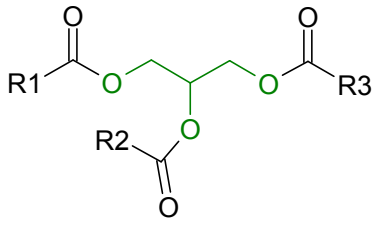 </td></tr>
<tr><td> 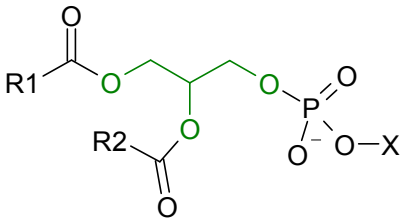 </td><td>
<table>
<tr><th>Formula of X:</th><th>Name of the phospholipid</th></tr>
<tr><td>H</td><td>Phosphatidic acid</td></tr>
<tr><td> 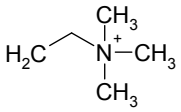 </td><td>Phosphatidylcholine</td></tr>
<tr><td> 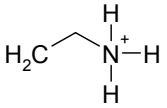 </td><td>Phosphatidylethanolamine</td></tr>
<tr><td> 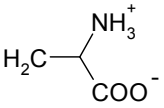 </td><td>Phosphatidylserine</td></tr>
<tr><td> 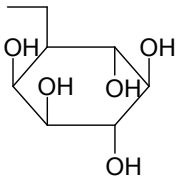 </td><td>Phosphatidylinositol</td></tr>
</table>
</td></tr>
<tr><td>Sphingolipids</td><td>Sphingosine backbone
 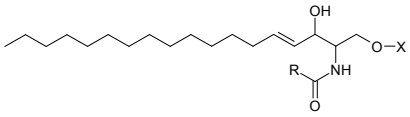
acyl chain</td><td>
<table>
<tr><th>Formula of X:</th><th>Name of the sphingolipid</th></tr>
<tr><td>H</td><td>Ceramide</td></tr>
<tr><td> 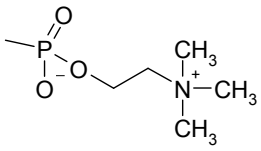 </td><td>Sphingomyelin</td></tr>
</table>
</td></tr>
<tr><td>Cholesterol</td><td colspan="2"> 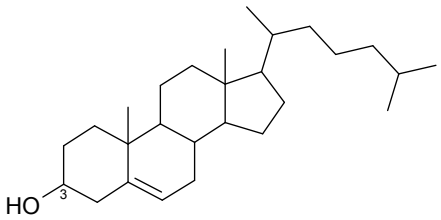 </td></tr>
</table>

Membrane proteins are the molecules responsible for most cell functions, such as enzymes, transporters, receptors and pores. They are generally associated to the membrane through noncovalent bonds, such as the hydrophobic effect or electrostatic

interactions, and may be classified as extrinsic (or peripheral) or intrinsic (or integral) depending of the degree of harshness of the treatment required to release them from the membrane. [32] Extrinsic proteins are weakly bound to the membrane surface by electrostatic interactions, either with the lipid head groups or with other proteins on one face of the bilayer, and may be removed from membranes by washing with buffers at different pHs or ionic strengths. Lipid-anchored membrane proteins, which are also peripheral proteins, have one or more covalently attached lipid molecules that penetrate one leaflet of the membrane. These proteins are anchored to the plasma membrane by acylation or prenylation. In the case of acylation, a N-terminal glycine residue of the protein is covalently attached to the 14-carbon fatty acid residue (myristoylation) or a cysteine residue is attached to the 16-carbon fatty acid residue (palmitoylation). Prenylation occurs when the –SH group of a cysteine residue at or near the C-terminus of the protein is bound through a thioether bond to either a farnesyl or a geranylgeranyl (prenyl) group. Cell-surface proteins and heavily glycosylated proteoglycans are present on the exoplasmic face of the membrane and are attached there by a glycosylphosphatidylinositol (GPI) anchor. [34-36] Intrinsic proteins are bound to the bilayer interior by nonpolar interactions, and may only be removed by treatment with detergents that disrupt the lipid bilayer. These proteins usually pass through the lipid bilayer and are therefore composed of three domains: a cytosolic domain exposed on the cytosolic face of the bilayer, an exoplasmic domain exposed on the exoplasmic face of the bilayer, and a membrane-spanning domain, which passes through the bilayer and connects the cytosolic and exoplasmic domains.

II.1.2.1 – Membrane Density Profile

In order to understand the organizational and functional principles of membranes, it is important to realize that a lipid bilayer is not just a homogeneous thin slab of a low dielectric medium immersed in water, but a highly stratified structure with a distinct molecular profile. The membrane trans-bilayer structure is described by the "Four Region" model [24], dividing de bilayer in four regions: 1- *Low Headgroup Density*, from the point where the presence of the membrane begins to result in a perturbation of the bulk water structure until the water density and the headgroup density are comparable; 2- *High Headgroup Density*, where the water density drops to less than 1% and bulk-like water is no longer present; 3- *High Tail Density*, starting at the edges of the penetrating strands of water until the

density of the membrane has dropped to that of liquid hexadecane; and 4- *Low Tail Density*, the remaining part of the membrane centre.

The total free-volume inside the membrane and the electron density profile, obtained from MD simulations [37], Figure II.3, are two physical aspects in accordance with the model introduced above. Symmetrically, at the bilayer interface in region 2 the free volume is minimal while the electron density is maximal, and at the bilayer center, in region 4, the free volume is maximal while the electron density presents a minimum. The ordering of alkyl chains in the bilayer decreases the free volume fraction. The free volume is elongated in the highly ordered chain region with its long axis normal to the bilayer interface, approaching spherical symmetry in the center of the bilayer. Small free volume is more elongated than large free volume. [38] These special features of bilayers play important roles in insertion, desorption and permeation of solutes through biological membranes.

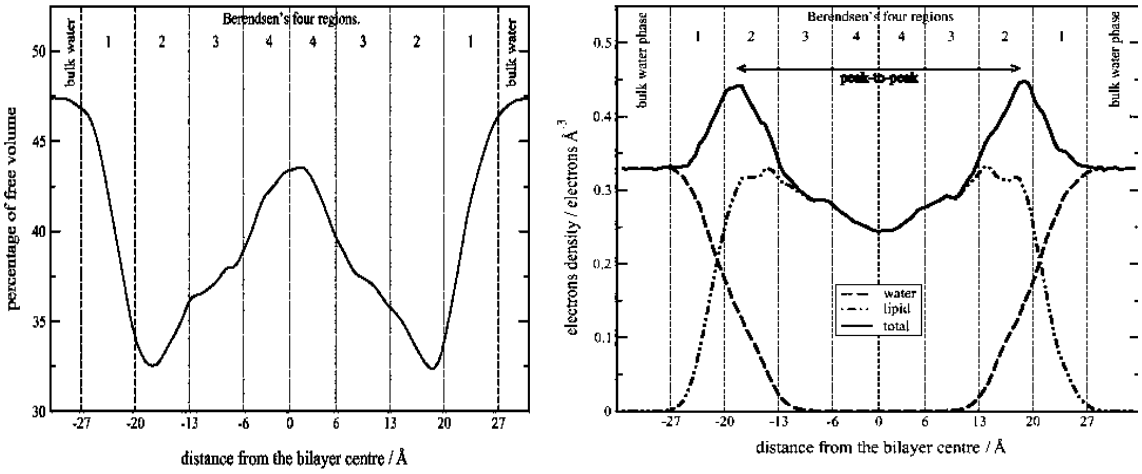

Figure II.3: Free volume distribution (left) and electron density profile (right) along the bilayer normal. Adapted from [37].

II.1.2.2 – Membrane Lateral Pressure

The main driving force for the formation of lipid aggregates is the hydrophobic effect. However this is not always the perfect situation for lipid molecules, as they are confined to the aggregate shape being subject to large stresses. The membrane lateral pressure profile, Figure II.4, is built up from three contributions that at equilibrium must sum up to zero: a positive pressure resulting from the repulsion between the head groups, a negative pressure that acts in the hydrophobic-hydrophilic interface and a positive

pressure arising from the entropic repulsion between the flexible alkyl chains. The lateral pressure density (force per unit area) of the bilayer amounts on average to about 350 atm. [39]

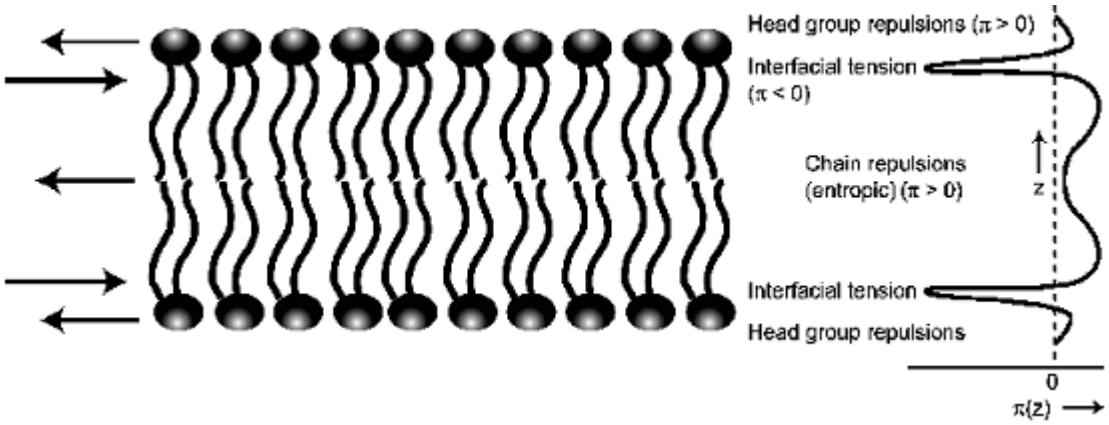

Figure II.4: Lateral pressure profile of a lipid bilayer. Schematic illustration of a cross section through a symmetric lipid bilayer with an indication of the forces that act within the layer (left) and the resulting pressure or stress profile (right). Adapted from [39].

The lateral pressure profile gives an important contribution to the molecular conformation and function of intrinsic proteins. Anesthetic action is a typical example of the perturbation of lipid protein interaction. It has been argued [40, 41] that a change in bilayer composition due to anesthetic incorporation, alters the lateral pressure profile, which in turn is directly coupled, through the mechanical work that accompanies lateral expansion or compression of the protein as a function of depth in the bilayer, to the protein conformational free energy landscape. This has influence in the function of ion channel proteins if channel opening is accompanied by a non-uniform change in cross-sectional area of the protein [40, 41]. Supporting evidence comes from atomistic and coarse-grained computer simulations on the effects of alcohols and volatile anesthetics on membranes. [42, 43]

II.1.2.3 – Electrical Properties

The electrical profile associated with lipid membranes strongly influences the interaction of charged and polar molecules with them. Anions bind with higher affinity and translocate more rapidly across bilayers than structurally similar cations. [44] The

electrical profile associated with a lipid membrane consists of three components: i) the transmembrane potential, ii) the surface potential, and iii) the dipole potential.

The transmembrane potential represents the electrical potential difference between the two bulk aqueous phases separated by the membrane, due to a difference in ionic composition between the aqueous phases of both sides of a membrane. The distribution of specific ions inside and outside cells generates a charge unbalance which leads to a transmembrane potential of about 10-100 mV being the cytoplasmic side negative relative to the outside. [45] This transmembrane potential has an important role in the regulation of protein function, such as in the case of ion-pumps [33].

The surface potential is an electrical potential near the membrane surface, resulting from the surface density charge and the bulk concentration of ions, as described by the Gouy-Chapman theory [46]. Most biological membranes have negatively charged phospholipids, resulting in a negative surface charge and a surface potential of about -8 to -30 mV [45]. Therefore, the evaluation of membrane electrostatic potential, in the presence of charged lipids, must consider the surface potential component in addition to the transmembrane potential. The common experimental method to measure the surface potential is through the measurement of the zeta potential.

The dipole potential, which is positive in the center of the bilayer, comes from the alignment of dipoles in the system. In a bilayer, lipids are subject to a restricted orientation, with the hydrocarbon chains facing each other forming a nonpolar region, and the headgroups in contact with the aqueous solution. This orientation of the lipids leads to preferential orientation of their dipoles as well as to an orientation of the water molecules interacting with the interface. It is accepted that the phospholipid headgroups, the carbonyl groups, the terminal methyl groups and the interfacial water molecules give the major contribution to the global membrane dipole potential [47, 48]. This results mainly from the orientation of water dipole on the interface, the orientation of fatty ester carbonyls of each phospholipid molecule and the dipole moment of the terminal methyl groups in the chains. The alignment of dipoles leads to a potential of ≈ 400 mV in PC monolayers and ≈ 280 mV in bilayers [47], affecting both ion transport processes across model lipid membranes and protein insertion [44]. It has also an important role in the solubility of amphiphilic molecules in different membrane phases, because of their different dipole magnitudes and orientations [2, 49].

II.1.3 – Dynamics and Organization of Biological Membranes

The importance of lipid dynamics for membrane function was recognized with the fluid-mosaic model [15] of biomembranes. The model recognized the liquid–crystalline nature of the lipid bilayer [50] as the matrix of biological membranes, a stable bilayer of mostly phospholipids that maintain liquidlike properties in their molecular motions [50]. The membrane fluidity implies that all its components, even the proteins, are able to have different types of motions with different time scales. The fluid character of the biological membrane is very important for its functions. It enables rapid diffusion of membrane proteins within the bilayer plane and allows protein-protein interactions to take place (important for cell signaling), facilitates distribution of membrane lipids and proteins from insertion, or synthesis sites to other regions of the cell, allows membranes to fuse and mix molecules and ensures even distribution of membrane molecules between daughter cells following division. Studies in which membranes of certain organisms have to adapt themselves in response to several stimuli, such as exposure to drugs, altering their lipid composition, show that maintenance of membrane fluidity has a vital role in their functions. [51] Moreover, an important movement is the spontaneous desorption and insertion of lipids, a type of motion also relevant for the interaction of other molecules with biomembranes.

Lipid order and dynamics of biomembranes may be studied by nuclear magnetic resonance (NMR), infrared and Raman spectroscopy, fluorescence spectroscopy (using fluorescent labels), electron paramagnetic resonance (EPR) (using spin labels), differential scanning calorimetry (DSC), X-ray and neutron diffraction experiments. [52] The increase in computing power opened the way to sophisticated molecular simulations where the time-dependent location of all atoms in the bilayer permits the most detailed description of molecular motions [25, 53]. Lipids on a membrane may present conformational, translational and rotational movements. The time scale of motions covers over 15 orders of magnitude, from femtoseconds to hours, as illustrated in Figure II.5. Movements of individual bonds are fastest, followed by motions of lipid segments. Vibrations and bond torsional oscillations occur on a subpicosecond range, and *trans*/*gauche* isomerizations can occur in pico- to nanoseconds time scale. Motions of entire lipid molecules and undulatory motions of patches of the bilayer are slower, and occur on longer time scales. Rotation about a long axis and wobble of lipids occur in nanoseconds, lateral diffusion in the plane of the bilayer in nano- to microseconds,

and undulatory motions can occur in microseconds to seconds. Flip-flop of lipids between the two monolayers of a bilayer spans a time scale from milliseconds to hours. Membrane order and dynamics can be influenced by changes in phospholipid headgroup structure, hydrocarbon chain length and unsaturation, cholesterol content, temperature, state of hydration, but also by interaction with solvents and solutes like alcohols [54].

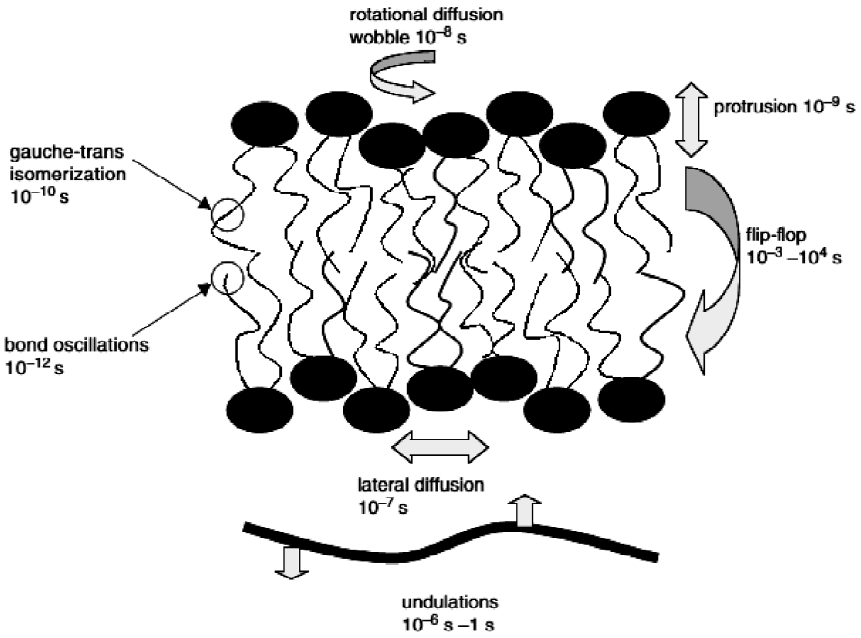

Figure II.5 - Lipid motions in biomembranes and their approximate characteristic times. Adapted from [52].

The order parameter (S_{CD_i} **)** of lipids is one of studied properties of lipid membranes to assess dynamics and perturbation by solutes:

$$S_{CD_i} = \frac{1}{2}\left\langle 3\cos^2\theta_i - 1 \right\rangle \tag{II.2}$$

where θ_i is the angle between the normal to the bilayer surface, and a chemical bond labeled *i*. However, a low order parameter value per se does not differentiate between a particular fixed orientation of the vector to the axis of reference that results in low S_{CD_i}, and rapid averaging over many orientations. The order parameter may be zero because a bond is oriented at a fixed magic angle (θ_i = 54.7º) to the bilayer normal, or because its orientation is perfectly random over time.

The glycerol backbone is the least flexible region of phospholipids, in agreement with the small free volume in this region of the bilayer. NMR and neutron diffraction results indicate that the head groups of PC and PE have a preference for orienting parallel to the bilayer plane. [55-58] The relative rigidity of the glycerol structure is seen in the difference between the orientation of *sn*-1 and *sn*-2 chain carbonyl groups. [59] It follows that the order profiles in *sn*-1 and *sn*-2 chains are quite distinct. In *sn*-1 chains, order parameters are high, almost invariant for carbon atoms up to the middle of the chain, and decreasing toward the terminal methyl group. [60-62] In contrast, *sn*-2 chains have lower order parameters at carbon C2, and order of the two hydrogens (or deuteriums) at C2 is nonequivalent. The order profile of the remainder of the *sn*-2 chain resembles that of the *sn*-1 chain. The lower order at C2 is a reflection of differences in chain orientation near the glycerol. [62, 63] The higher order of chains near the lipid/water interface is the consequence of anchoring one end of the flexible chains to the rigid glycerol group. The methyl end of chains is permitted to move freely, resulting in the characteristic order parameter profile.

Figure II.6 shows data recently obtained for the order parameter profiles of POPC [64]. Most phospholipids in biomembranes carry an unsaturated *sn*-2 chain which increases its hydration [65], and reduces the fluid–gel phase transition temperature of lipids in about 50 ºC compared to saturated phospholipids with a similar number of carbons per hydrocarbon chain [66, 67]. This is frequently view as an indication of higher fluidity of membranes with unsaturated hydrocarbon chains. Although lower order parameters are not necessarily the result of higher motional freedom, lipid order parameters in unsaturated fluid membranes are indeed lower [62, 67] and have a tendency to decrease with increasing unsaturation of the bilayer [67]. The lower chain order is related to packing disorder resulting from the bulky *cis* double bonds of unsaturated chains.

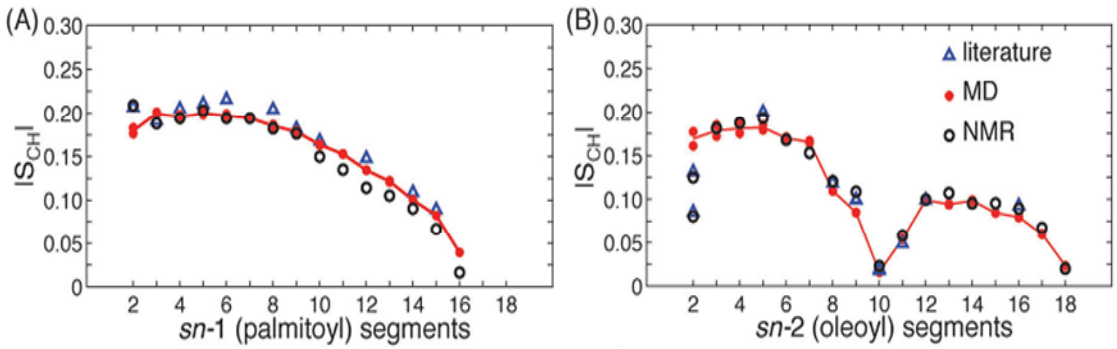

Figure II.6 – Order parameter magnitude $|S_{CH}|$ vs. carbon segment number for the *sn*-1 (A) and *sn*-2 (B) acyl chains of POPC. Adapted from [64]. Black dots and red dots refer to experimental data and MD simulations from [64]. Blue triangles refer to data from references therein.

Lipid diffusion can be studied by NMR [68] and fluorescence techniques [69]. Macroscopically, the lateral diffusion of lipids can affect signal transduction processes. Microscopically, the membrane fluidity and order has a considerable impact in solute permeation and uptake/release processes. Rapid lateral diffusion with values of the diffusion coefficient (D) in the range of 10^{-8} to 10^{-7} cm^2/s is one of the hallmarks of a fluid lipid bilayer. Assuming that lipids do not encounter any barriers during the diffusion process over the cell surface, they travel around 10 μm within 1 s, equivalent to the typical dimension of mammalian cells. However, membranes compartmentalize into domains with different lipid/protein composition, which induce some restrictions to the diffusion of membrane components. [70]

Lipid membranes undergo thermally driven undulations with correlation times that cover more than six orders of magnitude from a fraction of a microsecond to seconds. The corresponding wavelength of such undulations covers nano to micrometers. Membrane undulations are collective movements of the entire bilayer that are distinct from the movement of individual lipids or lipid segments along the bilayer normal. The latter is called protrusion and most likely is related to lipid head group movements. Protrusion of the entire lipid could be restricted because of the necessity to correlate movements between neighboring lipids in the membrane. A variety of cellular processes are related to membrane undulations, such as membrane fusion, exocytosis and endocytosis, cell–cell interaction, and adhesion of cells to solid surfaces. [52]

The movement of lipids between the two monolayers of a bilayer, flip-flop, as introduced by Kornberg and McConnell [71] (also known as translocation), requires a

translational movement along the bilayer normal and a rotation by 180º. Translocation rates have been measured by EPR [71], NMR [72], and fluorescence techniques [73, 74]. In fluid model membranes composed of lipids with saturated hydrocarbon chains and no protein, the half-time of flip-flop ranges from hours to days. Because such transbilayer movement of phospholipids requires that the hydrophilic head group traverses the hydrophobic bilayer core, a very unfavorable event, the process is slow. In contrast, the energy barrier for molecules with less distinct polarity, like cholesterol and fatty acids, is much lower. Correspondingly, they have half-times of flip-flop from seconds to milliseconds. Flip-flop times ranging from a few seconds [75, 76] to hours [77-80] have been reported for cholesterol in reconstituted and biological membranes, depending on the experimental method. Typical rates of phospholipid flip-flop in biomembranes are much higher than in model membranes. The differences have been assigned to the action of flippases, proteins that actively or passively facilitate transbilayer movement of lipids. [81]

A marked feature of the organization of biological membranes is the lateral heterogeneity. Membrane domains, "rafts", are cholesterol and sphingolipid enriched regions [82, 83] within a heterogeneous membrane bilayer, which are specialized membrane domains. In the liquid-ordered phase (*lo*) of membrane domains the acyl chains of lipids are extended and tightly packed, as in the gel phase, but have a higher degree of lateral mobility [84]. Experimental evidence suggests that rafts vary in size from nanometers to domains as large as microns [85-87]. The cohesive forces, which maintain these assemblies as principal elements of the membranes, originate from within a microdomain structure, where lipid–lipid, protein–protein, and protein–lipid interactions, as well as sub- and supra-membrane effectors (cytoskeletal, extracellular matrix, other cell), many of them genetically predestined, play equally important roles. [20] Due to the free amide and free hydroxyl group on sphingomyelin, this lipid has both hydrogen bond–accepting and donating groups. In addition, the amide-linked acyl chains of sphingomyelin are most often saturated. Together, these properties allow this lipid to facilitate the formation of extensive hydrogen-bonded networks. In contrast, the predominant glycerophospholipids consist of a glycerol backbone with ester-linked fatty acids in the *sn*-1 and *sn*-2 positions. Glycerolphospholipid acyl chains are usually 16 to 18 carbons in length, most often unsaturated at the *sn*-2 position, and have only hydrogen bond–accepting capacity. Thus, they are organized within the membranes in a

manner distinct from that of sphingolipids. The naturally occurring phospholipids, frequently containing unsaturated acyl chains at the *sn*-2 position, tend to have a much lower affinity for the *lo* phase and are thus largely excluded from these domains. A number of protein and lipid signaling molecules have been localized to membrane rafts. [88] The association of the components of signal transduction processes with membrane rafts has important functional and regulatory consequences. Membrane domains are proposed to be involved in a wide variety of cellular processes, such as protein sorting [19], signal transduction [88], internalization of toxins, bacteria, and viruses [89-91], and cholesterol transport [92, 93].

II.1.4 – Membrane Asymmetry

Since biomembranes form closed compartments, one face of the bilayer is automatically exposed to the interior while the other is exposed to the exterior of the compartment. Each face therefore interacts with different environments and performs different functions, which are in turn directly dependent on its specific molecular composition [32, 94], which is different for the distinct cell types and organelles. The asymmetric distribution of proteins in cell membranes is well established and vital for cells. The observation that some proteins require specific surrounding lipids to acquire their native structure points towards an asymmetric distribution of lipids as well. [95] Different types of phospholipids and lipid-anchored membrane proteins are typically present on the two faces, and different domains of integral proteins are exposed on each face of the bilayer. In the case of the plasma membrane, the lipids and proteins of the exoplasmic face are often modified with carbohydrates, which due to simplicity reasons are not considered in most model membrane systems. However, lipid asymmetry is not absolute being almost every type of lipid present on both sides of the membrane bilayer, but in different amounts, as illustrated in Figure II.7.

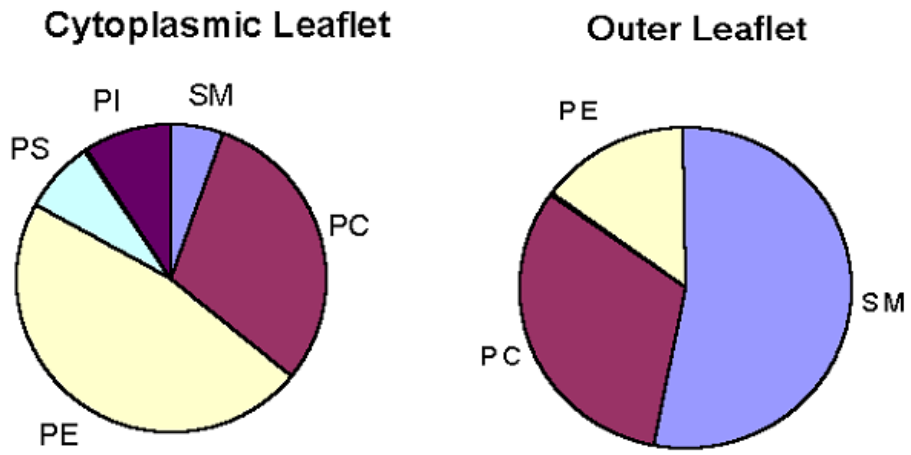

Figure II.7 – Illustration of the distribution of major phospholipids, sphingomyelin (SM), phosphatidylcholine (PC), phosphatidylethanolamine (PE); phosphatidylserine (PS) and phosphatidylinositol (PI), between the outer and cytoplasmic leaflets of the human erythrocyte membrane. Adapted from [96]

The plasma-membrane is well characterized regarding asymmetric lipid distribution. The outer leaflet lipid composition of this membrane is enriched in PC and SM, while the inner cytoplasmic leaflet includes considerable amounts of PE and negatively charged phospholipids. [30, 81, 94] The erythrocyte membrane has large amounts of SM, PC and cholesterol with significant amounts of PE, PS and PI. [81, 94, 97-101] It is usually considered that SM is located mostly in the outer monolayer [81, 94, 98] and that a significant amount of PC is located in the inner monolayer together with all PS and almost all PE [81, 98]. The distribution of cholesterol between the outer and inner leaflets is controversial but, given the fast rate of translocation expected for cholesterol, it is expected to be equilibrated with similar concentrations in both leaflets. [94, 102, 103] Another important characteristic of the erythrocyte membrane lipid distribution is the higher abundance of unsaturations in the fatty acyl chains of the inner leaflet lipids [100], in agreement with the lower viscosity and more fluid state of this monolayer [81]. Molecular Dynamics have been used to study membrane asymmetry [104] including the spontaneous curvature and stability. [105]

Translocation of phospholipids in membranes is slow due to the polar headgroup, generally with charges, whose solubility in the hydrophobic core of a membrane is very low. Therefore, a number of proteins have evolved to either dissipate or maintain this lipid gradient, which can be divided in three classes [106]: i) cytofacially-directed, ATP-dependent transporters, aminophospholipid translocases also known as flippases;

ii) exofacially-directed, ATP-dependent transporters known as floppases; and iii) bidirectional, ATP-independent transporters known as scramblases. Flippases transfer PS and PE from the outer to the inner leaflet of the plasma membrane, in a selective manner (PS transfer is faster than PE), while PC is not transferred [107, 108]. Floppases are less specific, promoting the transfer of PS, PE and PC, at much smaller rate than flippases [107, 108]. Scramblase is much less lipid specific and promotes a bidirectional transfer of phospholipids between leaflets. Plasma membrane scramblase is ATP-independent, but in order to be effective it needs the presence of high concentration of cytoplasmic Ca^{2+}. Therefore, under normal physiological conditions it is inactivated [107-109]. Whereas a concerted action of flippase and floppase accounts for the maintenance of lipid asymmetry, activation of the scramblase and concomitant inhibition of the aminophospholipid translocases contributes to its collapse.

The indicated transmembrane asymmetry of membrane cells can be related to relevant biological phenomena such as maintenance of membrane proteins activity or mechanical stability. [106, 110, 111] One of the more significant events associated with dissipation of phospholipid asymmetry is the appearance of PS on the surface of the cell. [96] This provides a clear signal for altering the haemostatic balance, since several procoagulant and anticoagulant reactions depend on interfaces containing PS. This lipid is well known as a signaling molecule for clearance by the reticuloendothelial system [112] and, by restraining its localization to the inner leaflet, the removal of healthy functional erythrocytes is avoided [31, 112]. The appearance of PS on the cell surface appears to be the primary reaction mediating recognition and clearance of apoptotic cells by macrophages, so as to prevent release of inflammatory cell contents associated with lysis. The role of the scramblase protein is essential, since once active it facilitates the transbilayer movement, exposing PS lipids to the surface of these cells [109].

II.2 – The role of Cholesterol in Lipid Membranes

Cholesterol plays critical roles in normal cell biology and in the pathogenesis of disease. [113] Despite being a cause of serious diseases, namely atherosclerosis, cholesterol is ubiquitous in mammal biological membranes. Although it can be orally absorbed, cholesterol is the end product of a series of complicated and energetically expensive enzyme-catalyzed steps that transform lanosterol into cholesterol [33]. It plays its

biological roles from its location in the membranes of cells, where it modulates membrane structure, dynamics, and function. The distribution of cholesterol varies among different cell membranes. Compared to the plasma membrane, intracellular membranes contain significantly less cholesterol. [114] Cholesterol is very hydrophobic and exhibits very low solubility in aqueous media (CAC of 25 to 40 nM) [115], accumulating in membranes at high levels, up to 1:1 mole ratio with phospholipids, or even higher under some circumstances.

Cholesterol is an amphipathic molecule consisting of a planar ring system of four fused carbon rings with a single hydroxyl group attached to carbon 3, and with an hydrocarbon tail at the opposite direction, as shown in Table II.1. The fused ring system, in *trans* configuration, is considered to be rigid, whereas the hydrocarbon tail is much more flexible. In a lipid bilayer, the fused-ring system is oriented parallel to the hydrocarbon chains of the lipids. Although small, the 3β-hydroxyl group is sufficient to orient cholesterol in the membrane and is located in the interfacial region of the bilayer. X-ray and neutron diffraction experiments indicate that the 3β-hydroxyl is in the immediate vicinity of the ester carbonyl of the phospholipid [116, 117], where it is suggested to be hydrogen-bonded [118].

One of the earliest studies on cholesterol in phospholipid bilayers reported that cholesterol altered the gel to liquid–crystalline (Lα) phase transition of the phospholipid. [119] Cholesterol was suggested to induce a new physical state, separate from the gel and liquid-crystalline states, which is known as liquid-ordered state (*lo*). [120] This phase, in which the lipid chains are conformationally ordered, is distinct from the Lα phase with conformationally disordered chains (the *ld* phase) observed in cholesterol-free lipid bilayers at temperatures above the melting temperature, *Tm*. The formation of the *lo* phase is the consequence of the flat and rigid cholesterol structure that maximizes its interaction with the lipid acyl chains in a Lα phase by forcing these to predominantly *trans* conformations. This effect retains the essentially *all-trans* configuration of the chains and simultaneously maintains the translational order of the fluid phase. Cholesterol also inhibits the formation of a true gel or solid state, much as an impurity in the bilayer [121, 122]. In lipid bilayers enriched in cholesterol, two fluid phases may coexist in the lipid bilayer. [123, 124]

The most widely recognized property of cholesterol in lipid bilayers and biological membranes is the ordering of the membrane lipids. Cholesterol has a condensing effect

on the bilayer indicated by its ability to reduce the average cross-sectional area of the phospholipids in the membrane, upon increasing the sterol content of the bilayer. [49, 125, 126] Molecular dynamics simulations show that increasing cholesterol concentration reduces the total amount of free volume in a bilayer. The effect of cholesterol on individual voids is most prominent in the region where the steroid ring structures of cholesterol molecules are located. [127]

A decrease in the *trans-gauche* isomerizations of the carbon–carbon single bonds induced by cholesterol increases the effective length of the hydrocarbon chain. Therefore, it is expected that cholesterol increases the thickness of the hydrocarbon portion of a phospholipid bilayer, and this is in fact observed for saturated phospholipids with up to 16 carbon atoms in the hydrocarbon chain. [128]. The ordering of the membrane lipid hydrocarbon chains by cholesterol is observed in biological membranes, as well. [99, 129, 130] However, for phospholipids with longer chains, cholesterol may lead to a decrease in the bilayer thickness [128]. If cholesterol is not as long as the phospholipid chains, its presence leads to a packing defect in the center of the bilayer. The phospholipid hydrocarbon chain must fill this packing defect, and to do so the end of the phospholipid hydrocarbon chain must become more disordered. This should lead to an effective shortening of the chain. Cholesterol does not interact as well with unsaturated lipids, showing more disordering of the sterol in polyunsaturated bilayers than in less unsaturated bilayers. [131] However, there is no clear evidence for the preference of cholesterol for saturated or unsaturated lipid acyl chains. [64]

A distinct effect of cholesterol occurs for the phospholipid headgroup–headgroup interactions in membranes. Normally, headgroups like those of PC and PE lie parallel to the bilayer surface and interact with each other by hydrogen bonds or by weak electrostatic interactions [132]. These intermolecular headgroup interactions are disrupted by the insertion of cholesterol among the lipids in the bilayer [133]. Cholesterol is found to increase the hydration of PC when complexed with this phospholipid.

The exchange of cholesterol between membranes can have implication in its homeostasis [134, 135]. It is accepted that cholesterol can exchange between two membranes through the aqueous phase without close approach of the membranes. [136, 137] Cholesterol is soluble at nM concentrations, and thus a monomer in the aqueous phase is a possibility as part of the transfer mechanism. Sphingomyelin decreases

dramatically the exchange rate of cholesterol between membranes [138], which may be relevant for membrane domain formation. Cholesterol transfer between membranes and blood proteins has been successfully mimicked by the fluorescent analog of cholesterol, dehydroergosterol (DHE). [10, 139] The naturally occurring fluorescent sterol DHE has proven to be a powerful probe for studies on membrane structure and cholesterol domain dynamics, for examining cholesterol-protein interactions, and for first time visualization in real-time of the distribution of cholesterol in the plasma membranes in living cells. [140-142]

Cholesterol rich bilayers also show slower translational diffusion when compared with cholesterol-free bilayers. In addition, ordering of membrane lipids by cholesterol changes the membrane permeability to small molecules. Passive permeability of phospholipid bilayers to glucose is inhibited by cholesterol [143, 144].

II.3 – Membrane Permeation

Membrane transport of solutes regulates the cellular uptake and release of substances, and different pathways exist for a molecule to pass through a lipid membrane. Transport processes can make use of protein pumps, protein carriers, and channels that control the uptake and efflux of various solutes, including sugars, amino acids, nucleotides, inorganic ions and drugs. [145] Small solutes and drug-like molecules can also permeate the lipid matrix by a diffusion process driven by a concentration gradient between the water regions at the two sides of a bilayer. [146] Although some authors argue that permeation through biological membranes results exclusively from the action of transporters [147], several arguments have been given in defense of the role of passive permeation in the transport of drugs through biological membranes, and it is generally accepted that drug molecules are transported across biological membranes via passive diffusion. [148, 149] Indeed, if the permeation of most solutes, across membranes, were done through carriers the cell would spend a considerable amount of energy synthesizing these highly distinct protein assemblies. Moreover, most of the pharmaceutically active drugs are not substrates of the carriers available in biomembranes, implying that passive diffusion should be a major process for their absorption.

Meyer and Overton observed for the first time that the hydrocarbon interior of the lipid bilayer is a barrier to free diffusion of polar solutes between two aqueous compartments. Overton found that lipid-soluble solutes penetrated fastest the cell membrane, and adopted the concept that the determinant for solute permeation through the membrane barrier is its solubility in the membrane. [12, 16] The permeability coefficient of a molecule through a biological membrane can be calculated according to the solubility-diffusion model, also called Overton's rule. [16, 32] This model assumes that the properties of the hydrophobic region are approximated by those of an oil-like liquid such as octanol or a long-chain hydrocarbon, where the bilayer structure is assumed to be static, with well defined boundaries at which the change from the hydrophilic to the hydrophobic environments occurs abruptly. The model also assumes that the diffusion through the hydrophobic region is the rate-limiting step of the overall process. The solubility-diffusion model describes permeation as a three step process:

i. partition into the hydrophobic region of the membrane;

ii. diffusion across the membrane;

iii. partition into the aqueous phase on the other side of the membrane;

According with Overton´s observations, this model leads to satisfactory results in the prediction of the relative rates of transport of very small and neutral solutes across lipid bilayers, calculating the permeability coefficient (P) by the following relation:

$$P = \frac{K_P D}{d} \tag{II.3}$$

where K_P is the membrane/water partition coefficient, D is the diffusion coefficient across the hydrocarbon region and d is the bilayer thickness. Based on the assumptions of the model, the determination of diffusion coefficients and partition coefficients of a solute between water and octanol or long chain hydrocarbons has been used to predict its permeability across a membrane of a certain thickness. Following this model, the partition coefficient between the aqueous media and the cell membranes is of fundamental importance in the passive permeability of the membrane barriers [150] and dictates the distribution of the drug between the different compartments in the target tissue and therefore the concentration of active drug.

The validity of this model is qualitatively good within a given homologous series of solutes with varying hydrophobicity but it fails when structurally unrelated solutes are

considered. [151] In addition to the model assumptions, an important limitation of the current approach is the prediction of solute concentration in the membrane from its general hydrophobicity as measured (or estimated) by partition to organic solvents such as octanol or alkanes, logP. [151, 152] Those homogeneous solvents cannot capture the properties of the lipid bilayers and the predicted partition coefficient does not reflect the affinity of the solute for biological membranes. [153-156] As shown in Section II.1.2, the lipid bilayer is a very structured environment presenting regions with very distinct polarity and density that determine the partition of a given ligand. [24, 37, 156, 157] As typical drugs are amphiphilic compounds with sizes similar to membrane lipids, a drug molecule partitioning into a lipid bilayer occupies thus approximately the space of a lipid molecule and also arranges in a similarly aligned manner. Unlike partitioning into a bulk solvent where the compound has no preferred orientation, partitioning into the bilayer guides the compound into an energetically favored position.

A major discrepancy between the predicted and the experimentally obtained permeability was observed for ions. The main source for this inconsistency is their low partition coefficient into the membrane. This is mainly due to the Born energy, which reports the energy involved in the transfer of an ion or dipole from a medium with a high dielectric constant, as water, to a medium with a low dielectric constant, as the membrane core. Permeability coefficients of many ions and small neutral molecules have been determined experimentally and vary over a remarkably broad range. [158] In order to explain discrepancies in several orders of magnitude between the predicted and measured permeation coefficients for small charged ions, an alternative mechanism has been proposed, which suggests that the particle can permeate the bilayer passing through pores. The “pore model” suggests that permeation occurs through transient defects produced by thermal fluctuations originating hydrated pores within the bilayer. Charged particles, such as protons or hydroxyl ions may overcome the Born energy required to dissolve in the membrane, by passing through these water filled “holes” and *via* hydrogen bond exchange, presenting permeation rates several orders of magnitude above the values expected from comparisons with other monovalent ions [159]. Permeation through pores seems to be the dominant mechanism for ions, but only if the membrane is sufficiently thin. Ion permeation by partitioning and diffusion appears to become of greater importance as the membrane thickness increases, because the number

of pores in the membrane produced by thermal fluctuations decreases as the bilayers become increasingly stable [158, 160].

Molecular simulations, which are becoming increasingly accessible due to the rapid development of computing power and the availability of many software packages, are a very interesting tool to characterize the location and permeation of solutes through lipid bilayers. In the literature, several reviews have explored this subject for a number of solutes with a wide range of polarities. [26, 161-163]

II.3.1 – Potential of Mean Force (PMF) Profiles through Lipid Bilayers

In pharmaceutical research, determination of binding free energies has been important for the purpose of computer-aided drug design. Two major goals of computational chemistry are to provide physical insight by modeling details not easily accessible to experiment, and to make predictions in order to aid and guide experiments. Both of these goals frequently involve the calculation of free energy differences, since the free energy change involved in a chemical process governs the balance between the different chemical species present and the amount of chemical work available. Therefore, researchers are generally more interested in calculating relative quantities, in order to rank chemically similar lead candidates according to their affinity toward a given target, than in estimating absolute binding constants. [164]

The concept of potentials of mean force (PMFs), originally introduced by Kirkwood [165], is frequently used to characterize the energetics of transitions in solid, fluid, and biomolecular systems. Regarding the interaction of solutes with lipid bilayers, the energy profile through the bilayer normal allows the calculation of the free energy barriers for the processes of insertion, desorption and translocation, which are the microscopic steps for the permeation. Umbrella sampling (US) [166, 167] is probably the most popular technique to compute the PMF along a given reaction coordinate. This technique aims to overcome limited sampling at energetically unfavorable configurations by restraining the simulation system with an additional (typically harmonic) potential. [166] Conjugated with the explicit umbrella potential, stratification strategies are used [168], whereby the reaction pathway is broken down into a large number of small overlapping windows. Accordingly, a set of N_w separate umbrella simulations are carried out, with an umbrella potential

$$w_i(\zeta) = \frac{K_i}{2}\left(\zeta - \zeta_i^c\right)^2 \tag{II.4}$$

which restrains the system at the position ζ_i^c (i =1, ..., N_w) with a force constant K_i. From each of the N_w umbrella simulations (also referred to as "umbrella windows"), an umbrella histogram $h_i(\zeta)$ is recorded, representing the probability distribution $P_i^b(\zeta)$ along the reaction coordinate biased by the umbrella potential $w_i(\zeta)$.

After completion of the simulations, the umbrella windows are subsequently pasted together using histogram based algorithms. The technique most widely used to compute the PMF from histograms, that is, to unbias the distributions $P_i^b(\zeta)$, is probably the weighted histogram analysis method (WHAM). [169] The purpose of WHAM is to estimate the statistical uncertainty of the unbiased probability distribution given the umbrella histograms, and subsequently to compute the PMF that corresponds to the smallest uncertainty. [168-170] In the g_wham [170] tool of GROMACS simulation package the WHAM equations are applied as:

$$P(\zeta) = \frac{\sum_{i=1}^{Nw} g_i^{-1} h_i(\zeta)}{\sum_{j=1}^{Nw} n_j g_j^{-1} \exp\left[-\beta\left(w_j(\zeta) - f_i\right)\right]} \tag{II.5}$$

and

$$\exp\left(-\beta f_j\right) = \int d\zeta \exp\left[-\beta w_j(\zeta)\right] P(\zeta) \tag{II.6}$$

where, β denotes the inverse temperature $1/(k_B T)$, with the Boltzmann constant k_B and the temperature T, and n_j is the total number of data points in histogram h_j. The statistical inefficiency g_i is given by $g_i = 1+2\tau_i$, where τ_i is the integrated autocorrelation time of umbrella window i (in units of the simulation frame time step). The g_i's cancel from the WHAM equations if (and only if) the autocorrelation times in all umbrella windows are equal. In contrast, if the g_i differs between different histograms, the factors g_i^{-1} assign lower weights to histograms with longer autocorrelations. $P(\zeta)$ denotes the unbiased probability distribution that is related to the PMF by

$$W(\xi) = -\beta^{-1} \ln\left[\frac{P(\zeta)}{P(\zeta_0)}\right] \tag{II.7}$$

where, ζ_0 is an arbitrary reference point where the PMF $W(\zeta_0)$ is defined to be zero. The WHAM equations contain two unknown quantities, that is, the free energy constants f_j and the unbiased distribution $\mathrm{P}(\zeta)$, and must therefore be solved iteratively. Following this procedure an energy profile, over a reaction coordinate is obtained, e.g. the energy profile of a molecule through the direction normal to a lipid bilayer.

II.3.2 – Quantitative Evaluation of Permeation of the Amphiphiles through Lipid Bilayers – the Inhomogeneous Solubility-Diffusion Model

According to the solubility-diffusion model, permeation of molecules across membranes occur by a three-step process involving the partition of the molecule from the aqueous phase on one side into the bilayer, its diffusion across the bilayer, and its partition from the bilayer into the aqueous phase on the other side. This model may be improved by considering different regions z of the bilayer normal with a specific partition coefficient and different diffusion coefficients within each region. At a microscopic detail, the overall membrane resistance R to solute permeation, defined as the inverse of the permeability coefficient *P*, can be expressed as the integral over the local resistances across the membrane:

$$\mathrm{R} = \frac{1}{P} = \int_0^d \frac{dz}{K(z)D(z)} \tag{II.8}$$

where $K(z)$ and $D(z)$ are the depth-dependent partition coefficient from water into the membrane and the diffusion coefficient in the membrane at depth z, respectively, and d is the membrane thickness. The above equation refers to the "inhomogeneous solubility-diffusion model" [24] introduced by Marrink and Berendsen to calculate permeability coefficients from MD simulations. Using MD with special sampling techniques it is possible to calculate those equilibrium and dynamic properties related to the permeation process.

The equilibrium property is the solute partition between water and different regions in the membrane, and is expressed by the free energy of solute transfer from water into various depths z of the membrane, $\Delta G(z)$. This parameter is calculated as the potential

of the mean force, which in the case of sampling by the "constraint method", where the solute is constrained at a fixed position z, can be obtained by:

$$\Delta G(z) = -\int_{outside}^{z} \langle F(z') \rangle_t \, dz' \tag{II.9}$$

where $\langle ... \rangle_t$ indicates an average over the simulation time. When z is considered until the water phase on the other side of the lipid bilayer, the free energy profile for the entire membrane thickness is obtained. The solute $\Delta G(z)$ is related to its partition coefficient $K(z)$ through:

$$K(z) = \exp\left(-\frac{\Delta G(z)}{RT} \right) \tag{II.10}$$

with R being the gas constant and T the absolute temperature.

The dynamic property is the solute diffusion coefficient at position z in the membrane. Considering solute diffusion in a medium, the local time dependent friction coefficient of the diffusing molecule $\xi(z,t)$ is related to the time autocorrelation function of the fluctuations of the instantaneous $F(z,t)$ from the mean $\langle F(z) \rangle_t$ by:

$$\xi(z,t) = \frac{\langle \Delta F(z,t) \bullet \Delta F(z,0) \rangle}{RT} \tag{II.11}$$

where

$$\Delta F(z,t) = F(z,t) - \langle F(z) \rangle_t \tag{II.12}.$$

Assuming that $\xi(z,t)$ is large and decays rapidly compared to other time scales in the system, a satisfactory description of the full dynamics is provided by the static friction coefficient $\xi(z)$:

$$\xi(z) = \int_0^\infty \xi(z,t)\, dt = \int_0^\infty \frac{\langle \Delta F(z,t) \bullet \Delta F(z,0) \rangle}{RT} dt \tag{II.13}.$$

When studying diffusion across a free energy barrier, the above condition is met if the slope of the free energy barrier over a distance covered by the particle during the decay time of its friction coefficient is lower than the thermal fluctuation, RT. In this case, $\xi(z)$ is related to the local diffusion coefficient $D(z)$ of the permeating solute at depth z by:

$$D(z) = \frac{RT}{\xi(z)} = \frac{(RT)^2}{\int_0^\infty \langle \Delta F(z,t) \bullet \Delta F(z,0) \rangle \, dt} \tag{II.14}.$$

Calculating $\Delta G(z)$ and $D(z)$ the overall resistance R to permeation is obtained integrating over the local resistances R(z) at different depths in the membrane, and the permeability coefficient P of the solute is obtained as the inverse of R:

$$\mathrm{R} = \int_{outside}^{z} \mathrm{R}\left(z'\right) dz' = \int_{outside}^{z} \frac{\exp\left(\Delta G\left(z'\right)/RT\right)}{D\left(z'\right)} dz' = \frac{1}{P} \qquad \text{(II.15).}$$

The inhomogeneous solubility-diffusion model has been applied to several hydrophilic and hydrophobic molecules calculating the local resistance of the membrane to the permeation as the inverse of the local permeability coefficient. It was found that for hydrophilic molecules the main barrier is represented by the hydrocarbon core, while for the hydrophobic molecules the main barrier to permeation is offered by the head group region. [157]

II.4 – Delivery of Drugs through the Tight Endothelium of the Blood-Brain Barrier

An enormous cost is associated with brain disorders ($1 trillion in Europe in 2010 [171]), which has created an enormous market for drugs to treat those disorders ($80 billion in the United States in 2010 [172]). In spite of this, many large, well-capitalized pharmaceutical companies have either closed their neuroscience divisions or abandoned their efforts to find treatments for brain disorders using traditional drug-discovery methods, owing to the difficulty of developing new drugs for those disorders. [172] Obtaining molecules with high activity does not warrant their effectiveness *in vivo* because the drug must achieve therapeutic concentrations at the sites of action. The access to the therapeutic targets implies crossing biological barriers. This question is of great relevance especially for two groups of drug products: (i) oral drug products in which the drug must be absorbed through the intestinal barrier to reach the systemic circulation, and (ii) those drugs whose sites of action are located in the so-called “drug sanctuaries” such as the central nervous system (CNS), for which a blood−brain barrier (BBB) must be crossed. Drug dissolution and permeation through the intestinal membrane are the essential steps to reach the systemic circulation; consequently solubility and permeability are two of the key biopharmaceutical properties that determine drug product “developability”. CNS drugs have in general lower success rates

and longer development times [173] than in other therapeutic areas because of the complexity of the brain, the BBB, and the low predictability of CNS animal models.

II.4.1 – The Blood-Brain Barrier

The BBB, Figure II.8, must protect the CNS from the compositional fluctuations that occur in the blood in order to maintain homeostasis in the CNS, a condition essential for proper function of the nervous system. The BBB controls the exchange of nutrients, hormones, metabolites, drugs, toxins, macromolecules, and immunological cells between the blood and the brain in both directions. This barrier is formed by brain capillary endothelial cells that have at least three properties which distinguish them from their peripheral counterparts: (i) absence of fenestrations due to high density of tight junctions (TJs) of extremely low permeability; (ii) low rates of fluid-phase endocytosis; (iii) specific transport and carrier molecules. [174] In addition to endothelial cells, the BBB is composed of the capillary basement membrane (BM), astrocyte end-feet ensheathing the vessels and pericytes embedded within the BM. [175] Astrocytes are star shaped cells with multiple ramifications. Astrocytes in white matter are complex cells with long branches that radiate from the cell body and terminate in end-feet at the pia matter surface, on blood vessels, or freely among axons. White matter astrocytes are usually called fibrous astrocytes. Astrocytes in gray matter, called protoplasmic astrocytes, have profuse, short branches that contact blood vessels and the pia matter surface, and surround neurons. Astrocytes are involved in energy storage function and direct contact between endothelial cells and astrocytes is necessary to generate an optimal BBB. Pericytes are the cells of microvessels including capillaries, venules, and arterioles that wrap around the endothelial cells. They are thought to provide structural support and vasodynamic capacity to the microvasculature, playing a key role in the structural stability of the vessel wall.

The BBB is present in all brain regions, except for the circunventricular organs including area postrema, median eminence, neurohypophysis, pineal gland, subfornical organ and lamina terminalis. Blood vessels in these areas of the brain have fenestrations that permit diffusion of blood molecules across the vessel wall. These unprotected areas of the brain regulate autonomic nervous system and endocrine glands of the body. [175]

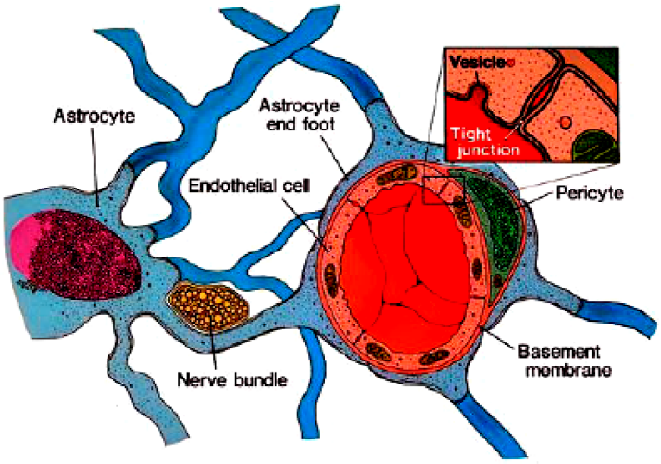

Figure II.8 – Schematic drawing of the blood-brain barrier, showing endothelium, basement membrane, pericytes, astrocytes and tight junctions. Adapted from [176].

Breakdown of the BBB is associated with a variety of CNS disorders and results in aggravation of the disease condition. The tightness of the brain endothelium is reflected in its high trans-endothelial electrical resistance (TEER), which values for pial endothelium are 1500–2000 $\Omega \cdot cm^2$ [177], whereas the value estimated for brain parenchyma is 8000 $\Omega \cdot cm^2$ [178]. BBB endothelium forms a much tighter interface than peripheral endothelia, whose TEER values can be as low as 2–20$\Omega \cdot cm^2$ [177]. Restoration of the BBB is thus one strategy during therapy of CNS diseases.

The gaps between capillary endothelial cells in most parts of the brain are tightly sealed by TJs. The TJ consists of three integral membrane proteins, namely, claudin, occludinn and junction adhesion molecules, and a number of cytoplasmic accessory proteins. Cytoplasmic proteins link membrane proteins to actin, which is the primary cytoskeleton protein for the maintenance of structural and functional integrity of the endothelium. The TJs appear as sites of apparent fusion involving the outer leaflets of the plasma membrane of adjacent endothelial cells. The TJ divides the plasma membrane into an apical and a basolateral side. [17] Therefore, the cells are polarized, the two sides show distinct patterns of membrane proteins, and presumably also of lipids. The TJ hinders the migration of molecules, between the apical and basolateral sides in the outer lipid leaflet of the plasma membrane, while molecules in the inner leaflet can move freely around the whole cell. [179]

In combination, BBB features restrict the nonspecific flux of ions, proteins, and other substances into the CNS environment. [174] In fact, the presence of the BBB results in a

nearly complete separation of the CNS from the rest of the body. However, it also imposes that many therapeutically active compounds cannot enter the brain in sufficient amount.

II.4.1.1 – Routes for Drug Delivery through the BBB

Potential routes for transport across the brain endothelium forming the BBB are shown in Figure II.9. Cells may cross the BBB adjacent to, or by modifying the tight junctions. Small nonpolar solutes may passively diffuse through the cell membrane and cross the endothelium, being generally accepted that greater lipid solubility favours this process. However, active efflux carriers may intercept some of these passively penetrating solutes, and pump them out of the endothelial cell. Carrier-mediated influx, which may be passive or secondarily active, is responsible for the transport of many essential polar molecules, such as glucose, amino acids and nucleosides. Receptor-mediated transcytosis (RMT) can transport macromolecules such as peptides and proteins, and adsorptive mediated transcytosis (AMT) appears to be induced non-specifically by positively charged macromolecules, and can also result in transport across the BBB. Tight junction (TJ) modulation may also occur, which relaxes the junctions and wholly or partially opens the paracellular aqueous diffusional pathway.

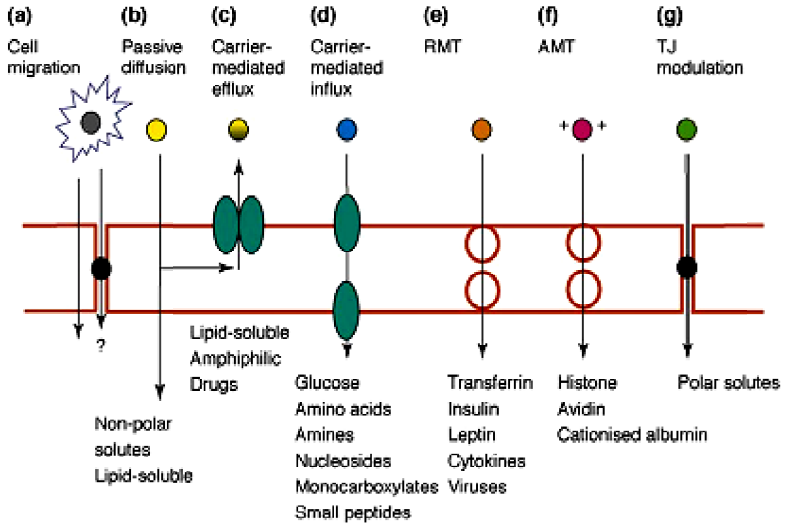

Figure II.9 – Pathways across the blood–brain barrier. The main routes for molecular traffic across the BBB are shown: a) cell migration, b) passive diffusion, c) carrier mediated efflux, d) carrier mediated influx, e) receptor-mediated transcytosis (RMT), f) adsorptive mediated transcytosis (AMT), g) tight junction modulation. Adapted from [180].

As passive permeation across the BBB is restricted to lipophilic solutes, brain endothelial cells possess a number of carrier mechanisms transporting hydrophilic nutrients, nucleotides and precursors for neurotransmitters into the brain, and other compounds, such as metabolites, out of the brain. Some transport systems simply facilitate the passage of their substrates along the concentration gradient, while others are able to transport them against an electrochemical gradient and require either a direct source of energy, from ATP dephosphorylation, or an indirect source of energy, such as the sodium gradient maintained by Na^+/K^+-ATPase. [151] In terms of transport out of the brain and into the blood, some of the key efflux transporters are P-glycoprotein (P-gp) and other multidrug-resistance proteins (MRPs) [181-183]. P-gp is a membrane transporter first identified in multidrug-resistant (MDR) tumor cells, but is also expressed in normal tissue including intestinal epithelium and the BBB. It is also present in human intestinal cell cultures such as the Caco-2, and also in MDCK cell lines. [152] The multi-drug resistance efflux transporter P-gp, predominantly localized at the luminal (apical) side of the barrier, binds its substrates within the lipid bilayer on the level of the cytosolic membrane leaflet before they reach the cytosol, and flips them to the outer leaflet [184]. P-gp transport competes with lipid-bilayer permeation [185]. However, affinity to P-gp may not necessarily compromise the absorption of a compound. Fast permeating solutes may be recognized by P-gp, but the transporter may not be efficient enough to cause net counter-transport. Compounds with small cross-sectional areas (A_D<70 Å^2) and/or intermediate or low charge exhibit higher passive influx than efflux and, therefore, cross the BBB despite being intrinsic substrates. Large (A_D>70 Å^2) or highly charged compounds show higher efflux than influx. [186]

Due to the inability of drugs to penetrate into the brain and spinal cord, a multitude of techniques and strategies were developed to increase the delivery of drugs and therapeutic agents into the CNS through paracellular pathways. Those lead to direct access to the brain or BBB disruption, as is the example of direct injections of drugs into the brain and cerebrospinal fluid, intracranial implants, and slow-release devices, osmotic disruption of the BBB, chemically mediated modulation of tight junctions, incorporation of drugs into liposomes and nanoparticles. [187] Another type of techniques uses transcellular pathway based on the BBB transport. This is the case of drugs that enter to the brain requiring their modification to use existing transport

systems, and conjugation of drugs or drug-containing liposomes to antibodies directed at BBB receptor/endocytosis systems [187-189].

II.4.1.2 – Model Systems for the BBB

The increased throughput of combinatorial chemistry demands for systems that can be used for high throughput screening, for which animal models and associated *in vivo* studies are not appropriate. Although none of the available *in vitro* models covers all BBB functions, they occupy an important position between the computational approach and animal experiments, being widely used in permeation studies. [152] An optimal BBB model would feature the following properties: 1) a continuous TJ network, 2) high TEER and low permeability for small hydrophilic compounds such as mannitol or sucrose, 3) BBB-specific carriers for influx as well as efflux, 4) low unspecific endocytosis activity, and 5) BBB-characteristic metabolic enzymes. [151]

In the last few years, several methodologies have been developed to characterize the interaction and permeation of small solutes through biomembranes, in an attempt to overcome the limitations of the predictors based on logP [190]. Parallel artificial membrane permeation assay (PAMPA) [191] and immobilized artificial membrane (IAM) chromatography [192] are examples of high throughput methods to evaluate drug partition to biomembranes. The PAMPA approach has the additional advantage of enabling direct evaluation of the permeability. However, PAMPA and IAM chromatography still rely on hydrophobic phases that do not capture the properties of biomembranes. The phospholipid layer in the artificial membranes used in PAMPA accounts for only a few percent of its volume, enclosing a thick layer of organic solvent, and the electrostatic and packing constrains of the lipids in IAM are affected by the covalent attachment to the solid support.

Cell cultures have been successfully applied to mimic epithelial and endothelial barriers with respect to passive permeation, carrier-mediated transport, and possible metabolization of drug compounds upon passage through cells. The cell monolayer permeability assay consists of two chambers, donor and acceptor, separated by a porous support material in which a monolayer of cells grows, until confluence is attained and sufficient cell differentiation is reached. [152] Those cell-based methodologies can be of cerebral origin, such as brain capillary endothelial cells (BCECs) and immortalized

brain endothelial cells. However, non cerebral cells, such as MDCK and Caco-2, have been preferentially used. Using cell-based methods, and also PAMPA, the permeability coefficient (P) is commonly calculated using the expression:

$$P = \frac{\frac{dS^{A}(t)}{dt} V^{D}}{A^{b} S^{D}(0)} \tag{II.16}$$

where $S^{A}(t)$ is the total amount of solute (in the aqueous phase plus bound to binding agents when present) in the acceptor compartment at time t, V^{D} is the total volume of the donor compartment, A^{b} is the area of the barrier in contact with the donor compartment, and $S^{D}(0)$ is the total amount of solute in the donor compartment at $t = 0$. Equation (II.16) is an approximate solution which is only valid at initial stages of the permeation process, and relies on the following assumptions: i) negligible backflow of solute (irreversibility); ii) concomitant and simultaneous increase of solute in the acceptor compartment due to its disappearance in the donor compartment. The latter assumption requires that there is no significant mass imbalance due to solute decomposition or binding to the barrier or experimental apparatus. Under those conditions, the rate of solute accumulation in the acceptor compartment is maximal at very short times and remains nearly constant up to a few percent deviation from the initial conditions.

Although none of the existing models is perfect, they have been widely applied in pharmaceutical research.

II.4.2 – Blood Composition

The Blood Circulation is used for the transport of all solutes to animal cells. Therefore, drugs are also bound to the circulating proteins. [193] These blood proteins can modulate the distribution of drugs to tissues, a possibility that should be taken into account when designing for high or low plasma binding. In broad terms, binding to agents in the blood can either limit or favor the distribution of drugs to tissues. Blood binding can also direct drugs to their targets (receptors) in the plasma, blood cells or vessels. Binding to plasma proteins can allow the transport of drugs in plasma at concentrations much higher than expected from their water solubility. However, the

high-affinity binding of a compound is very suggestive of restrictive plasma binding, with low tissue permeability. Several blood components, Figure II.10, such as serum albumin, lipoproteins, and cells like erythrocytes have an important role on the specific transport of several solutes, such as fatty acids, sterols, oxygen and also a wide variety of drugs.

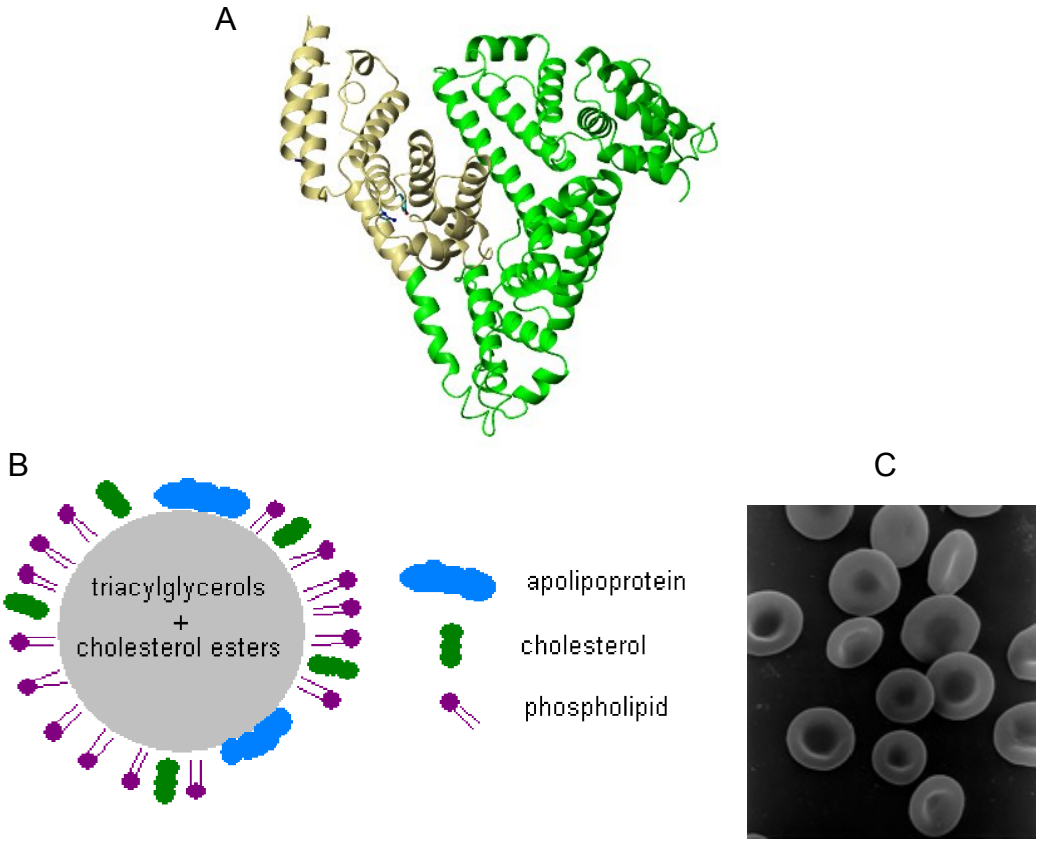

Figure II.10 – Illustration of several blood components. a) X-ray crystallographic Structure of Human Serum Albumin (HSA), adapted from http://www2.hawaii.edu/~chungeun/; b) Schematic illustration of a Lipoprotein, adapted from http://lipidlibrary.aocs.org/Lipids/lipoprot/index.htm; c) A micrograph of Erythrocytes, adapted from http://en.wikipedia.org/wiki/Red_blood_cell.

II.4.2.1 – Serum Albumin

Serum Albumin [194] is one of the earliest known and probably the most studied of all proteins, the most abundant in the body of all vertebrates (with a concentration between 35 to 50 mg/mL in human blood), and the most prominent protein in plasma. Initially, and based on hydrodynamic studies, there was a general consensus that albumin had a cigar-shaped form, but X-ray diffraction [195] and ^{1}H-NMR [196] showed that fatty acid-free albumin in crystal has a triangular heart-like shape, Figure II.10A. The

albumin released into circulation possesses a half life of 19 days. [194] It is an aqueous soluble protein, with a molecular weight of about 66 kDa that contributes in 80% to colloidal osmotic blood pressure, regulates blood pH and is responsible for binding and transport of a large number of molecules, including drugs.

II.4.2.2 – Lipoproteins

The structure of all circulating lipoproteins is consistent with a spherical model in which a spherical liquid core of cholesterol esters and triglycerides is surrounded by a 2 nm monolayer of cholesterol and phospholipids with closely packed hydrophobic ends on the surface of the core [197], where proteins are also associated [33]. Lipoproteins may be separated by ultracentrifugation [198] and are classified into five general categories on the basis of their functional and physical properties: Chylomicrons (CM), Very Low Density Lipoproteins (VLDL), Intermediate Density Lipoproteins (IDL), Low Density Lipoproteins (LDL) and High Density Lipoproteins (HDL). Lipoprotein densities increase with decreasing particle diameter, because the density of their coating is greater than that of their inner core. Lipoprotein particles undergo continuous metabolic processing so that they have somewhat variable compositions.

Chylomicrons, the largest lipoprotein, transport exogenous triacylglycerols and cholesterol from the intestines to the liver, and have a half-life in circulation of about 4 to 5 minutes [199]. VLDL, with a half-life in circulation of 1 to 3 hours [200], and LDL with a circulation half-live of about 3 to 4 days [199, 201], transport endogenous triacylglycerols and cholesterol from the liver to the tissues. HDL is generally divided in two general classes of lipoproteins [202], HDL_2 (larger particles) and HDL_3 (smaller particles), with circulation half-life of about 2 to 3 days [203], and is involved in the reverse transport of endogenous cholesterol from the tissues to the liver.

II.4.2.3 – Erythrocytes

Erythrocytes, also known as red blood cells, are small cells with a biconcave disk form without nucleus, mitochondria, endoplasmic reticulum, or other organelles. The protein hemoglobin present on erythrocytes is responsible for the transport of oxygen from the lungs to the tissues. Due to the lack of internal membranes, mature erythrocytes have been the system of choice for experimental studies about structure and functions of

biological membranes. Due to this, erythrocyte properties have been referred several times in the previous sections, being its membrane asymmetry one of the most important features (Figure II.7). In addition, the plasma membrane of erythrocytes has about 20 prominent proteins, as well as dozens of minor ones that serve as transporters, each responsible for moving a specific solute across the membrane [33, 204]. Like other biological membranes, the outer leaflet of the lipid bilayer of erythrocytes is known to be enriched in sphingomyelin [81, 94, 98, 102].

In addition to the characteristics of the BBB, when modulating the permeation of drugs through this barrier, the contribution of blood components should be taken into account.

II.5 – Models to Predict the Permeation of Molecules through Cell Monolayers

Pharmacodynamic (PD) ("what the drug does to the body") and Pharmacokinetic (PK) ("what the body does to the drug") events have poorly defined boundaries, and therefore no reliable PD assessment can neglect PK factors. [151] Pharmacokinetics deals with the absorption, distribution, biotransformation, and excretion of drugs. These factors, coupled with dosage, determine the concentration of a drug at its sites of action, and influence the intensity and duration of its effects. A diversity of models to assess and predict the pharmacokinetic properties of drug candidates have been generated. They can be classified as "mechanistic", when there is some knowledge of the system in terms of structural connectivity and functional mechanisms, or "empirical", when hardly anything is known about these system properties, predictions being made on the basis of mathematical functional forms. Due to the complexity of the biological system, empirical models are predominant in the literature. In general, those models preferentially rely in the molecular physicochemical properties of drugs. Physicochemical properties used today in drug-discovery programs include aqueous solubility, lipophilicity, molecular size, hydrogen-bonding capacity, and charge, all of which are considered as important molecular features since they relate to various aspects of drug disposition. [151]

The first attempts to assess pharmacokinetics derived from the previously described Overton's rule being the logP or logD in the octanol/water system widely used in structure-permeation correlations. For ionizable compounds, it is accepted that the

distribution coefficient (logD) at a physiologically relevant pH (5 to 7.4) is the parameter to consider instead of the partition coefficient. The permeability of a large number of compounds is, however not properly predicted by partition (or distribution) in the octanol/water system and poor linear correlations were observed between Caco-2 flux and logD values. [205] In spite of this, it was reported that drugs which are completely absorbed in humans had permeability coefficients $> 1\times10^{-6}$ cm/s, while poorly absorbed drugs had permeability coefficients of $< 1\times10^{-7}$ cm/s. [205]

Although useful correlations have often been obtained within given chemical series, the predictive value of octanol/water tends to vanish when chemical diversity is increased. [151] Computational models for the prediction of passive transport usually rely on approaches or programs such as the rule-of-5, Polar Surface Area (PSA), Abraham's general solvation equation and Volsurf. [206]

The "Rule-of-5", developed at Pfizer by Lipinski and co-workers is one of the most well known and widely adopted computational screens for drug absorption. [207] It states that poor absorption or permeation is more likely when a compound possesses: i) more than 5 hydrogen-bond donors (defined as N-H or O-H groups), ii) more than 10 hydrogen-bond acceptors (defined as O or N atoms, including those forming part of hydrogen-bond donors), iii) a molecular weight greater than 500 daltons, or iv) ClogP > 5.0 or Moriguchi logP (MlogP) > 4.15. The rule-of-5 screen generates a permeability/absorption alert for any compound that breaks two or more of the rules [207]. Compounds which are absorbed *via* an active transport mechanism may form exceptions to these rules. The rule-of-five can be seen as a qualitative absorption/permeability predictor and should not be used as a quantitative predictor. [151]

The PSA of a molecule is defined as the part of the molecular surface (either van der Waals or solvent-accessible) that arises from oxygen or nitrogen atoms, or hydrogen atoms attached to nitrogen or oxygen atoms. It is clearly related to the capacity of a compound to form hydrogen bonds. Palm and co-workers employed a measure termed the "dynamic" PSA (PSA_d), which is a Boltzmann-weighted average value computed from an ensemble of low-energy conformers obtained by a detailed conformational search. [208] It was suggested that compounds with a $PSA_d > 140$ Å^2 would tend to show poor absorption, while compounds with $PSA_d < 60$ Å^2 could be predicted to show complete absorption. [209]

Abraham's General Solvation Equations were developed by Abraham and co-workers as set of five so-called solute descriptors that could be combined in linear free energy relationships to form correlations with solute properties [210]. The descriptors originally considered were: R_2, an excess molar refraction (obtained from the refractive index for solutes that are liquid at 20 ºC); π_2^H, a dipolarity/polarizability parameter; $\sum\alpha_2^H$, the solute hydrogen-bond acidity; $\sum\beta_2^H$, the solute hydrogen-bond basicity; and V_x, the McGowan characteristic volume. Blood-brain distribution data were compiled for 157 compounds and an equation that correlates logBB (BB=[brain]/[blood]) values with these descriptors was derived. [211] It is apparent that increasing molecular size and polarizability tend to favor partitioning into the brain, while increasing polarity and hydrogen bonding properties tends to favor compounds remaining in the blood. The need for an additional indicator variable for carboxylic acids is viewed as an indication that this type of compound is particularly difficult to deliver into the brain by passive diffusion.

VolSurf is a computational procedure that allows the generation and exploration of the physicochemical property space of a molecule (or library of molecules), starting from 3D maps of interaction energies between the molecule and chemical probes. It compresses the information present in 3D grid maps into a few 2D numerical descriptors, and may be used to generate structure-property or structure-activity relationships, such as the prediction of brain penetration. Using this methodology it was concluded that hydrophilic regions and hydrogen-bonding capacity are detrimental to BBB permeation. [212] Of particular interest is the ability of the Volsurf descriptors to map the distribution of charge over a molecular surface. From this type of descriptors, it was noted that diffuse polar regions in molecules may be tolerated for BBB permeation, but concentrated regions of charge or polarity are not. Similarly, it is not merely the number of hydrogen bonds that influences permeation, but their spatial distribution in the molecule. Hydrophobic descriptors were found to favor BBB permeation but, their effect was less marked than the polar descriptors. Size and shape descriptors did not appear to have a significant impact on permeation. Therefore, it appears that it is the balance between a compound's hydrophilicity and lipophilicity that governs brain penetration.

As a final remark, linear relationships between biological activity and hydrophobic character are often obtained for a large number of homologous series. However, this

linear relationship cannot go on infinitely, otherwise compounds with infinite activity would exist. A cut-off point should be reached in each homologous series: biological activity increases with increasing lipophilicity, reaches a maximum, and then decreases with further increase of hydrophobic character. While hydrophilic molecules tend to remain in the aqueous phases and lipophilic molecules tend to go into the lipid phases, molecules with an optimal hydrophilic-lipophilic balance will have the best chance to penetrate all barriers and to reach the receptor sites. Intuitively, a "parabolic like" dependency would approximate the relationship between the concentration of drug administered and the concentration at the active site. [213, 214] The optimal hydrophobicity, and the factors that limit the activity at lower and higher values is not however well characterized, and may depend on other molecular parameters of the drugs and properties of the barriers.

Chapter III

Methods

III.1 – Molecular Dynamics Simulation of Biological Systems

The increasing availability of powerful computers has opened new ways to study chemical systems in atomic detail. Namely, computer simulations are able to provide a detailed picture of the structure and dynamics of biological systems. Molecular modeling is the general process of describing complex chemical systems in terms of a realistic atomic model, with the goal being to understand and predict macroscopic properties based on detailed knowledge on an atomic scale. Macroscopic properties are always ensemble averages over a representative statistical ensemble of molecular systems. For molecular modeling, this has important consequences. Detailed knowledge of a single structure is not sufficient, even if it is the structure of the global energy minimum. It is necessary to generate a representative ensemble at a given temperature, in order to compute macroscopic properties. The generation of a representative equilibrium ensemble may be performed using Monte Carlo and Molecular Dynamics (MD) simulations. For the generation of non-equilibrium ensembles and for the analysis of dynamic events, only MD is appropriate, which makes it a more universal technique. Assuming the ergodic hypothesis [215], average values of several system properties can be evaluated from MD simulations. Therefore, to study the events occurring in biological systems in the relevant time scale we may use the MD technique which allows following the time evolution of a molecular system.

MD simulations are seen as a priceless tool and have been used to obtain detailed atomic-scale information on biological systems, as all the details of the atomic interactions may be established. The MD technique has developed over the last decades from a method to study the dynamics of liquids of solid spheres and Lennard–Jones particles, to a versatile method to study many different types of systems at atomic resolution [216]. Its biophysics applicability strongly increased in the 1980s, when a number of general force fields for water, proteins and DNA as well as some general simulation computer programs became available. Also in the 1980s the first studies of lipid systems appeared in the literature, at first not taking the solvent into account [21, 22], and then counting for solvent effects [217, 218]. Currently there are several Software Packages for MD simulations, such as GROMACS [219, 220], NAMD [221, 222], Amber [223], CHARMM [224], LAMMPS [225], and Espresso [226]. In this

work we have used GROMACS, which is free and one of the most used in the scientific community.

III.1.1 – The Molecular Dynamics Method

In MD simulations all atoms in the system are treated classically, assuming that the Born-Oppenheimer approximation holds and the nuclei can be treated as classical particles. The atomic interactions are divided in bonded interactions between atoms connected by chemical bonds, and non-bonded interactions, usually between any pair of atoms that are within a given cutoff radius. The bonded interactions consist of bond, angle and dihedral terms. Bonds and angles are usually described as harmonic oscillators and dihedral angles are usually described by a suitable cosine expansion. For the non-bonded interactions, electrostatic and van der Waals, a partial charge and parameters for repulsion and attraction are assigned to each atom. A typical potential function, also known as force field, has the form illustrated in Figure III.1. The molecules are depicted as consisting of balls (the atoms) connected by springs (the bonds). The first and second terms describe the van der Waals and Coulombic interactions, respectively, for atoms i and j. The next set of terms describes the bond, bond angle and torsional energy of the molecules comprising the system. For the bonded terms, the potential energy is relative to the atoms being in their equilibrium (preferred) state, for which the energy is taken as zero. The Lennard Jones parameters ε_{ij} and σ_{ij}, partial charges q_i and q_j, and the force constants k_b, k_a, and k_ϕ are all atom-specific parameters that are inputs to the simulation. This general form shows the most important assumptions that are made in the MD simulation: only pair-additive non-bonded interactions are taken into account, non-bonded interactions involving three or more atoms are neglected, atoms are represented as point charges, electronic polarizability is usually neglected and simple quadratic forms are used. The precise form of the potential function is a choice for which there are many options. In particular, different forms for the van der Waals interactions and the dihedrals are in common use, and the bonds are often constrained [227, 228] in simulations.

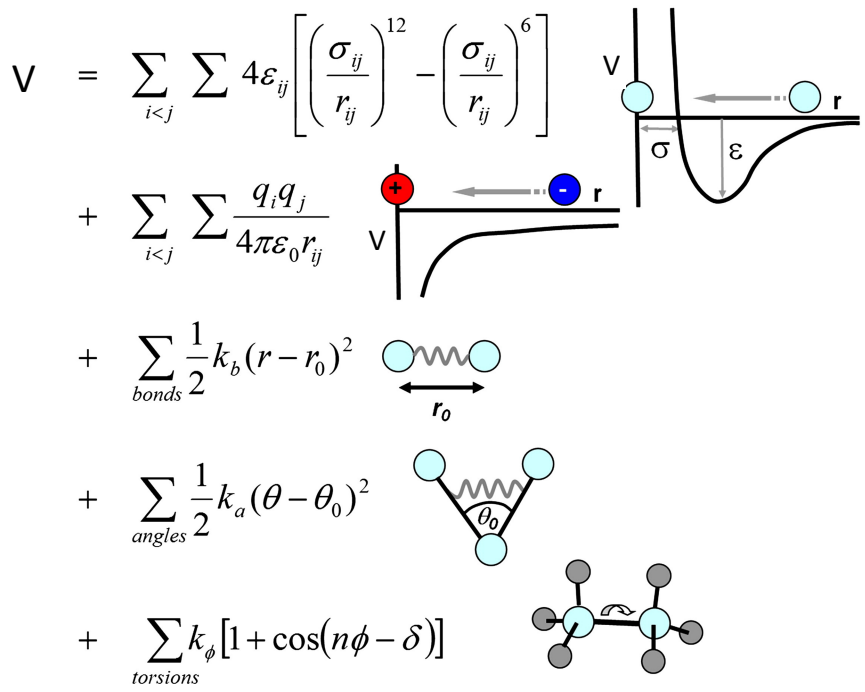

Figure III.1 – Potential energy function for molecular interactions in the molecular mechanics approximation. Adapted from [229]

Using this potential function, MD simulations solve Newton's equations of motion for a system of N interacting atoms:

$$m_i \frac{\partial^2 \boldsymbol{r}_i}{\partial t^2} = \boldsymbol{F}_i, \quad i = 1 \ldots N \tag{III.1}$$

where the forces are the negative derivatives of a potential function $V(r_1, r_2, \ldots, r_N)$

$$F_i = -\frac{\partial V}{\partial r_i} \tag{III.2}.$$

The equations are solved simultaneously in small time steps, typically 1 fs to 4 fs when atomic detail is required. Usually, the duration of simulations goes from less than a nanosecond to the microsecond time scale. Despite today's computational power most simulations are still on the 100 ns time scale. Taking care that the temperature and pressure remain at the required values, after a certain number of steps have been accomplished the simulation is concluded. If a starting configuration is very far from equilibrium, the forces may be excessively large and the MD simulation can fail. In those cases, a prior energy minimization is required in order to avoid such interactions in the system. In the simulation output, the written coordinates (and eventually velocities) as a function of time represent a trajectory of the system, which is its main

result. After initial changes, the system usually reaches an equilibrium state. By averaging over an equilibrium trajectory (output file), many macroscopic properties can be extracted.

III.1.2 – Force fields, Constraints and Topologies

The force field is the description of interactions as illustrated in Figure III.1, used to generate the potential energies and their derivatives, the forces, and the parameters used in the set of equations. The force field is pair-additive, which means that all non-bonded forces result from the sum of non-bonded pair interactions. Non pair-additive interactions, the most important example of which is interaction through atomic polarizability, are represented by effective pair potentials, and therefore only average non pair additive contributions are incorporated. Force fields which account explicitly for atomic polarizability already exist, albeit at high computational cost. Bonded interactions which are based on a fixed list of atoms are not exclusively pair interactions, but also include 3 and 4 particle interactions. Therefore, there are bond stretching (2-particles), bond angle (3-particles), and dihedral angle (4-particle) interactions. Improper dihedrals are used to force atoms to remain in a plane or to prevent transition to a configuration of opposite chirality.

Force fields may be classified regarding the description detail of the interactions. All atom (AA) force fields consider all atoms in the systems, united atom (UA) force fields treat each CH, CH_2 or CH_3 group as a single particle and coarse grain (CG) force fields consider beads of heavy atoms as a single particle. The most used force fields in biological simulations containing proteins and lipids are united atom GROMOS87, GROMOS-96, all-atom OPLS/AA, AMBER, CHARMM, and coarse grain MARTINI (CG). For water, several force field descriptions are specifically available such as, SPC, SPC/E and TIP3P. Force fields are an independent part of the simulation method, and their parameters can be user-modified as the need arises or knowledge improves. The use of different force fields should be made with caution. Parameters in different force fields are internally consistent, but this is not necessarily true between different force fields or simulation methods. Specifically considering water/lipid systems, SPC/E was compared to SPC waters and it was found that SPC has a better chemical potential in mixed systems, which makes it the better choice in studies of interfaces [25, 230].

The properties of lipid membranes can be studied at different time and length scales. For some properties it is important to take into account all the details of a system, all atoms including hydrogens. Other properties require much larger length and time scale than what is possible using atomistic simulations. Examples are undulations of membrane surface, formation of different aggregates as micelles, vesicles, lamellar or hexagonal phase transformations or problems related to domain formations at the membrane surfaces. [231] In such cases, a simplified description of individual lipids is needed, so that groups of atoms are lumped into pseudo-particles to arrive at a coarse-grained, or mesoscopic, description of a bilayer. Coarse-grained (CG) models are emerging as a practical alternative to all-atom simulations for the characterization of membrane phenomena over long time scales. Marrink and coworkers [232, 233] have developed the so-called MARTINI CG model, which is used by many researchers worldwide.

Special restraint potentials, which are not really part of the force field, may be used for imposing restraints on the motion of the system, either to avoid disastrous deviations or to include knowledge from experimental data. Special interactions, known as "exclusions" and "1-4 interactions", are considered in the force field. Atoms within a molecule that are covalently bonded, or linked by one or two atoms are called first neighbors, second neighbors and third neighbors, respectively, Figure III.2. Since the interactions of atom i with atoms i+1 and i+2 are mainly quantum mechanical, they cannot be modeled by a Lennard-Jones potential. Instead it is assumed that these interactions are adequately modeled by a harmonic bond term or constraint (i, i+1) and a harmonic angle term (i, i+2). The first and second neighbors (atoms i+1 and i+2) are therefore excluded from the Lennard-Jones interaction list of atom i; atoms i+1 and i+2 are called exclusions of atom i. For third neighbors, the normal Lennard-Jones repulsion is sometimes still too strong, which means that when applied to a molecule, the molecule would deform or break due to the internal strain. Therefore, for some of these interactions, the standard Lennard-Jones parameters are reduced, and the Coulomb interactions are scaled.

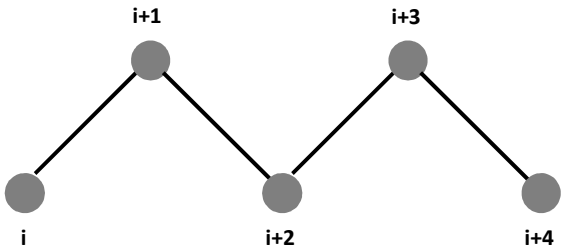

Figure III.2 – Atoms along an alkane chain.

In GROMACS, constraints can be imposed using LINCS (or its parallel version P-LINCS) or the traditional SHAKE method. LINCS is an algorithm that resets bonds to their correct lengths after an unconstrained update [227, 228]. LINCS is more stable and faster than SHAKE. Because of its stability, LINCS is especially useful for Brownian dynamics. LINCS is implemented in such a way that even when it is impossible to reset the constraints, it will generate a conformation which fulfills the constraints as well as possible. However, LINCS will generate a warning when in one step a bond rotates over more than a predefined angle, which is set by the user. Specifically for water, GROMACS uses the SETTLE algorithm [234], which is an analytical solution of SHAKE.

In order to correctly perform the calculations, simulation packages such as GROMACS must know on which atoms and combinations of atoms the various contributions to the potential functions must act. It must also know what parameters must be applied to the various functions. All this information is described in the topology file (*.top), which lists the constant attributes of each atom. In the force field, there are many more atom types than elements, which mean that several atom types apply to different bond types of a given element. Usually, only atom types present in biological systems are parameterized in the force field, plus some metals, ions and silicon. The bonded and special interactions are determined by fixed lists that are included in the topology file. In some cases molecular topologies may be included in separate files (*.itp), that in those cases should be called by the *.top files. There are molecular databases that can be used to easily obtain topologies [235, 236]. However, their data should be carefully verified before use.

Several methodological studies were devoted to validation of the different force fields used in bilayer simulations. To validate simulation models there is a critical need to

examine a range of experimental data as opposed to focusing on a single parameter. The average area per lipid defined at constant pressure (zero tension simulations) is a parameter which is most often used to define the quality of the force field. Area per lipid is one of the most fundamental properties of a lipid bilayer, and one of the most common ways to determine whether the bilayer system has reached equilibrium. When the area per lipid reaches a stable value, usually other structural properties (density distributions, NMR order parameters) converge, too. Simulated area per lipid can be compared with experimental values available from X-ray or neutron diffraction and volumetric data. A collection of average lipid areas for several bilayers composed from different lipids and computed from different force fields, as well as experimental values, is available in [237]. More reliable validation of a force field can be done by comparison of simulated and experimental structure factors, as shown in [238]. An additional important source of data for validation of a force field used in lipid bilayer simulations is NMR bond order parameters.

III.1.3 – Ensembles and Boundary Conditions

MD simulations performed using default integration methods samples the microcanonical ensemble in which the number of particles N, the volume V, and total energy E are constant (NVE). In order to simulate real systems it is useful to define schemes to follow the evolution of the system under conditions of constant volume and temperature (NVT), or constant pressure and temperature (NPT). Constant pressure algorithms allow the surface area per lipid to adjust. This makes possible to verify the area per lipid obtained in simulations against experimental data. For these reasons, it is generally accepted now that it is advantageous to use constant pressure in simulations of lipid systems, although many simulations in the literature used constant volume conditions. [53] The use of a surface tension in lipid bilayers simulations may also be found in the literature. [239, 240] However, this should not be needed, since the main contribution to the surface tension in an air/monolayer/water system comes from the air/monolayer interface. [241, 242]

The current computational power allows the simulation of systems with an increasing number of particles. However, even larger systems (say, one million particles) still have finite size and a number of particles will have unwanted boundaries with its

environment (vacuum). The classical way to minimize border effects, when simulating bulk systems in a finite system, is to apply periodic boundary conditions. The atoms of the system to be simulated are put into a space-filling box, which is surrounded by translated copies of itself, Figure III.3. Each unit cell (cubic, rectangular or triclinic) is surrounded by 26 translated images. Thus there are no boundaries to the system. Molecules that leave the cell will be replaced by their images entering the cell from the opposite side. However, the artifact caused by unwanted boundaries in an isolated cluster is now replaced by the artifact of periodic conditions. Since liquids are not ordered as crystals, something unnatural remains. The errors can be evaluated by comparing various system sizes and are expected to be less severe than the errors resulting from an unnatural boundary with vacuum. For large systems, the errors are small, but for small systems with a lot of internal spatial correlation, the periodic boundaries may enhance internal correlation, which may give rise to simulation artifacts.

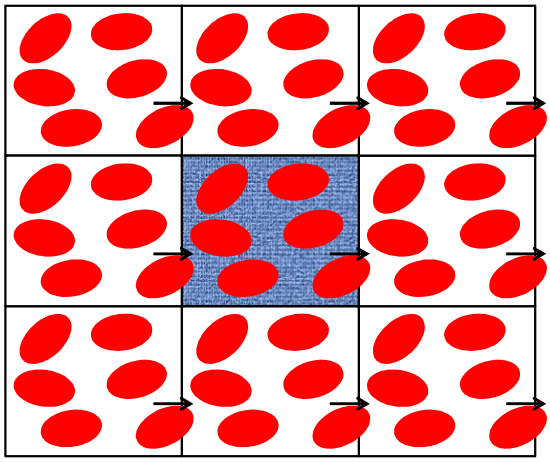

Figure III.3 – Periodic boundary conditions in two dimensions with the primary cell surrounded by its image cells.

III.1.4 – Temperature and Pressure Control

As mentioned above, whereas direct use of molecular dynamics gives rise to the NVE ensemble, most observables of interest are more conveniently obtained using constant temperature (NVT) or constant temperature and constant pressure (NPT) ensemble. The temperature in a system is given by the kinetic energy of all atoms. However, there are several other reasons why it might be necessary to control the temperature of the system. Due to drift during equilibration, numerical inaccuracy, and cutoff effects, the

temperature in a system will tend to drift away from the starting temperature. To prevent this, some type of temperature control is necessary. The pressure of a system depends on the forces and positions of all atoms and determines whether the system expands or contracts and, therefore, how the size of the simulation box fluctuates.

There are several algorithms for temperature control, and some of them are commonly used in lipid simulations. In GROMACS, we can use either the weak coupling scheme of Berendsen [243], the extended ensemble Nosé-Hoover scheme [244, 245], or the velocity rescaling scheme [246] to simulate constant temperature. In the weak coupling scheme of Berendsen [243], the system is coupled to a "bath" of constant pressure or temperature *via* some suitable coupling parameters, and therefore it allows temperature and pressure control. The main advantages of this scheme are its simplicity and little perturbation of the system. The main drawback is that this method generates an unknown statistical mechanical ensemble. The velocity rescaling thermostat is essentially a Berendsen thermostat with an additional stochastic term that ensures a correct kinetic energy distribution. In GROMACS temperature coupling can be performed on groups of atoms, typically a protein and solvent. The reason why such algorithms were introduced is that energy exchange between different components is not perfect, due to different effects including cut-offs. A typical example is that if the whole system is coupled to one heat bath, water (which experiences the largest cut-off noise) will tend to heat up and e.g. the protein will cool down. Typically 100 K differences can be obtained. [247] However, a separate thermostat should not be defined when using ions in the solvent, and ions temperature control should be done using a global solvent thermostat.

In the same spirit as the temperature coupling, the system can also be coupled to a "pressure bath". GROMACS supports both the Berendsen algorithm [243] that scales coordinates and box vectors every step, the extended ensemble Parrinello-Rahman approach [248, 249], and for the velocity Verlet variants, the Martyna-Tuckerman-Tobias-Klein (MTTK) implementation of pressure control [250]. Parrinello-Rahman and Berendsen can be combined with any of the temperature coupling methods above. MTTK can only be used with Nosé-Hoover temperature control. [247] When setting the pressure coupling method, a pressure coupling type must be chosen. Although isotropic water systems should use isotropic pressure coupling, for lipid membrane systems the most common approach is the use of semiisitropic pressure coupling, which is isotropic

in the *x* and *y* (bilayer plane) directions, but independent in the *z* (bilayer normal) direction.

III.1.5 – Electrostatic Interactions and Cutoffs

Figure III.1 suggests that the interactions between a given atom and all other atoms are calculated, but this is highly inefficient for large systems. Since the interactions between atoms become weaker at longer distances, it makes sense to cut them off at some point, i.e. no longer calculate interactions between atoms when their separation distance is more than a certain value. Such a cutoff means that a part of the interactions is neglected. How serious this is depends on the type of interactions, and the size and scheme of the cutoffs used. Van der Waals interactions rapidly decrease with increasing distance, but Coulomb interactions between dipoles, and especially between whole charges, are quite long-ranged. The "minimum-image convention" used by GROMACS requires that only one image of each particle in the periodic boundary conditions is considered for a pair interaction, so the cut-off radius cannot exceed half the box size. The simplest way to deal with these long-ranged interactions is by ignoring them, but in practice this does not work for systems with fully charged atoms. Therefore, for van der Waals interaction, the cut-off scheme is the one most used, but alternative shift or switch schemes with a "smother cut-off" implementation may be employed. For long range electrostatics, several schemes may also be used, such as reaction field or the sophisticated and most used Particle-Mesh Ewald (PME) method. [251, 252]

III.1.6 – Output and Analysis

As stated above, the most important output of the MD run is the trajectory file, which contains particle coordinates and optionally velocities at regular intervals. Since the trajectory files are lengthy, one should not save every step. The frequency of saving of this information depends on the purpose of the simulation. Short time intervals may generate very long and unnecessary trajectories whereas with a too long time interval relevant information may be lost. In addition to the setup and integration programs, the GROMACS software package has several tools that allow the user to analyze the main properties of the simulated biological systems. In most analysis programs, specified groups of atoms must be defined. GROMACS tools can generate several default index

groups, but groups can always be read from an index file (index.ndx). Groups can consist of a series of atom numbers, but in some cases also of molecule numbers. It is also possible to specify a series of angles by triplets, dihedrals by quadruples and bonds or vectors by pairs of atom numbers. Regarding lipid membrane systems, several properties are usually obtained from MD simulations including area per lipid, lipid order parameters, position and distance between different atoms, orientation of planes or atom vectors, hydrogen bonding, electrostatic potential and diffusion coefficients.

III.2 – Method Details of the MD Simulations Performed on Chapters IV to VII

III.2.1 – Simulation Details for the Study of the Interaction of NBD-Labeled Fatty Amines with Lipid Bilayers

For the study of the interaction with POPC bilayers, MD simulations and analysis of trajectories were carried out using the GROMACS 3.2 package [219, 253], while for the study of the interaction with cholesterol-containing bilayers, GROMACS 4.5.3 package [220, 254] was used. The SPC water model [255] was used in all simulations.

For the interaction with pure POPC bilayers, the topology of the POPC molecule (using an united-atom description for CH, CH_2, and CH_3 groups, based on the parameters presented by Berger et al. [256] for 1,2-dipalmitoyl-*sn*-glycero-3-phosphatidylcholine (DPPC)) and the coordinate file of a POPC bilayer were obtained from Dr. Peter Tieleman's group webpage (http://moose.bio.ucalgary.ca/index.php?page=Structures_and_Topologies) [257]. One POPC molecule from the downloaded POPC bilayer coordinate file was used to build a fully hydrated (3902 water molecules) 128-lipid bilayer using GROMACS model set-up programs. For the CH_2 and CH_3 groups of NBD-C_n molecules, parameters were based on those of the phospholipid. The NBD fluorophore was parameterized as described in detail by Loura et al [258]. Briefly, a preliminary topology was obtained using the PRODRG server [259]. Equilibrium bond lengths, angles and dihedrals were obtained through energy minimization carried out with the Gamess-US package [260, 261]. Other parameters were taken from the OPLS all-atom force field [262]. All bonding and non-bonding parameters are shown in the supplemental information file of reference

[258]. Partial charges of the NBD group atoms were derived from *ab initio* quantum mechanical calculations [263] using Gamess-US, and their values are given in Table 1 of reference [264]. Bilayers containing 2 and 4 NBD-C_n molecules (1 and 2 in each leaflet, respectively) were obtained by randomly inserting probe molecules inside the POPC bilayer without replacement of phospholipids.

For the interaction with cholesterol-containing bilayers (POPC:Chol (1:1) and SpM:Chol (6:4)), the topology of the POPC molecule [237] was downloaded from lipidbook [236] (http://lipidbook.bioch.ox.ac.uk/). For SpM, a previously described GROMOS87 parameterization [265], also downloaded from lipidbook, was adapted to GROMOS53A6 force field. The explicit hydrogens in SpM were parameterized as virtual sites. The cholesterol parameterization was downloaded from ATB [235] (http://compbio.biosci.uq.edu.au/atb/). The NBD fluorophore was parameterized by translation of the parameters described by Loura et al. [258, 264] to GROMOS53A6, maintaining the atomic charges. The initial coordinates for POPC:Chol (1:1) bilayer were obtained from previous simulations [266]. The initial coordinates for SpM:Chol (6:4) were adapted from a POPC:Chol (6:4) bilayer [267], replacing the POPC by SpM at the same phosphorus coordinates. The POPC:Chol (1:1) bilayer is composed by 144 lipids hydrated by 5824 water molecules, and the SpM:Chol (6:4) is composed by 150 lipids hydrated by 6612 water molecules. Bilayers containing 4 NBD-C_n molecules (2 in each leaflet, respectively) were obtained by randomly inserting probe molecules inside the POPC:Chol and SpM:Chol bilayers without replacement of phospholipids.

In all systems, unfavorable atomic contacts were removed by steepest descent energy minimization. For each system, a short (100 ps) MD run was then carried out using a 1 fs integration step, followed by a 100 ns run using a 4 fs integration step. The use of this time step was made possible by constraining bond lengths and angles to their equilibrium values, using the SETTLE algorithm [234] for water and the LINCS algorithm [227] for all other bonds (see also discussion in [268, 269]). All simulations were carried out under constant number of particles, pressure (1 bar) and temperature (298.15 K), and with periodic boundary conditions. Pressure and temperature control were carried out using the weak-coupling Berendsen schemes [243], with coupling times of 1.0 ps and 0.1 ps, respectively. For cholesterol-containing bilayers, the temperature control (298.15 K) was carried out using the V-rescale scheme [246] with

coupling time of 0.1 ps. Semi-isotropic pressure coupling was used. Van der Waals and Coulomb interactions were cut-off at 1.0 nm, whereas for long-range electrostatics the Particle Mesh Ewald treatment [252] was applied.

The first 20 ns of each simulation were used for equilibration, and the remaining 80 ns were used for analysis. Error estimates for time averages of correlated data were computed using the block method as described by Flyvbjerg and Petersen [270].

III.2.2 – Simulation Details for the Calculation of Free Energy Profiles of Long Amphiphiles Interacting with Lipid Membranes

MD simulations and analysis of trajectories were carried out using the GROMACS 4.5 package. [219, 220] For water, we used the SPC water model. [255] NBD-C_n amphiphiles parameters were as described in the preceding section for the interaction with POPC bilayers.

For simulations in pure POPC bilayers, the POPC parameters were as described in the preceding section. The fully hydrated (3902 water molecules) bilayer was used. Additionally, a super-hydrated (7704 water molecules) symmetric bilayer comprised of 128 lipids was built using GROMACS model set-up programs.

For simulations in POPC:Chol and SpM:Chol membranes, the topology of the POPC [257], based on Berger et al. [256] parameters was used, as described in the preceding section, with the dihedrals around the double bound described according to [271], which is reported to be more appropriate for cholesterol-containing bilayers. The topology of the SpM molecule [265], was downloaded from lipidbook [236]. For cholesterol, we used the description of Holtje et al. [272]. The POPC:Chol (1:1) bilayer is composed by 144 lipids hydrated by 5824 water molecules, and the SpM:Chol (6:4) is composed by 150 lipids hydrated by 6612 water molecules. An asymmetric SpM:Chol (6:4)/POPC:Chol (1:1) bilayer was built by pasting a SpM:Chol (6:4) monolayer on the top of a POPC:Chol (1:1) monolayer. However, the small bilayer dimensions (needed to perform the simulations in a reasonable time and computational cost) may rise size artifacts, resulting from the fact that there are more lipid molecules in the SpM:Chol (6:4) monolayer. To avoid this, an extra molecule was added to the POPC:Chol (1:1) monolayer. Therefore the asymmetric bilayer is composed by 45 SpM

and 30 Chol molecules in the top monolayer and 37 POPC and 37 Chol molecules in the bottom monolayer.

MD runs were carried out using a 2 fs integration step. Ensemble, boundary conditions, constraints, pressure control and intermolecular interactions were used as described in the preceding section. Temperature control (298.15 K) was carried out using the V-rescale scheme [246] with coupling time of 0.1 ps.

III.2.2.1 – Umbrella Sampling Simulations in Pure POPC Bilayers

The distance of the NBD's center of mass (COM) to the membrane COM along the normal coordinate z was chosen as the reaction coordinate for solute permeation, where z = 0 nm is defined by the COM of the lipid molecules. Two sets of simulations were carried out. In the first (pull geometry distance, PGD), the COM was computed using an average over all lipid atoms in the bilayer. In the second set (pull geometry cylinder, PGC), the COM was computed using a weighted sum over the lipid atoms that were within a cylinder of radius 17 Å, centered at the respective solute and aligned along the z-axis. Here, a weight of 1 was assigned to all atoms within a distance of 12 Å to the cylinder axis, and the weights were switched to 0 between 12 and 17 Å.

Two sets of initial structures (PGD and PGC) were generated by pulling the amphiphile NBD-C_{16} from the NBD's COM, first moving from the bilayer center to bulk water (CW direction) with a pulling rate of 0.005 nm/ps and a force constant of 500 kJ mol^{-1} nm^{-2}. For the other NBD-C_n molecules (n = 4, 8, 12), initial structures were adapted from the ones of NBD-C_{16}. For PGD, the initial structures of NBD-C_{16} were also generated by pulling the amphiphile from bulk water to the center of the membrane (WC direction), with the same pulling parameters as in the CW case.

Adjacent umbrella windows spanned the space between the membrane center (z = 0) into the bulk water region (z = 4.3 nm or 4.5 nm for the PGC and PGD simulations, respectively), separated by 1 Å. For umbrella windows with $z \leq$ 2.1nm and $z \geq$ 2.2nm, the fully hydrated and super-hydrated lipid bilayers were used, respectively. To avoid potential amphiphile-amphiphile interactions, only one molecule was sampled in each simulation.

A harmonic umbrella potential, acting on the COM of the NBD moiety, was applied (force constant 3000 kJ mol^{-1} nm^{-2}). After the simulations were completed, the unbiased PMF was obtained using the weighted histogram analysis method (WHAM) [168, 170].

The convergence of free energy profiles was assessed according with the described in the section III.2.2.3. The converged PMF profiles that were used to determine the free energy barriers in the permeation process of the amphiphiles are shown in Figures A.8 and A.9 (see Appendix). For the PGC method, we carried out 100 ns simulations, where the first 20 ns of each simulation were used for equilibration and the last 80 ns for analysis. For the PGD method, the PMF for NBD-C_{16} was first obtained by simulating for (at least) 110 ns, where the first 20 ns were considered as a period for equilibration. For the other molecules, the initial structures were generated from the simulations of the equilibrated NBD-C_{16} PMF and were simulated for 50 ns, thus in this case only the first 10 ns were used for equilibration.

III.2.2.2 – Umbrella Sampling Simulations in Cholesterol-Containing Bilayers

The distance of the NBD's center of mass (COM) to the membrane COM along the normal coordinate z was chosen as the reaction coordinate for solute permeation, where z = 0 nm is defined by the COM of the lipid molecules. The simulations were carried according with the PGC method as described before, with a cylinder of radius 15 Å. Here, a weight of 1 was assigned to all atoms within a distance of 10 Å to the cylinder axis, and the weights were switched to 0 between 10 and 15 Å.

The initial structures for each umbrella window were generated by pulling the amphiphile NBD-C_{16} from the NBD's COM, moving from the bilayer center to bulk water (CW direction) with a pulling rate of 0.005 nm/ps and a force constant of 500 kJ mol^{-1} nm^{-2}. For the other NBD-C_n molecules (n = 4, 8, 12), initial structures were adapted from those of NBD-C_{16}. Adjacent umbrella windows spanned the space between the membrane center (z = 0) into the bulk water region, separated by 1 Å.

A harmonic umbrella potential, acting on the COM of the NBD moiety, was applied (force constant 3000 kJ mol^{-1} nm^{-2}). After the simulations were completed, the unbiased PMF was obtained using WHAM [168, 170].

The convergence of free energy profiles was assessed according with the described in the next section. For NBD-C_{16}, 200 ns simulations were carried out. For the other

amphiphiles, 100 ns simulations were performed, with longer simulations at specific values of the reaction coordinate. The first 20 ns of each simulation were used for equilibration and the remaining time for analysis.

III.2.2.3 – Convergence of Free Energy Profiles

There are two issues regarding the computation of free energy profiles: for each window used in umbrella sampling, how long simulation times are needed to equilibrate the system, and how long times are needed to sample the system appropriately? If the equilibration and sampling times for the given system and for the given sampling windows are not sufficiently long, then the results do not converge to their true values.

Here we use an approach where we fix the total simulation time in each umbrella sampling window to be about 100 ns to 200 ns (and since there are about 45 windows, separated by 0.1 nm, the total simulation time is about 4.5 to 9 microseconds). We use three ways to consider the above problems:

i) We assume (incorrectly) that no equilibration is needed, and in each sampling window we use increasing amounts of simulation data for sampling of the PMF.

ii) In each sampling window we systematically increase the slice of the simulation time used for equilibration, and use the rest of the simulation data for analysis.

iii) Again in each sampling window we systematically increase the amount of data used for equilibration, and the analysis for the PMF profile (in each window) is carried out over a fixed period of 20 ns.

In all three schemes, not only the values of the barriers but also the shapes of the profiles are compared to each other.

III.3 – Simulation Details for the Kinetic Modeling of the Passive Distribution of Free Cholesterol in the Blood

In this section we will describe the lipoproteins, erythrocytes and albumin as used to model the cholesterol homeostasis and blood distribution. All structural, equilibrium and kinetic parameters are summarized in Tables A.1 and A.2 in the Appendix.

Lipoproteins: The structural parameters of the lipoproteins are summarized in Table A.1 in the Appendix. Briefly, the number of unesterified cholesterol molecules *per* lipoprotein was: 3539, 475, 50 and 13 [197] and the concentration of each lipoprotein in the serum was 0.08, 1.5, 4 and 30 μM [273] for VLDL, LDL, HDL_2 and HDL_3, respectively. The amount of cholesterol in the lipoproteins may be calculated from the number of cholesterol *per* particle and the concentration of the lipoproteins in the blood. This leads to 1.6 mM total concentration of free cholesterol in the plasma, in accordance to the values reported in the literature for plasma that is considered to have a "normal" cholesterol concentration (1.4-1.6 mM) [197, 274, 275].

Erythrocytes: This model assumes an average hematocrit of 44%. Together with the volume of each erythrocyte (94 μm^3) [276], this allows the calculation of the concentration of erythrocytes, equation (III.3), being equal to 8.36×10^{12} particles per liter of plasma.

$$n_{\mathrm{Ery}} = \frac{0.44}{1-0.44}\frac{V_{\mathrm{P}}}{V_{\mathrm{Ery}}} \qquad \text{(III.3)},$$

where V_{P} is the volume of plasma and V_{Ery} is the volume of each erythrocyte.

The number of phospholipid and cholesterol molecules in each erythrocyte was taken from literature [97], being 2.4×10^8 and 1.9×10^8, respectively. This was used to calculate the extracellular lipid surface area of each erythrocyte membrane considering a lipid surface area of 40 $Å^2$ [126, 277] (total lipid area of each erythrocyte equal to $(2.4\times10^8+1.9\times10^8)\times40$ $Å^2$= 174 μm^2) and that the inner and outer leaflets of the membrane have the same surface area (extracellular lipid surface area=174/2= 87 μm^2). The total surface area of the erythrocytes *per* liter of plasma is calculated from the number of erythrocytes being equal to: $A^{\mathrm{o}}_{\mathrm{Ery}} = A^{\mathrm{i}}_{\mathrm{Ery}} = 7.28\times10^4$ dm^2 *per* liter of plasma. The volume of the erythrocyte membrane was calculated from its surface considering 2 nm for the thickness of each lipid monolayer ($V_{\mathrm{L}}^{\mathrm{Ery^o}} = V_{\mathrm{L}}^{\mathrm{Ery^i}} = 1.46\times10^{-3}$ dm^3 *per* liter of plasma). From the concentration of erythrocytes and number of lipids *per* particle, the total concentration of free cholesterol in the erythrocytes may be calculated leading to 2.7 mmol *per* liter of plasma. Adding the amount of cholesterol in the lipoproteins, the total concentration of free cholesterol considered in the model is therefore equal to 4.3 mmol *per* liter of plasma.

The lipid composition given in the literature for the erythrocyte membrane of normal men has been reviewed [81, 97-101], being equal to 39 ± 10 mol% cholesterol and 61 ± 9 % phospholipids from which 22 ± 5 mol% is PC, 17 ± 2 mol% is SpM, 5 ± 4 mol% is PS and 17 ± 4 mol% is PE. It is usually considered that SpM is located mostly in the outer monolayer and that a significant amount of PC is located in the inner monolayer together with all PS and almost all PE [81, 98]. The distribution of cholesterol between the outer and inner leaflets is controversial but, given the fast rate of translocation expected for cholesterol, one should expect it to be at equilibrium and with similar concentrations in both leaflets. The above information leads to SpM 33 %, Chol 39 % and PC 28 % for the lipid composition of the outer monolayer and Chol 39%, PC 17 %, PS 10 % and PE 34 % in the inner leaflet. However, the uncertainty associated with those values is very large, and taking into account the standard deviation indicated, the amount of PC in the outer layer may be as low as 4 mol% and as high as 30 mol% in the cytoplasmic leaflet. Another important characteristic of the erythrocyte membrane lipids is the higher abundance of unsaturations in the fatty acyl chains of the lipids enriched in the inner leaflet [100] in agreement with the lower viscosity of this monolayer [81]. In this work we have modeled the interaction of DHE with the erythrocyte membranes considering that the outer leaflet is composed of SpM:Chol (6:4) and that the cytoplasmic leaflet is composed of POPC:Chol (1:1), because those represent the lipid compositions most similar with the predicted ones for which the kinetic and equilibrium parameters of DHE interaction have been characterized [139].

Serum albumin: The concentration of Human Serum Albumin considered in the model was 0.6 mM and their binding properties were modeled by Bovine Serum Albumin (BSA). To compute the total concentration of free cholesterol in the blood, it was assumed that the fraction of HSA with bound cholesterol is equal to 0.01. The contribution of this cholesterol to the total concentration in the blood is negligible.

III.4 – Simulation Details for the Quantitative Modeling of the Passive Permeation through a Cell Monolayer

In this section we will describe the approximations and definitions of the compartments used to quantitatively model the passive permeation through a cell monolayer. All

parameters and conversion factors are summarized in Tables A.3, A.4 and A.5 in the Appendix.

Serum components: The parameters for interaction of NBD-C_n with serum albumin were experimentally obtained in earlier works [5, 6]. We have not directly measured values for interaction of NBD-C_n with lipoproteins. However, we have experimentally measured values for interaction of NBD-dimyristoylphosphatidylethanolamine (NBD-C_{14}PE) with POPC bilayers [3] and all lipoprotein classes [9]. The ratio of the two values gives a conversion factor for interaction parameters of NBD-C_{14}PE with POPC bilayers and lipoproteins. This conversion factor was assumed to be the same for interaction of NBD-C_n with POPC bilayers [5, 6] and lipoproteins (see Table A.4 of the Appendix), which is supported by the similar conversion factors obtained independently for dehydroergosterol. [10, 139] For all tested amphiphiles, the interaction with albumin and with lipoproteins occurs at much faster rates than with lipid bilayers representative of the outer monolayer of endothelial cells [3, 9, 10, 139]. We have therefore assumed fast equilibrium for the interaction of the amphiphiles with albumin and lipoproteins. As a consequence, those binding agents behave as reservoirs that release amphiphile as it is transferred to the tissue.

Membrane cell compartments: The lipid composition of the various cell membranes is distinct, and lipids are asymmetrically distributed between the inner and outer leaflets of plasma membranes [17], with the outer leaflet being enriched in sphingomyelin and cholesterol [81, 94, 98, 102]. However, at this stage, we have opted to consider equal lipid composition for all membranes to simplify the system and facilitate the interpretation of the effect of the various compartments on the kinetics of the overall permeation process. All membranes have therefore been modeled by a bilayer of POPC, which is the most abundant phospholipid in eukaryotic cells [278].

Cell Cytoplasm: The intracellular cytoplasm is a very crowded medium composed by organelles and several types of molecules and supra-molecular assemblies. This is expected to have significant effects on the amphiphiles' sequestration inside cells. To simplify the model and highlight the effects of sequestration by the serum components and tissue, we have modeled the cell contents as water.

Inter and Intracellular exchange: Cells in tight endothelia are joined by TJ that are impermeable to water-soluble molecules [174]. In addition, no exchange of amphiphile between neighboring cells or between the apical and basolateral side of the outer leaflet

in the same cell is allowed [17, 174]. TJ are a diffusion barrier for small molecules associated with the outer leaflet of the plasma membrane, but not for solutes in the inner leaflet [179]. We have therefore allowed unconstrained lateral diffusion of the amphiphiles within the inner leaflet of the plasma membrane. The rate constant considered for the distribution between the apical and basolateral sides of the inner leaflet was the reciprocal of the time, *t*, required to diffuse through the total area of the membrane of one cell, $area \sim \left\langle r^2 \right\rangle = 4Dt$. These calculations yielded $k_{ld}^{a \to b}$ = 0.2 s^{-1} and $k_{ld}^{b \to a}$ = 0.13 s^{-1} by considering the diffusion coefficient of a single acyl chain amphiphile, $D^i = 5.0 \times 10^{-8}$ cm^2/s [279].

Target Tissue: Binding of the amphiphile at the target tissue influences the amount of amphiphile that permeates the cell monolayer, and this affects the overall permeation rate observed. This parameter depends strongly on the amphiphile and metabolic state of the target tissue. We have opted to simulate three situations, where the first two of which represent extremes: *i*) complete and irreversible transfer of amphiphile to the tissue, which was modeled as an infinite-capacity sink (M1); *ii*) minimal transfer of amphiphile, where the tissue was modeled by the relevant volume of water (M2, reversible transfer); and *iii*) intermediate situations where partial binding capacity is considered (M3 and M4). M3 considers a binding capacity in the tissue equivalent to an albumin concentration equal to that in the serum, and in M4 the binding capacity is increased to match that of the serum (with albumin and lipoproteins).

Structural details, concentrations and parameters considered in the model. The rate constants for insertion and desorption into/from the membranes considered in this model have been calculated from those reported for the interaction of the amphiphiles with POPC LUVs taking into account the topology of the lipid phase [6, 10]. The relationship between the previous rate constants ($k_+^{L_V}$ and $k_-^{L_V}$) and those used in this study (κ_+^L and κ_-^L) is given by equations (III.4):

$$\kappa_+^L = k_+^{L_V} \frac{1}{\overline{A_{L_V}^o}}; \quad \kappa_-^L = k_-^{L_V} \; h \qquad \text{(III.4)}.$$

Here $\overline{A_{L_V}^o}$ is the molar surface area of the outer leaflet in contact with the aqueous phase of the 50 nm radius POPC LUVs used to obtain the rate constants,

1.89×10^{12} dm^2 mol^{-1}. The thickness of the membrane leaflet (*h*) was considered equal to 2 nm. Details of the derivation of the above equations can be found in section A.VIII.2 of the Appendix. The kinetic parameters for the shorter chain amphiphiles (n = 2, 4 and 6) as well as the translocation rate constant for NBD-C_8 were obtained by extrapolation of our previously reported experimental results [6]. According to our results from molecular dynamics simulations, Chapter VI, the variation in free energy for the transition state of translocation in POPC bilayers is linear from n = 4 to 16 carbons. [280] Therefore the translocation rate constant for n = 2 to 8 carbons was obtained assuming an exponential dependence of the experimental rate constants obtained for the amphiphiles with $n \geq 10$. To obtain the insertion and desorption rate constants for n = 2 to 6, the association/dissociation processes were considered to occur through the formation of an encounter complex between the amphiphiles and the lipid vesicles. [9] As discussed in detail in section A.IX.2 of the Appendix, kinetics of the insertion of amphiphiles into membranes is not a simple diffusion-limited process, but must take into consideration both diffusion-limited encounter complex formation and the (much slower) insertion into the bilayer *per se*. The same arguments apply to desorption of amphiphiles from membranes. Thus, the insertion and desorption rate constants were obtained assuming linear dependence on the free energy variation of the transition step associated with k_{in} and k_{out} (exponential dependence on the rate constants).

The concentrations of serum albumin and lipoproteins were taken from [194, 273], and 5 dm^3 of serum were considered [281]. The total surface area considered in the model for the apical portion of the cell monolayer in contact with the serum was A^{a^o} $=1.52\times10^4$ dm^2 [281] and the surface area of the basolateral membrane in contact with the tissue was considered to be 1.5 times larger, A^{b^o} $=2.28\times10^4$ dm^2 [282]. The volume of each lipid leaflet was calculated from its surface assuming a thickness of 2 nm. The structural parameters are collected in Table A.5 in the Appendix. The total amount of amphiphile is 5 μmol.

Chapter IV

Interaction of NBD-Labeled Fatty Amines with POPC Bilayers: A Molecular Dynamics Study

This work was published as: Filipe, H. A. L.; Moreno, M. J.; Loura, L. M. S. Interaction of 7-Nitrobenz-2-Oxa-1,3-Diazol-4-Yl-Labeled Fatty Amines with 1-Palmitoyl, 2-Oleoyl-Sn-Glycero-3-Phosphocholine Bilayers: A Molecular Dynamics Study. *J. Phys. Chem. B* **2011**, *115*, 10109-10119.

Hugo A. L. Filipe contributed with the preparation, execution and analysis of the simulations, and also contributed to the writing of the manuscript.

IV.1 – Introduction

The interaction of amphiphilic molecules with lipid bilayers is a very important step that determines their location inside the cells and the rate of permeation across the different hydrophobic barriers in the cell or organism. Molecules with pharmacological or biological activity are usually amphiphilic due to their need to cross the different cell membranes before they reach the target site and become active molecules. The establishment of quantitative relationships between the amphiphile structure and its rate of permeation through biomembranes is therefore an important tool in the rational development of new drugs and this has been addressed by us [3-5, 9, 139] and other authors (see e.g. [283-291]).

In addition to applications in the enhancement of drug bioavailability, the interaction between amphiphilic molecules with different lengths in the alkyl or acyl chain and lipid bilayers is also of fundamental importance for the understanding of the consequences of protein modification by acylation [285, 288, 292, 293]. This is a prevalent cell regulation process where the association between the protein and a given membrane is enhanced, leading to an increased activity *via* its local concentration or inhibition by sequestration [293, 294].

In the last years, this research team has been characterizing in detail the interaction of amphiphiles with serum proteins and lipid bilayers regarding both equilibrium and kinetic parameters [3-5, 9, 139, 295]. More recently, the homologous series of fatty amines labeled with the fluorescent moiety 7-nitrobenz-2-oxa-1,3-diazol-4-yl (NBD [296]), Figure IV.1, has been studied and the effect of the length of the alkyl chain on their solubility in aqueous media, binding to serum proteins and partition to lipid bilayers [5, 6] has been characterized. The results obtained revealed non-monotonic behavior along the homologous series. This has prompted us to characterize their interaction with lipid bilayers using molecular dynamics (MD) simulations, so as to gain molecular detail on the interactions established.

The interaction of fluorescent molecules with lipid bilayers is also a very important tool in the characterization of the lipid bilayer itself [297]. For that purpose, in addition to equilibrium and kinetic parameters for the interaction, it is necessary to know the location of the amphiphile in the membrane and its effects on the properties of the

system under study. MD simulations are a priceless tool for this purpose, as all the details of the interaction may be established, and have been used to obtain detailed atomic-scale information on phospholipid bilayers (e.g., see [231] for a review). They are suitable for calculation of a variety of properties of fluorescent probes in the bilayer, as well as their effect on the organization of the latter. This has been demonstrated recently for several different fluorophores [257, 258, 264, 298-307], including NBD-labeled lipids by ourselves [258, 264, 301].

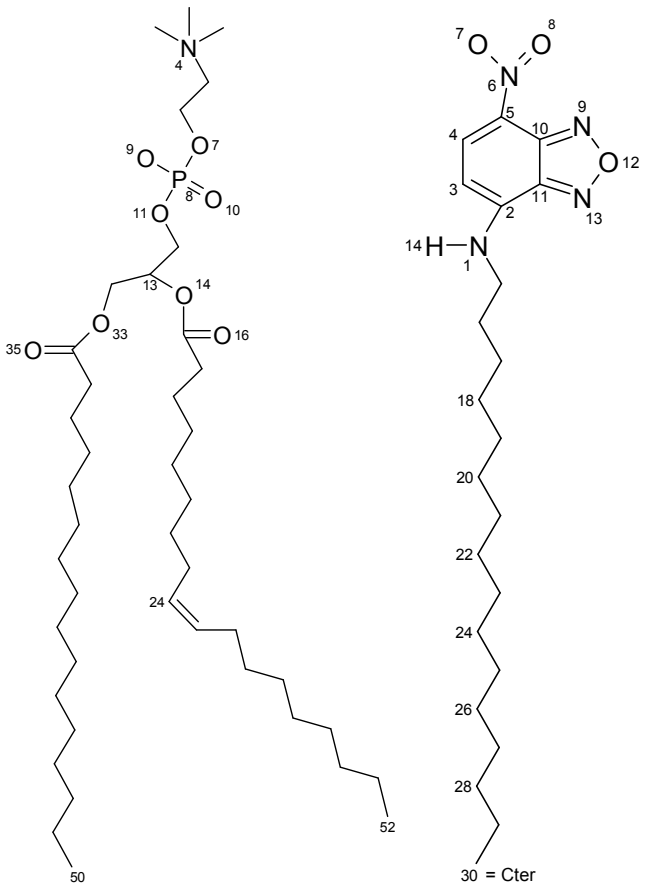

Figure IV.1 – Structures of POPC (left) and NBD-C_{16} (right), showing the atom numbering as used throughout the text.

In this work, we have undertaken the systematic characterization of the association of NBD-C_n amphiphiles (Figure IV.1) with 1-palmitoyl, 2-oleoyl-*sn*-glycero-3-phosphocholine (POPC) bilayers using atomistic MD simulations, to obtain information regarding the effects of the alkyl chain length on the location, orientation and dynamics of the polar group in the bilayer and thus complement the experimental work recently carried out on the association of these molecules with serum proteins and POPC

vesicles [5, 6]. Unless stated otherwise, and for the purpose of a better statistical description of the amphiphile properties, the analyzed results here reported concern the POPC:4-NBD-C_n systems, as no significant differences in behavior were observed in the POPC:2-NBD-C_n simulations.

IV.2 – Results and Discussion

IV.2.1 – Area per Lipid

The instant area per lipid molecule, *a*, was calculated as the instant box area divided by the number of lipid molecules in each monolayer (64), for both pure POPC bilayers and 4-NBD-C_n/128 POPC bilayers. The time variation of the area per lipid is a common indicator of the equilibration of the bilayer, whereas its average value is often used to assess the adequacy of the simulation methodology, due to its sensitiveness to simulation details [269].

Figure A.1 in the Appendix shows that whereas variations of this parameter's value are large in the initial stages of the simulations, they are considerably reduced for $t > 20$ ns. In an attempt to clarify this situation, the cumulative moving averages of *a* in the [20 ns, *t*] interval are represented in Figure A.2 (Appendix). Although some systems appear to be still slowly evolving near the end of the simulation (possibly NBD-C_{12} and NBD-C_{16}), in all cases variation of this cumulative average is < 1% (or 0.0052 nm^2) for $t > 60$ ns and less than 0.5% (or 0.0030 nm^2) for $t > 80$ ns. This indicates that even if those particular systems might not be completely equilibrated, they should be very close to equilibrium, validating the use of the last 80 ns of the full length simulations for analysis. As expected, incorporation of two NBD-C_n molecules in each bilayer leaflet (keeping the number of POPC molecules constant) generally increases the area/lipid values. The average values of *a* for the simulations are shown in Table IV.1, and fall between $a = 0.625$ nm^2 for both POPC/NBD-C_8 and POPC/NBD-C_{14} (these values are in fact identical to that recovered for a pure POPC bilayer) and 0.644 nm^2 for POPC/NBD-C_6 and POPC/ NBD-C_{10}. As shown in Table IV.1, non-monotonic variations, not larger than the standard error, are observed. However, even at this point it should be stressed that these relatively slight variations correlate with several other observables obtained from this work, as well as previous experimental data, as

discussed in detail below. The results for pure POPC agree with the experimental values of 0.65 nm^2 (T = 298 K) [308], 0.64 nm^2 (T = 298 K) [309] and 0.63 nm^2 (T = 297 K) [125], as well as with those obtained from MD simulations by Böckmann et al. (T = 300 K, a = 0.655 nm^2) [310], Mukhopadhyay et al. (T = 298 K, a = 0.62 nm^2) [311], Gurtovenko and Anwar (T = 310 K, a = 0.65 nm^2) [312], and Pandit et al. (T = 303 K, a = 0.630 nm^2) [313].

Table IV.1– Average area per lipid and average P-P distance obtained from MD simulation.

System	Area per lipid, a/nm^2	P-P distance/nm
POPC	0.625±0.015	3.80±0.11
POPC/NBD-C_4	0.628±0.020	3.82±0.13
POPC/NBD-C_6	0.644±0.021	3.74±0.12
POPC/NBD-C_8	0.625±0.020	3.82±0.12
POPC/NBD-C_{10}	0.644±0.020	3.76±0.12
POPC/NBD-C_{12}	0.639±0.020	3.78±0.13
POPC/NBD-C_{14}	0.625±0.021	3.85±0.12
POPC/NBD-C_{16}	0.633±0.020	3.82±0.13

IV.2.2 – Bilayer Thickness and Position of Different Atoms

Figure IV.2 shows average transverse positions <z> for selected atoms along the POPC and NBD-C_n molecules. It should be noted that, in the course of the simulations, one amphiphile molecule in each of the 4 NBD-C_4, 4 NBD-C_6 and 4 NBD-C_8 simulations was observed to escape the bilayer into the water medium. In the 4 NBD-C_6 and 4 NBD-C_8 systems (not in the 4 NBD-C_4 system), these molecules returned to the bilayer during the course of the simulation run, essentially to the same transverse location as displayed by the 3 remaining molecules. In any case, these escaping molecules were omitted from the results here presented. The positions of the atoms of the NBD-fatty amines are consistent with the perpendicular orientation relative to the bilayer plane, with the NBD group near the glycerol backbone/upper acyl chain region (similar to the location of this fluorophore in 1-palmitoyl-2-[6-(7-nitrobenz-2-oxa-1,3-diazol-4-

yl)aminohexanoyl]-*sn*-glycero-3-phosphocholine (C_6-NBD-PC) and 1-palmitoyl-2-[12-(7-nitrobenz-2-oxa-1,3-diazol-4-yl)aminododecanoyl]-*sn*-glycero-3-phosphocholine (C_{12}-NBD-PC), determined by molecular simulation [264] and verified experimentally [314, 315]) and the fatty-chain end methyl group, Cter, directed to the center of the bilayer.

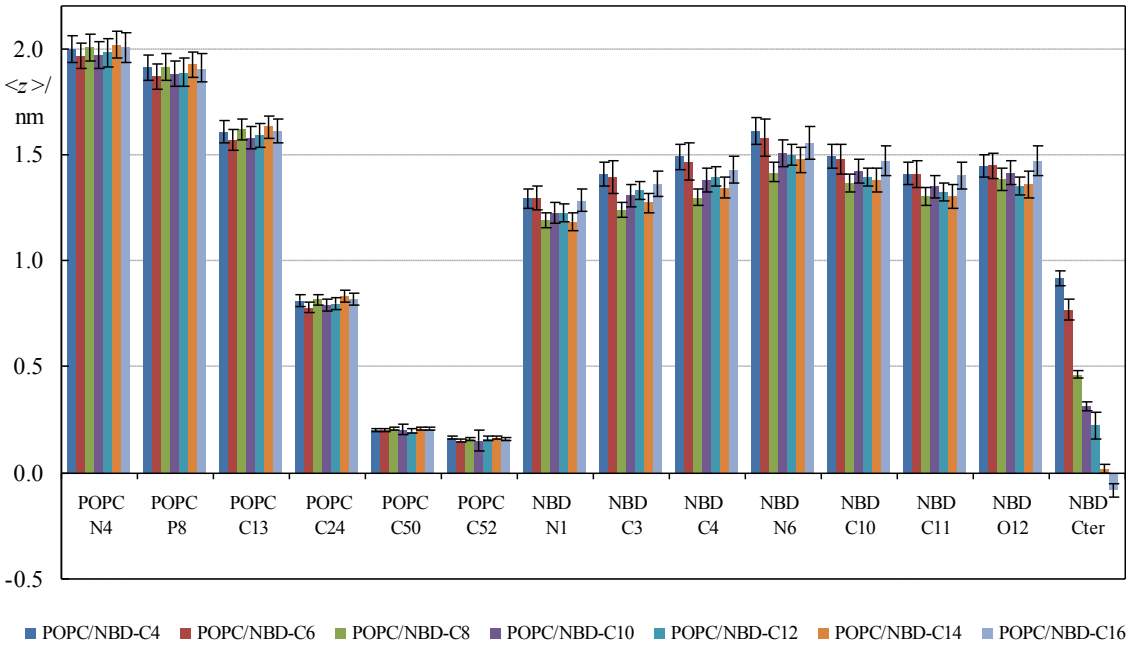

Figure IV.2 – Average transverse position <z> of specific atoms in the POPC/NBD-C_n systems. See Figure IV.1 for atom numbering. Cter represents the methyl group at the end of the fatty amine chain.

From the average transverse position <z> of the POPC P atoms we can calculate the thickness of the bilayer as the distance between the average transverse locations of these atoms in opposing leaflets ($(P\text{-}P)_{dist}$; see Table IV.1). The results show a minimum $(P\text{-}P)_{dist}$= 3.74±0.12 nm for POPC/NBD-C_6 and a maximum $(P\text{-}P)_{dist}$= 3.85±0.12 nm for POPC/NBD-C_{14}, which correlate with maximal and minimal (respectively) area per lipid values in these systems, see Table IV.1. In fact, the variation of $(P\text{-}P)_{dist}$ with the amphiphile chain length is almost a mirror image of that of *a*, as could be expected, and similarly to the latter, the variations in $(P\text{-}P)_{dist}$ fall within the calculated standard errors.

To gain insight on the conformation of the hydrocarbon chain of the amphiphiles, the transverse distance between the NBD N1 and Cter atoms was calculated for each amphiphile. Figure IV.3 shows that this distance increases almost linearly with the chain length of the amphiphiles, with a slope of 0.083 nm/CH_2 group. This value is

considerably smaller (because of *gauche* defects) than the limit for an *all-trans* chain of 0.127 nm [316], and is very similar to that observed for the *sn*-1 chain of POPC (not shown). From this result it may be inferred that the average angle between C-C bonds in the carbon chain (or the fraction of *gauche* defects along the chain) is similar for all amphiphiles. In any case, as shown in Figure IV.3, the average distances observed for $n \geq 12$ are somewhat smaller than expected from the trend established by the $n < 12$ values (with the slope of 0.091 nm/CH_2 shown in the figure). Additionally, the standard error associated with the average transverse N1-Cter distance increases with n. This effect was not observed for z(N1) (Figure IV.2). The shift in behavior between the shorter-chained ($n \leq 10$) and longer-chained ($n \geq 12$) amphiphiles correlates with experimental observables previously measured by our group, such as the rate of translocation [6].

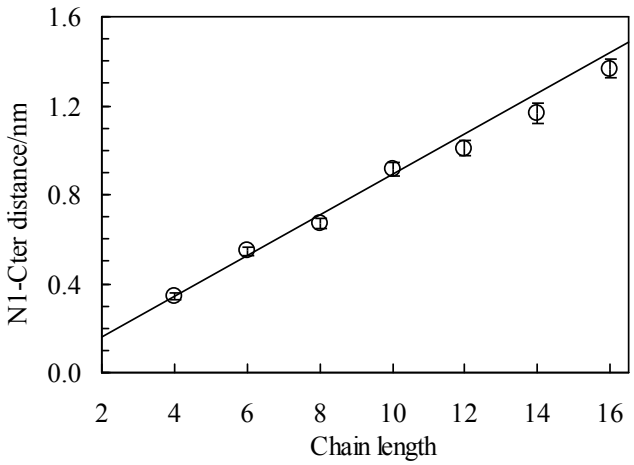

Figure IV.3 – Variation of the transverse distance between N1 and the terminal methyl group of the amphiphiles (Cter). The line is the best linear fit to the $n \leq 10$ points, with a slope equal to 0.091 nm/CH_2.

Figure IV.4 shows a comparison between $\langle z \rangle$ of C13 of POPC and N6 of NBD-C_n (panel A), and between $\langle z \rangle$ of C24 of POPC (carbon 9 of the *sn*-2 chain) and the Cter of NBD-C_n (panel B). The results show that C13 of POPC and N6 of NBD are essentially positioned at the same depth in the bilayer for the shorter chain amphiphiles. For the longer chained amphiphiles, the NBD N6 atom presents a smaller $\langle z \rangle$, and the deepest and most shallow transverse locations of this fluorophore atom are observed for NBD-C_8 and NBD-C_{16}, respectively. With the exception of these two values, variations of the NBD N6 $\langle z \rangle$ for $n \geq 8$ are of the order of the estimated errors. Even so, it should

be pointed that these variations are mostly parallel to those of the area/lipid molecule *a*, with NBD-C_8 and NBD-C_{14} presenting both the deepest NBD transverse locations (Figure IV.2 and Figure IV.4A) and smaller *a* values (Table IV.1). This can be understood taking into account that these analogs have the bulky NBD group located in a less crowded region of the bilayer, where it can be accommodated without pushing aside nearby POPC molecules. Probably for this reason, *a* values in these systems are essentially identical to that of unlabeled POPC bilayers (Table IV.1). This is at variance with the other NBD-C_n analogs, for which the fluorophore has a more shallow location, near the maximum of POPC mass density profile (see Figure IV.11 below).

On the other hand, as shown in panel B, as the fatty amine chain becomes longer, the average transverse location of the Cter group becomes increasingly deeper in the bilayer. Cter of NBD-C_4 and NBD-C_6 are located above the *sn*-2 *cis* double bond (which connects POPC C24 and POPC C25, the coordinates of the former also shown in the figure) whereas those of NBD-C_8, -C_{10}, -C_{12}, -C_{14} and -C_{16} are located more internally.

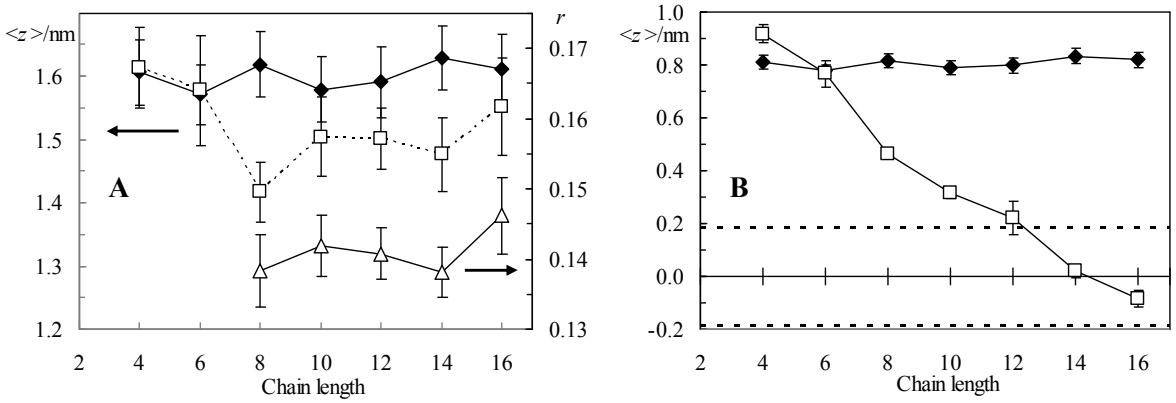

Figure IV.4 – (A): Comparison between the average transverse positions <*z*> of C13 of POPC (black diamonds) and N6 of NBD-C_n (white squares). Also shown is the steady state fluorescence anisotropy (*r*) measured for $n \geq 8$ (white triangles) [5]. (B): Comparison between average transverse positions of C24 of POPC (carbon 9 of the *sn*-2 chain) and the chain end methyl group (Cter) of NBD-C_n. The two dotted lines represent the average transverse location of the acyl chains' end methyl group in the two bilayer leaflets.

Interestingly, <z>(Cter) = (-0.083 ± 0.032) nm for NBD-C_{16} is negative, indicating interdigitation of this amphiphile's chain and the POPC acyl chains in the opposing leaflet. This effect is not limited to this molecule, as e.g. already <z>(Cter) = (0.020 ±

0.023) of NBD-C_{14} indicates an average transverse location in the bilayer midplane. The snapshot of Figure IV.5 (left panel) illustrates clear interdigitation for one of the represented molecules.

A possible way to quantify this phenomenon is to calculate the fraction of frames for which z(Cter) < 0 (during the 20 ns – 100 ns time range of the trajectories), and this is shown in Figure IV.6 for the studied amphiphiles. This figure also shows the expected fraction of interdigitated conformations, assuming that: i) the NBD N1 atoms have transverse position equal to the average of those obtained from simulation of NBD-C_8, -C_{10}, -C_{12}, -C_{14} and -C_{16}; ii) the average transverse NBD N1-Cter distance varies linearly with n, with slope equal to that recovered from linear regression of all the values obtained from simulation (0.083 nm/CH_2); and iii) the transverse position of the Cter atom follows a Gaussian distribution, with average value calculated taking into account i) and ii) above, and standard deviation equal to the average of the standard deviations (obtained from simulation) of the Cter z coordinate of NBD-C_8, -C_{10}, -C_{12}, -C_{14} and –C_{16}.

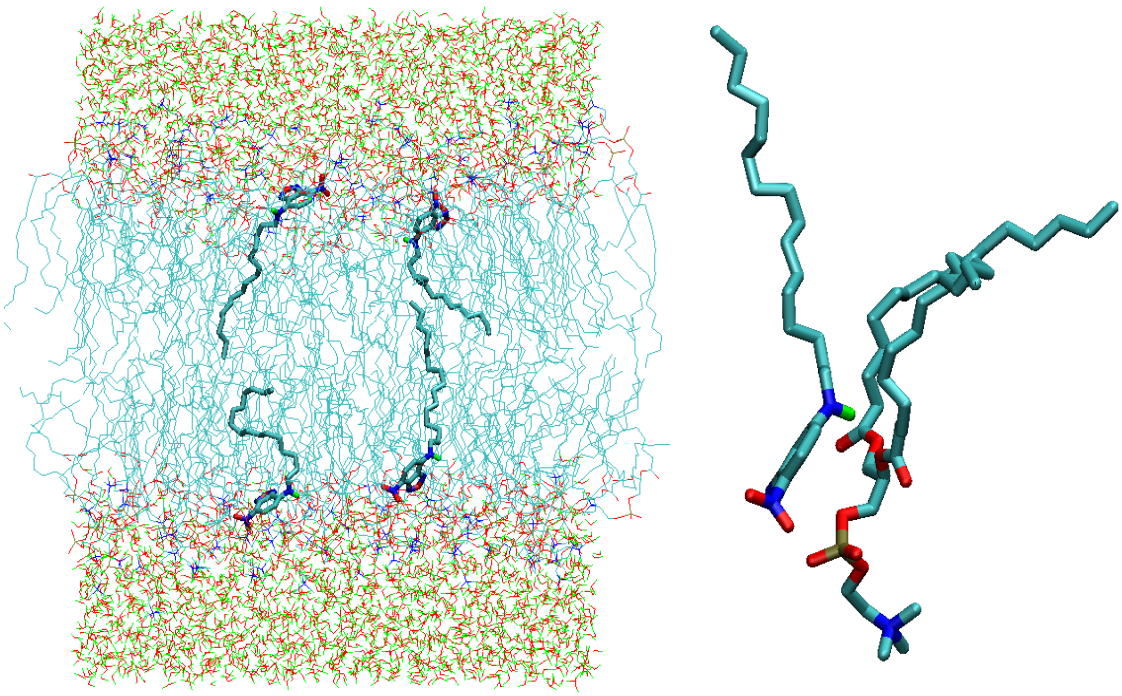

Figure IV.5 – Left: typical snapshot of a POPC bilayer containing 4 NBD-C_{16} molecules, one of which displays clear interdigitation behavior. Right: zoomed snapshot of this interdigitating NBD-C_{16} and a nearby POPC molecule, showing NBD N1 – NBD H14 – POPC O14 hydrogen bonding. CH_n groups (n=0–3), O atoms, N atoms, P atoms and polar H atoms are displayed in cyan, red, blue, tan and green, respectively.

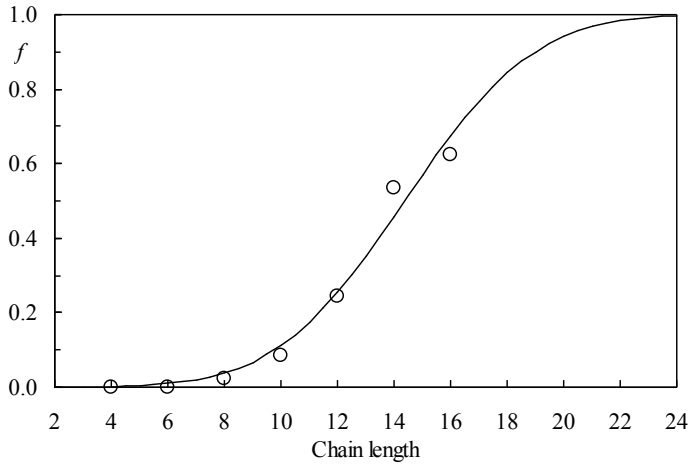

Figure IV.6 – Fraction of interdigitated conformations (*f*) as a function of the amphiphile chain length *n*. The points are the values obtained from simulation, whereas the line was calculated assuming linear variation of <*z*>(Cter) and normal distribution of *z*(Cter) (see text for details).

It can be seen that for $n \geq 10$ there is a sizeable amount of simulation frames showing interdigitation of NBD-C_n, and for $n \geq 14$ interdigitation occurs during 50% or more of the analyzed time window. Due to the transverse location of the NBD fluorophore in the glycerol backbone/carbonyl region, it is not surprising that the longer chained amphiphiles are able to interdigitate. A similar effect was reported in the MD simulation of C_{18}-chained 1,1′-dioctadecyl-3,3,3′,3′-tetramethylindocarbocyanine ($DiIC_{18}(3)$), whose fluorophore has a similar transverse location to that of NBD, in fluid DPPC [303]. For interdigitation not to occur, the chains would have to present a higher amount of *gauche* defects, at an energetic cost. The fact that the variation of Cter <*z*> with *n* remains mostly linear and with a slope similar to that typical of fluid phospholipid acyl chains, implies that this does not occur to a significant extent. In any case, Cter of the longer-chained derivative, NBD-C_{16}, is on average closer to the bilayer midplane than the terminal methyl groups of the POPC molecules of the opposing leaflet (see Figure IV.4B), and the former remain thus located well within the highly disordered bilayer centre. Probably, an even higher degree of interdigitation of NBD-C_{16}'s acyl chains (which, to some degree, could be anticipated from the calculated line shown in Figure IV.6) is not favored, which may also explain the relatively shallow location of the fluorophore for this analog (Figure IV.4A). It is also noteworthy that NBD-C_{14} has a slightly lower Cter <*z*> than estimated from interpolation of the NBD-C_{12} and NBD-C_{16} values (Figure IV.4B), and also displays a somewhat higher degree of interdigitation

than expected (Figure IV.6). This correlates with the slightly lower position of the fluorophore atoms observed for NBD-C_{14} compared to NBD-C_{10}, -C_{12}, and -C_{16} (Figure IV.4A), and is in line with experimental reports of a minimum in the activation enthalpy for the translocation process for NBD-C_{14} [6]. This experimental study also revealed a maximum in the entropic contribution for the activation Gibbs function of the desorption process of NBD-C_{12}, which could be explained taking into account that this probe is better accommodated within its bilayer leaflet than the others (because it stretches to the same extent as the host lipid chain, neither creating free space below it as the shorter chained amphiphiles, nor disturbing the opposite leaflet significantly, as the longer chained ones). On the other hand, the slightly deeper location of the fluorophore in NBD-C_{14} (into a less ordered region of the bilayer) agrees with a minimal value of average fluorescence anisotropy (despite the minimum in lifetime) observed for this amphiphile [5]. As seen in Figure IV.4A, fluorescence anisotropy also presents a minimum for NBD-$C_{8,}$ following the trend observed in the <z> of NBD N6 calculated in this study. The variation of fluorescence quantum yield reported for $n \geq 8$ is also almost parallel to that of the calculated <*z*> [5]. Slight deviations (e.g., the average value of the quantum yield of NBD-C_8 is essentially identical – not clearly lower, as observed for NBD <*z*> – to those of NBD-C_{10} and NBD-C_{12}) probably reflect the increased uncertainty associated with experimental determination of fluorescence quantum yield values in turbid media.

The physical reason for the deeper location of NBD-C_8 is not entirely clear although it is most likely a consequence of the position of Cter just below carbon 9 of the POPC acyl chain. Smaller alkyl chain amphiphiles are well accommodated and located exclusively in the region of the POPC bilayer with properties of a soft polymer, while longer amphiphiles extend into the disordered region of the bilayer [53, 157]. The location of the longer amphiphiles is therefore a balance between two forces: i) maximization of the interactions with the lipids in the cavity around the amphiphile, which pulls the latter into the center of the bilayer; and ii) maximization of the interactions between the polar portion of the amphiphile and the polar interface of the bilayer. Because the cavity below NBD-C_8 is larger than for longer amphiphiles, the first effect is expected to be maximal for this probe, leading to a deeper location.

IV.2.3 – Orientation of the NBD Fluorophore

Figure IV.7 shows the frequency distributions $P(\theta)$ of the angles between the long axis (defined as the vector between atom O12 and the center of mass of atoms C3 and C4), the short axis (defined as the vector between atoms C10 and C11), and the normal to the NBD plane (defined as the vector product of the short and long axes) relative to the bilayer normal. For the short axis, similar $P(\theta)$ distributions are recovered for all systems. All distributions are wide, but values $\theta > 90°$ predominate clearly, corresponding to C10 being closer to the interface than C11. Given the rigidity of the NBD moiety, this is a necessary consequence of the higher $\langle z \rangle$ obtained for the NO_2 group compared to the remainder of the fluorophore, as illustrated above (Figure IV.2 and Figure IV.5). For the long axis, $\theta \leq 90$ predominates for all systems, corresponding to O12 being closer to the interface than the opposing end of this molecular axis. In any case, very similar $P(\theta)$ functions are obtained for the angle between the normal to the NBD plane and the bilayer normal.

Subtle variations in orientation correlate with differences in transverse position of the fluorophore. For example, NBD-C_4, -C_6 and -C_{16} have short axis angle distributions shifted to higher values relative to the other molecules, in accordance with the more external placement of the N6 atom for these molecules (Figure IV.4A). This correlation, found both within each molecule's simulation run and across all systems, is evidenced in Figure A.3 (Appendix). In any case, on the whole, the preferred orientations of the NBD group in all systems are close to each other and similar to that of the same fluorophore in C_{12}-NBD-PC in fluid DPPC bilayers [264]. This general orientation behavior, in which all electronegative O atoms (especially those of the $–NO_2$ group, O7 and O8, but also O12 in the ring system) point towards the water/lipid interface, is illustrated in the instant configurations of the left panel of Figure IV.5.

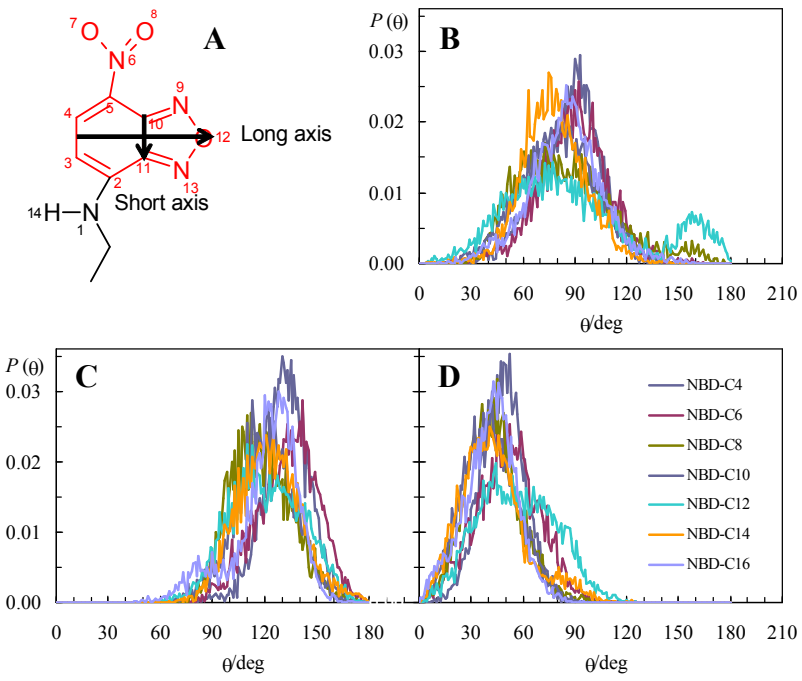

Figure IV.7 – (A) Definition of long and short axes of the NBD fluorophore. (B–D) Probability density functions $P(\theta)$ of the angles between the long axis (B), the short axis (C), and the normal to the NBD plane (defined as the vector product of the short and long axes; D), relative to the bilayer normal.

IV.2.4 – Hydrogen Bonding

The NBD fluorophore has an H atom bound to an amino N atom. This nitrogen can act as H-bond donor to water or POPC O atoms. On the other hand, there are several O and N atoms in the fluorophore, which can act as H-bond acceptors from water oxygen atoms. These interactions can be easily monitored in an MD simulation. For the following analysis, which used the last 80 ns of the simulations, an H-bond for a given donor–H–acceptor triad was registered each time the donor–acceptor distance was <0.35 nm and the H-donor-acceptor angle was < 60º.

Figure IV.8A shows the frequency of H-bonding from NBD N1-H14 to each of the possible acceptor atoms. As can be readily seen by summing over all acceptors, the NBD NH group is almost continuously involved in H-bonds. Note that due to the adopted definition of H-bonding, there can be more than one acceptor at the same time (if they are simultaneously located at a distance <0.35 nm to the NBD N1 atom and the H-donor-acceptor angle is < 60º for both), hence the totals can be higher than 100%. Low frequencies, in relative terms, are observed for all amphiphiles regarding H-bonding to water O atoms (except in the case of NBD-C_{12}), and to phosphate O atoms.

In all cases, H-bonding is most common to O atoms within the glycerol backbone (O14 and O33), or to carbonyl O atoms (in the case of NBD-C_{12}, in which H-bonding to POPC O16 atoms was observed for ~17% of the frames). This behavior is identical to that reported for C_{12}-NBD-PC [264] and correlates with the transverse location of the NBD group in the upper chain/glycerol region of the bilayer. In closer inspection, the H-donor-acceptor angle and the H-acceptor distance distributions reveal some degree of specificity. The preferred angle of the H-bond triad is below 20º, being ~15º for the case of the H-bond to O14. The almost perfect co-linearity of the triad probably indicates preference of NBD N1-H14 for establishing H-bonds with this oxygen atom of POPC. This interaction is visible in the snapshot detail of Figure IV.5 (right panel).

The H-bonding between the -OH groups of water (donors) and the various O and N atoms of NBD (acceptors) shows preference for the O7 and O8 of the NBD (Figure IV.8B), in agreement with the higher exposure to the solvent of these two atoms and their significant negative charge (≅-0.5 each [264]). Slight differences among amphiphiles can be correlated with other calculated properties. For example, both Figure IV.7A and Figure IV.7B show a slightly different behavior of NBD-C_{12}, which displays decreased H-bonding from NBD N1 to POPC O14, increased H-bonding from NBD N1 to POPC O16 (Figure IV.8A), and increased H-bonding from water to NBD O7 (Figure IV.8B). This is probably related to the somewhat distinct orientation profiles of the NBD-C_{12} fluorophore (evident in the minor peak of the long axis angular profile at ~160º, see Figure IV.7B, and in the wider normal-to-NBD angular profile, Figure IV.7D). In any case, on detailed inspection, we found this to be due to the behavior of a single NBD-C_{12} molecule which equilibrates very slowly, maintaining an anomalous conformation for roughly the first half of the simulation run (not shown), rather than from a distinct behavior of NBD-C_{12} when compared to the other analogs.

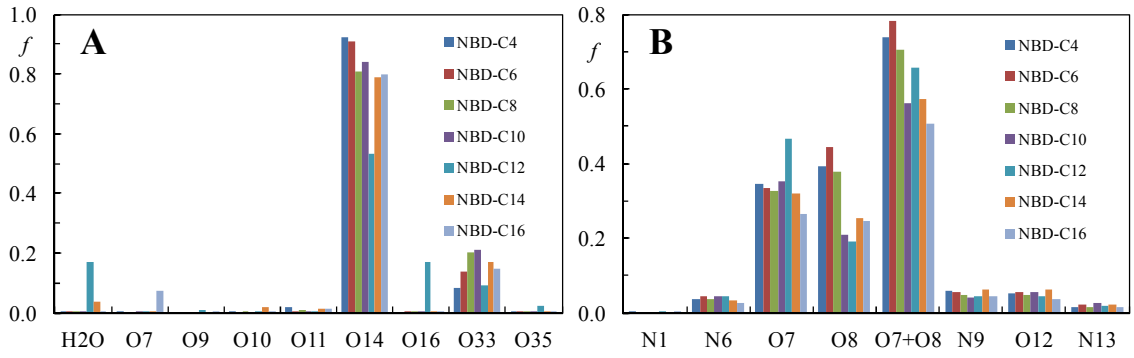

Figure IV.8 – NBD N1-H14-POPC or water acceptor atom (A) and water donor-NBD acceptor atom (B) H-bond fractional frequencies (*f*).

As described above, in the NBD-C_4, NBD-C_6 and NBD-C_8 simulations, one amphiphile molecule escaped the bilayer to the water medium. Whereas in the NBD-C_4 system this molecule did not return to the bilayer during the simulation, for the other systems the escaping molecule (which was omitted from the results shown in Figure IV.8) re-entered the bilayer at a later stage of the run, to a transverse location identical to the other three molecules. In the case of NBD-C_6, the returning amphiphile proceeds to establish H-bonding with POPC O14 and O33 atoms, similarly to the vast majority of molecules in all systems. In the case of NBD-C_8, however, the returning molecule goes on to establish H-bonds exclusively with the deeper O16 atoms of POPC. This difference illustrates the difficulty in obtaining complete equilibration when inserting amphiphiles from the water medium. In any case, on the whole, these results indicate that the NBD -NH group preferably acts as H-bond donor to the ester O atom of the *sn*-2 acyl chain. This behavior was already apparent for the NBD fluorophore in C_{12}-NBD-PC in fluid DPPC bilayers [264].

IV.2.5 – Order of the NBD-C_n and POPC Acyl Chains

In our simulations, using a united atom force field, deuterium order parameters (S_{CD}) for saturated (S_{CD}^{sat}) and unsaturated (S_{CD}^{unsat}) carbons are determined using the following relations [317]:

$$-S_{CD}^{sat} = \frac{2}{3}S_{xx} + \frac{1}{3}S_{yy} \qquad \text{(IV.1)}$$

$$-S_{CD}^{unsat} = \frac{1}{4}S_{zz} + \frac{3}{4}S_{yy} + \frac{\sqrt{3}}{2}S_{xy} \qquad \text{(IV.2)}$$

where S_{ab} are the order tensor coordinates, given by

$$S_{ab} = \frac{1}{2}\left\langle 3\cos\theta_a \cos\theta_b - \delta_{ab} \right\rangle \qquad a, b = x, y, z \qquad \text{(IV.3)}$$

where in turn θ_a (or θ_b) is the angle made by ath (or bth) molecular axis with the bilayer normal and δ_{ab} is the Kronecker delta (<> denotes both ensemble and time averaging).

$-S_{CD}$ can vary between 0.5 (full order along the bilayer normal) and −0.25 (full order along the bilayer plane), whereas S_{CD}=0 denotes isotropic orientation. Due to the slow convergence of this parameter [53], analysis was restricted to the last 50 ns of the simulations. Order parameters were calculated for both acyl chains of POPC (Figure A.4 in the Appendix). For pure phospholipid bilayer, the profiles obtained agreed with both experimental (e.g., [62, 318]) and simulated (e.g., [310, 312, 319, 320]) data. Incorporation of NBD-C_n leads to non-monotonic alterations, correlated with those of area/lipid discussed above (i.e., systems for which a higher *a* was obtained tend to present slightly lower $-S_{CD}$ profiles).

Focusing on the NBD-C_n chain order parameters, Figure IV.9A shows $-S_{CD}$ for the chain C atoms of the different amphiphiles. As expected, the order parameter decreases along the chain for each molecule, pointing to an increased fraction of *gauche* conformations near the end of the chain. However, comparison of all systems together is rendered difficult due to poor statistics resulting from the low number of amphiphile molecules simulated in each run. To get further insight, we plotted the order parameter of each carbon segment as a function of the total number of carbons of the alkyl chain (Figure IV.9B). Two patterns may be identified from the plot: first, the order of each carbon segment generally increases with the total number of chain carbons. For every segment, the shorter-chained amphiphiles present lower $-S_{CD}$ values than the longer-chained amphiphiles. This is expected, because a higher number of carbons will induce a stronger anchoring effect of the amphiphiles in the bilayer for the same absolute position along the chain. Second, this increase is not smooth, and up to and including the C7 position along the chains local minima or maxima can be identified. For C2 and C3, these minima occur for NBD-C_8 and NBD-C_{14}, the amphiphiles for which the NBD atoms presented deeper penetration (Figure IV.2), implying a deeper location of the first

carbon atoms of their chains, into a less ordered region of the bilayer. These two minima imply the existence of a maximum for an intermediate chain length (verified for n = 10) for these chain atoms. These features gradually vanish, and can no longer be observed from chain atom C8 onwards.

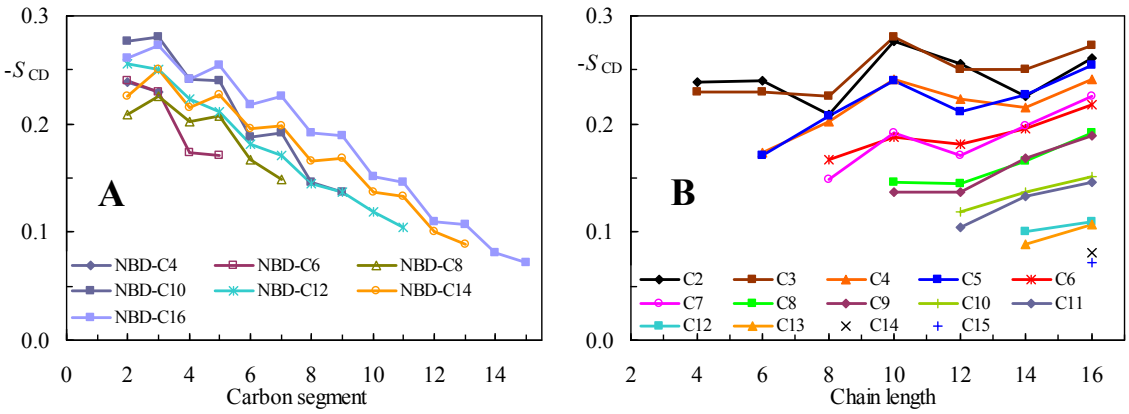

Figure IV.9 – Deuterium order parameter of the NBD amphiphiles. (A) – a perspective of the order of each amphiphile as a function of the carbon segment. (B) – a perspective of the order of each carbon segment as a function of the number of total carbons of the alkyl chain.

IV.2.6 – Electrostatic Potential

Given the polarity of the NBD fluorophore, it can be expected beforehand that incorporation of NBD-C_n in the bilayer affects the electrostatic profile. Figure IV.10 shows the potential at the center of the bilayer (relative to that in the water region) as a function of the number of chain carbons of the amphiphile. The value for pure POPC, -514 mV, agrees with recent MD studies, in which values ranging from -500 mV to -600 mV are reported [310, 320, 321]. Inclusion of the NBD-C_n amphiphiles increases the difference in electrostatic potential between the interior of the bilayer and the bulk water phase. These values are subject to uncertainty due to cancellation errors, because the observed potential profile is the difference between the water and lipid contributions, which almost cancel each other (not shown). In any case, the observed variation reflects in part the measured average area/lipid a. Systems with smaller a values (such as NBD-C_8 and –C_{14}, see Table IV.1) tend to present higher electrostatic potential in the membrane relative to the water medium (compatible with their higher average surface charge density), and conversely for systems with larger a (e.g. NBD-C_{10}). In any case, there is no doubt that insertion of NBD-C_n amphiphiles increases the

difference in electrostatic potential in the membrane relative to water. Similar effects were observed and discussed for the C_6-NBD-PC and C_{12}-NBD-PC probes [301].

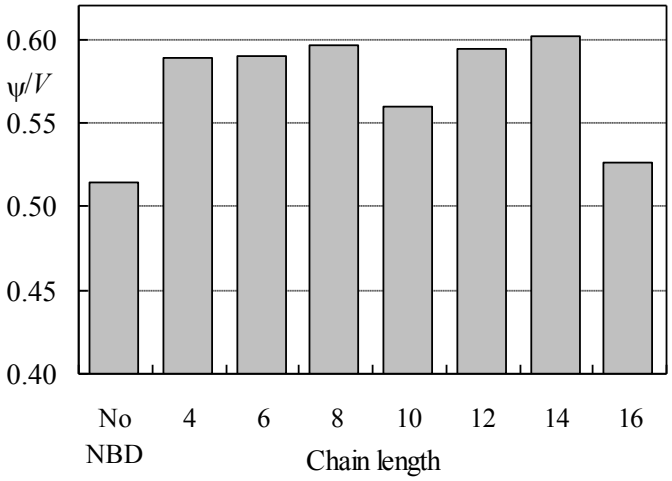

Figure IV.10 – Electrostatic potential in the center of the bilayer (relative to the water region) as function of the total number of carbons of the NBD-C_n alkyl chains.

IV.2.7 – Mass Density Profiles

Figure IV.11 shows the mass density profiles across the bilayer obtained for water, POPC, and selected (for clarity reasons) NBD-amphiphiles for the different POPC/NBD-C_n systems. To this effect, and because the bilayers' centers of mass may fluctuate in time, the positions of all atoms were determined relative to the instantaneous center of mass in all simulations, for each frame. Relative to pure POPC, alterations in the density profiles for water or POPC atoms in bilayers containing NBD-C_n are small and non-monotonic (not shown), pointing to limited probe perturbation (already evidenced in the area/lipid and P-P distance results commented above). The most interesting result from this analysis is that an increase in the mass density at the center of the bilayer is observed for amphiphiles with alkyl chains longer than NBD-C_6. For the amphiphiles NBD-C_4 and NBD-C_6 the mass density profiles indicate that Cter does not reach the center of the bilayer, unlike for NBD-C_8 and NBD-C_{10}. For the amphiphiles with $n \geq 12$ there is a considerable increase in mass density, even presenting a local maximum, close to the bilayer center (unlike POPC itself). These results correlate with the fraction of interdigitated frames in each system (Figure IV.6), which becomes significant for $n \geq 12$.

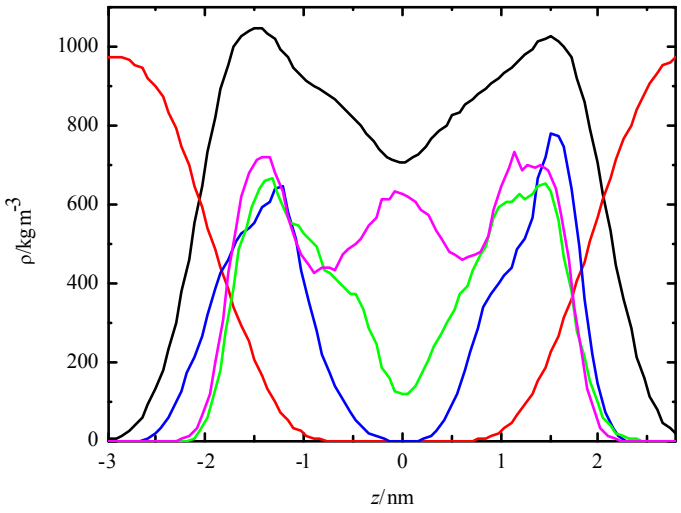

Figure IV.11 – Mass density distributions of POPC (black) and water (red), both recovered from pure POPC bilayers, and NBD-C_6 (blue), -C_{10} (green) and –C_{16} (magenta), recovered from the respective 4 NBD-C_n/POPC systems. The profiles of the NBD amphiphiles were multiplied by 32 for better visualization.

IV.2.8 – Lateral Diffusion

Lateral diffusion coefficients of POPC in all systems were calculated from the two-dimensional mean square displacement (MSD), using the Einstein relation:

$$D = \frac{1}{4}\lim_{t\to\infty}\frac{d\mathrm{MSD}(t)}{dt} \qquad \text{(IV.4)}.$$

In turn, MSD is defined by

$$MSD(t) = \left\langle \left\| \vec{r}_i(t+t_0) - \vec{r}_i(t_0) \right\|^2 \right\rangle \qquad \text{(IV.5)}$$

where $\vec{r}_i$ is the (x, y) position of the center of mass of molecule i of a given species, the averaging is carried out over all molecules of this kind and time origins t_0. To eliminate noise due to fluctuations in the center of mass of each monolayer, all MSD analyses were carried out using trajectories with fixed center of mass of the corresponding monolayer [269, 322], and, to improve statistics, the final result was averaged over the two monolayers of all simulations carried out for each system.

Figure IV.12A shows the variation of lateral diffusion coefficient determined for POPC for systems labeled with the different amphiphiles. All calculated values are similar and close to that obtained for pure POPC, $(2.1\pm0.3)\times10^{-8}$ cm^2s^{-1}, which in turn agrees well with values obtained both from NMR experiments [323, 324] and MD simulations [310] ($1\text{-}4\times10^{-8}$ cm^2s^{-1} for POPC near room temperature). The invariance of the calculated D upon incorporation of these single-chained amphiphiles is another indicator of their relatively mild perturbation of the bilayer, in contrast with NBD acyl-chain labeled PC [301].

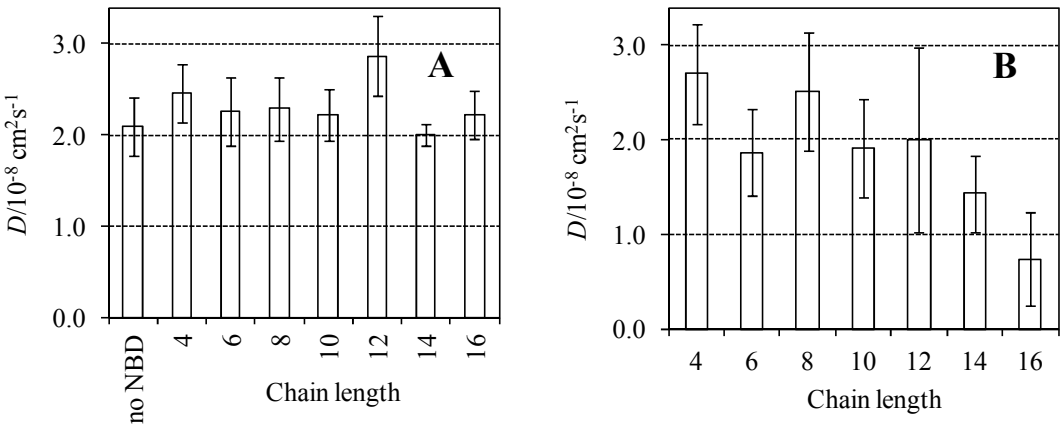

Figure IV.12 – Diffusion coefficients of POPC (A) and NBD-C_n (B) for all studied systems.

Figure IV.12B shows the diffusion coefficients obtained for NBD-C_n. For $n \leq 12$, the calculated D values are similar to the corresponding values for POPC. A minimal average value is observed for NBD-C_6, though its difference relative to NBD-C_4 and NBD-C_8 is probably not significant. A decrease is observed from $n = 8$ onwards, but, for $n \leq 12$, D(NBD-C_n) is still statistically indistinguishable from that of POPC. Curiously, NBD-C_{12} is the amphiphile whose Cter is, on average, located at the same depth as the acyl-chain methyl groups of same-leaflet POPC molecules (Figure IV.2 and Figure IV.4B). For NBD-C_{14} and NBD-C_{16}, the diffusion coefficient is clearly lower than that of POPC. This correlates with the increased degree of interdigitation observed for these amphiphiles' chains, and a probable cause of reduced lateral mobility is hindrance caused by the acyl chains of lipid molecules of the opposing bilayer leaflet.

IV.3 – Concluding Remarks

Atomistic MD simulations of POPC bilayers labeled with fluorescent fatty amines of varying alkyl chain length, NBD-C_n, were carried out. For the first time, a complete series of homologous fluorescent membrane probes is studied using MD simulations. It is likely that other commonly studied homologous series (such as fatty acid derivatives [283-290, 292]) display many of the features unveiled by the present work. The results obtained for pure POPC in this work, as discussed throughout this chapter, agree with both experimental and simulation published data, and validate our choices for MD parameters.

We found that the NBD fluorophore locates near the glycerol backbone/carbonyl region of POPC for all derivatives. However, subtle differences in calculated parameters such as area/lipid, POPC deuterium order parameter, NBD-C_n chain order parameter (for the first atoms of each chain) and bilayer thickness (P-P_{dist}) correlate with each other and also with the observed transverse location of the fluorophore. In turn, the variation of the latter parameter with probe chain length agrees well with small discrepancies measured in the photophysical properties of the various molecules. In particular, the slightly deeper location of the fluorophore in NBD-C_{14} agrees with lower fluorescence quantum yield and anisotropy measured for this amphiphile [5]. Location and orientation of the NBD fluorophore in this homologous series is similar to that determined for the acyl-chain labeled phospholipids C_6-NBD-PC and C_{12}-NBD-PC [264]. However, compared to the latter, the perturbation induced by moderate concentrations (up to 3.1 mol%) of NBD-C_n is relatively mild, as small, non-systematic variations were observed for parameters such as average area/lipid, bilayer thickness, POPC order parameters and lateral diffusion coefficient. In C_6-NBD-PC and C_{12}-NBD-PC, the NBD group was observed to loop to a transverse location closer to the interface than to the center of the bilayer, thus creating a U-turn in the *sn*-2 chain of the probe, which explains the increased perturbation induced by these molecules [264, 301]. This effect is absent in the NBD-C_n series. The longer chained NBD-C_n amphiphiles show significant mass density near the bilayer midplane, and the chains of these derivatives interdigitate to some extent the opposite bilayer leaflet. This phenomenon leads to a slower lateral diffusion for the longer-chained derivatives ($n > 12$). Amphiphiles with chain lengths inside the $8 \leq n \leq 12$ range have lateral diffusion coefficients similar to that of POPC, and, also taking into account their relatively mild

perturbing effect, are useful fluorescent reporters of bilayer dynamics. The same cannot be said for NBD-C_{14} and NBD-C_{16}, whose lateral diffusion coefficients are significantly lower than that of POPC (by a factor of ~3 for NBD-C_{16}). On the other hand, it was also observed that the shorter-chained amphiphiles ($n \leq 8$) are able to leave the bilayer and in some instances return during the course of a 100-ns MD run.

The molecular details obtained by this work regarding the interaction of the NBD-C_n amphiphiles with the POPC lipid bilayer allow the rationalization of the non-monotonic behavior obtained experimentally for the photophysical parameters of the amphiphiles and the kinetic and thermodynamic parameters for their interaction with the membranes: i) the variation of the fluorescence quantum yield and anisotropy correlates with the location of the NBD group; ii) the reduced dependence of the rate of NBD-C_n translocation with the increase in the length of the alkyl chain length for $n \geq 12$ correlates with the location of the terminal portion of the alkyl chain in the disordered region of the bilayer center; iii) the maximal entropy variation obtained upon formation of the transition state in the desorption of NBD-C_{12} is due to the good structural matching between this amphiphile and the lipid bilayer, leading to the minimal entropy in the inserted state along the series.

Chapter V

Interaction of NBD-Labeled Fatty Amines with POPC:Chol and SpM:Chol Bilayers: A Molecular Dynamics Study

This work is part of a manuscript in preparation.

Hugo A. L. Filipe contributed with the preparation, execution and analysis of the simulations, and also contributed to the writing of the manuscript.

V.1 – Introduction

Molecules with pharmacological or biological activity are usually amphiphilic due to their need to cross the different cell membranes before they reach the target site and become active molecules. Moreover, the interaction of amphiphilic molecules with lipid bilayers determines their location inside the cells. Therefore, the establishment of qualitative and quantitative relationships between the molecular structure and the rate of permeation through lipid bilayers mimicking biomembranes contributes significantly to the rational development of new drugs. In the last years, this research team has been characterizing in detail the interaction of amphiphiles with serum proteins and lipid bilayers regarding both the equilibrium and the kinetic parameters [3-5, 9, 139, 295]. More recently, the homologous series of fatty amines labeled with the fluorescent moiety 7-nitrobenz-2-oxa-1,3-diazol-4-yl (NBD [296]) has been studied and the effect of the length of the alkyl chain on their solubility in aqueous media, binding to serum proteins and partitioning to lipid bilayers has been characterized [5], as well as their kinetics of interaction [6].

Fluorescent membrane probes are widely used in membrane biophysics studies. [297] In the above mentioned studies the NBD fluorophore has been very useful in the characterization of the interaction of molecules with albumin and lipid bilayers mainly due to its significant alteration in fluorescent properties when located in different media [3, 8, 296]. In addition, when inserted in bilayers of different compositions, slight changes in quantum yield, fluorescence life time and anisotropy, as well as ionization constants of NBD, may be related with the variations in environment/location in the bilayer. For that purpose, in addition to equilibrium and kinetic parameters for the interaction, it is necessary to know the location of the amphiphile in the membrane (i.e. the region of the bilayer the probe is reporting), and its effects on the properties of the system in study (i.e. the degree of perturbation the probe induces upon the host bilayer). Molecular dynamics (MD) simulations have been used to obtain detailed atomic-scale information on phospholipid bilayers (e.g., see [231] for a review) and are suited for calculation of a variety of properties of fluorescence probes in the bilayer, as well as their effect on the organization of the latter. This has been demonstrated recently for several different fluorophores [141, 257, 267, 298-300, 302-307], including NBD-

labeled lipids by ourselves [258, 264, 301, 325]. The behavior of the homologous series of NBD-fatty amines in POPC bilayers has been also accessed by us [326].

The study of the interaction between amphiphilic molecules with different lengths in the alkyl or acyl chain and lipid bilayers is also of fundamental importance for the understanding of the consequences of protein modification by acylation. [285, 288, 292, 293] Protein acylation with fatty acids chains, as summarized in Table V.1, is a prevalent cell regulation process. Myristoylation and palmitoylation in animal cells and protein prenylation in animals, fungi and plants are common forms of protein modification. [327] This modification enhances the association between the protein and a given membrane, leading to an increased activity via its local concentration or inhibition by sequestration [293, 294, 328], being in some cases fundamental for protein function [329].

Table V.1 – Structures of lipid modifications found on intracellular proteins. Adapted from [330]

N-Myristoyl	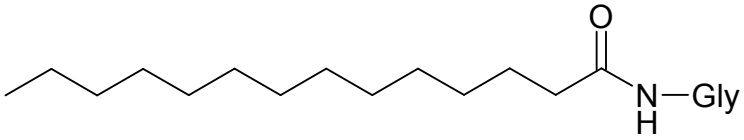
S-Palmitoyl (S-acyl)	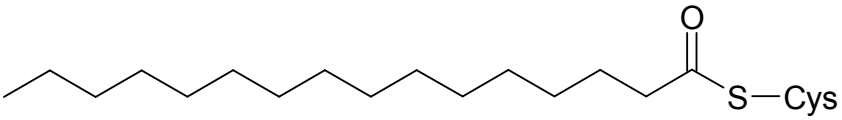
S-Prenyl:	
Farnesyl	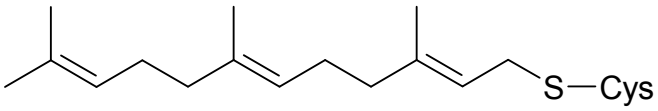
Geranylgeranyl	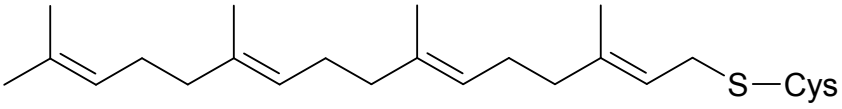

A large number of studies suggest that lipid modifications such as palmitoylation, myristoylation, or glycosylphosphatidylinositol anchors provide the affinity of proteins for lipid rafts [19, 34, 328, 331, 332]. Lipid rafts are heterogeneous, and highly dynamic sterol- and sphingolipid-enriched membrane domains with tightly packed saturated fatty acids dispersed in the liquid-disordered phase, the latter being enriched in more unsaturated lipids. [18, 333] Therefore, the higher order of those domains will be

reflected in a higher membrane thickness compared to other membrane regions. Signaling proteins with affinity for rafts can become concentrated in these membrane domains, thus facilitating formation of protein complexes and activation of specific signaling pathways [334]. Also, protein palmitoylation is a reversible process that is dynamically regulated by specific cellular stimuli. [335] Therefore, palmitoylation serves both to bind proteins to membranes and to direct their localization to membrane microdomains in a regulated form. The study of the interaction between amphiphilic molecules with different acyl chain lengths and lipid bilayers may therefore contribute for understanding the reason why myristoylation and palmitoylation were chosen by the living systems as prevalent protein modifications.

In this report, we have undertaken the systematic characterization of the association of NBD-C_n amphiphiles (Figure V.1) with POPC and palmitoylated sphingomyelin (SpM) bilayers, containing cholesterol (Chol), POPC:Chol (1:1) and SpM:Chol (6:4), respectively. Using atomistic MD simulations, we will obtain information regarding the effects of the order of the lipid bilayers and the alkyl chain length on the location, orientation and dynamics of the polar group in the bilayer as well as the distribution of the acyl chain atoms of the amphiphiles. The results complement the experimental work (including unpublished results) recently carried out on the association of these molecules with such cholesterol-containing bilayers.

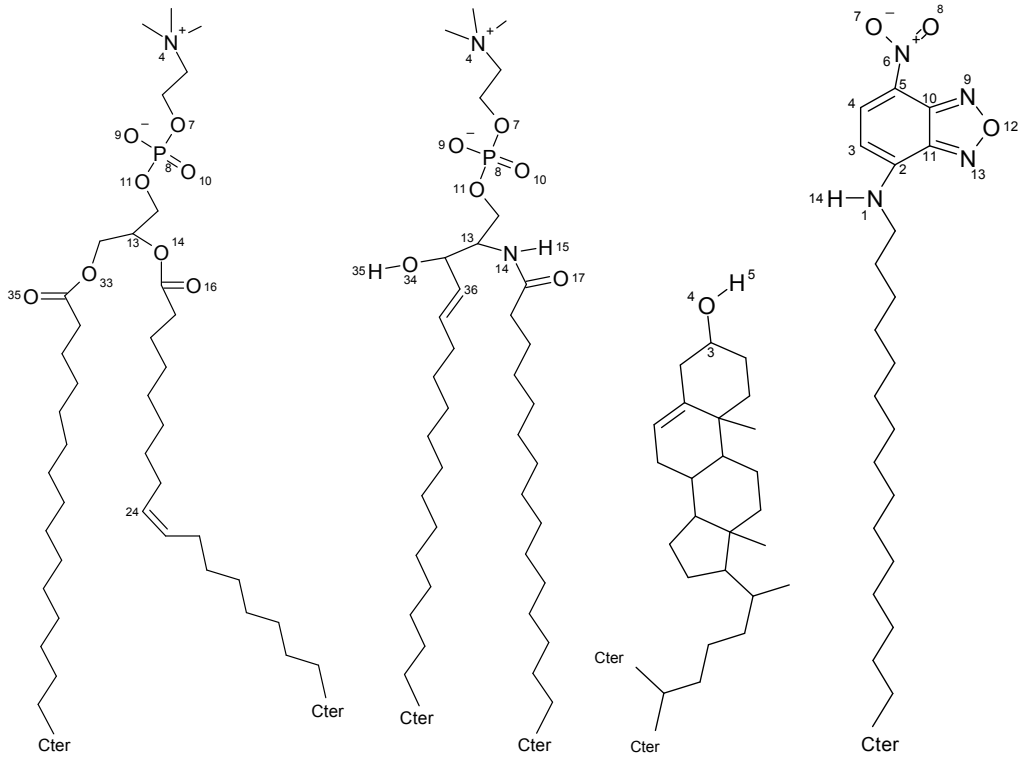

Figure V.1 – Structures of POPC, SpM, Chol and NBD-C_{16} (from left to right, respectively), showing the atom numbering as used throughout the text.

V.2 – Results and Discussion

V.2.1 – Area per Lipid

The instant average area per lipid molecule, *a*, was calculated as the instant box area divided by the number of lipid molecules in each monolayer, for both pure lipid bilayers and NBD containing bilayers. The surface areas of each type of molecules composing each bilayer, POPC:Chol(1:1) and SpM:Chol(6:4) were calculated as described in [336]:

$$A_{PL} = \frac{2A_{box}}{V_{box} - N_W V_W}\left[\frac{V_{box} - N_W V_W - xN_{lipid}V_{Chol}}{(1-x)N_{lipid}}\right] \quad \text{(V.1)}.$$

$$A_{Chol} = \frac{2A_{box}V_{Chol}}{V_{box} - N_W V_W}$$

In these equations, A_{PL} is the cross-sectional area per phospholipid molecule, A_{Chol} is the cross-sectional area per Chol molecule, A_{box} is the area of *xy* plane of the simulation

box, V_{box} is the total volume of the simulation box, N_W is the number of water molecules, V_W is the volume of the water molecule (0.0312 nm^3) [336], x is the Chol mole fraction, N_{lipid} is the number of lipid molecules and V_{Chol} is the volume of the Chol molecule (0.593 nm^3) [336].

The time variation of the area per lipid is a common indicator of the equilibration of the bilayer, whereas its average value is often used to assess the adequacy of the simulation methodology, due to its sensitiveness to simulation details. [269] Figure A.5 in the Appendix shows that the initial configurations of POPC:Chol (1:1) were already equilibrated at the beginning of the simulations, whereas SpM:Chol (6:4) bilayer rapidly approached equilibrium. Complete equilibration of the bilayers, including the NBD location, Figure A.6 (Appendix), was achieved in less than 20 ns, validating the use of the last 80 ns of the full length simulations for analysis. As expected, incorporation of two NBD-C_n molecules in each bilayer leaflet (keeping the number of lipid molecules constant) generally increases the area/lipid values. The average values of a for the simulations are shown in Table V.2, where non-monotonic variations, not larger than the standard error, are observed. For POPC:Chol the area per lipid falls between a = 0.418 nm^2 for pure POPC:Chol (1:1) and 0.426 nm^2 for POPC:Chol:NBD-C_{10}. For all simulations the area per Chol is identical, between 0.275 nm^2 for POPC:Chol:NBD-C_{16} and 0.278 nm^2 for POPC:Chol:NBD-C_6 and POPC:Chol:NBD-C_{10}, while the area per POPC increases from 0.560 nm^2 in POPC:Chol (1:1) to 0.574 nm^2 in POPC:Chol:NBD-C_{10}, reflecting the introduction of the amphiphile. For SpM:Chol the area per lipid lies between a = 0.408 nm^2 for pure SpM:Chol (6:4) and 0.414 nm^2 for SpM:Chol:NBD-C_8. As with POPC:Chol, the area per Chol is the same for all simulations, while the area per SpM increases from 0.501 nm^2 SpM:Chol to 0.510 nm^2 SpM:Chol-C_8, again reflecting the introduction of the amphiphile.

The results of average area per lipid for pure POPC:Chol (1:1) agree with the experimental values of 0.44 nm^2 (POPC:Chol (66:34) at T = 297 K) [125], as well as with those obtained from MD simulations, 0.429 nm^2 (T = 323 K) [337]. The results of average area per lipid for pure SpM:Chol (6:4) also agree with the experimental values of 0.41 nm^2 (T = 298 K) (1:1) [126], as well as with those obtained from MD simulations, 0.388 nm^2 (T = 323 K) [338], 0.437 nm^2 (18:0-SM:Chol (7:3) at T = 293 K) [339], 0.394 and 0.412 nm^2 (323 K) for 18:0-SM:Chol (66:34) and 18:1-SM:Chol (66:34), respectively. [337]. The average areas per lipid here presented are

also similar to the area obtained for the ternary mixture POPC:SpM:Chol (1:1:1), 0.41 nm^2 [340].

Table V.2 – Average area per lipid and average P-P distance obtained from MD simulation. Data for the pure POPC bilayer were taken from [326] (Chapter IV), and are shown for comparison.

	POPC		POPC:Chol(1:1)		SpM:Chol(6:4)	
System	Area per lipid, a/nm^2	P-P distance/nm	Area per lipid, a/nm^2	P-P distance/nm	Area per lipid, a/nm^2	P-P distance/nm
Bilayer	0.625±0.015	3.80±0.11	0.418±0.013	4.43±0.14	0.408±0.013	4.56±0.14
NBD-C_4	0.628±0.020	3.82±0.13	0.423±0.013	4.41±0.14	0.409±0.013	4.56±0.14
NBD-C_6	0.644±0.021	3.74±0.12	0.425±0.013	4.40±0.14	0.409±0.013	4.56±0.14
NBD-C_8	0.625±0.020	3.82±0.12	0.425±0.013	4.39±0.14	0.414±0.013	4.56±0.14
NBD-C_{10}	0.644±0.020	3.76±0.12	0.426±0.013	4.39±0.14	0.410±0.013	4.58±0.14
NBD-C_{12}	0.639±0.020	3.78±0.13	0.425±0.013	4.42±0.14	0.411±0.013	4.58±0.14
NBD-C_{14}	0.625±0.021	3.85±0.12	0.424±0.013	4.45±0.14	0.410±0.013	4.58±0.14
NBD-C_{16}	0.633±0.020	3.82±0.13	0.424±0.013	4.45±0.14	0.413±0.013	4.58±0.14

V.2.2 – Bilayer Thickness and Position of Different Atoms

Figure V.2 shows average transverse positions <z> for selected atoms along the lipid and NBD-C_n molecules for POPC:Chol and SpM:Chol bilayers. Most of the data obtained in the present simulations will be compared with results obtained by us for the interaction of the amphiphiles with POPC using a different force field. The interaction of the NBD-Cn amphiphiles with POPC was also simulated using GROMOS53A6, giving similar results to that reported in Chapter IV [326] (results not shown).

In general, the positions of the atoms of the NBD-fatty amines are consistent with the perpendicular orientation relative to the bilayer plane, with the NBD group near the glycerol backbone/upper acyl chain region (similar to that found for this amphiphiles in POPC bilayers and the location of this fluorophore in C_6-NBD-PC and C_{12}-NBD-PC [264], and verified experimentally [314, 315]) and the fatty-chain end methyl group, Cter, directed to the center of the bilayer. An exception to this behavior is observed for the shorter chain amphiphiles, NBD-C_4 in POPC:Chol and NBD-C_4, NBD-C_6 for SpM:Chol reflecting shallow localization and poorer anchoring of these amphiphiles.

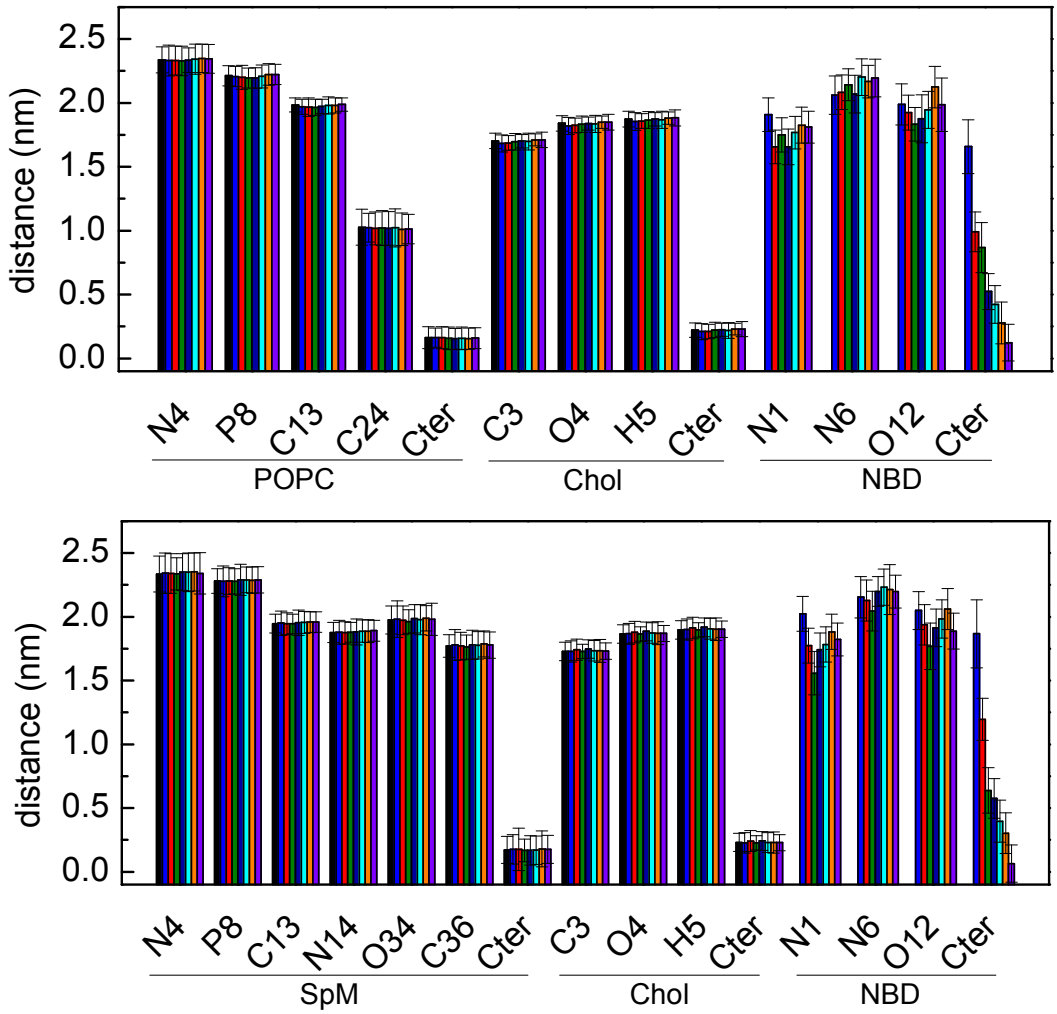

Figure V.2 – Average transverse position <z> of specific atoms in the POPC:Chol:NBD-C_n (top) and SpM:Chol:NBD-C_n (bottom) systems. Error bars represent standard deviations calculated over molecules and frames. See Figure V.1 for atom numbering. Cter represents the methyl group at the end of the fatty amine chain. For each atom of the POPC, SpM and Chol, the first (black) bar concerns the system without NBD-Cn. Following this bar, the order is that of increasing amphiphile chain length (from 4 to 16). The same applies to NBD-Cn atoms (which, however, lack the black bar).

From the average transverse position <z> of the POPC and SpM phosphorus atoms, we can calculate the thickness of the bilayer as the distance between the average transverse locations of these atoms in opposing leaflets ($(P\text{-}P)_{dist}$; see Table V.2). The results show an average $(P\text{-}P)_{dist}$= 4.42 nm for POPC:Chol (1:1) and an average $(P\text{-}P)_{dist}$= 4.57 nm for SpM:Cho (6:4)l. The obtained bilayer thickness agrees with simulation results of 4.55 nm POPC:Chol (66:34) [125], 4.57 nm for DPPC:Chol (1:1) and 4.63 nm for SpM:Chol (6:4) [338], 4.86 nm for and 4.68 nm (323 K) for 18:0-SM:Chol (66:34) and 18:1-SM:Chol (66:34), respectively [125].

To gain insight on the conformation of the hydrocarbon chain of the amphiphiles, the transverse distance between the NBD N1 and Cter was calculated for each amphiphile. Figure V.3 shows that this distance increases almost linearly with the chain length of the amphiphiles both for POPC:Chol and SpM:Chol systems, with a slope of 0.111 and 0.110 nm/CH_2 group, respectively. These slope values are considerably higher than obtained for these amphiphiles in POPC (0.091 nm/CH_2 for n≤10), closer to the limit for an *all-trans* chain of 0.127 nm [316], indicating a smaller number of *gauche* defects in agreement with a more ordered bilayer. The linear fits exclude the values of NBD-C_4 for POPC:Chol and NBD-C_4 and NBD-C_6 for SpM:Chol, due to the poor anchoring of those amphiphiles. NBD-C_{16} was also excluded in both fits due to significant interdigitation. From this result it may be inferred that the average angle between C-C bonds in the carbon chain (or the fraction of *gauche* defects along the chain) is similar for all amphiphiles. In any case, as shown in Figure V.3, the average distances observed for the amphiphiles excluded from the linear fits are somewhat smaller than expected from the trend established by the 6≤ *n* ≤14 for POPC:Chol and 8≤ *n* ≤14 for SpM:Chol values. Additionally, the standard error associated with the average transverse N1-Cter distance is higher for NBD-C_{16}. This effect was not observed for *z*(N1).

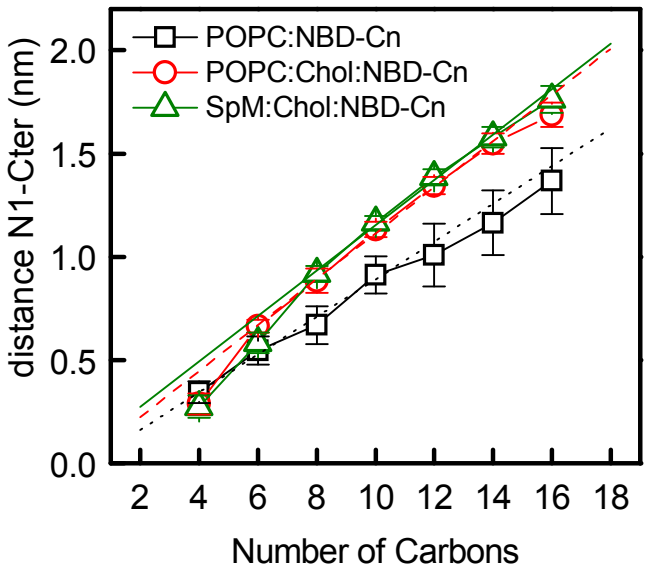

Figure V.3 – Variation of the transverse distance between N1 and the terminal methyl (Cter) group of the amphiphiles in POPC:Chol:NBD-C_n and SpM:Chol:NBD-C_n systems. The lines are the best linear fits to the 6≤ n ≤14 points, with a slope equal to 0.111 nm/CH_2 and 8≤ n≤ 14 points, with a slope equal to 0.110 nm/CH_2 for, POPC:Chol:NBD and SpM:Chol:NBD, respectively. Data obtained for POPC:NBD-Cn systems are added for comparison.

Figure V.4 shows a comparison of <*z*> position of N1, N6, NBD center of mass (COM) and Cter of NBD-C_n with <*z*> position of P8, C13, C24 (carbon 9 of the *sn*-2 chain) and average Cter of POPC (panel A and B for POPC and POPC:Chol, respectively), and of <*z*> position of N1, N6, NBD COM and Cter of NBD-C_n with <*z*> position of P8, C13 and average Cter of SpM (panel C). The results show that N6 and COM of NBD is positioned between the P8 and C13 of phospholipid, both for POPC:Chol and SpM:Chol, essentially at the same depth in the bilayer for all amphiphiles, therefore in a more external position than in POPC. For the shorter amphiphile, NBD-C_4, the <z> position of N1 is closer to N6 indicating the more poorly defined binding of this amphiphile. The more external position of the NBD group in the ordered membranes is in agreement with experimental unpublished results from this research group, (shown in Figure V.5 for sake of comparison), namely the lower quantum yield of these probes in these ordered bilayers compared to pure POPC bilayers in the liquid disordered state. Additionally, the ionization constant of the NBD group is higher in POPC:Chol (1:1) (smaller pKa) compared to POPC bilayers, indicating a higher accessibility of the fluorophore to the aqueous media.

Also shown in Figure V.4, as the fatty amine chain becomes longer, the average transverse location of the Cter group becomes increasingly deeper in the bilayer. Cter of NBD-C_4 and NBD-C_6 are located above and at the position of the *sn*-2 *cis* double bond (which connects POPC C24 and POPC C25, the coordinates of the former also shown in the figure), respectively, whereas those of NBD-C_8, -C_{10}, -C_{12}, -C_{14} and -C_{16} are located more internally. In POPC:Chol, Cter of NBD-C_4 is at higher <*z*> than predicted by the tendency of the other amphiphiles, due to the poor anchoring to the bilayer. A similar behavior is observed for the amphiphiles in the SpM:Chol bilayer.

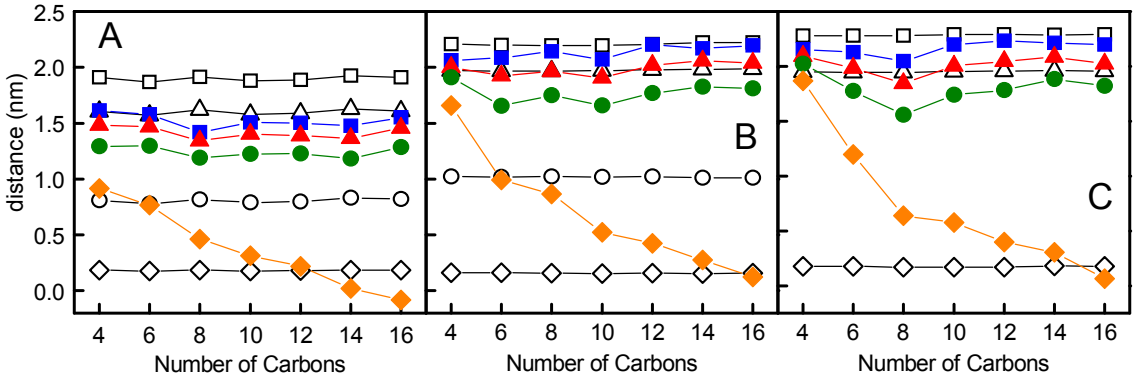

Figure V.4 – Comparison between the average transverse positions <*z*> of some relevant atoms in POPC (A), POPC:Chol:NBD-C_n (B) and SpM:Chol:NBD-C_n (C) systems. In plot (A) and (B) the host lipid atoms represented are P8 (black squares), C13 (black triangles) C24 (black circles) and average Cter of POPC (black diamonds) while in plot (C) they are P8 (black squares), C13 (black triangles) and average Cter of SpM (black diamonds). In all plots the amphiphiles are represented by N1 (green), N6 (blue), NBD COM (red) and Cter (orange).

For POPC:Chol and SpM:Chol, <z>(Cter) of NBD-C_{16} is positive. However, the standard deviation is higher than the distance to the bilayer center, indicating a high frequency of interdigitated conformations of this amphiphile's chain and the phospholipid acyl chains in the opposing leaflet, as was also discussed for POPC [326]. In general, biological membranes have domains composed by a complex mixture of lipids and proteins, with considerable amounts of cholesterol, and therefore it is expected that such bilayer domains have a thickness closer to the more ordered membranes, such as the POPC:Chol and SpM:Chol systems addressed in this study. The finding that the Cter of the amphiphiles with 14 or 16 carbons in the alkyl chain locates closer to the Cter of the phospholipid in each membrane with cholesterol, compared to the result obtained in the POPC bilayer (in which the best match was for n = 12), is in agreement with the choice of myristoyl and palmitoyl chains in protein acylation to anchor and stabilize proteins in membranes due to better packing in the lipid bilayer.

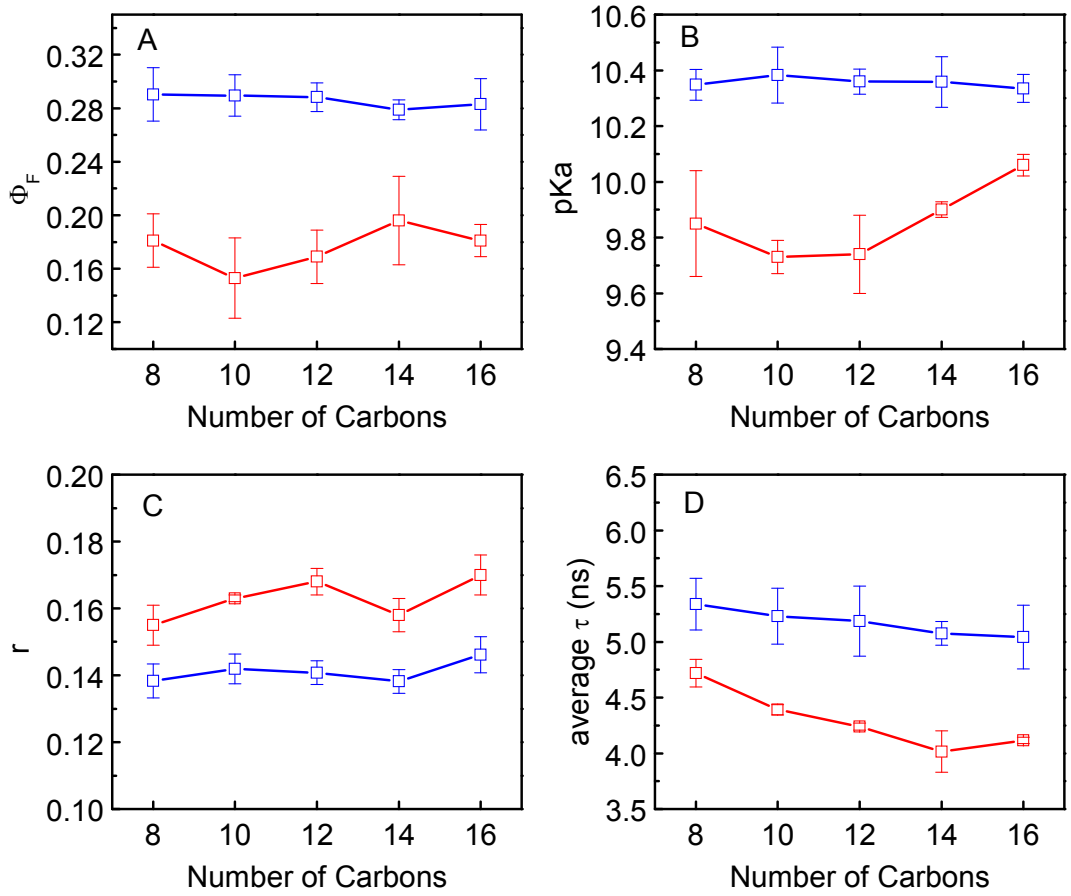

Figure V.5 – Experimental parameters of the NBD-C_n homologous series in POPC (blue) [5] and POPC:Chol (1:1) (red) (unpublished results). (A) fluorescence quantum yield (Φ_F), (B) negative logarithm of the ionization constant (pKa), (C) fluorescence anisotropy (*r*) and (D) average fluorescence life time (τ).

As in Chapter IV, the interdigitation phenomenon was quantified calculating the fraction of frames for which *z*(Cter) < 0 during the 20 ns – 100 ns time range of the trajectories, which can be identified as the fraction of interdigitated conformations, and is shown in Figure V.6 for the studied amphiphiles. It can be seen that up to $n = 14$ less than 10% of the simulation frames show interdigitation of NBD-C_n, and for $n = 16$ interdigitation occurs during 30% and 40% of the analyzed time window for POPC:Chol and SpM:Chol, respectively. The more external location of the fluorophore and the larger thickness of the POPC:Chol and SpM:Chol ordered bilayers justifies the lower fraction of interdigitation compared to that found in the POPC disordered bilayers.

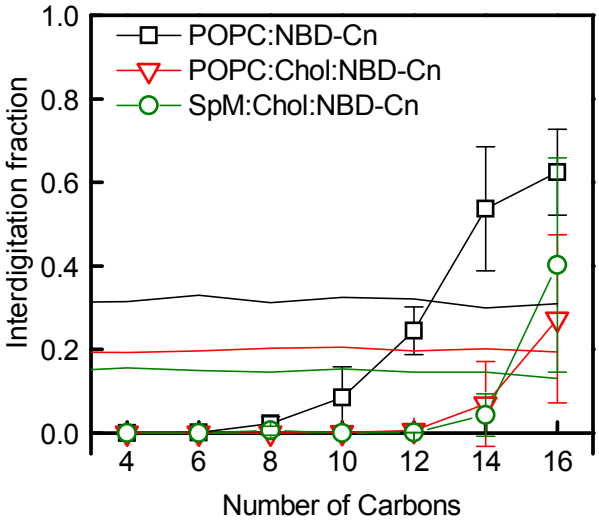

Figure V.6 – Fraction of interdigitated conformations (*f*) as a function of the amphiphile chain length *n* for NBD-Cn amphiphiles in POPC (black squares), POPC:Chol (red triangles) and SpM:Chol (green circles). The fraction of interdigitated frames of the phospholipid is also shown for POPC (black line), POPC:Chol (red line) and SpM:Chol (green line).

V.2.3 – Orientation of the NBD Fluorophore

Figure V.7 shows the frequency distributions $P(\theta)$ of the angles between the long axis (defined as the vector between atom O12 and the center of mass of atoms C3 and C4), the short axis (defined as the vector between atoms C10 and C11), and the normal to the NBD plane (defined as the vector product of the short and long axes) relative to the bilayer normal (see Figure IV.7 for an illustrated definition).

For the short axis, the recovered $P(\theta)$ distributions are wide, but values $\theta > 90°$ predominate clearly, corresponding to C10 being closer to the interface than C11. Given the rigidity of the NBD moiety, this is a necessary consequence of the higher $\langle z \rangle$ obtained for the NO_2 group compared to the remainder of the fluorophore, as illustrated above (Figure V.2 and Figure V.4). For the long axis, a wide/bimodal distribution is found for all systems, corresponding to essentially to three characteristic positions: long axis perpendicular to the bilayer normal, O12 pointing to the water or O12 pointing to the bilayer center. In any case, similar $P(\theta)$ functions are obtained for the angle between the normal to the NBD plane and the bilayer normal.

On the whole, the preferred orientations of the NBD group in all systems are similar to that of the same amphiphiles in POPC and for C_{12}-NBD-PC in fluid DPPC bilayers [264]. In this general orientation, all electronegative O atoms (especially those of the

NO_2 group, O7 and O8) point towards the water/lipid interface. However, in some cases broader or bimodal distributions are found. For the case of shorter amphiphiles, the lower anchoring capacity and the poorer binding of the amphiphiles to the bilayers could be invoked as an explanation of such broad distributions; however, this cannot be said for the cases of longer amphiphiles. Therefore a more reasonable explanation is related to the simulation time and to insufficient sampling of NBD orientations. In spite of the location of the NBD COM being well equilibrated during the simulations, the rotational motion of NBD plane in the more ordered bilayers is slow, and therefore this also applies to the equilibration of the fluorophore orientation.

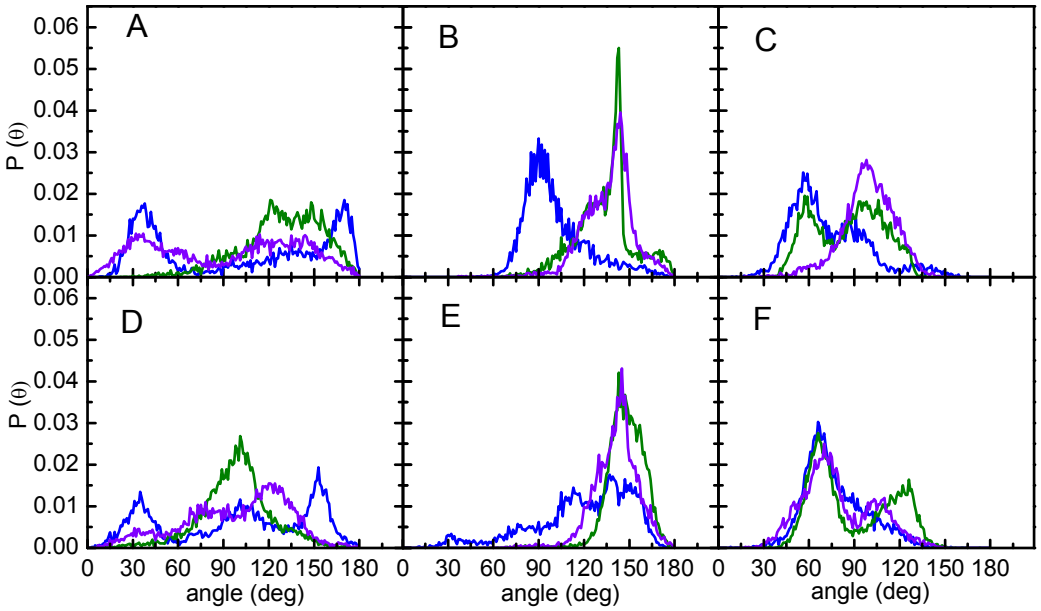

Figure V.7 – Orientation of the NBD group in POPC:Chol:NBD (A, B, C) and SpM:Chol:NBD (D, E, F) bilayers. Probability density functions $P(\theta)$ of the angles between the long axis (A, D), the short axis (B, E), and the normal to the NBD plane (defined as the vector product of the short and long axes; C, F), relative to the bilayer normal. The amphiphiles shown are NBD-C_4 (blue), NBD-C_8 (green) and NBD-C_{16} (violet).

V.2.4 – Hydrogen Bonding

Similarly to that was performed in Chapter IV, the hydrogen bond interactions of the NBD with the lipid constituents of the bilayers were analyzed. For this purpose, an H-bond for a given donor–H–acceptor triad was registered each time the donor-acceptor distance was less than 0.35 nm and the H-donor-acceptor angle was < 30º.

Compared to pure POPC [326] (Chapter IV), higher frequencies are observed for all amphiphiles in both ordered bilayers regarding H-bonding to water O atoms, induced by the more external position of the NBD. The H-bonding between the -OH groups of water (donors) and the various O and N atoms of NBD (acceptors) shows preference for the O7 and O8 of the NBD (Figure V.8A and C), in agreement with the higher exposure to the solvent by these two atoms and their significant negative charge (≅-0.5 each [264]), similarly to observed in pure POPC bilayers.

Figure V.8B and D show the frequency of H-bonding from NBD N1-H14 to each of the possible acceptor atoms in POPC:Chol and SpM:Chol bilayers. As can be readily seen by summing over all acceptors, the NBD NH group is involved in H-bonds roughly about 80% of simulation time, with exception of NBD-C_6 and NBD-C_{10} in SpM:Chol (~60%). The frequency of binding to cholesterol O atom is low in both bilayers; however it seems to increase with the number of carbons for POPC:Chol. With the presence of cholesterol, the preference for hydrogen bonding to the POPC oxygen atoms of the glycerol backbone vanishes, being these bonds roughly equally distributed among all POPC oxygens. This is also a consequence of the more external position of the amphiphiles in bilayers containing cholesterol, compared to pure POPC. In the case of SpM:Chol, the NBD NH binds preferentially with the hydroxyl oxygen (O34) of SpM. In closer inspection, the H-donor-acceptor angle and the H-acceptor distance distributions reveal some degree of specificity (not shown), similarly to that mentioned before for the interaction with pure POPC bilayers in Chapter IV. The preferred angle of the H-bond triad is below 20º, being ~15º for the case of the H-bond to O atoms which the binding is significant. The almost perfect co-linearity of the triad indicates the preference of NBD N1-H14 for establishing H-bonds with these atoms.

The H-bonding between the -NH group of SpM (donor) and the various O and N atoms of NBD (acceptors) shows preference for the O12 and N13 of the NBD (Figure V.8E), compatible with NBD oriented with the NO_2 group to the water. However, there is high variability, also due to the difficulty in sampling the NBD orientation. We note that whereas NBD N1-H14 may establish H-bond during a considerable amount of time, as a donor to the hydroxyl oxygen (O34) of SpM, it shows less ability for binding to N14 and or to O17. The lower partial charges of atoms N14 and O17 compared to O34 of SpM can explain this difference. NBD N1 does not establish H-bonds (as acceptor) with the hydroxyl hydrogen of SpM, probably due to orientation hindrance.

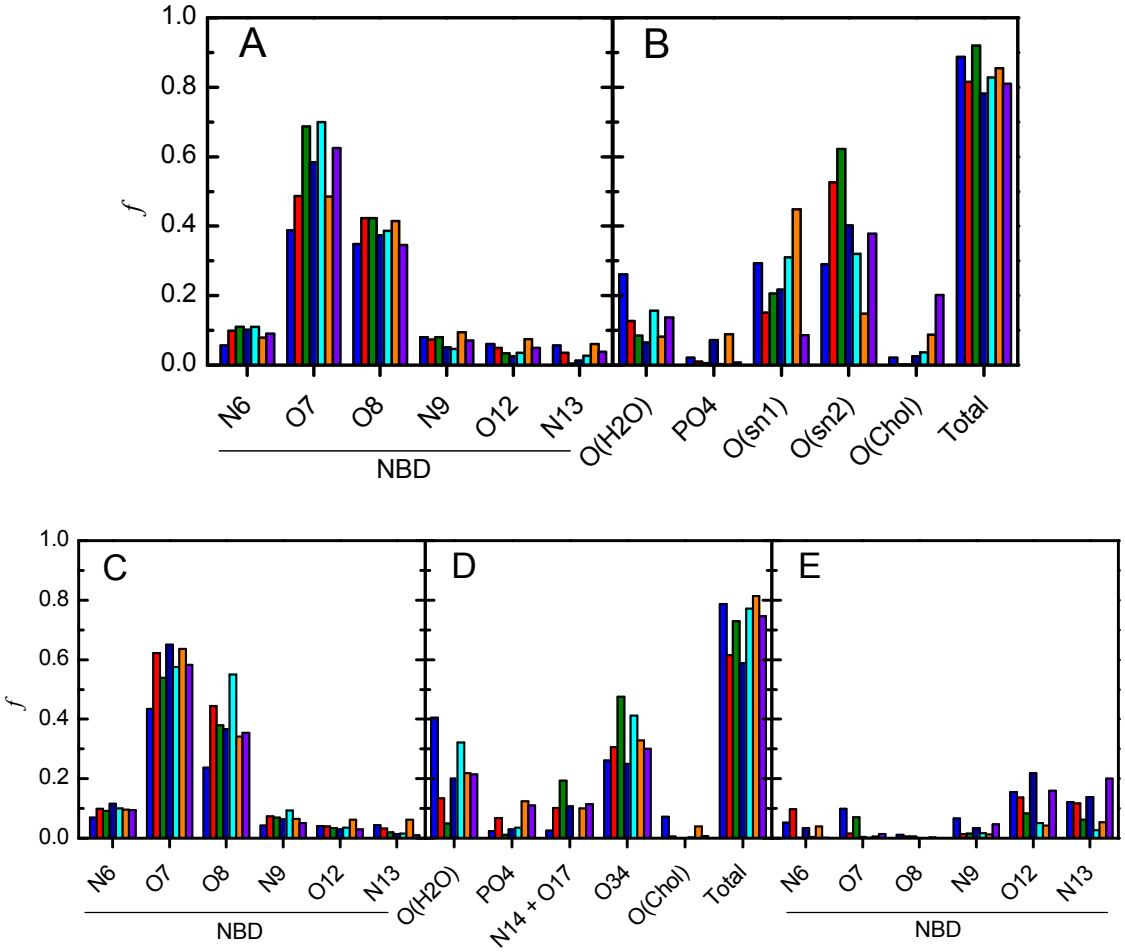

Figure V.8 – H-bond fractional frequencies (*f*) of the amphiphiles in POPC:Chol:NBD (A, B) and in SpM:Chol:NBD (C, D, E) bilayers: (A) H_2O as donor for NBD acceptor atoms, (B) NBD as donor for H_2O, POPC and Chol acceptor atoms, (C) H_2O as donor for NBD acceptor atoms, (D) NBD as donor for H_2O, SpM and Chol acceptor atoms, (E) NH-SpM as donor for NBD acceptor atoms.

V.2.5 – Order of the NBD-C_n, POPC and SpM Acyl Chains

The order parameters of the lipids and amphiphiles were analyzed as described in the preceding chapter. Due to the slow convergence of this parameter [53], analysis was restricted to the last 50 ns of the simulations. Order parameters were calculated for both chains of POPC and SpM (Figure A.7 in the Appendix). The profiles obtained agreed reasonably with both experimental and simulated data for POPC:Chol [64, 337], as well as for SpM:Chol [337, 341] bilayers. Incorporation of NBD-C_n does not induce any significant perturbation in the bilayer.

Focusing on the NBD-C_n chain order parameters, Figure V.9A and B shows $-S_{CD}$ for the chain carbon atoms of the different amphiphiles in both bilayers. The profile of the

order parameter for the alkyl chain of the amphiphiles is similar to the profiles obtained for POPC *sn*-1 and SpM chains, and typical of profiles of phospholipid acyl chains in the liquid ordered state. Note that, in Figure V.9 the axis of the carbon segments of lipids and amphiphiles start at different values due to their relative positions in the bilayer. In general, the order parameter profile has a parabola-like shape with a maximum around the middle of the alkyl chain. Below this location, the order parameter decreases for each molecule, pointing to an increased fraction of *gauche* conformations near the end of the chain. In the ordered bilayers studied here, the order parameters of the chains are higher than those found in pure POPC (Chapter IV), reflecting the higher order of the systems. Exceptions to this behavior were found for the smaller amphiphiles, NBD-C_4 in POPC:Chol and NBD-C_4 and NBD-C_6 in SpM:Chol, for which the order parameter is significantly smaller compared to the other amphiphiles, reflecting the more external location and the poorer anchor of the chain. Indeed, for NBD-C_4, the order parameters found here are even lower than in POPC.

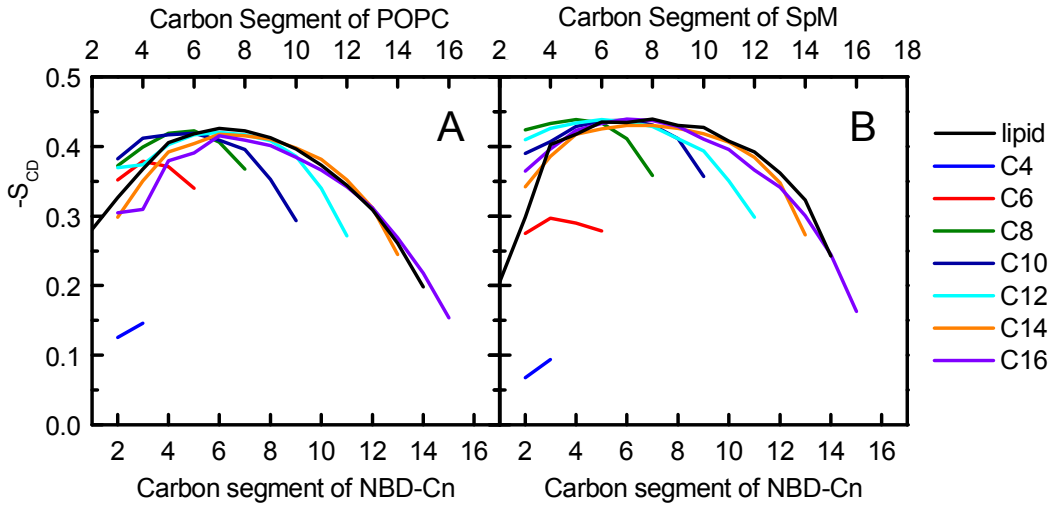

Figure V.9 – NBD-Cn alkyl chain deuterium order parameter profiles (S_{CD}) in POPC:Chol:NBD (A) and in SpM:Chol:NBD bilayers (B). Order parameter profiles of POPC *sn*-1 and SpM sphingosine chains in amphiphile free systems are also included in the plots A and B, respectively.

V.2.6 – Electrostatic Potential

Given the polarity of the NBD fluorophore, it can be expected that incorporation of NBD-C_n in the bilayer affects the electrostatic profile. Figure V.10 compares the profiles obtained for the POPC:Chol (1:1) and POPC:Chol:NBD-C_n systems, and for the SpM:Chol (6:4) and SpM:Chol:NBD-C_n systems. The values for POPC:Chol (1:1),

-730 mV, and for SpM:Chol (6:4), -680 mV seem to be very high. Those values are higher than obtained in pure POPC with recent MD studies, in which values ranging from -500 mV to -600 mV are reported [310, 320, 321, 326], in agreement with the lower area/lipid of the ordered bilayers. The smaller value of SpM:Chol may be explained by the replacement of an carbonyl group by an hydroxyl group in SpM. [342]

In Figure V.10 the potential at the center of the bilayer (relative to that in the water region) is shown as a function of the number of chain carbons of the amphiphile. It can be seen that inclusion of the NBD-C_n amphiphiles increases the difference in electrostatic potential between the interior of the bilayer and the bulk water phase. These values are subject to uncertainty due to cancellation errors, because the observed potential profile is the difference between the water and lipid contributions, which almost cancel each other (not shown). In any case, there is no doubt that insertion of NBD-C_n amphiphiles increases the difference in electrostatic potential in the membrane relative to water. Similar effects were observed and discussed for the NBD-C_n amphiphiles in POPC [326] and the C_6-NBD-PC and C_{12}-NBD-PC probes [301].

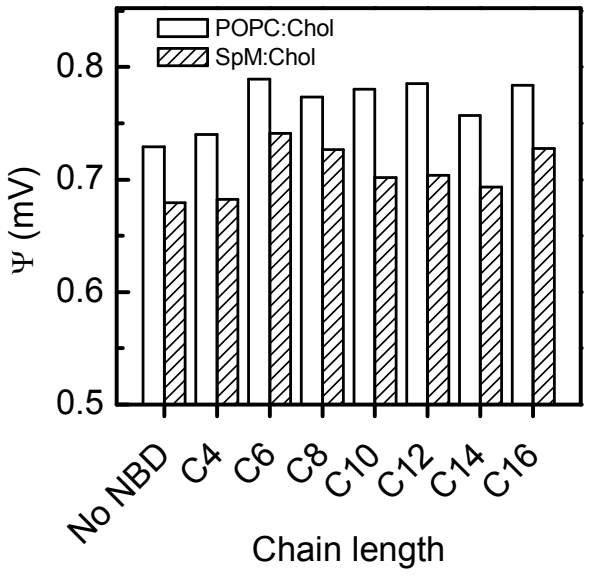

Figure V.10 – Electrostatic potential in the center of the bilayer (relative to the water region) as function of the total number of carbons of the NBD-C_n alkyl chains in POPC:Chol:NBD and SpM:Chol:NBD bilayers.

V.2.7 – Mass Density Profiles

Figure V.11 shows the mass density profiles across the bilayer obtained for different components of each system, water, phospholipid, cholesterol, and selected (for clarity reasons) NBD-amphiphiles for the different POPC:Chol:NBD-C_n and SpM:Chol:NBD-C_n systems. Relative to the pure bilayer components, alterations in the density profiles for water or phospholipid (POPC or SpM) atoms in bilayers containing NBD-C_n are small and non-monotonic (not shown), pointing to limited probe perturbation (already evidenced in the area/lipid, P-P distance and lipid order parameter results commented above). Similar to previous results in pure POPC, the more interesting result from this analysis is an increase in the mass density at the center of the bilayer, observed for amphiphiles with alkyl chains with 14 and 16 carbons. For the amphiphiles smaller than NBD-C_{14} the mass density profiles indicates that Cter does not reach the center of the bilayer. For the amphiphiles with $n \geq 14$ there is a considerable increase in mass density, even presenting a local maximum for NBD-C_{16}, close to the bilayer center (unlike the phospholipid itself). These results correlate with the fraction of interdigitated frames in each system (Figure V.6), which becomes significant for $n \geq 14$.

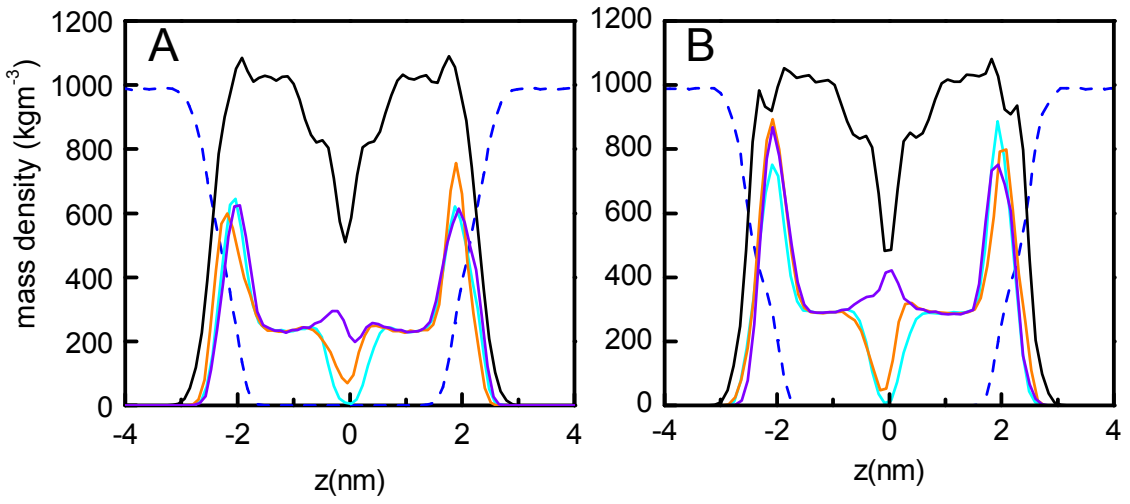

Figure V.11 – Mass density distributions of some selected POPC:Chol:NBD (A) and SpM:Chol:NBD (B) systems. Mass density distributions of POPC:Chol or SpM:Chol (black) and water (blue), both recovered from pure bilayers, and NBD-C_{12} (cyan), -C_{14} (orange) and –C_{16} (violet), recovered from the respective lipid:4-NBD-C_n systems, are shown. The profiles of the NBD amphiphiles were multiplied by 18 (POPC:Chol) or 23 (SpM:Chol) for better visualization.

V.2.8 – Lateral Diffusion

Lateral diffusion coefficients of all bilayer lipids, including the amphiphiles, in all systems were calculated from the two-dimensional mean square displacement (MSD), using the Einstein relation as described in the last chapter. Figure V.12A and B shows the variation of lateral diffusion coefficient determined for POPC or SpM, Chol and NBD-Cn for the POPC:Chol and SpM:Chol systems labeled with the different amphiphiles, respectively. The results presented here do not intend to be quantitatively interpreted. Actually, it is being well established that simulation times on the order of that used in this study cannot describe quantitatively diffusion coefficients [343]. The calculated values for POPC, SpM and Chol in each monolayer are similar and on the order of 10^{-9} cm^2s^{-1}. Those values are intermediate between diffusion coefficients in gel (10^{-10} cm^2s^{-1}) and fluid (10^{-8} cm^2s^{-1}) phases [70], therefore considerably smaller than that obtained for pure POPC, which qualitatively agree with the increased order of the bilayers. The lack of systematic changes of the calculated *D* of the bilayer components upon incorporation of these single-chained amphiphiles, similarly to POPC bilayers, is another indicator of their relatively mild perturbation of the bilayer, in contrast with NBD labeled acyl-chain PC [301].

Concerning the NBD-Cn molecules, there is no clear distinction in the lateral diffusion coefficients. In the lipid:Chol bilayers the NBD-Cn molecules diffuse slower than in pure POPC bilayers, according to the slower dynamics of the bilayer. However, the short chain amphiphiles, located more externally in the ordered bilayers may diffuse considerably faster, making them poor reporters for diffusion experiments. Contrary to the results in pure POPC, in the ordered bilayers the smaller fraction of interdigitation does not represent a problem for using the long chain amphiphiles as diffusion reporters.

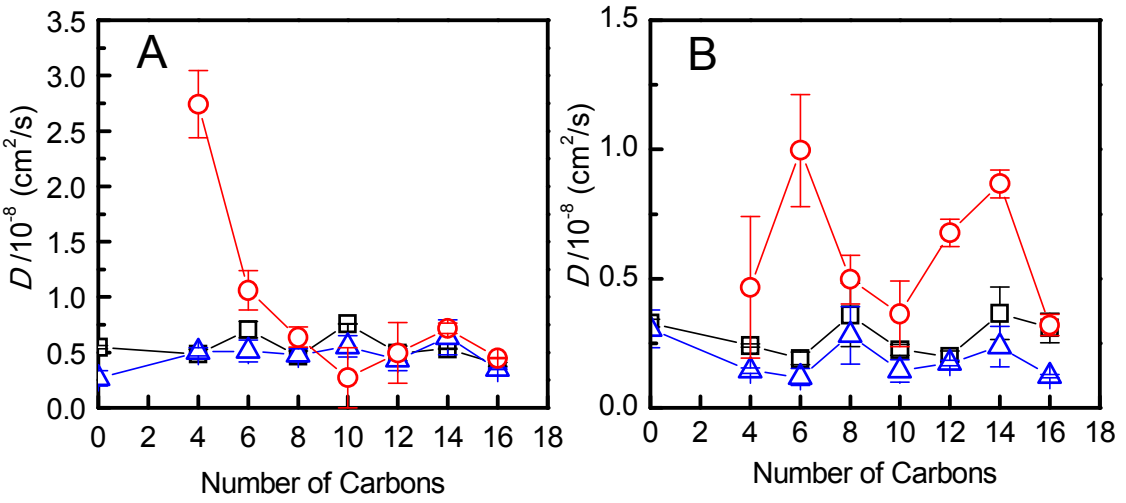

Figure V.12 – Diffusion coefficients (cm^2/s) of (A) POPC (black), Chol (blue) and NBD-C_n (red) for POPC:Chol:NBD and (B) SpM (black), Chol (blue) and NBD-C_n (red) for SpM:Chol:NBD bilayers.

V.3 – Concluding Remarks

Following our work on the interaction of the homologous series of fluorescent fatty amines of varying alkyl chain length, NBD-C_n, with POPC [326], atomistic MD simulations of POPC:Chol (1:1) and SpM:Chol (6:4) bilayers labeled with the same fluorescent fatty amines, were carried out. The results obtained for pure POPC:Chol and SpM:Chol bilayers, in this work, as discussed throughout this Chapter, agree with both experimental and theoretical published data, and validate our choices for MD parameters. For all amphiphiles in both bilayers, the NBD fluorophore locates at the interface, in a more external position than it was located in pure POPC bilayers. The more external position of the amphiphiles in the more ordered bilayers agrees with the low fluorescent quantum yield and higher ionization constants (smaller pKa) determined experimentally. The higher order parameter of the alkyl chains, induced by the overall higher order of the bilayers, also seems to agree with the experimental results of fluorescence anisotropy, which is higher in POPC:Chol than in POPC bilayers for all amphiphiles. However, there is a compensation effect on anisotropy and fluorescence lifetime between the amphiphiles in those two lipid bilayers. Similarly to POPC bilayers, the longer-chained NBD-C_n amphiphiles show significant mass density near the bilayer midplane, and the chains of these derivatives, mainly NBD-C_{16}, interdigitate to some extent the opposite bilayer leaflet. However, as the fraction of interdigitation in the thicker bilayers is smaller, this phenomenon does not lead to a slower lateral

diffusion for the longer-chained derivatives, unlike in POPC bilayers. On the other hand, although events of amphiphile desorption from the bilayer were not observed in any system, the shorter-chained amphiphiles ($n < 8$) show poor anchoring capacity, and therefore it is very likely that they may be able to leave the bilayers at longer time scales. As determined for the interaction with POPC, the effects of these amphiphiles on the structure and dynamics of the host lipid were found to be relatively mild, in comparison with acyl-chain-labeled NBD probes. For ordered bilayers, amphiphiles with chain lengths inside the $8 \leq n \leq 16$ range have lateral diffusion coefficients similar to that of the pure bilayer components, and, also taking into account their relatively mild perturbing effect, they can be useful fluorescent reporters of bilayer dynamics.

As a matter of speculation, considering that biological membrane domains such as lipid rafts are rich in sphingomyelin and cholesterol, they are expected to exist in a relatively ordered state, not dissimilar to that of the systems addressed in this study. Therefore, for proteins which sit/locate in the head group region, with similar locations to that of the NBD group in our systems, the almost perfect fit of $-C_{14}$ or $-C_{16}$ chains attached to the protein and the host lipids' own chains in the same bilayer leaflet may be one of the reasons why the acylation of proteins occurs mainly with myristoyl and palmitoyl acyl chains. Acyl chains that fit the thickness of a monolayer will allow the anchoring of proteins without perturbing the opposing membrane leaflet.

Chapter VI

How to Tackle the Issues in Free Energy Simulations of Long Amphiphiles Interacting with Lipid Membranes: Convergence and Local Membrane Deformations

This work was published as: Filipe, H. A. L.; Moreno, M. J.; Róg, T.; Vattulainen, I.; Loura, L. M. S. How to Tackle the Issues in Free Energy Simulations of Long Amphiphiles Interacting with Lipid Membranes: Convergence and Local Membrane Deformations. J. Phys. Chem. B 2014, 118, 3572-3581.

Hugo A. L. Filipe contributed with the preparation, execution and analysis of the simulations, and also contributed to the writing of the manuscript.

VI .1 – Introduction

Many severe diseases are related to malfunctions in the central nervous system. There are drugs able to treat the malfunctions, but the challenge is to bring the drugs to the brain tissue through the blood-brain barrier. This barrier is a dynamic interface comprised of highly specialized endothelial cells surrounded by complex membrane structures, and the understanding of how drugs could cross this barrier is currently quite limited. In the same spirit, the principles that govern the translocation of drugs across even simpler membranes are not well understood, yet they are of profound importance in broad contexts such as immunology. In essence, the challenge is to unlock how drugs could be transported across a number of membranes composed of lipids, proteins, and carbohydrates.

Development of new drugs has therefore two related problems that should be solved together: finding drugs with desired effects, and fostering their ability to cross complex membrane structures such as the blood-brain barrier. While the challenge is significant, the benefit for health would be even more substantial, with important social and economical implications. [173]

In this regard, during the last years, with a focus on passive permeation, the kinetics and thermodynamics of several amphiphiles interacting with membranes of different lipid composition have been characterized experimentally in quite considerable detail. [5-7, 74] The experimental data allows one to calculate the rate of passive permeation through biological membranes, which in turn is expected to pave the way for a better understanding of the rules and molecules' structural details that govern the rate of passive permeation.

The currently accepted model for passive permeation across biomembranes is based on the Overton rule [16], equation (II.3), which predicts a linear dependence of the permeability coefficient (P), through a membrane of thickness h, on the partition coefficient of the amphiphile between the lipid and aqueous phases (K_P). This model results from the assumption that the diffusion of the amphiphile through a membrane (characterized by a diffusion coefficient D) is the rate-limiting step in the overall permeation process, an approximation that is valid for most amphiphiles. In a modified

version of equation (II.3), the permeability coefficient may be obtained from [44, 74, 344, 345]

$$P = k_f \lambda K_P \quad \text{(VI.1)},$$

where k_f is the rate constant for the translocation process (the equivalent to diffusion through membranes for amphiphilic molecules), and the factor λ is required to convert the ligand concentration from volume to surface units. For an amphiphilic molecule translocating through a lipid membrane, λ is equal to the thickness of the monolayer. [44, 74, 344, 345] Therefore, determination of k_f and K_P of a drug in a given membrane type may be used to calculate its permeability coefficient due to passive permeation. This approach has been used recently for chlorpromazine, one of the commonly used antipsychotic drugs, with good agreement with the permeability coefficients obtained *in vitro* with cell monolayers. [7]

Atomistic molecular dynamics (MD) simulations are a powerful tool to study the interaction of amphiphiles with lipid membranes, as they give atomistic insight into processes and phenomena that often cannot be considered experimentally in sufficient detail. [26, 162] MD simulations allow one to better understand what really happens in experimental observations, and why. Even more importantly, the field of MD simulations in biological sciences has matured to a level where predictions of new phenomena are being made more and more often, thereby generating quite profound added value to complement experiments.

In the context of small molecules interacting with lipid membranes, one of the central simulation techniques to study molecular translocation across membranes is free energy computation. Most commonly, one typically uses biased simulations through the Umbrella Sampling (US) [166, 167] method to calculate the Potential of Mean Force (PMF) profiles for a solute interacting with a lipid bilayer. Previous work has resulted in PMF profiles for a variety of solutes with different bilayer compositions. [160, 346-356] These data are highly useful since they depict the free energy barriers associated with translocation and desorption, and hence allow one to compute their rates as well as equilibrium constants.

Generally, to calculate the PMF using umbrella sampling, a set of initial structures is first generated by pulling the molecule across a bilayer along the reaction coordinate, which is usually the distance from the molecule to the membrane's center of mass along

the bilayer normal direction. Then, a set of production runs is carried out, applying a biasing harmonic potential between the molecule and the bilayer, relative to a reference position. From these simulations, distance distributions of the molecule around the reference position are obtained. Finally, the PMF is generated, correcting for the contribution of the biasing potential. [168, 170]

While the technique is seemingly simple, there are several potential problems that may compromise the quality of the results. Sampling problems have been actively discussed in the literature [354-356], meaning that if the sampling is not appropriately extensive, then the condition of ergodicity is broken and the free energy values found through the analysis are not accurate enough. A related problem concerns equilibration, since prior to production simulations for sampling, for each simulation window along the reaction coordinate the system should be allowed to reach true equilibrium. [354, 355] If these issues are not taken care of, the simulation data may include artifacts.

Recently, the use of advanced simulation techniques has been proposed to improve sampling in the study of solute permeation through lipid membranes, focusing on the importance of orientational and conformational motions. [355, 357-361] However, the studied solutes are considerably less flexible than the long amphiphilic molecules now considered. In this work, we discuss this general issue in terms of two related problems (see below). In both cases we focus on long amphiphilic molecules interacting with membranes, since structurally related molecules [362-364] have been shown to be efficient drugs against, e.g., immunological diseases, and these drugs have to cross membranes in order to do their function. Furthermore, long aliphatic chains have potential for the development of pro-drugs to increase the rate of passive permeation through tight endothelia, such as in the blood-brain barrier, provided that the free drug is released once inside the target tissue. [146, 365, 366] In this context, our objective is therefore to understand the limitations of umbrella sampling free energy calculations in cases where both enthalpic and entropic degrees of freedom are very important, and long chain-like amphiphile molecules (see Figure IV.1 in Chapter IV for structures and the numbering of relevant atoms) are quite convenient for this purpose since with increasing chain length the role of entropy becomes more and more relevant.

We first focus on potential hysteresis in the PMF. We show that when the amphiphile is shifted from membrane center to the water phase, we find results that are qualitatively consistent with experimental data. [5, 6] Conversely, when the amphiphile is pulled

from the water phase to the inside of the lipid bilayer, we find artifacts that are shown to arise from sampling problems at the membrane-water interface, where the simulation results do not converge despite extensive simulation times.

Second, we show that the choice of the reaction coordinate – the key parameter in free energy profile computations – is a highly non-trivial matter especially with complex molecules, and it turns out that its appropriate choice is decisive for finding physically correct results. Previous work has shown that the definition of the reaction coordinate may influence the results through generation of membrane deformations during the production runs. [354] We observe similar features but, importantly, we also find that different schemes for the reaction coordinate generate data that are not consistent. In this context we focus on two techniques, where the first one chooses the reference plane for the reaction coordinate as the center of mass of all lipids in a membrane, while the second case chooses the reference plane locally in terms of the lipids that are inside two concentric cylinders around the translocating molecule. When we compute PMFs for a homologous series of NBD-C_n amphiphiles in POPC bilayers, we observe that the local arrangement tends to avoid the contribution of bilayer undulations to the determination of the bilayer's center of mass. [346] Importantly, its data is qualitatively consistent with experiments, unlike the results of the first approach.

The results highlight the urge to understand how PMF calculations should be performed to avoid any problems that would result in unphysical data. In this spirit, we close the Chapter by discussing the implications of our findings and the means to avoid potential related pitfalls.

VI.2 – Results and Discussion

VI.2.1 – Convergence of PMF should not be Taken for Granted with Complex Long Molecules

The convergence of the PMF profiles is a central issue in the determination of free energy barriers from MD simulations. For small molecules the topic has been addressed previously [354, 356], however for long flexible chain-like molecules where entropic degrees of freedom become more and more important for increasing chain length, the

understanding of conditions for convergence and sufficient sampling is an important practical matter that remains to be clarified. Here we address this issue.

Figure VI.1 shows data for NBD-C_{16} in the CW case. Figure VI.1A illustrates that, for increasing simulation time in each of the umbrella sampling windows, the shape of the profile evolves systematically until it converges after ~70 ns. The results suggest that the time needed to equilibrate the system is quite short, and the sampling is adequate for simulation times close to 70 ns, for which contributions from non-equilibrated configurations become negligible. Figure VI.1B assesses the convergence of the PMF for increasing periods used for equilibration. It is apparent that equilibration times larger than about 20 ns are not needed.

In Figure VI.1C, the convergence is evaluated by disregarding an increasing amount of data from the beginning of each simulation, and then using a 20 ns period for analysis. The results show that equilibration takes place during the first 20 ns, and that a period of 20 ns is not representative of the entire simulation due to insufficient sampling.

The above results suggest that the convergence overall should be assessed by increasing the total simulation time, and the amount of time/data needed for equilibration should be tested second. In the present systems, this approach led us to choose the last 80 ns for PGC, and the last 90 ns for NBD-C_{16} (40 ns for the other amphiphiles) for PGD to generate the PMF profiles.

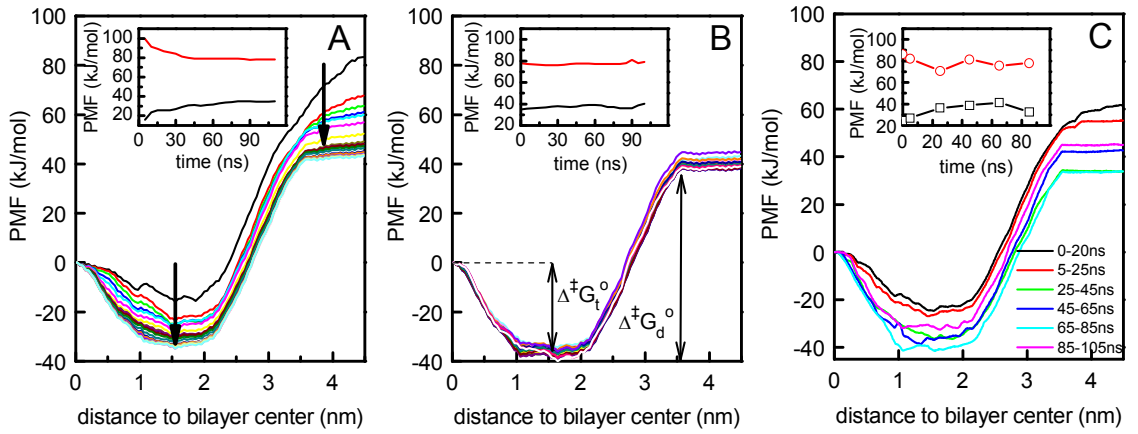

Figure VI.1 – Convergence of the PMF of NBD-C_{16} calculated from PGD simulations in the CW case: (A) Increasing the total simulation time by 5 ns intervals until the maximum of 110 ns. The arrows indicate the evolution of the PMF profiles (black line stands for a 5 ns simulation, red being 10 ns, etc.). (B) Discarding successive 5 ns intervals from the simulation data (for equilibration) with a maximum simulation time of 110 ns. (C) Data analyzed over 20 ns intervals (see inset). The time dependence of the free energy barriers for translocation/flip-flop (black) and desorption (red) are shown as insets in each plot. In the middle panel, $\Delta^{\ddagger}G_t^o$ and $\Delta^{\ddagger}G_d^o$ indicate the free energy barriers for the translocation and desorption processes, respectively.

To assess the ability of the CW approach to represent the PMF, we consider the same system in the WC case using the convergence procedures i) and ii) described in section III.2.2.3. Figure VI.2 shows that in the WC case the PMF profile does not converge. Even when the total simulation time is increased to ~130 ns, the PMF profiles are still evolving in time (Figure VI.2A,B), highlighting lack of convergence. When the period used for equilibration is increased systematically, we again find that the profiles do not converge (Figure VI.2C,D). These conclusions are quantified by the data in the insets of Figure VI.1 and Figure VI.2, which show the convergence of the free energy barriers for desorption and translocation of NBD-C_{16} determined with different simulation time intervals. The convergence of the free energy barriers for the other amphiphiles, and for the PGC simulations is shown in Figures A.10 and A.11 of the Appendix.

Clearly the results of the CW and WC approaches do not match, thus what is the cause of the effect? We found that during the pulling in the WC scenario, the amphiphile entered the bilayer in an orientation that is totally different from that observed in the equilibrium position (that is, in the latter case, the alkyl chain is facing the bilayer center and the polar NBD group is directed towards the aqueous medium).[326] Therefore, the

amphiphile has to rotate along the bilayer normal, which is a slow dynamic process, thereby slowing down equilibration and the rate of convergence.

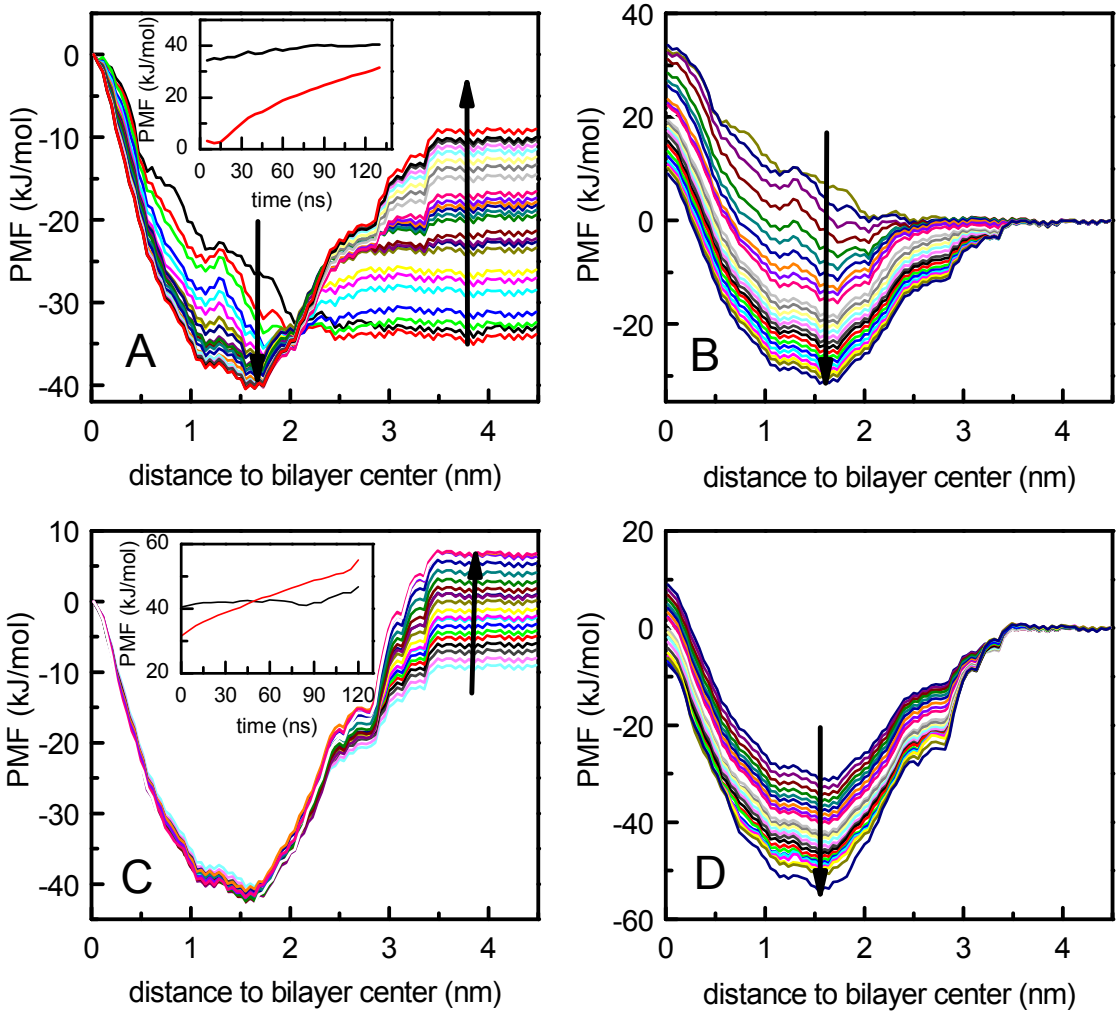

Figure VI.2 – Convergence of the PMF calculated from PGD simulations for WC: (A, B) increasing the total simulation time by 5 ns intervals until the maximum simulation time of 130 ns; (C, D) discarding successive 5 ns intervals for equilibration with a maximum simulation time of 130 ns. The profiles shown in panels (A, C), and (B, D), have the reference position defined to be at the center of the bilayer and in the water region, respectively. The arrows show how the PMF profile evolves. The time dependence of the free energy barriers for translocation (black) and desorption (red) are shown as insets in panels (A, C).

Figure VI.3 shows the PMF profiles obtained from the CW and WC scenarios. Due to the non-convergence of the PMF profiles in the WC scheme, the curves shown in the plot were obtained from simulation times larger than 120 ns. Still, the WC profile is clearly distinct from the one obtained for CW. This brings up the question that which of the two profiles, if any, describes the process appropriately. For this purpose, we show in Figure VI.3 the two profiles with different reference positions (bilayer center used as

reference in Figure VI.3A and the water region in Figure VI.3B). Upon going from the reference position along the reaction coordinate, the two profiles diverge in the 2.5 nm < z < 3.5 nm region, which is shadowed in the figure. Outside this interval, the profiles match. The region between 2.5 nm < z < 3.5 nm is the one where the amphiphile interacts with lipid head groups. Sampling difficulties in this region have also been identified in calculation of PMF profiles for other large molecules. [349] In our systems, the PMF profile obtained from the WC direction shows small flat regions in this part of the reaction coordinate. These flat regions arise from simulations where the alkyl chain of the amphiphile does not insert itself into the bilayer during the simulation time scale. Therefore, if the simulation time were increased (possibly up to a microsecond time scale), it would be expected that insertion of the long chain of the amphiphile would take place in the WC case, too, and the WC profile would approach the one obtained by the CW procedure. This view is supported by the data in Figure VI.2, which shows that the free energy barriers increase systematically for increasing simulation times used for analysis.

This gives us confidence to conclude that the CW profile is the most appropriate representative of the systems studied here, in agreement with a previous study. [349]

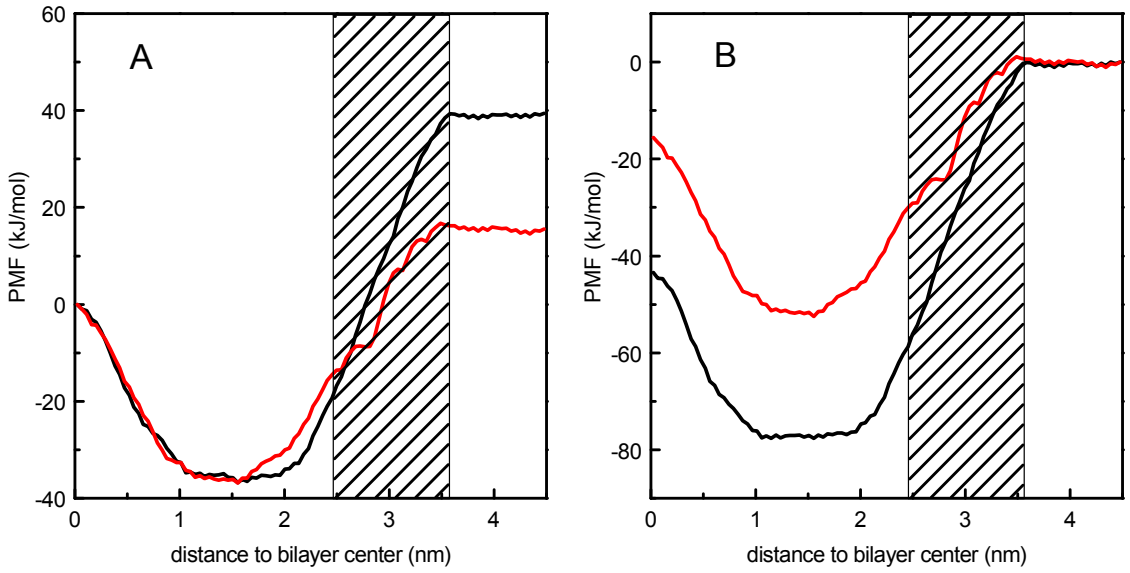

Figure VI.3 – PMF profiles of NBD-C_{16} calculated from PGD simulations with the CW (black) and WC (red) schemes. In CW, the data used for analysis covered a period from 20 ns to 110 ns, and in WC a period from 120 ns until the end of the simulation. In (A) the PMF is defined to be zero in the center of the bilayer, and in (B) the PMF is defined to be zero in the water region.

VI.2.2 – How to Deal with Local Membrane Deformations During PMF Calculations: PMFs for the NBD-C_n Homologous Series

Having performed the analysis of the PMF convergence, the barriers for translocation and for the interaction of the amphiphiles with the lipid bilayer can be calculated. Figure VI.4A and B show the PMF profiles obtained for the simulated amphiphiles (NBD-C_4, NBD-C_8, NBD-C_{12}, NBD-C_{16}) using the CW scheme. Results are shown for both the PGC and PGD schemes; see discussion below. Because the calculation of PMF profiles is very computationally expensive, the simulation of the whole homologous series characterized experimentally [6] (NBD-C_n, n = 8, 10, 12, 14, 16) was not undertaken here, and the amphiphiles were instead selected based on their representation of short, medium, and long chain amphiphiles. Additionally, an amphiphile with a shorter alkyl chain, which could not be accessed experimentally, was included to the study.

Two different methodologies (PGD and PGC, see section III.2.2.1) were applied to sample the system and to obtain the PMF profiles. The PMFs obtained with both methodologies are similar, however PGC performs better compared to the available experimental data [6]. Unlike PGD, the PGC scheme results in a free energy barrier for desorption that depends linearly on the number of carbons, in agreement with experimental data. [6] In addition, with PGC, for NBD-C_4 the free energy barrier for desorption is lower than the free energy barrier for translocation, also in qualitative agreement with the extrapolation of the experimental data. [6] The poorer performance of PGD will be discussed below.

As expected from the similarities between the amphiphiles (that have the same polar fluorophore), and in accordance with our previous equilibrium MD simulations for this homologous series [326], all PMF profiles have a minimum value at a distance of about 1.5 nm from the bilayer center, just beneath the region of the system with largest density (Figure VI.4C). For distances closer to the bilayer center, the PMF raises due to the presence of the translocation barrier, while for distances closer to water the PMF raises due to the transfer of the amphiphile to the water that is a poor solvent for these molecules.

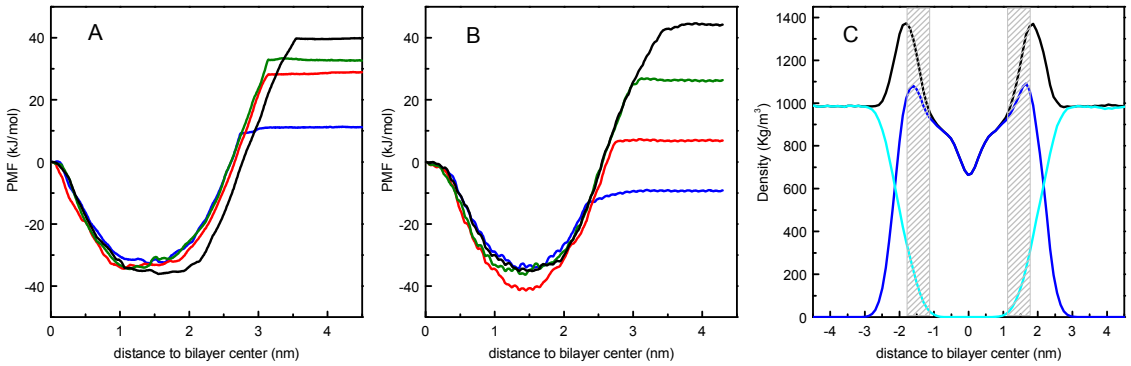

Figure VI.4 – (A) PMF profiles of the NBD-C_n molecules calculated with the PGD method in the CW case. (B) PMF profiles of the NBD-C_n molecules calculated with the PGC method using the CW scheme. PMFs of NBD-C_4, -C_8, -C_{12}, and -C_{16} are depicted as blue, red, green, and black lines, respectively. (C) Density profile for the unperturbed bilayer taken from the system with NBD-C_4 at a distance of 4 nm from the bilayer center. The blue, cyan, and black lines refer to POPC, water, and the whole system, respectively. Grey areas show the region where the free energy is at RT (kJ/mol) from the minimum, using PGC.

Interestingly, none of the PMF profiles show a notable free energy barrier for insertion into the bilayer. The lack of the barrier is clear in the PGD scheme, and the barrier is quite negligible (about 1 kJ/mol or less) in the PGC scheme with the longest amphiphiles, and essentially non-existent with the shorter ones. The absence of the barrier may be interpreted as a diffusion-controlled process, and has been observed in other works. [160, 350, 352] Those results are not in agreement with experimental results that show insertion not to be diffusion controlled, at least for the amphiphiles with longer alkyl chains [6], and predict an energy barrier of the order of 10 kJ/mol for the insertion of NBD-C_{16}. [1] This is a potential issue that is often not discussed in studies reporting PMF profiles, and could be interpreted as resulting from force field issues or insufficient sampling. The latter situation would reflect the fact that amphiphiles restrained at the lipid/water interface are either exclusively in the aqueous phase or inserted in the bilayer without insertion/desorption events of the alkyl chain occurring during the simulation. This problem was not overcome when we extended the simulations to 200 ns, or when additional simulations were carried out at 50 ºC, where again no insertion/desorption events occurred at z = 3 nm. In any case, it should be stressed that, for this homologous series, insertion free energy barriers estimated from experimental kinetic data are considerably lower than the corresponding barriers for both desorption and translocation. [6]

The quantitative comparison between the simulated free energy barriers and those calculated from the experimentally measured rate constants is shown in Figure VI.5. For many cases, the computational results clearly underestimate the free energy barriers for the translocation and desorption of the amphiphiles. However, in agreement with experiments [6], the results obtained with the PGC method show a linear dependence of the desorption free energy barrier on the number of carbons *n*. The slope based on simulations is 4.4 kJ/CH_2, and 3.5 kJ/CH_2 based on experiments. With PGD, the linear dependence is not as clear, in disagreement with the experimental data. Therefore, the comparison indicates that PGC performs better than PGD, mainly for the case of desorption, where the deformation of the membrane-water interface may influence the results.

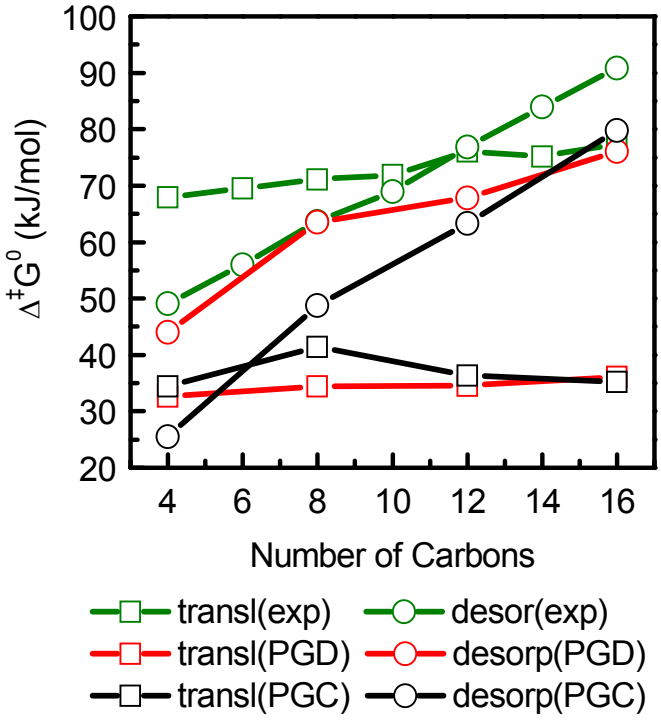

Figure VI.5 – Experimental [6] and calculated (PGD and PGC) free energies $\Delta^{\ddagger}G^{o}$ for the translocation and desorption processes of the amphiphiles in the POPC bilayer.

It should be emphasized that the experimental values shown in Figure VI.5 for the Gibbs activation free energies $\Delta^{\ddagger}G^{o}$ were calculated from the observed rate constants assuming the absolute rate theory. [367] This means that the frequency of conversion from the transition to the final states was taken as $k_B T/h$ (~10^{12} s^{-1}) for all amphiphiles in both processes. The quantitative disagreement between experimental and simulation

results is in part a consequence of the application of this theory, as the actual reaction frequency is likely much lower than this limiting value. [368] Further discussion of this broad topic will be provided in Chapter VII. However, the value of this reaction frequency is expected to depend more on the dynamics of the bilayer than on the solute itself, therefore conserving the linear dependence of the energy barriers. In the remainder of this Chapter, we focus on the amphiphile-induced membrane deformations and the amphiphile's conformational properties, which explain why the PGC and PGD schemes result in different free energy profiles.

VI.2.3 – Membrane Deformations Characterized by Bilayer Thickness

When molecules are transported to or from lipid membranes, it is quite possible that the membrane-water interface next to the adsorption/desorption process is altered. Here we consider how the membrane deformation depends on the scheme (PGC versus PGD) used for the free energy calculation. We gauge membrane thickness defined in terms of the P-P distance (average distance between phosphorous atoms in the opposing leaflets).

The dependence of the P-P distance on the position of the NBD group during umbrella sampling simulations is shown in Figure VI.6. The results indicate that the P-P distance is higher (about 3.9 nm) when the center of mass of the NBD moiety is positioned around ~2.5 nm from the bilayer center, compared to the P-P distance of ~3.8 nm when the NBD moiety is in bulk water at ~4 nm from membrane center (cf. Figure VI.4C). This reflects that as the amphiphile approaches the membrane, some lipids protrude from the membrane towards the amphiphile. The P-P distance in this region is smaller in the simulations using PGC, compared to simulations based on PGD, indicating deformations of the membrane to be more minor with PGC. This is a direct consequence of the local definition of the bilayer's COM. It is worth stressing that the data in Figure VI.6 has been computed over all the lipids in a membrane, thus if the same analysis were carried out for the lipids in the right vicinity of the amphiphile, the perceptible effect would be considerably larger. Figure A.12 (Appendix) highlights this matter in terms of POPCs' phosphate group's density maps for the given NBD transmembrane locations. Inspection of these maps confirms that bilayer deformations are generally more evident for the PGD than for the PGC scheme. Perturbations were

also observed when the amphiphiles were inserted inside the membrane, with a local reduction in P-P distance (Figure A.12B in the Appendix).

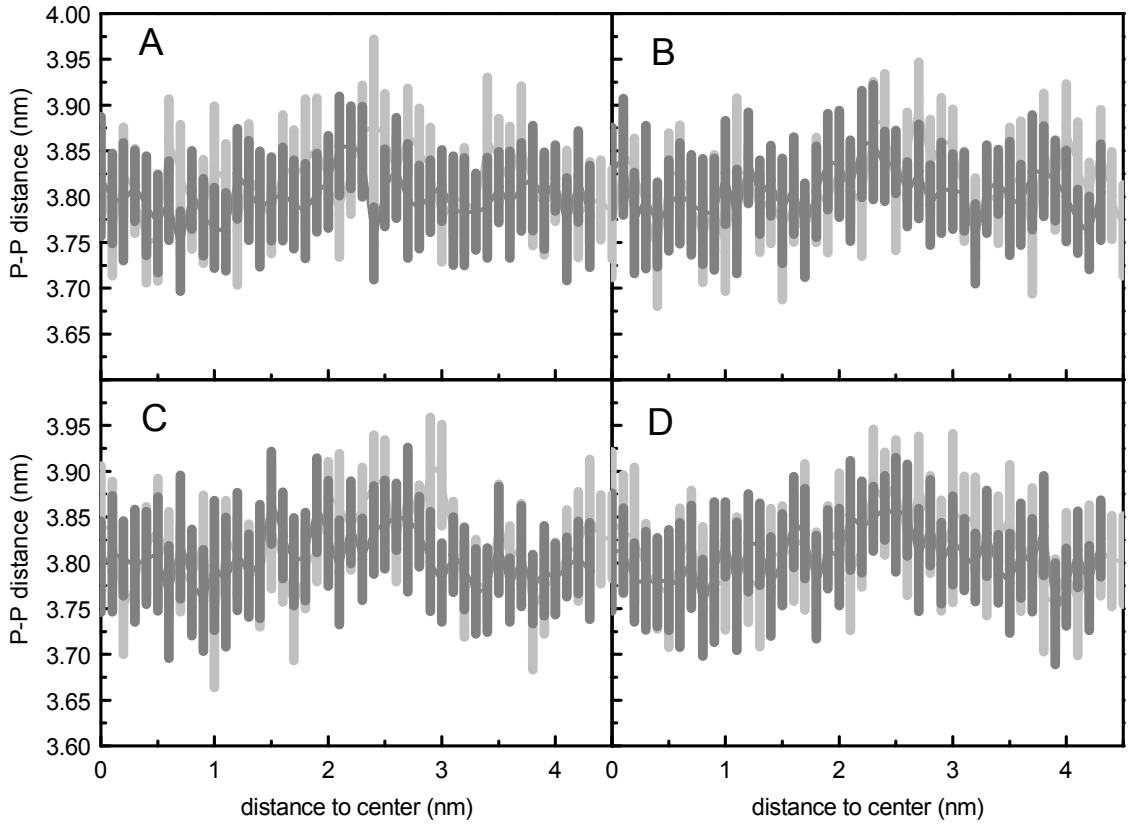

Figure VI.6 – Average membrane thickness in terms of the P-P distance computed over all the lipids in the membrane. Results are given as a function of distance from the center of mass of the NBD moiety to membrane center: (A) NBD-C_4; (B) NBD-C_8; (C) NBD-C_{12}; and (D) NBD-C_{16}. Results are given for the PGD (gray) and PGC (black) schemes. The length of each bar represents the standard deviation of the calculated P-P distance.

VI.2.4 – Conformation of the Amphiphile Markedly Depends on its Location and Sheds Light on the Cause of the Sampling Problem at the Membrane-Water Interface

The transverse distance (along membrane normal direction) between the N1 and Cter atoms (see numbering in Figure IV.1) of the alkyl chain of the amphiphile gives an overall picture of how the amphiphile interacts with the membrane. The average transverse distance between N1 and Cter of each amphiphile, $\langle z \rangle_{N1\text{-}Cter}$, is shown in Figure VI.7 as a function of the constrained location of the fluorophore, z. When the NBD group is close to the center of the bilayer, the distance is minimal, indicating that

the amphiphile's chain samples a wide range of conformations/orientations in the free volume pockets in the membrane plane, in its center. As the distance of the NBD group from the center of the bilayer increases, $\langle z \rangle_{N1\text{-}Cter}$ also increases, highlighting how the chain elongates and interacts more strongly with lipid acyl chains. This continues up to a point where the stretched alkyl chain abruptly leaves the bilayer, resulting in a drop of $\langle z \rangle_{N1\text{-}Cter}$ to a value close to zero. A similar behavior was described previously for phospholipid acyl chains. [160, 350, 352] In accordance with the lower increase in the P-P distance for the simulations with PGC described in the previous subsection, the sudden drop in $\langle z \rangle_{N1\text{-}Cter}$ occurs at shorter distances from the center of the bilayer, indicating that in PGC simulations the alkyl chain leaves the bilayer earlier compared to PGD. This demonstrates the smaller membrane deformations with PGC and highlights why it yields results that are superior compared to those obtained with PGD.

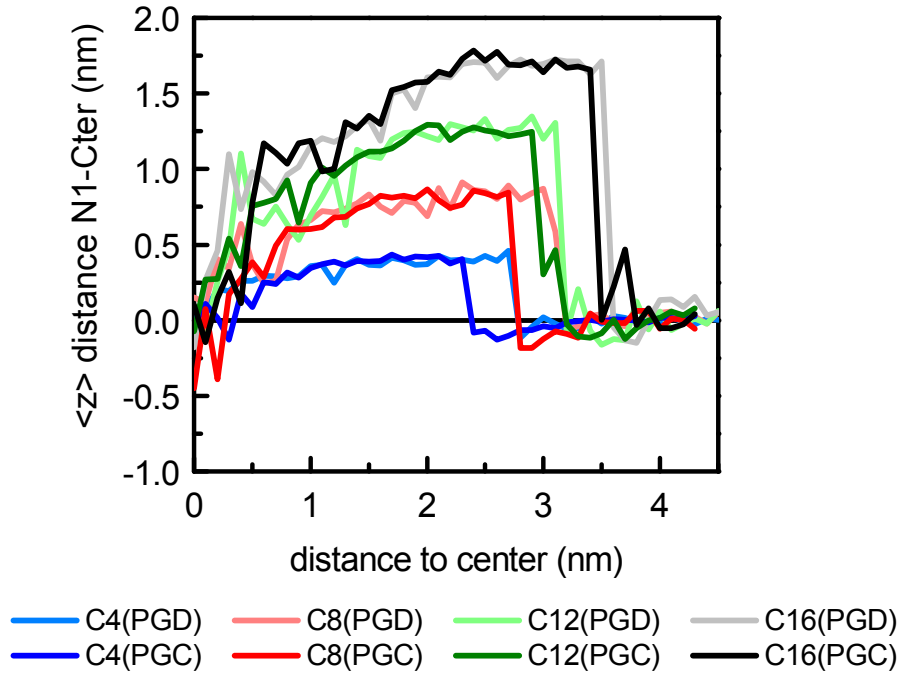

Figure VI.7 – Average distance (along the membrane normal direction) between the N1 and Cter units (see Figure IV.1) of each amphiphile, $\langle z \rangle_{N1\text{-}Cter}$, for varying distance z to the bilayer's center. Here, the membrane-water interface is approximately at 2.5 nm. The distance to center used here corresponds to the distance from the COM of the NBD unit to the local COM of the bilayer (PGC), or to the center of the whole membrane (PGD).

In most of the simulations, once released from the bilayer, the alkyl chain did not re-insert during the remaining simulation time. This lack of desorption/insertion events in a single simulation points to difficulties in sampling at the membrane-water interface,

close to lipid head groups, as discussed above, and gives evidence to the existence of a hidden barrier that precludes the correct sampling of the system.

Several recent studies have focused on the identification and attempt to circumvent hidden energy barriers in the calculation of free energy profiles across lipid bilayers, resulting from degrees of freedom orthogonal to the usual intuitive reaction coordinate *z*. [354, 357, 358, 360, 361] In our study, the possibility of additional barriers due to abrupt transitions in bilayer structure as a function of solute insertion depth, similar to those reported by Neale et al. [354], is largely minimized through the use of the PGC scheme. On the other hand, we analyzed the orientation of the NBD moiety as a function of its transverse location, and verified that it behaves as physically expected (nearly isotropic when $z = 0$, and pointing the polar nitro group in the direction of water near the interface; discussed in detail in next Chapter), therefore ruling out this variable as a possible source of hidden barriers. While we were not able to positively identify the source of the sampling problems, it is clearly linked to the interfacial region of the bilayer and the abovementioned lack of insertion/desorption events within the course of a simulation.

VI.3 – Concluding Remarks

Understanding the interaction of amphiphiles with lipid bilayers is of fundamental importance for their bioavailability and permeation across tight endothelia such as the blood-brain barrier. In this work, we have considered this topic through free energy calculations of lipid-like amphiphiles across a lipid membrane. We have determined the PMF (potential of mean force) profiles for a homologous series of amphiphiles, with a purpose to understand the challenges and limitations in related free energy calculations, and thereby to gain knowledge about appropriate criteria for convergence and sampling to avoid undesired artifacts.

We found that the most challenging environment for free energy computations with long amphiphiles is the membrane-water interface. This is highlighted by our data for PMF calculations, when the amphiphiles in question were first taken from the membrane to the water phase, and second back to the membrane. Despite quite extensive simulation times (beyond 20 microseconds), these two cases resulted in substantial hysteresis at the membrane-water interface. The analysis revealed that the

cause of the hysteresis is the small frequency of insertion/desorption events of the amphiphile's alkyl chain in the membrane interface, and this artifact was most pronounced when the amphiphile was pulled from water to the membrane.

As a second and related topic we observed lipids in a membrane to protrude towards the water phase, when an amphiphile around them was leaving the membrane, or approaching it from the water phase. It turned out that the magnitude of these membrane perturbations depended on how the free energy profile computation was carried out. With the PGD (pull geometry distance) scheme, the alterations in membrane structure were observed to be larger than with the PGC (pull geometry cylinder) method. Also the free energy profiles given by the two schemes were different. The free energy results given by PGC were qualitatively consistent with experimental data, [5, 6] which is encouraging, while the PGD results were not.

The present work provides one with an outlook of the issues that one has to deal with when free energy calculations of more and more complex molecules across membranes are being computed. Yet, these studies are crucial, since the added value of atomistic simulations for fields such as drug discovery and drug transfer can be substantial. As free energy calculations across lipid membrane structures are among the most difficult and computer-intensive simulations in the field, [160, 346-355] it is of prime importance that the people doing them are aware of the possible concerns that could compromise the data in terms of artifacts. Overall, it seems apparent that the membrane-water interface is the region where the greatest care is warranted.

Chapter VII

Free Energy of Interaction of a Homologous Series of NBD-Labeled Fatty Amines with Lipid Bilayers

A Molecular Dynamics Simulation Study of Permeation of Amphiphilic Molecules through Biomembranes

This work is part of a manuscript in preparation.

Hugo A. L. Filipe contributed with the preparation, execution and analysis of the simulations, and also contributed to the writing of the manuscript.

VII.1 – Introduction

Permeation of amphiphilic molecules through biomembranes is a ubiquitous process for a drug to reach its active site. Despite great controversy [146, 147, 149], passive transport of drugs through membranes is the main process of permeation, limiting their penetration into cells and thus being a key step in their availability at the target site. The inability of molecules to cross tight endothelia such as the blood-brain barrier (BBB) is a major drawback for the discovery of new drugs to treat Central Nervous Systems (CNS) disorders, with important social and economical implications. Following this subject, the kinetic and thermodynamic characterization of the interaction of amphiphiles with lipid bilayers is important to predict the interaction of amphiphilic drugs with biological membranes, a property that determines their pharmacokinetics and bioavailability.

This research group has characterized experimentally the kinetics and thermodynamics of the interaction of several amphiphiles with bilayers of different lipid composition [5-7, 74]. From the parameters obtained it is possible to calculate the rate of passive permeation through biological membranes. According to Overton's rule [16], which is the currently accepted model for passive permeation across biomembranes, a positive linear dependence of the permeability coefficient through a cell monolayer with the partition coefficient is predicted, assuming the diffusion through the lipid bilayer as the rate limiting step. For amphiphilic drugs, this diffusion step corresponds to their translocation across the bilayer. Therefore, the determination of the translocation rate constant and the partition coefficient of a drug into a lipid bilayer may be used to determine its rate of passive permeation. This approach has been used recently for the case of the drug chlorpromazine, with good agreement with the permeability coefficients obtained in vitro with cell monolayers [7]. The characterization of different (but structurally related) amphiphiles may lead to the establishment of rules to predict the rate of passive permeation from the structure of the amphiphile.

In addition to permeability, the equilibrium position of specific drugs in target membranes also affects their metabolism. The free-energy profiles of a set of 25 drug-like molecules in a 1,2-dioleoyl-snglycero-3-phosphocholine (DOPC) bilayer showed that the molecules accumulate in the membrane environment, with the majority

lying just below the polar head group region. [369] The positioning of drugs on lipid bilayers might also affect their interaction with drug metabolizing cytochrome P450 (CYP) enzymes [370], and as a consequence affect the metabolism of drugs. Further, the positioning on and affinity to a membrane may play an important role in other biologically significant processes, such as antioxidant inhibition of lipid peroxidation. [371]

The importance of drug-membrane interactions in biology, pharmacology, and medicine has called for extensive research, which is rather challenging due to the complexity of biological membranes. Biological membranes have complex mixtures of lipids and proteins in approximately equal mass proportions [114] the former being determinant for the rate of passive permeation. The most important membrane for drug administration is the plasma membrane, through which drugs must penetrate to reach the internal milieu of target cells and tissues. The most abundant lipids in mammalian membranes are phosphatidylcholines (PC), although phosphatidylserines (PS), phophatidylethanolamines (PE), sphingomyelins (SM), and cholesterol (Chol) are also present. Compositional asymmetry across the two bilayer leaflets is a striking feature in many eukaryotic plasma membranes. [94] Sphingolipids are almost exclusively distributed in the exoplasmic leaflet, whereas the cytoplasmic leaflet contains large amounts of glycerophospholipids, Chol being equilibrated between both. [96] This bilayer asymmetry should be included in the models used to understand and predict the rate of passive permeation of amphiphiles through biological membranes. The use of intact biological membranes is not a good alternative to obtain the rules of passive permeation due to their intrinsic complexity that may generate case specific exceptions only valid for each particular membrane. However, the experimental preparation of stable asymmetric membranes is very difficult, which makes theoretical work very important in this kind of systems.

Molecular Dynamics (MD) is a powerful tool to study the interaction of amphiphiles with lipid bilayers as it gives atomistic details that often cannot be obtained experimentally. Additionally, MD simulations may be performed on asymmetric bilayers as the translocation rate for phospholipids (hours to days) [74] and cholesterol (seconds to minutes) [76] is much longer than the typical time scale used on atomistic simulations, maintaining the lipid asymmetry stable during the sampling process. In fact, MD has proved successful in the simulation of stable asymmetric bilayers, for up

to several hundreds of nanoseconds [372-374]. MD simulations using the Umbrella Sampling (US) [166, 167] technique has been applied to a long list of solutes of increasing size and complexity. [355] The most common application of US to studies of solute interaction in a lipid bilayer uses the displacement of the solute along the bilayer normal as the order parameter to compute the PMF for the insertion of the solute from bulk water to the bilayer center. [163] Such studies can be used to predict the conformations associated with the lowest-energy insertion depths, as well as on-pathway intermediates or transition states for solute insertion/desorption or translocation.

The penetration properties of small molecules on lipid bilayers can be well described by considering the free energy profile along the bilayer normal, also called the potential of mean force (PMF). The PMF of solutes through lipid bilayers measures the free energy cost (ΔG) of moving the solute over a specific distance away from its equilibrium position in the membrane. The free energy minimum on this profile shows the energetically most favorable position of the molecule on the bilayer. For polar molecules, the most probable location is in an energy minimum at the membrane/water interface. As the molecule proceeds further into the lipid bilayer, the hydrophobicity of the membrane environment increases and the free energy rises, and thus the molecule must overcome an energy barrier. The bilayer center penetration barrier is related to the velocity of transfer of the molecule to the other lipid leaflet, and the membrane/water barrier reflects the affinity to the bilayer in comparison to the water environment. In the bilayer center, a local energy minimum is usually also observed [157]. The mass density in this area is slightly lower than in the lipid upper chain region, and the molecules can reside here for some time. [356] The free energy of a molecule in the water environment is constant when the molecule is far from the bilayer. For symmetric lipid bilayers the free energy profile is usually calculated for one leaflet, and the other leaflet is plotted symmetrically. For an asymmetric bilayer, sampling of the reaction path must be done through the entire membrane.

In this Chapter, we propose to calculate the PMF for the interaction of the homologous series fatty amines (NBD-Cn, n=4 to 16) in lipid bilayers with different compositions. We perform the simulations in cholesterol-containing and cholesterol-free membranes regarding the possibility to characterize the permeation process in lipid bilayers that may emulate several biological membranes, namely apical and the basolateral sides of

the plasma membrane and the membranes of internal organelles, respectively. In order to keep simplicity, we mimic the cellular external monolayer with palmitoyl sphingomyelin (SpM):Chol (6:4) and the inner monolayer with 1-palmitoyl-2-oleoyl-sn-glycero-3-phosphocholine (POPC):Chol (1:1). The choice of this lipid composition was discussed in sections III.3 and III.4. The effects of the asymmetric distribution of lipid in membranes are assessed through independent simulations in a SpM:Chol (6:4)/POPC:Chol (1:1) asymmetric bilayer. To gain predictive power for the permeation of amphiphilic drugs, the parameters obtained must be understood in terms of the interactions established. This may be achieved through the calculation of the PMFs and through the detailed analysis of each individual simulation where the amphiphile is restrained at certain bilayer depth.

VII.2 – Results and Discussion

VII.2.1 – Characterization of the Lipid Membranes

The goal of the work developed in this chapter is to provide a description of the pathway of an amphiphilic molecule going through a lipid bilayer, and if possible to relate and compare the energy profiles obtained with the experimental kinetic rate constants available in the literature. This comparison is intended to be done in POPC, POPC:Chol (1:1) and SpM:Chol (6:4) symmetric bilayers and also in asymmetric SpM:Chol (6:4)/POPC:Chol (1:1) bilayers.

To better understand the results obtained it is useful to address the comparison of the pure lipid bilayers, which is done in Table VII.1 for the mean area/lipid and in Figure VII.1 for the order parameter profiles of the lipidic chains. In contrast with the cholesterol-containing bilayers in the liquid ordered state, pure POPC has higher area/lipid and lower order parameters. POPC:Chol and SpM:Chol bilayers show equal average area/lipid and the maximum the order parameter profile is also similar. Regarding the effects of the asymmetry, it does not affect significantly the POPC:Chol leaflet. However, the SpM:Chol side is slightly compressed, showing a somewhat lower area/lipid and higher order parameter than in the symmetric bilayer. This small change is not a translation of the entire order profiles, Figure VII.1, and therefore it should reflect small differences in the orientation of the SpM. Although small, this difference in the SpM:Chol leaflet is probably not related to any effect of the asymmetry itself, but

it should be viewed as an artifact of the small size of the asymmetric bilayer as mentioned in the methods section III.2.2.

Table VII.1 – Areas per lipid of the components of the bilayers.

Area/Lipid (A^2)	POPC	POPC:Chol (1:1)	SpM:Chol (6:4)	SpM:Chol (6:4)/ POPC:Chol(1:1)
Average area	62.5±1.5	38.6±1.2	38.6±1.3	38.0±1.2/ 38.5±1.2
POPC	62.5±1.5	49.9±1.5	-	49.9±1.8
SpM	-	-	46.0±1.5	45.3±1.4
Chol	-	27.4±0.8	26.9±0.9	27.1±0.9

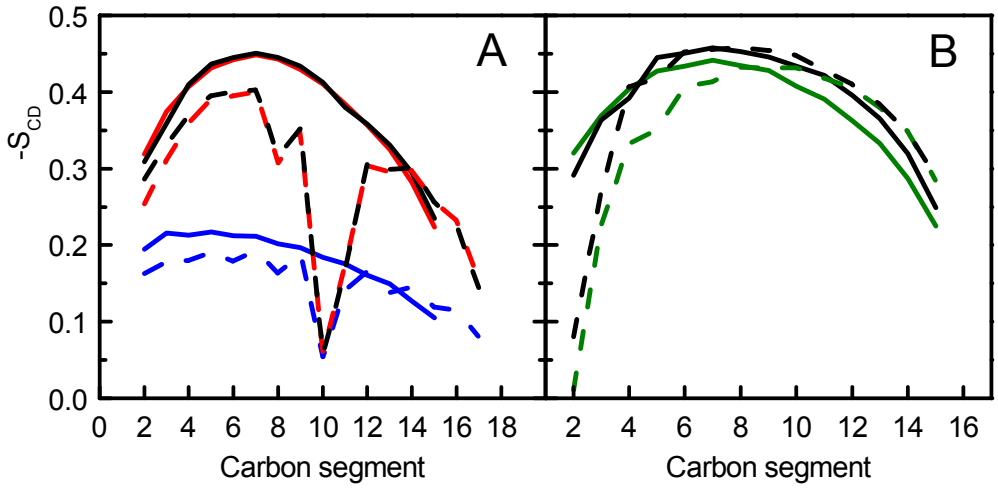

Figure VII.1 – Order parameter of the POPC (A) and SpM (B) chains in the symmetric POPC (blue), POPC:Chol (1:1) (red) and SpM:Chol (6:4) (green) and of the asymmetric SpM:Chol (6:4)/POPC:Chol (1:1) (black) lipid bilayers. Solid lines refer to POPC *sn*-1 and SpM acyl chains, while dashed curves refer to POPC *sn*-2 acyl chain and SpM sphingosine.

VII.2.2 – PMF Profiles for the NBD-Cn Homologous Series through Lipid Membranes

The PMF allows the calculation of free energy differences (ΔG) between distinct positions along a reaction coordinate. However, as described in Chapter VI, sampling problems can preclude a rigorous quantitative evaluation, being the qualitative interpretation of the results much more straightforward. Considering the results of the

preceding Chapter, here all results are given by simulations using the PGC (pull geometry cylinder) scheme. The convergence of the free energy barriers for all amphiphiles, in POPC:Chol (1:1), SpM:Chol (6:4) and POPC:Chol (1:1)/SpM:Chol (6:4) is shown in Figures A.13, A.14 and A.15 (Appendix).

The PMF profiles for the symmetric bilayers are summarized in Figure VII.2, showing in separate plots the PMF of all amphiphiles for each studied bilayer. For better comparison of the data the reference value of the PMF profiles were defined at the equilibrium position (minimum energy location in the reaction coordinate). As expected from the similarities between the amphiphiles (that have the same polar fluorophore), and in accordance with our previous unrestrained MD simulations for this homologous series in POPC membranes (Chapter IV) [326] and in cholesterol-containing membranes (Chapter V), all PMF profiles have a minimum value when the NBD is located at the head group region. For distances closer to the bilayer center, the PMF raises due to the presence of the translocation barrier, while for distances closer to water the PMF raises due to the transfer of the amphiphile to the water that is a poor solvent for these molecules. As shown in equilibrium unrestrained simulations the minimum in the free energy path is located at higher distance from the center of the bilayer for the cholesterol-containing membranes. This is due not only because of the higher membrane thickness but also because the equilibrium position of the NBD group is indeed in a more external position in the membranes with cholesterol (Chapter V). An interesting feature of the PMF profiles in the membranes with cholesterol is the existence of a local minimum at the center of the bilayer. Although the presence of the local minimum was at first quite unexpected, it is indeed present in several PMF profiles of several solutes in cholesterol-containing membranes [351, 352, 375]. Moreover, it is shown experimentally that cholesterol accumulates in the middle of 1,2-diarachidoyl-*sn*-glycero-3-phosphocholine (DAPC) bilayers with high cholesterol fractions [376, 377]. However we should note the considerable difference between the lipid bilayers used in this study compared to DAPC and the different structures of the NBD-Cn amphiphiles and cholesterol. The existence of a local minimum at the bilayer midplane may be justified by the low density in that region of the membrane, which in the cholesterol-containing membranes has an accentuated decrease compared to pure phospholipid bilayers (Figure IV.11 and Figure V.11 in Chapters IV and V, respectively).

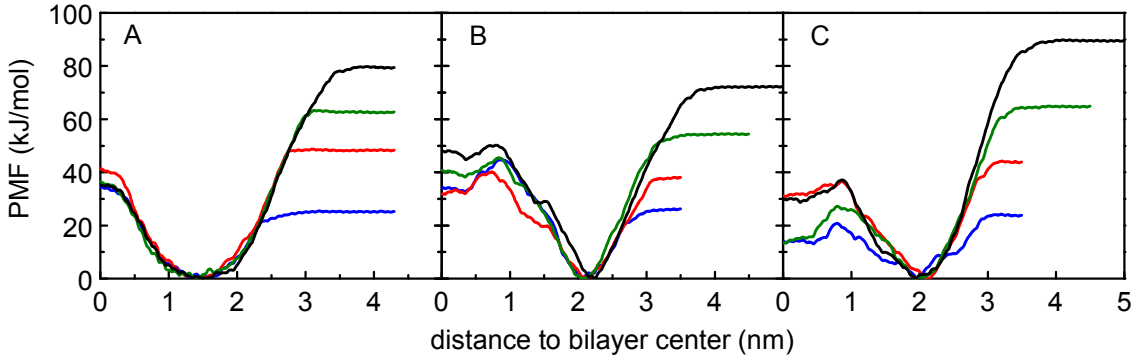

Figure VII.2 – PMF of NBD-C_4 (blue), NBD-C_8 (red), NBD-C_{12} (green) and NBD-C_{16} (black) in POPC (A), POPC:Chol (1:1) (B) and SpM:Chol (6:4) (C) bilayers.

Figure VII.3 shows the energy barriers for the processes of desorption and translocation of each amphiphile in each symmetrical bilayer. The energy barrier for the desorption increases linearly with the number of carbons as expected for interactions dominated by the hydrophobic effect. On the other hand, there is no clear tendency regarding the dependence of the translocation energy barrier on the number of carbons, both for pure POPC and cholesterol-containing bilayers. Variations of the height of the energy barriers at the bilayer center seem to be caused by possible sampling issues in the less dynamic cholesterol-containing systems. The dependence of energy barriers on the number of carbons of the amphiphile's alkyl chain is in agreement with experimental results for the transfer of labeled phospholipids between vesicles [378], and with the kinetics of interaction of these amphiphiles with POPC bilayers [6]. It is clear that for NBD-C_{12} and NBD-C_{16}, the energy barrier for desorption is higher than that for translocation. In opposition, for NBD-C_4 the energy barrier for translocation is higher than for desorption, except in the SpM:Chol bilayer where the PMF is probably affected by poor sampling.

In general the translocation rate constants measured experimentally are smaller in the membranes with cholesterol than in POPC pure bilayers. [74] This seems to be in contradiction with the size of the translocation energy barrier shown in the plots. This may be related to the free energy minimum in membranes with cholesterol, which implies that the amphiphiles need to cross a second barrier to complete the translocation process, thus considerably decreasing the translocation rate constant. Another possible explanation for the slower translocation in spite of the slower energy barriers lays in distinct frequencies of conversion between the transition state and the equilibrium

position (frequency factor in the absolute rate theory). This parameter was evaluated through unrestrained simulations following the NBD group from the center of the bilayer to the equilibrium position. The results are shown in the next section. Considering the computational cost to achieve the task, the characteristic times for POPC were measured. However, for the membranes with cholesterol, this was not possible. The slower dynamics of the cholesterol-containing membranes significantly increases the time needed for the amphiphiles to relax from the center of the bilayer to their equilibrium position, therefore decreasing the translocation rate considerably.

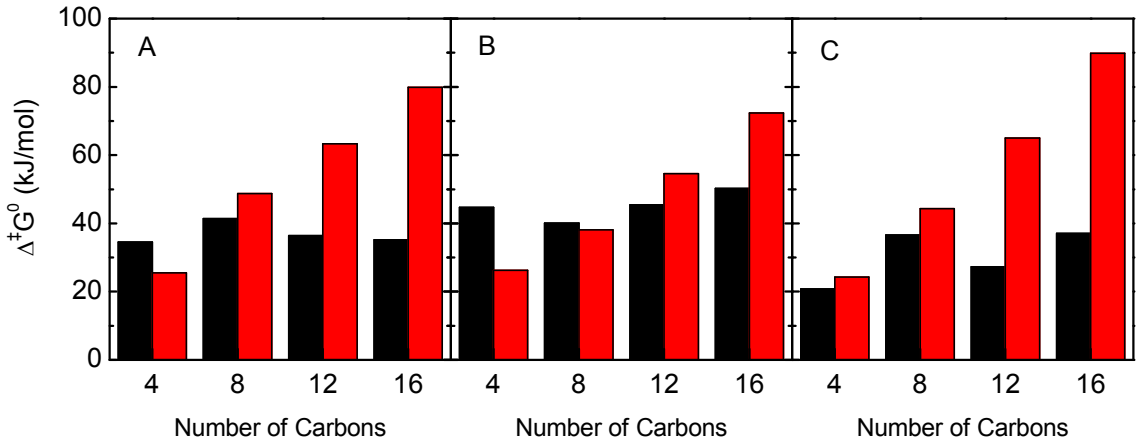

Figure VII.3 – Energy barriers ($\Delta^{\ddagger}G^0$) for the processes of translocation (black) and desorption (red) of each amphiphile in POPC (A), POPC:Chol (1:1) (B) and SpM:Chol (6:4) (C) bilayers.

A goal of this Chapter is to assess the effect of asymmetry of lipid bilayers in the interaction with amphiphilic molecules. Therefore we calculated the free energy profiles of the NBD-C_8, NBD-C_{12} and NBD-C_{16} amphiphiles in the asymmetric bilayer, composed by POPC:Chol (1:1) on one leaflet, and SpM:Chol (6:4) on the other, herein referred as SPC (the profile of NBD-C_4 could not be obtained due to lack of CPU time). Figure VII.4 compares the calculated profiles for the symmetrical and asymmetrical systems. This representation assumes the reference of the PMF in the bilayer center, for better comparison between the profiles in the symmetric systems with the transmembrane profile obtained for the asymmetric system. Although the profiles are not qualitatively dissimilar, the free energy barrier for desorption from the SpM:Chol side in the asymmetrical bilayers seems consistently lower than that determined in the corresponding symmetrical SpM:Chol systems, namely for the longer-chained NBD-C_{12}

and NBD-C_{16} amphiphiles. For the latter two molecules, the free energy profiles from the center to water through the two different leaflets are considerably more similar than could be anticipated by simply superimposing the curves obtained in the symmetric systems. In summary, and considering possible sampling issues detected from the apparent roughness of the profiles, we were not able to found evidence of systematic effects caused by this membrane asymmetry in the interaction with the NBD-Cn homologous series.

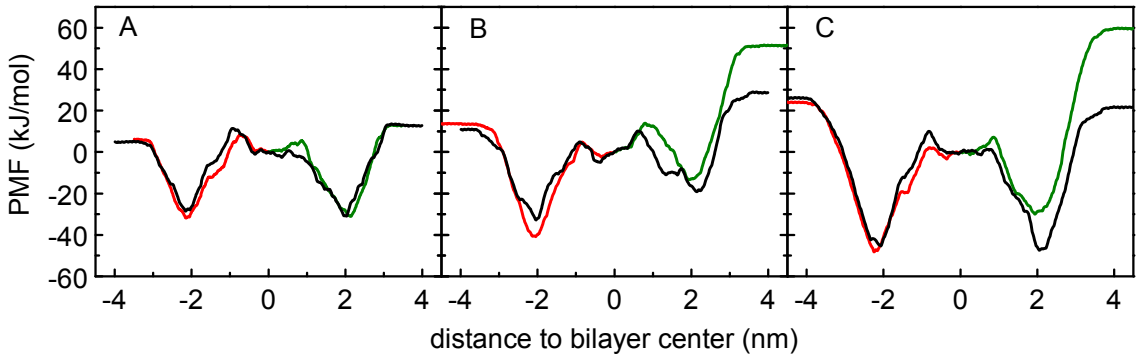

Figure VII.4 – Comparison between the PMF profiles obtained for the POPC:Chol (1:1) (red) and SpM:Chol (6:4) (green) and the PMF profiles obtained for the asymmetric bilayer (black). Data is shown for NBD-C_8 (A), NBD-C_{12} (B) and NBD-C_{16} (C).

In addition to the free energy profiles, several different properties were evaluated from the trajectories of all performed simulations, including variations in NBD orientation, H-bonding and alkyl chain conformation with transverse location of the amphiphile, as well as application of the inhomogeneous solubility-diffusion model [24] to the quantitative evaluation of permeation of the amphiphiles through the studied systems. The kinetics of relaxation of the amphiphiles from the transition states to the equilibrium position in symmetric bilayers was also evaluated.

VII.2.3 – Time Relaxation of the Amphiphiles from the Transition States to the Equilibrium Position: Distance of the NBD Group to the Bilayer Center.

As previously shown in Chapter VII, there are considerable differences between the calculated and the experimentally obtained free energy barriers. It was emphasized that

the experimental values shown for the Gibbs activation free energies $\Delta^{\ddagger}G^{o}$ were calculated from the observed rate constants assuming the absolute rate theory.

The temperature dependence of the kinetic rate constants, *k*, can be described by the Arrhenius equation and/or by the Transition State Theory (TST), also known as absolute-rate theory. Both equations are usually applied to insertion, desorption and translocation rate constants of amphiphilic molecules in lipid bilayers. [3, 6, 71, 136]

The empirical Arrhenius equation relates the activation energy (E_a) with the reaction rate constant *k* as:

$$k = Ae^{-E_a/RT} \tag{VII.1}$$

where *A* is the pre-exponential term, *T* the temperature in kelvin and *R* the universal gas constant. Applying the natural logarithm to both sides of equation (VII.1), its linear form is obtained and E_a can be determined from the slope of ($\ln(k)$ *vs* $1/T$). However, the Arrhenius equation only relates the rate constants with the activation energy. Therefore, to obtain all thermodynamic parameters for the transition state of the amphiphiles in the interaction with lipid bilayers the TST must be used.

The TST was introduced in 1935 by Eyring [367, 379], and Evans and Polanyi [380], for elementary reactions. This theory has three postulates:

i) from the reactants to the products, along a surface potential, the molecule has to overcome a region of high potential energy, which is the transition state. This must be the energy maximum along the reaction coordinate.

ii) it is assumed that there is quasi-equilibrium between the molecules in the transition state and the reactants.

iii) the rate of reaction (*k*) is given by the concentration of molecules in the transition state, multiplied by the frequency at which they pass towards the product state.

The TST was the first theoretical attempt to determine the absolute reaction rates [381]. Eyring, and Evans and Polanyi developed a thermodynamic formulation of the transition state theory,

$$k = \frac{k_B T}{h} e^{-\Delta^{\ddagger}G^{o}/RT} \tag{VII.2}$$

which can be expressed as

$$k = \frac{k_B T}{h} e^{\frac{\Delta^{\ddagger} S^o}{RT}} e^{-\frac{\Delta^{\ddagger} H^o}{RT}} \quad \text{(VII.3)}$$

using

$$\Delta^{\ddagger} G^o = \Delta^{\ddagger} H^o - T\Delta^{\ddagger} S^o \quad \text{(VII.4)},$$

and where $k_B T/h$ is the frequency factor, associated to the conversion from the transition state to the products.

This formulation permits to obtain the enthalpic ($\Delta^{\ddagger}H^0$) and entropic ($T\Delta^{\ddagger}S^0$) contribution from the temperature dependence of the experimental rate constants. Reformulating the equation (VII.3), applying the natural logarithm to both sides, gives:

$$\ln(k) = \ln\left(\frac{k_B T}{h}\right) + \frac{\Delta^{\ddagger} S^{\circ}}{R} - \frac{\Delta^{\ddagger} H^{\circ}}{RT} \quad \text{(VII.5)}.$$

According to equation (VII.5), $\Delta^{\ddagger}H^0$ and $\Delta^{\ddagger}S^0$ can be obtained from the theoretical fit to the dependence ($\ln(k)$ *vs* $1/T$). The Gibbs free energy, $\Delta^{\ddagger}G^0$ is then usually obtained from equation (VII.4).

The quantitative disagreement between experimental and simulated energy barriers is in part a consequence of the use of this theory, as the actual frequency factor is probably much lower than the limiting value $k_B T/h$ (~10^{12} s^{-1}). [368] Regarding the translocation step, we carried out several simulations where the amphiphile is allowed to relax from the transition state (assumed as z = 0 for all bilayers), in an initial position with the NBD group at the center of the bilayer, towards its equilibrium position, as shown in Figure VII.5. Several initial configurations were considered and taken from the trajectory obtained for z = 0, at distinct simulation times. The plots show an average of 40 simulations, and also the equilibrium position, which was determined from unrestrained and US biased simulations. The curves were fitted with a monoexponential function for the first 20 ns of simulation. Although a definite value for the reaction frequency could not be obtained (a statistically significant value would require a much larger number of simulations), the values obtained (shown in Figure VII.6) range from 7.2×10^8 s^{-1} to 3.7×10^8 s^{-1} for NBD-C_4 and NBD-C_{16}, respectively. Therefore, the frequency factor for this transfer is on the order of 10^8 s^{-1}, which is considerably smaller than pre-exponential value used when applying TST (10^{12} s^{-1}), precluding a quantitative comparison between simulation and experiments.

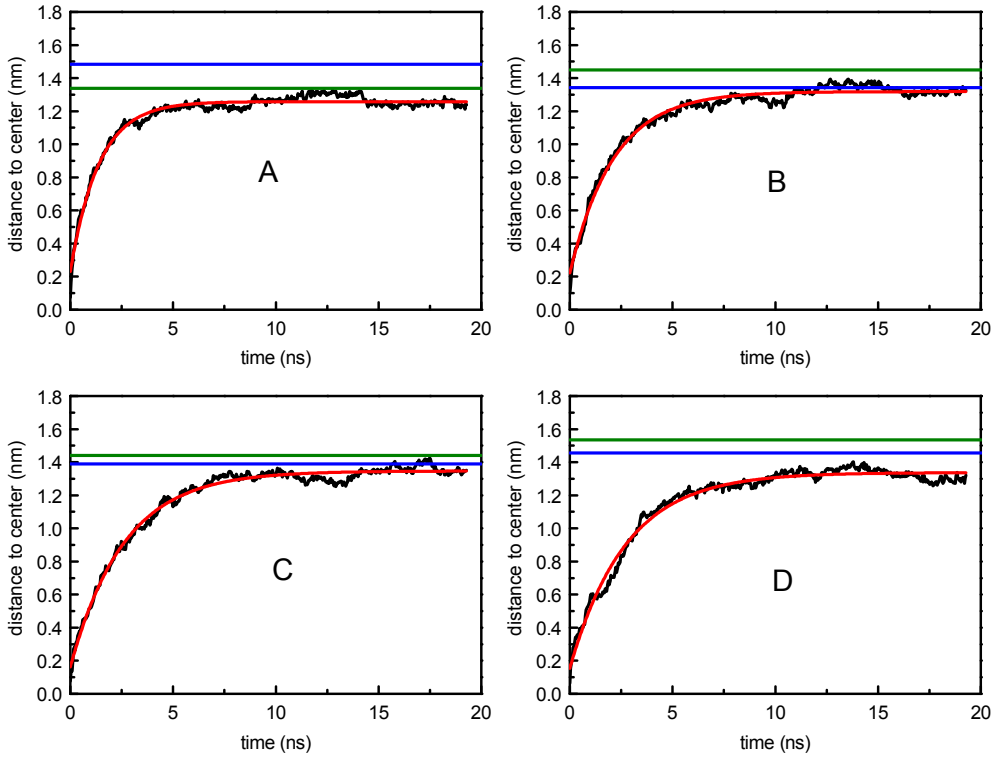

Figure VII.5 – Transfer of the amphiphiles from the center of the bilayer to the equilibrium position evaluated as the z(t) distance from the NBD COM to the bilayer center, in POPC bilayers: (A) NBD-C_4, (B) NBD-C_8, (C) NBD-C_{12}, (D) NBD-C_{16}. NBD equilibrium positions determined from unrestrained simulations (blue) and from PMF minima (green) are shown for comparison.

An alternative approach to estimate the frequency factor is to assume exact matching between the experimental and simulated energy barriers. The conversion factor would then be obtained from equation (VII.6)

$$f = \frac{k}{e^{-\Delta^{\ddagger}G^{0}/RT}} \qquad \text{(VII.6)}$$

where k is the experimental rate constant (s^{-1}), $\Delta^{\ddagger}G^{0}$ the Gibbs free energy of the barrier (kJ/mol) determined from the PMFs, R the gas constant (kJ mol^{-1} K^{-1}) and T the temperature (K). As shown in Figure VII.6, the conversion factors obtained from equation (VII.6), both for translocation or desorption, are lower than those used when applying the TST. For translocation, f is even lower than obtained from the relaxation simulations. This stresses the difficulties in quantitative comparison of the energy barriers obtained from PMF with the experimental rate constants. It was not possible to apply this approach to the cholesterol-containing membranes. However, in those cases, a reaction frequency at least one order of magnitude slower is expected.

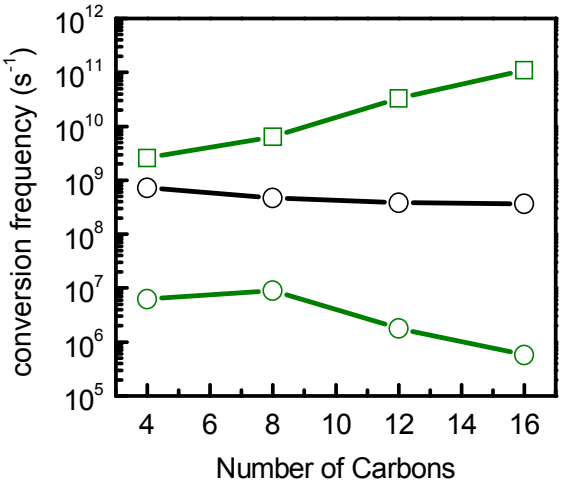

Figure VII.6 – Frequency factor for the transfer of the NBD group from the center of the bilayer to its equilibrium position as function of the number of carbons of the alkyl chain (○), and conversion factors for the deactivation of the transition state of desorption/translocation (□/○) of the amphiphiles, calculated from the ratio between the experimental desorption/translocation rate constant and the energetic component of the absolute rate theory, applying equation (VII.6).

Simulations where the amphiphiles were allowed to relax from the desorption transition state until the equilibrium position were also performed and are shown in Figure VII.7 for POPC (similar data for POPC:Chol and SpM:Chol bilayers are shown in Figures A.16 and A.17 of the Appendix, respectively). To analyze those data for the first 30 ns of simulation a biexponential function was used. A faster reaction frequency, on the order of 10^9 s^{-1}, may be attributed to a first relaxation of the anchored NBD until it approaches a position close to the bilayer interface, a position where this group starts to feel the influence of the lipid head groups, while the slower reaction frequency, on the order of 10^7-10^8 s^{-1}, may be attributed to the penetration of the NBD through the bilayer interface itself. However, these simulations show high variability with cases where the amphiphile completely desorbed to the water (that were discarded) and in some cases the NBD (on average) does not relax exactly to the equilibrium position. In any case the relaxation frequency factors are always lower than the conversion factor used in the TST.

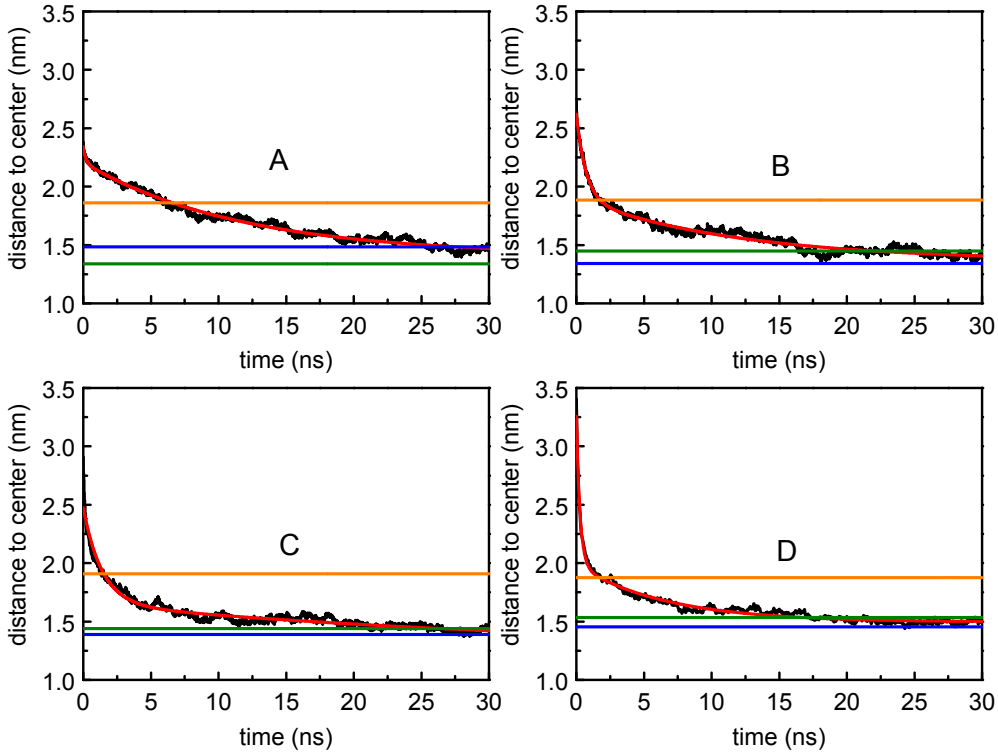

Figure VII.7 – Relaxation of the amphiphiles, NBD-C_4 (A), NBD-C_8 (B), NBD-C_{12} (C) and NBD-C_{16} (D), from the desorption transition state until the equilibrium position in POPC bilayers. The average data of several simulations (black) was fitted with a biexponential function (red). Reference for P atoms (orange), and NBD equilibrium positions determined from unrestrained simulations (blue) and from PMF minima (green) are shown for comparison.

VII.2.4 – Analysis of Several System Properties During the Permeation Process

Despite these difficulties in the quantitative comparison of some simulation results with experimental data, an important feature of MD is its ability to provide atomic detail of the studied systems. In this perspective, it is possible to describe the permeation of solutes in various aspects, and obtain an illustrative view of the process. In this regard the perturbation induced in the bilayer and the behavior of the amphiphiles during the permeation process will be explored.

VII.2.4.1 – Membrane Deformations Characterized by Bilayer Thickness

When molecules are transported to or from lipid membranes, it is quite possible that the membrane/water interface is altered due to the adsorption and desorption processes. The

dependence of the P-P distance on the position of the NBD group is shown in Figure VII.8. Regardless of fluctuations characteristic of calculating bilayer thickness values, it is quite clear that the overall bilayer thickness increases in the order POPC<POPC:Chol (1:1)<SPC<SpM:Chol (6:4). The POPC bilayer is in the liquid disordered phase and has a P-P distance below 4 nm, while the cholesterol-containing membranes, in the liquid ordered state, have P-P values on the order of 4.5 nm, being 4.6 nm for the thickest SpM:Chol membrane.

The results indicate that the pure POPC bilayer is more prone to deformations than the cholesterol-containing membranes. In pure POPC the P-P distance is higher (about 3.9 nm) when the center of mass of the NBD moiety is positioned at ~2.5 nm from the bilayer center, compared to the P-P distance of ~3.8 nm when the NBD moiety is in bulk water at ~4 nm from the membrane center. This reflects the protrusion of some lipids caused by the interaction with the amphiphile. For the cholesterol-containing membranes, such deformation is less evident. It seems however that when the NBD is restrained close to the bilayer midplane, the P-P distance increases. This is probably due to the presence of an additional molecule in the membranes with little free volume.

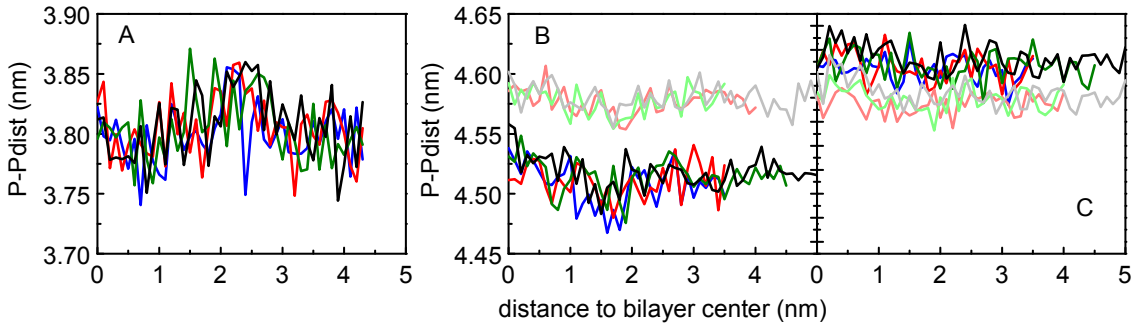

Figure VII.8 – Effect in the bilayer thickness induced by the NBD-Cn amphiphiles, -C_4 (blue), -C_8 (red), -C_{12} (green) and -C_{16} (black), when located at different depths in the bilayer. Data for POPC (A), POPC:Chol (1:1) (B), SpM:Chol (6:4) (C) bilayers and for the asymmetric bilayer (lightened curves in B and C).

VII.2.4.2 – Distance between N1 and Cter Atoms

The distance between the N1 and Cter atoms, $\langle d \rangle_{N1\text{-}Cter}$, (see numbering in Figure V.1) of the alkyl chain of the amphiphile as a function of the location *z* of the fluorophore, Figure VII.9(A, B, C), gives an overall picture of the amphiphile conformation as it

interacts with the membrane. The average transverse distance between N1 and Cter of each amphiphile, $\langle z \rangle_{N1\text{-}Cter}$, is shown in Figure VII.9 (D, E, F), and gives information about the orientation of the alkyl chain. The results are similar for all membranes studied. When the NBD group is close to the center of the bilayer, the distance and the z projection are minimal. As the distance of the NBD group from the center of the bilayer increases, $\langle d \rangle_{N1\text{-}Cter}$ and $\langle z \rangle_{N1\text{-}Cter}$ also increases, highlighting how the chain elongates and interacts more strongly with lipid acyl chains. This continues up to a point where the stretched alkyl chain abruptly leaves the bilayer, resulting in a drop of $\langle d \rangle_{N1\text{-}Cter}$ and $\langle z \rangle_{N1\text{-}Cter}$ to a value close to zero. A similar behavior was described previously for phospholipid acyl chains. [160, 350, 352]

Some differences between cholesterol-free and cholesterol-containing bilayers may be identified. In POPC membranes, the sudden drop in $\langle d \rangle_{N1\text{-}Cter}$ and $\langle z \rangle_{N1\text{-}Cter}$ occurs at shorter distances from the center of the bilayer. This effect is due to the reduced thickness, of the POPC membrane and is slightly attenuated by the membrane deformation. This difference is also attenuated by the number of insertion/desorption events of the alkyl chain in the membrane interface. In the cholesterol-containing membranes, a higher number of such events is observed. This is closely related to membrane deformation. Once inserted, the alkyl chain deforms the POPC membrane, being rarely released. In cholesterol-containing membranes the lack of deformation makes these events more dependent on the alkyl chain movements. More insertion/desorption events contribute to softer decays in the $\langle d \rangle_{N1\text{-}Cter}$ and <z>dist N1-Cter profiles.

It is also relevant to evaluate whether alkyl chains not aligned with the bilayer normal are stretched (tilted with respect to the orientation of the lipid acyl chains) or folded. This may be evaluated from the data in Figure VII.9, comparing $\langle d \rangle_{N1\text{-}Cter}$ (plots A, B, C) with the distance $\langle z \rangle_{N1\text{-}Cter}$ (plots E, F, G). This comparison is an overall measure of the orientation of the alkyl chain in the bilayer. It is evident that i) the alkyl chains are essentially parallel to the bilayer normal between the minimal energy position and the point of desorption, while ii) the alkyl chain samples a wide range of conformations/orientations, in the free volume pockets in the membrane, when the probe is in the center of the bilayer and in the aqueous phase.

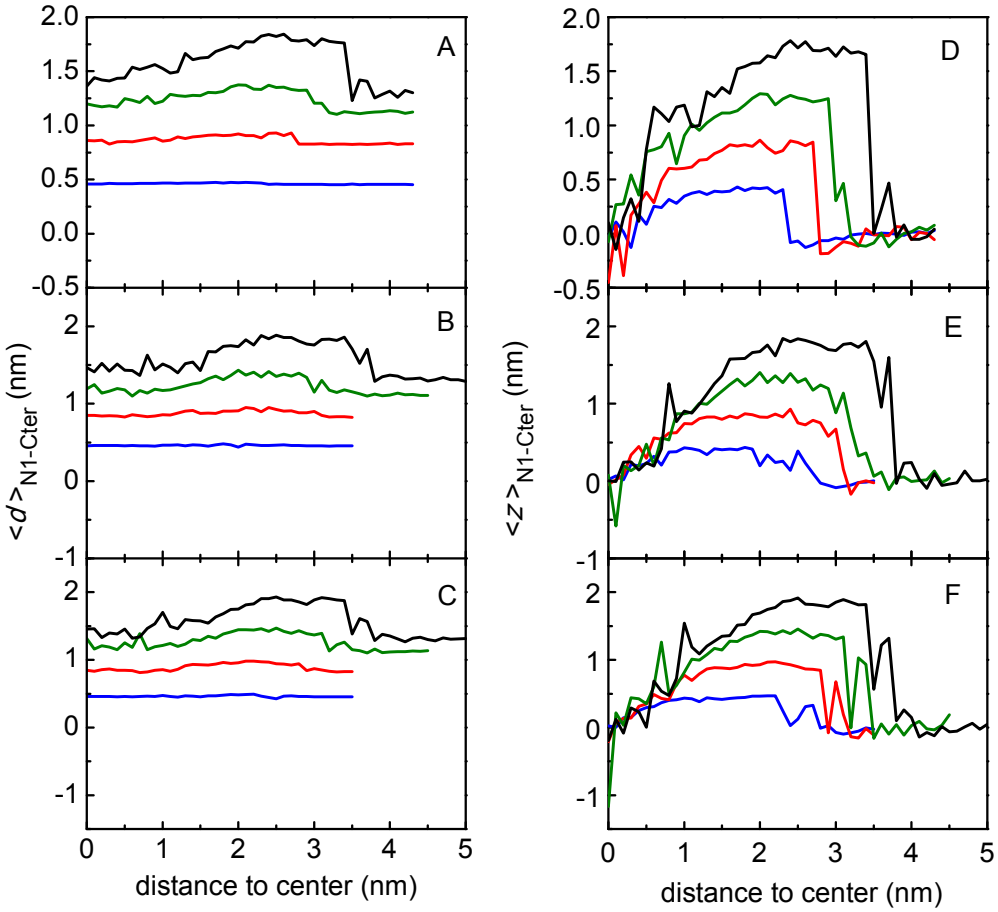

Figure VII.9 – Distance, $\langle d \rangle_{N1\text{-}Cter}$ (A, B, C) and projection in the z axis, $\langle z \rangle_{N1\text{-}Cter}$ (D, E, F) between the atom N1 and the atom Cter of alkyl chain of the amphiphiles, NBD-C_4 (blue), -C_8 (red), -C_{12} (green) and -C_{16} (black), as a function of the restrained position of the NBD group in POPC (A, D), POPC:Chol (1:1) (B, E) and SpM:Chol (6:4) (C, F).

To better clarify this discussion, the distribution of the chain dihedrals was analyzed and is shown in Figure VII.10 for POPC (see Figures A.18 e A.19 in the Appendix for data in POPC:Chol and SpM:Chol). According with the above discussion, the probability of *gauche* conformations (dihedral angles ~60º or ~-60º), here shown for the case of NBD-C_{16} in pure POPC membranes, is higher when the NBD is restrained close to the center of the bilayer and in the water region, Figure VII.10A. When the NBD is restrained close to the equilibrium position and close to the point of desorption of the alkyl chain, the number of *gauche* conformations is minimum. As shown in Figure VII.10B the fraction of *trans* conformations has a maximum around 85% for all amphiphiles close to the desorption point, except for NBD-C_4 due to the poor anchoring of this amphiphile.

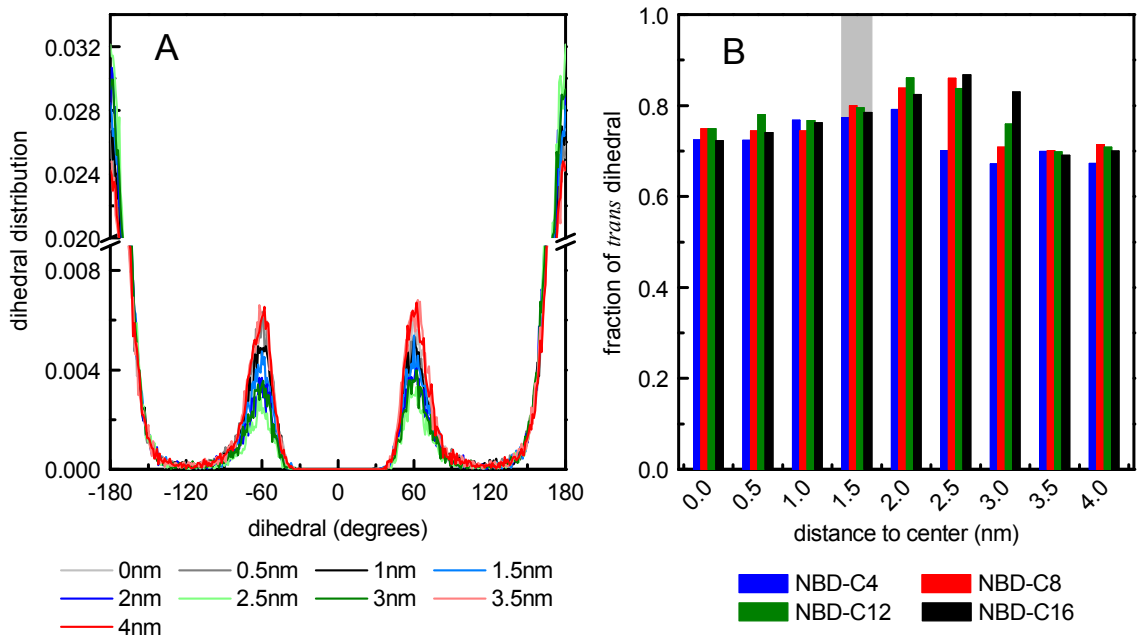

Figure VII.10 – Chain dihedrals in POPC bilayers. (A) distribution of the chain dihedrals of NBD-C_{16}, and (B) fraction of *trans* dihedrals of the alkyl chains of the NBD-C_n amphiphiles, as function of the distance of the NBD to the bilayer center. Gray bar indicates the equilibrium position of the NBD group.

VII.2.4.3 – Hydrogen Bonding

An interesting parameter to characterize the interaction of this homologous series of amphiphiles with lipid membranes is the ability of the NBD group to form hydrogen bonds at different bilayer depths. The NBD fluorophore has an H atom bound to an amino N atom. This nitrogen can act as H-bond donor to water or to phospholipid atoms. On the other hand, there are several O and N atoms in the fluorophore, which can act as H-bond acceptors from water. For the following analysis, an H-bond for a given donor–H–acceptor triad was registered each time the donor–acceptor distance was < 0.35 nm and the H-donor-acceptor angle was $< 30^{\circ}$. Figure VII.11 shows the frequencies of H-bonding between NBD and either water or phospholipid (NBD NH as donor with POPC O, or SpM O/N atoms as acceptor in Figure VII.11(A, D, G, J), NBD NH as donor with H_2O O as acceptor in Figure VII.11(B, E, H, K), and NBD N/O as acceptors with H_2O OH as donor in Figure VII.11(C, F, I, L)). The profile of the H-bonding as a function of the position of the NBD group is similar for all amphiphiles, as expected from their similar structures. For long distances from the center of the bilayer, NBD is surrounded by water, and therefore does not establish hydrogen bonds with the phospholipids. At those positions, H-bonding to the water molecules is

dominant (both considering NBD as donor or acceptor). As the NBD group approaches/inserts into the bilayer, the number of H-bonding of NBD NH with phospholipids' O atoms suddenly increases, becoming essentially permanent during the simulations. Near the equilibrium position of NBD (1 to 2 nm, with a broader region for pure POPC membranes), NBD NH makes preferentially hydrogen bonds with the phospholipids compared to water, in accordance to our previous simulations [264, 326].

For the pure POPC membranes, at an intermediate position between the center of the bilayer and the equilibrium position, some degree of H-bonding between NBD NH and H_2O O is observed, indicating the insertion of some water molecules in the membrane. Additionally, H-bonding between the N and O of NBD and water OH is significant for NBD positioned at all depths in the bilayer (except for z=0). When the NBD is in the center of the bilayer, the frequency of H-bonds, both to water and lipids, decreases significantly, indicating the lack of nearby groups capable of establishing H-bonds. In agreement with the lower deformation of the cholesterol-containing membranes, the probability of NBD to establishing hydrogen bonds with the phospholipids, when located close to the center of the bilayer is reduced. Therefore, in opposition to that reported in MD simulations of phospholipid permeation [160, 350], during the translocation process of the NBD-Cn molecules, a defect in the membrane may be created, but a pore is not formed.

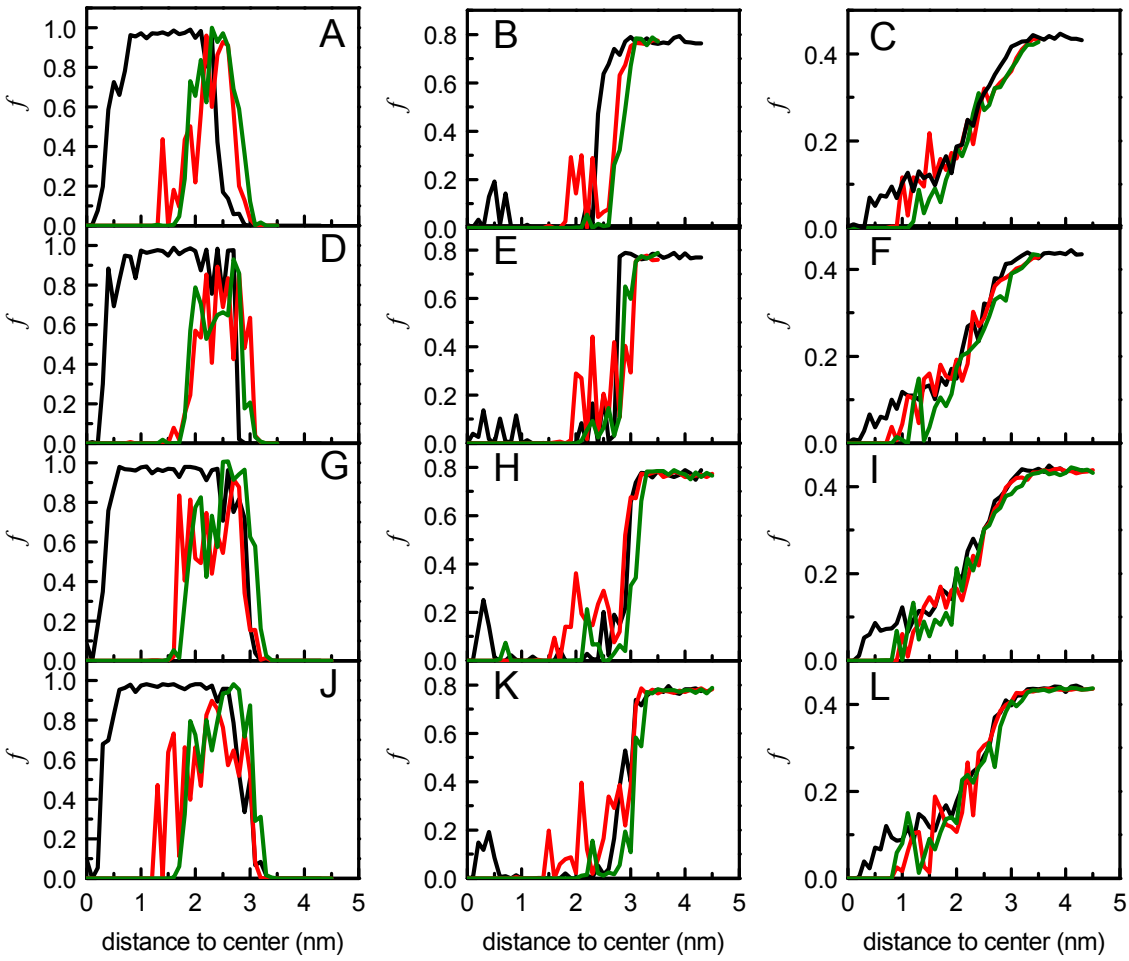

Figure VII.11 – Average fraction of hydrogen bonds over the simulation time. For each amphiphile, NBD-C_4 (A, B, C), NBD-C_8 (D, E, F), NBD-C_{12} (G, H, I), NBD-C_{16} (J, K, L), data is shown for the simulation in POPC (black), POPC:Chol (1:1) (red) and SpM:Chol (6:4) (green). Hydrogen bonds are evaluated between the NBD and the lipid (A, D, G, J) and between the NBD and the water oxygens (B, E, H, K) or water hydrogens (C, F, I, L).

VII.2.4.4 – Orientation of the NBD Group

The dipole moment of amphiphilic molecules like drugs may contribute importantly to their interaction with biomembranes. The NBD group has a dipole moment with an orientation very similar to the orientation of its short axis, defined as a vector between the C10 and the C11 atoms (pointing from the atom C10 to the atom C11, Figure IV.7A). On the other hand, the lipid bilayer has a strong dipole potential that interacts and influences the orientation of molecules/groups with large dipole moments. The dependence of the NBD orientation on the restrain position of the NBD in pure POPC bilayers is shown in Figure VII.12. In this analysis, an orientation of 180º means that the

group NO_2 of the NBD is pointing to the water and an orientation of 0º means that the NO_2 is pointing to the center of the bilayer (or pointing to lower z values).

When the NBD is restrained close to the center of the pure POPC bilayer (0.1 – 0.5 nm) it tends, in all amphiphiles, to orient the NO_2 towards the center of the bilayer, thus presenting angle distributions around 40º. This is in agreement with the orientation of the negative pole of the amphiphile to the positive potential of the bilayer in the center of the bilayer. As the restraint distance increases the hydrophobic chain serves as anchor and tends to orient the molecule according with the canonical orientation of the lipids in the bilayer, thus presenting angle distributions higher than 90º, with angles closer to 180º when the NBD is restrained near the desorption point. For higher distances, when the amphiphiles are in the water, the angle distributions are broad, covering all possibilities without an evident preference. The same behavior is observed at z = 0. This is common to all amphiphiles in all lipid bilayers. The well defined orientation of NBD-C_8 at z = 0 is an exception and should be interpreted as poor sampling.

The orientation of the NBD group when it is located close to the bilayer midplane in the POPC:Chol and SpM:Chol membranes should be considered with caution (see Figures A.20 e A.21 in the Appendix). Although the dipole potential of the POPC:Chol membrane is higher than that of pure POPC, [49] the NBD does not show preferential orientation with the NO_2 group directed to the center of the bilayer. This may be explained by the higher compactness of the POPC:Chol membrane. In order to orient the NO_2 toward the bilayer midplane, the alkyl chain has to visit the dense region of the bilayer in a more or less folded conformation. Therefore, the forces acting on the system will play into a compromise where the NBD is not allowed to correctly orient with the membrane dipole potential. This also seems to happen in SpM:Chol bilayers, for identical reasons.

At higher distances from the bilayer center, quantitative differences can also be found in the orientation of the NBD plane in POPC compared to POPC:Chol and SpM:Chol membranes. As the distance of the NBD to the bilayer center increases, it tends to orient with the NO_2 towards the water, as a consequence of the anchoring effect of the alkyl chain. However, in opposition to the pure POPC membrane where the transition from orientation angles $\leq 90°$ to angles close to 180° evolves smoothly, in the case of cholesterol-containing membranes there is a sharp variation. The need for the NBD to

fit in the higher density of the cholesterol-containing bilayer (with the alkyl chain preferentially in the bilayer midplane) sharply leads to higher angles, closer to 180°.

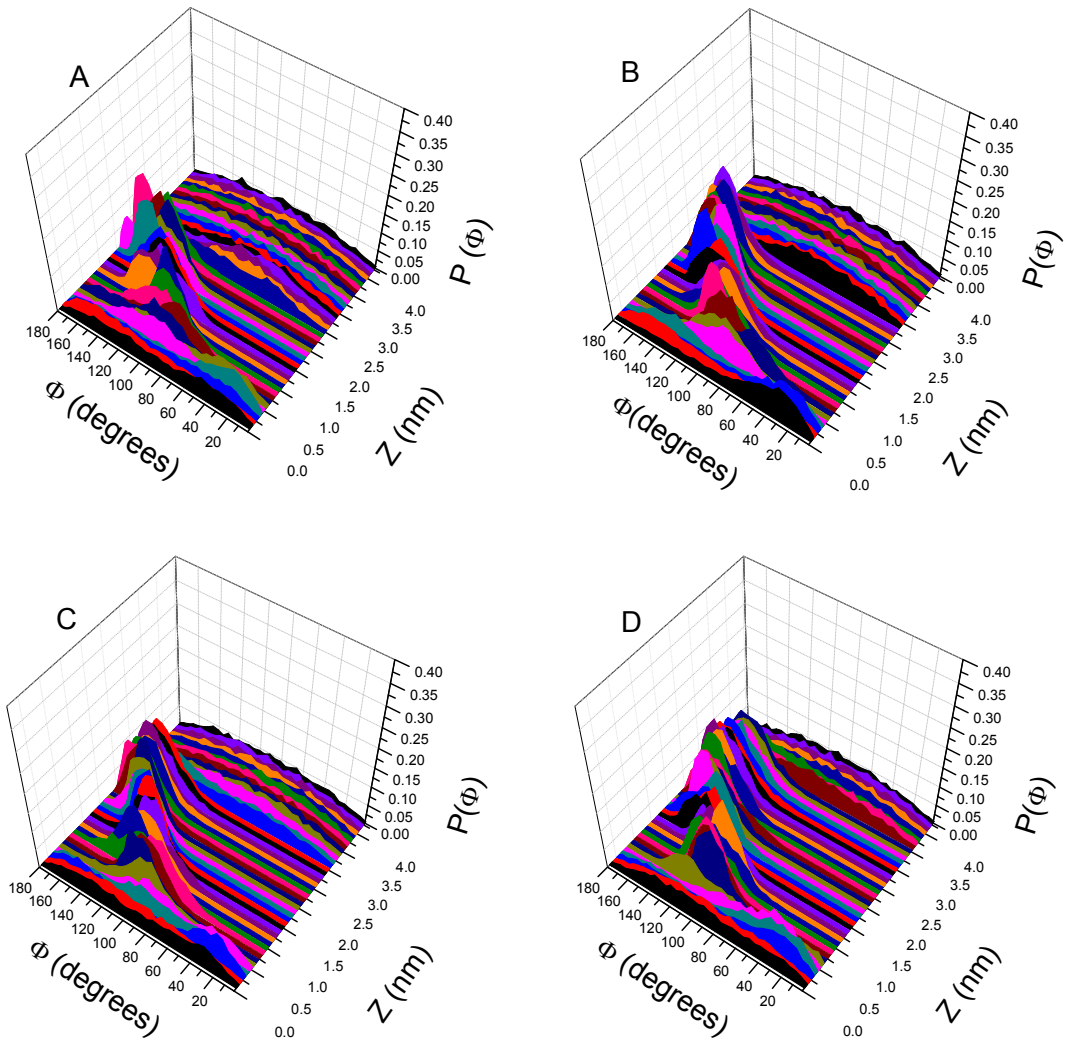

Figure VII.12 – Orientation of the NBD group at different bilayer depths in POPC bilayers for NBD-C_4 (A), NBD-C_8 (B), NBD-C_{12} (C) and NBD-C_{16} (D).

VII.2.5 – Quantitative Evaluation of Permeation of the Amphiphiles through the Lipid Bilayers – Application of the Inhomogeneous Solubility-Diffusion Model

The data obtained from MD simulations allows the calculation of permeability coefficients through lipid membranes. This can be achieved with the application of the so called inhomogeneous solubility-diffusion model [24] (section II.3.2), and has been applied to the permeation of small and more recently also large molecules [382]. To

apply this model, the PMF and the local diffusion rate constants through the lipid membrane are needed. Then, the local resistance to the permeation and the permeability coefficient may be obtained.

In Figure VII.13, we present the free energy, local diffusion coefficient and local resistance profiles for the amphiphiles, NBD-C_4, -C_8, -C_{12} and -C_{16} in the symmetric POPC, POPC:Chol and SpM:Chol bilayers. The PMF profiles were already discussed in previews sections. Regarding the local diffusion coefficients, $D(z)$, the profiles obtained are in accordance with those expected for molecules embedded in a lipid bilayer, and are similar to other profiles found in the literature [157]. Generally, when the molecules are totally in the water, $D(z)$ has values in the order of 10^{-5} cm^2/s as expected from the Stokes-Einstein relation. As the molecules start to interact with the lipid bilayer, $D(z)$ decreases and in general (the noisy profile precludes a clear statement) reaches a minimum at the high density region of the bilayer. At the middle of the bilayer, $D(z)$ increases again due to the lower density of the membrane in that region. Some considerations should be done regarding the calculation of $D(z)$. As a concept, the translocation of lipids and amphiphilic molecules similar to those studied in this work is generally described as a one-step process (hence the process is also called flip-flop). However, the trajectory of a solute through the membrane is continuous. This justifies the calculation of NBD $D(z)$ through the membrane. From the methodological side, the local diffusion coefficient is usually calculated from simulation data where the "constraint method" is applied to obtain the PMF profile, and in other cases, the PMF is obtained using US and then the forces used to calculate $D(z)$ are obtained from independent simulation where the "constraint method" is applied. The main reason behind this procedure is to maintain the solute in a position of absolutely constant free energy, which is difficult to achieve in US simulations where the solute is not constrained, but restrained in a broader sampling window instead. Concerns regarding convergence led us to choose from the beginning of the work the application of US. The simulation time needed to converge the energy profiles in these complicated systems does not allow the subsequent application of the "constraint method" to sample the forces. We therefore chose to calculate $D(z)$ using the forces obtained from our US simulations. The force autocorrelations (FAC) used to calculate $D(z)$ are shown in Figure A.22 (Appendix), from where the data of the first 3 ns were used to calculate the static friction coefficient. Although we realize that not all FAC have completely relaxed,

and in some positions of the reaction coordinate the solute samples an energy region higher than *RT*, the *D*(z) profiles are consistent with those expected for a lipid bilayer, and similar to those found in the literature [157].

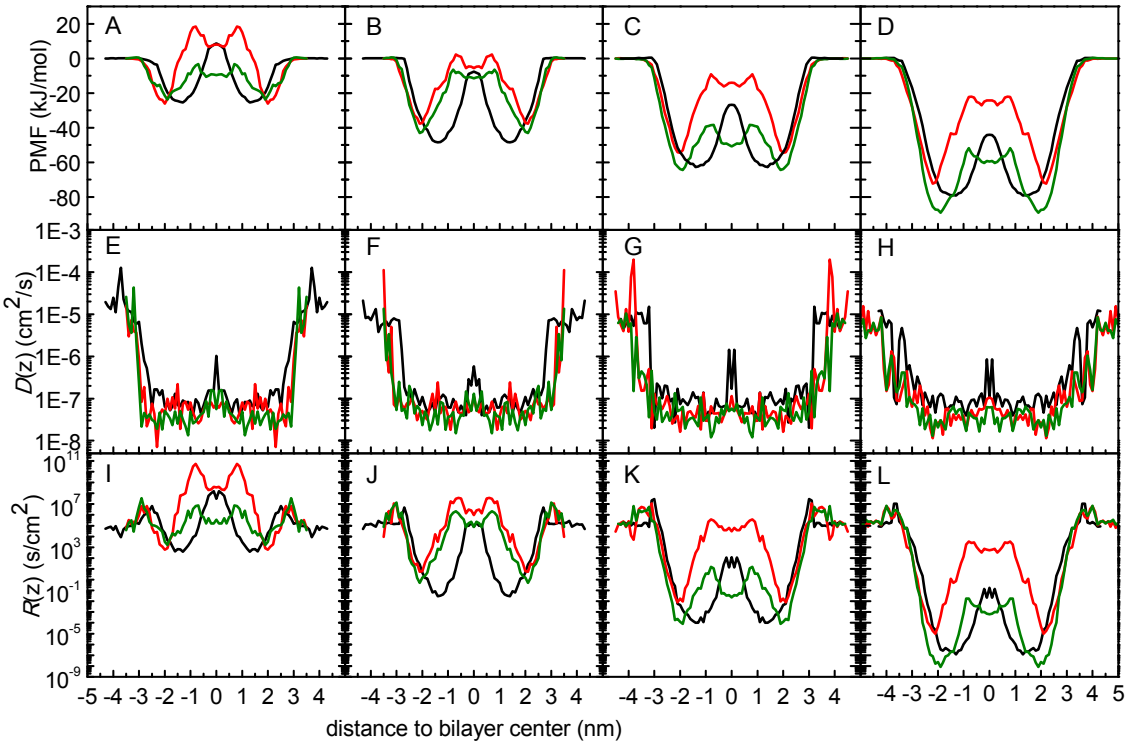

Figure VII.13 – Free energy (A, B, C, D), local diffusion coefficient (E, F, G, H) and local resistance (I, J, K, L) profiles for the amphiphiles NBD-C_4 (A, E, I), NBD-C_8 (B, F, J), NBD-C_{12} (C, G, K) and NBD-C_{16} (D, H, L) in POPC (black), POPC:Chol (1:1) (red) and SpM:Chol (6:4) (green) bilayers.

The analysis performed allowed us to obtain the resistance profile, *R*(*z*), of the amphiphiles through the lipid bilayers. As described in section II.3.2, the permeability coefficient is calculated as the inverse of the resistance to the permeability, obtained as an integration of the local resistances across the membrane. The resistance profiles obtained show a common pattern for all amphiphiles. In accordance with the inhomogeneous solubility-diffusion model equation, for equally spaced sampling windows, the resistance profile depends on the PMF and on the *D*(z) profiles. Starting at the pure water phase, as the NBD approaches the membrane, there is a small resistance barrier. This is mainly governed by a decrease in the local diffusion coefficient as amphiphiles start to interact with the bilayer in a region where the PMF profile is still flat. After a minimum in the resistance profile is achieved roughly at the same depth as the PMF minimum, the resistance rises again towards the bilayer center. Since *D*(z)

does not change significantly in this region of the membrane, the shape of the resistance profile is mainly governed by the PMF profile. Reflecting the symmetry of the bilayer, the resistance decreases again to a minimum and finally shows another barrier before reaching the water phase. In agreement with the PMF profiles in the cholesterol-containing bilayers the resistance profiles also show a minimum in the bilayer midplane.

The membrane regions that most contribute to the permeation resistance may be clearly evaluated plotting the integration of the resistances across the lipid bilayers as shown in Figure VII.14. Three main regions contributing to the resistance to permeation are identified: the entrance to the membrane, the transition through the bilayer midplane and finally the desorption from the bilayer. The relative contribution of each barrier depends on the amphiphile. For the cases where the energy barrier for the translocation is higher than that for desorption, such as NBD-C_4 in all membranes (except in SpM:Chol in our results) and NBD-C_8 in POPC:Chol, the center of the bilayer is the main resistance region. For the other cases where the translocation energy barrier is lower than that for desorption, the main regions contributing to the overall resistance are the water/lipid interfaces.

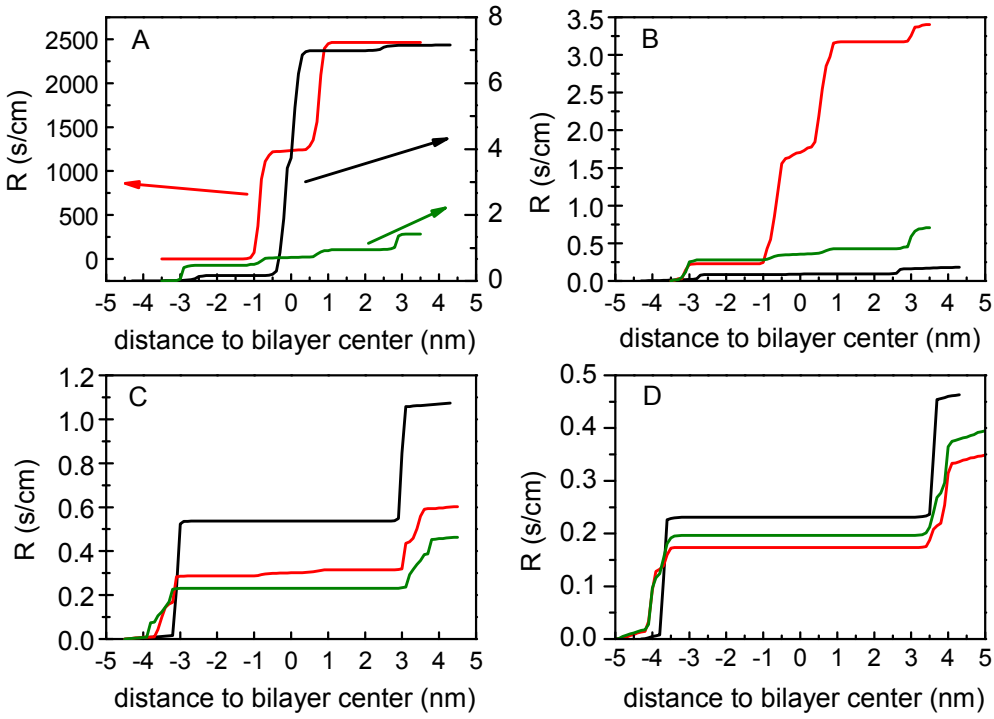

Figure VII.14 – Integration of the profile of the local resistances across the lipid bilayer of POPC (black), POPC:Chol (1:1) (red) and SpM:Chol (6:4) (green), for NBD-C_4 (A), NBD-C_8 (B), NBD-C_{12} (C) and NBD-C_{16} (D).

However, as a consequence of the application of a model that assumes the diffusion through the membrane as the rate limiting step in the permeation process, the resistance at the water/lipid interface is underestimated. The contribution to the resistance barrier at the water/lipid interface is only related with the slower dynamics of the membrane, neglecting the contribution of the desorption process itself, Figure VII.13. This is the reason why the increment in the overall resistance is the same regardless whether the molecule is inserting into or desorbing from the membrane. To apply the non-homogeneous solubility-diffusion model, the PMF value is defined as zero in the water interface. Hence, regions of the membrane where ΔG is negative contribute poorly to the overall resistance, resulting in the underestimation of the permeability resistance.

Since the solubility-diffusion model and the inhomogeneous solubility-diffusion model share the same assumptions, it is not expected that they are able to predict the permeability coefficients correctly, namely for cases where the desorption is the rate limiting step for the permeation. Following this analysis, we have applied the inhomogeneous solubility-diffusion model with a slight modification: instead of the water phase, we have used the equilibrium position as the reference of the PMF profile. In Figure VII.15 the integration of the MD data considering both the zero of the PMF profile in the water or in the minimum energy position is shown in comparison with the permeability coefficient calculated through a cell monolayer mimicked by POPC (a complete discussion of this data will be done in Chapter IX). The modification introduced allows the correct evaluation of the desorption as a rate limiting step in the permeation process, showing smaller permeation coefficients for longer chain amphiphiles as a result of their lower desorption rate constants [6]. Considering the zero of the PMF in the minimum energy position it is possible to qualitatively describe the regimes where the translocation or the desorption are the rate limiting steps. In any case quantitative comparisons are still far from satisfactory.

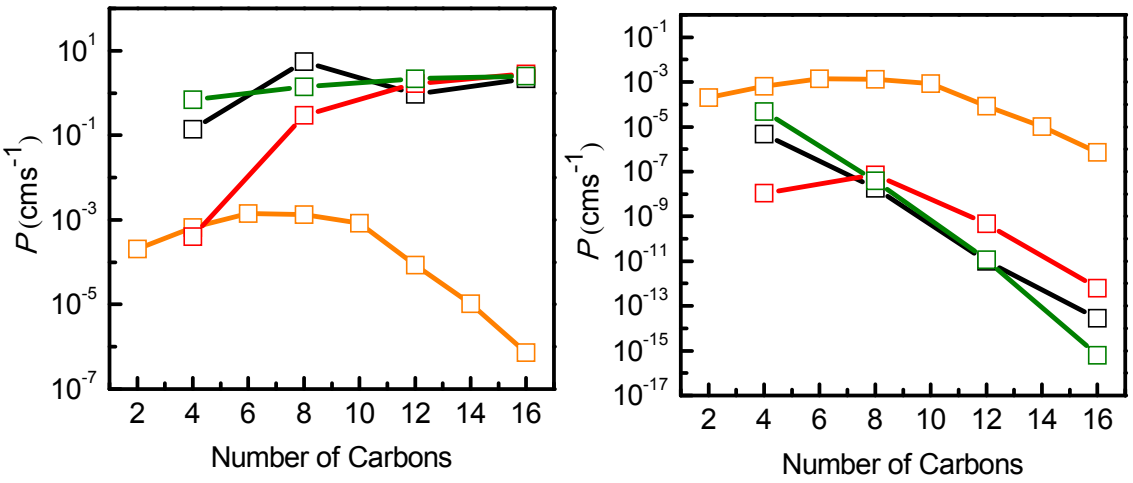

Figure VII.15 – Comparison of permeability coefficients of NBD-Cn, calculated from MD simulations using the inhomogeneous solubility-diffusion model, for POPC (black), POPC:Chol (1:1) (red) and SpM:Chol (6:4) (green), and calculated from the integration of the kinetic rate constants through a cell monolayer mimicked by POPC (Chapter IX) (orange). The application of the inhomogeneous solubility-diffusion model considers the origin of the PMF profiles in the water (A) or in the energy minimum of the system (B).

VII.3 – Concluding Remarks

In this Chapter, we describe the interaction of the homologous series of NBD-Cn amphiphiles with lipid bilayers of different composition, including an asymmetric bilayer. For all studied bilayers, PMF profiles have a minimum value when the NBD is at the head group region, which is more external in cholesterol-containing bilayers in agreement with other simulations and with unpublished experimental results from this research group (see Chapter V). The lack of evidence for systematic effects caused by membrane asymmetry tested in this work supports the idea that experimental studies in symmetric membranes mimicking each leaflet of biological membranes are reasonable approximations for membrane asymmetry.

The direct comparison between experimental and calculated free energy barriers is not straightforward. The frequency of conversion from the free energy barriers to the energy minimum is smaller by orders of magnitude than that calculated in the TST, which precludes a quantitative comparison between simulation and experiments.

The analysis of important system properties at different positions along the reaction coordinate gives an interesting description of bilayers and amphiphiles during the permeation process. Pure POPC, in liquid disordered state, is more prone to

deformations than the cholesterol-containing membranes. Regarding the amphiphiles, the maximal value of the distance between the head group and the Cter is attained near the critical point before desorption, and correlates well with a situation close to an *all-trans* conformation. However, regardless of the environment, the alkyl chains have preference for a stretched conformation. As the NBD approaches/inserts into the bilayer, the probability of H-bonding to the lipid suddenly increases. According with the lower deformation of the cholesterol-containing membranes, the probability of NBD establishing hydrogen bonds with the phospholipid, when deeply located inside the bilayer, is reduced. Inside the POPC membranes, the NBD group tends to orient according with the dipole potential of the lipid bilayer. When deeply restrained in the membrane core, it orients the NO_2 towards the center of the bilayer. As the restraint distance increases, the hydrophobic chain serves as anchor and tends to orient the molecule according with the lipids in the bilayer, presenting angle distributions closer to 180º when the NBD is restrained near the desorption point. In cholesterol enriched membranes NBD is constrained by the high density of the bilayers and is essential parallel to the lipids.

The permeation of the NBD-Cn amphiphiles was quantitatively evaluated by the application of the inhomogeneous solubility-diffusion model, resulting in higher permeability coefficients for more hydrophobic amphiphiles. However, as we will see in Chapter IX, this model underestimates the resistance to the permeation process at the water/lipid interface.

Chapter VIII

Homeostasis of Free Cholesterol in the Blood: a Preliminary Evaluation and Modeling of its Passive Transport

This work was published as: Estronca, L. M. B. B.; Filipe, H. A. L.; Salvador, A.; Moreno, M. J.; Vaz, W. L. C. Homeostasis of Free Cholesterol in the Blood: A Preliminary Evaluation and Modeling of Its Passive Transport. J. Lipid Res. 2014, 55, 1033-1043.

Hugo A. L. Filipe contributed to the development, execution and analysis of the simulations, and had a small contribution to the writing of the manuscript.

VIII.1 – Introduction

The overall homeostasis of cholesterol in humans is very complex [113, 134]. Whereas dietary cholesterol is absorbed only in the intestine, endogenous cholesterol is synthesized in several tissues, the most important being the liver. The liver is also the central clearing-house in cholesterol homeostasis. Lipoprotein nanoparticles play a key role in this process. They are grouped according to their densities and/or protein content as chylomicrons, very low density lipoproteins (VLDL), low density lipoproteins (LDL), and high density lipoproteins (HDL), each group having several subdivisions depending on particle size and chemical composition.

Chylomicrons transport cholesterol that is absorbed in the intestine and esterified with fatty acids to the liver. VLDL are produced in the liver by packing esterified cholesterol together with triglycerides and transport these lipids to peripheral tissues through the blood. Most of the VLDL triglycerides are taken up by muscle and adipose tissues, leaving particles with a cholesteryl ester-rich core (LDL) that are internalized by peripheral cells via endocytosis. Cells get rid of excess free cholesterol by transport across their plasma membranes using transporters of the ATP-binding cassette protein family. Members of this family of transporters, in addition to ejecting free cholesterol from the plasma membrane, also bind lipid-poor Apo-A1 particles (nascent HDL), facilitating direct transfer of the ejected cholesterol to these particles [113, 383, 384]. Free cholesterol in discoid HDL particles is esterified by a serum protein, Lecithin-cholesterol-O-acyl transferase (LCAT). Accumulation of cholesteryl esters in the HDL particles converts these to spherical HDL particles with a non-polar cholesteryl ester core. The cholesteryl esters in the HDL may undergo an exchange (catalyzed by cholesteryl ester transfer protein, CETP) for triglycerides with other lipoproteins in circulation, or removal from circulation by the liver. Cholesterol that reaches the liver is either reprocessed and circulated or converted to bile salts that are eliminated together with some amount of free cholesterol into the intestinal lumen, whence they may be re-absorbed or excreted. The involvement of specific transporters in the transfer of cholesterol between blood compartments and cell membranes is well established. However, the basal rate due to passive exchange processes is unknown, precluding the

evaluation of the relative importance of passive and catalyzed processes in cholesterol homeostasis.

The seminal work of Phillips [135, 385] and Steck [386] has shown that the kinetics of unesterified cholesterol exchange between lipoproteins and erythrocytes *in vitro* is slow and fully compatible with diffusion of cholesterol through the aqueous compartment. In contrast, when cyclodextrin is used as donor or acceptor of cholesterol, the exchange rate is much faster and proceeds via a activation-collision mechanism [76]. The distribution of unesterified cholesterol among the various compartments in the blood was characterized *in vivo* by Schwartz [387]. Cholesterol introduced in the blood, associated with lipoproteins, equilibrated in less than one hour between the distinct lipoprotein classes and it takes several hours to equilibrate with the unesterified cholesterol pool in the erythrocytes. The comparison between the results obtained *in vitro* for the rate of passive exchange between the different blood compartments and the *in vivo* studies could in principle allow the quantitative evaluation of the role of passive processes on the overall exchange of unesterified cholesterol among the various blood compartments. However, this has not yet been possible because some of the relevant rate and equilibrium constants were not known.

In this Chapter we are concerned with the non-catalyzed partitioning of free cholesterol in the blood from a kinetic and thermodynamic perspective. Because free cholesterol lacks spectroscopic signals that might enable the characterization of its association with relevant molecules and aggregates, we have used the fluorescent analogue ergosta-5,7,9(11),22-tetraen-3β-ol (dehydroergosterol, DHE) in our kinetic studies. This cholesterol analogue has been used extensively to simulate cholesterol in cellular trafficking [140]. Previously [139], we characterized the kinetics and thermodynamics of DHE interaction with serum albumin and lipid bilayers that simulate the chemical composition of cell membranes. We now report the relevant kinetic and thermodynamic parameters for association of DHE with the various lipoprotein subclasses, and proceed to use this information and our previous results to simulate its equilibrium distribution among all binding agents present in the blood: albumin, lipoproteins and erythrocyte membranes. We also use the kinetic information to simulate the time course of DHE distribution in the blood assuming that a bolus of free DHE is introduced directly into the blood compartment. We compare both these simulations with the distribution of free cholesterol in the blood observed *in vivo*.

VIII.2 – Results and Discussion

VIII.2.1 – Modeling the Distribution of Free Cholesterol in the Blood

Based on the experimental results shown in Table A.2 of the Appendix and on those obtained previously [139], we developed a kinetic model for the passive distribution of cholesterol in the blood. We consider the following donors/acceptors of free cholesterol: VLDL, LDL, HDL_2 and HDL_3, serum albumin (Alb) and erythrocytes (Ery). In turn, we neglected cholesterol binding by the apical portion of the endothelial cells' membrane because this membrane pool has similar properties to that of erythrocytes and is much smaller (<10 % [281]).

The parameters for the interaction with erythrocytes were derived from the results obtained for the association of DHE with vesicles [139] taking into account the asymmetry of the erythrocyte membrane and the difference in size between the erythrocytes and the lipid vesicles. The erythrocyte membrane has large amounts of sphingomyelin (SpM), phosphatidylcholine (PC) and cholesterol (Chol) with significant amounts of phosphatidylethanolamine (PE), phosphatidylserine (PS) and phosphatidylinositol (PI). [81, 94, 97-101] Most SpM is located in the outer leaflet [81, 94, 98], while cholesterol is distributed in both leaflets [94, 102, 103]. The acyl chains of the inner leaflet lipids have higher unsaturation levels [100], this monolayer being in a more fluid state [81]. Based on this information (see section III.3 for details) we have modeled the outer leaflet of the erythrocyte membrane by a SpM:Chol (6:4) bilayer and the inner leaflet by a POPC:Chol (1:1) bilayer.

We have previously shown that the insertion of DHE into lipid LUVs is not diffusion controlled [139] and therefore the amount of sterol associated with the lipid phase at equilibrium is only dependent on the partition coefficient and on the volume of the lipid phase. Additionally, the rate of insertion/desorption depends only on the total surface between the lipidic and aqueous phases, although the rate constant for insertion must be converted from $M^{-1}\ s^{-1}$ (rate constant *per* LUV particle) to the units of a permeability coefficient ($dm\ s^{-1}$). The rate constant for desorption could be used directly because, being a first order process, it is not dependent on the fragmentation of the phase. However, for consistency within the model, this rate constant was also converted into a permeability coefficient. The equations used to calculate the partition coefficient

between the aqueous phase and the erythrocyte membrane (K_P^{Ery}) and the rate constants for insertion into ($\kappa_+^{Ery^o}$) and desorption from ($\kappa_-^{Ery^o}$) the outer leaflet of the erythrocyte membrane are given below, (see section A.VIII.2 of the Appendix for details)

$$K_P^{Ery} = \frac{K_P^{Ery^o} V_L^{Ery^o} + K_P^{Ery^i} V_L^{Ery^i}}{V_L^{Ery}} = \frac{K_P^{S:C} + K_P^{P:C}}{2} \quad \text{(VIII.1)}$$

$$\kappa_+^{Ery^o} = k_+^{S:C} \frac{1}{\overline{A_{L_V}^o}}; \quad \kappa_-^{Ery^o} = k_-^{S:C}\, h \quad \text{(VIII.2)}$$

where $V_L^{Ery^o}$ and $V_L^{Ery^i}$ are the volumes of the outer and inner leaflet of erythrocyte membrane *per* liter of plasma being $V_L^{Ery} = V_L^{Ery^o} + V_L^{Ery^i} = 2\times\ 1.46\times10^{-3}$ liters; $\overline{A_{L_V}^o}$ is the molar surface area of the LUVs accessible to the external aqueous phase, being given by $4\pi r^2 N_A$ and equal to 1.89×10^{12} dm^2 mol^{-1} for $r = 50$ nm; and h is the thickness of the outer monolayer (taken as 2 nm for all monolayers considered in this model). The equilibrium and kinetic parameters considered were calculated from those obtained experimentally for SpM:Chol (6:4) and POPC:Chol (1:1) LUVs ($K_P^{S:C}$, $k_+^{S:C}$, $k_-^{S:C}$ and $K_P^{P:C}$ respectively).

The equilibrium distribution of cholesterol among the various binding agents in the blood is given by equation (VIII.3), and the time dependence of the concentration of cholesterol in each compartment is given by equation (VIII.4), where A_{Ery}^o is the surface area of the erythrocytes' outer leaflet (7.28×10^4 dm^2 *per* liter of plasma), and f_{Ch^o} is the fraction of cholesterol associated with the erythrocytes that is in the outer leaflet, being equal to $\frac{K_P^{S:C}}{K_P^{P:C} + K_P^{S:C}}$.

Structural properties of the lipoproteins, erythrocytes and relevant lipid bilayers, as well as the concentration of binding agents and number of cholesterol molecules *per* binding agent were taken from the literature [97, 126, 197, 273, 276, 277, 388-390] and are given in Table A.1 in the Appendix. Briefly, the number of unesterified cholesterol molecules *per* lipoprotein was: 3539, 475, 50 and 13 [197] and the concentration of each lipoprotein in the serum was 0.08, 1.5, 4 and 30 μM [273] for VLDL, LDL, HDL_2 and HDL_3, respectively. This leads to 1.6 mM total concentration of free cholesterol in

the plasma, in accordance with the values reported in the literature for plasma that is considered to have a "normal" cholesterol concentration (1.4-1.6 mM) [197, 274, 275]. Adding the unesterified cholesterol present in the erythrocytes (2.7mM) yields 4.3 mM for the total concentration of free cholesterol in the blood ($[\mathrm{Ch}]_\mathrm{T}$).

$$\left[\mathrm{Ch}_{x_i}\right] = \frac{K_{x_i}\left[x_i\right][\mathrm{Ch}]_\mathrm{T}}{1 + K_\mathrm{P}^{\mathrm{Ery}} V_\mathrm{L}^{\mathrm{Ery}} + \sum_i K_{x_i}\left[x_i\right]}$$

$$\left[\mathrm{Ch}_{\mathrm{Ery}}\right] = \frac{K_\mathrm{P}^{\mathrm{Ery}} V_\mathrm{L}^{\mathrm{Ery}}[\mathrm{Ch}]_\mathrm{T}}{1 + K_\mathrm{P}^{\mathrm{Ery}} V_\mathrm{L}^{\mathrm{Ery}} + \sum_i K_{x_i}\left[x_i\right]} \qquad \text{(VIII.3)}$$

for x_i = Alb, HDL_2, HDL_3, LDL and VLDL

$$\frac{d\left[\mathrm{Ch}_{x_i}\right]}{dt} = k_+^{x_i}\left[x_i\right][\mathrm{Ch}]_\mathrm{W} - k_-^{x_i}\left[\mathrm{Ch}_{x_i}\right]$$

$$\frac{d\left[\mathrm{Ch}_\mathrm{W}\right]}{dt} = \sum_i k_-^{x_i}\left[\mathrm{Ch}_{x_i}\right] - \sum_i k_+^{x_i}\left[x_i\right][\mathrm{Ch}]_\mathrm{W}$$

$$+\kappa_-^{\mathrm{Ery^o}} \frac{A_{\mathrm{Ery}}^\mathrm{o}}{V_\mathrm{L}^{\mathrm{Ery^o}}}\left[\mathrm{Ch}_{\mathrm{Ery}}\right] f_{\mathrm{Ch^o}} - \kappa_+^{\mathrm{Ery^o}} \frac{A_{\mathrm{Ery}}^\mathrm{o}}{V_\mathrm{W}}[\mathrm{Ch}]_\mathrm{W} \qquad \text{(VIII.4)}$$

for x_i = Alb, HDL_2, HDL_3, LDL and VLDL

$$\frac{d\left[\mathrm{Ch}_{\mathrm{Ery}}\right]}{dt} = \kappa_+^{\mathrm{Ery^o}} \frac{A_{\mathrm{Ery}}^\mathrm{o}}{V_\mathrm{W}}[\mathrm{Ch}]_\mathrm{W} - \kappa_-^{\mathrm{Ery^o}} \frac{A_{\mathrm{Ery}}^\mathrm{o}}{V_\mathrm{L}^{\mathrm{Ery^o}}}\left[\mathrm{Ch}_{\mathrm{Ery}}\right] f_{\mathrm{Ch^o}}$$

The equilibrium distribution of free cholesterol obtained from equation (VIII.3) was calculated from the rate and equilibrium constants obtained for DHE and is shown in Figure VIII.1, black bars. The agreement with the distribution expected from the literature (light grey bars) is very good for all the compartments considered. The estimated cholesterol content in the erythrocyte is only slightly lower than the experimental reference value (a factor of 0.93), which is a very good agreement given the differences between the LUV and erythrocytes. The predicted cholesterol contents of VLDL are also within the experimental range.

In turn, the model overestimates the free cholesterol content in HDL_3 and underestimates that in HDL_2. However, there is better agreement between predictions and observations as regards the cholesterol contents of HDL as a whole. This suggests that the discrepancies observed for HDL_2 and HDL_3 reflect the difficulty in

experimentally distinguishing HDL subclasses. Indeed, the percentage of HDL_2 particles within HDL lipoproteins ranges from 12 to 40 % depending on the reference considered [273, 391, 392]. The discrepancy between the results obtained for LDL and those reported in the literature may be related to the strong temperature dependence of the association predicted for cholesterol (Table A.2 in the Appendix), whose equilibrium constant increases as temperature decreases. [10] To experimentally quantify the amount of cholesterol in each blood compartment, the various lipoproteins must first be isolated and some exchange of cholesterol between compartments may occur. The extent of this effect depends on the rate of cholesterol equilibration among the various compartments, and on the duration and temperature during the sample processing.

It could be argued that the relative equilibrium constants obtained for the interaction between DHE and the different binding agents in the blood are not representative of the interactions observed for cholesterol. The absence of data in the literature for cholesterol precludes an unequivocal answer to this problem. However, the similar relative equilibrium constants obtained for DHE and the structurally unrelated phospholipid NBD-DMPE [9] gives support to the adequacy of DHE to model the equilibrium distribution of cholesterol, which is structurally very similar.

Another explanation for the deviations encountered between the equilibrium distribution predicted and the amount of unesterified cholesterol experimentally measured in each lipoprotein pool may reflect a non-equilibrium distribution *in vivo*. This will be explored in sections below.

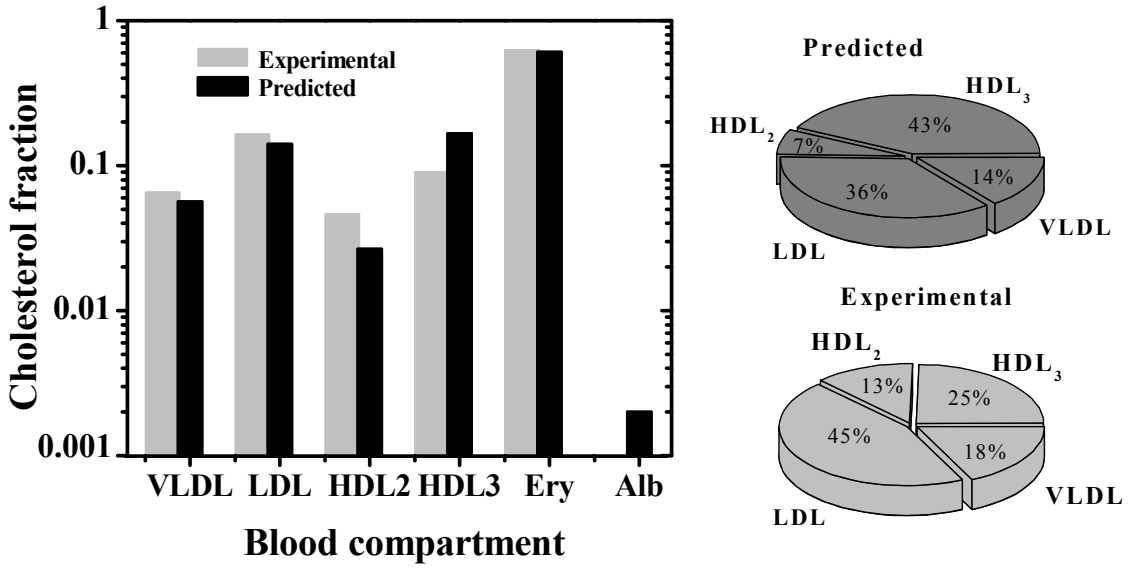

Figure VIII.1 – Equilibrium distribution of unesterified cholesterol in the various blood compartments considered in the model. Reference values in vivo (light grey bar) and equilibrium values predicted from the model using equation (VIII.3) and the parameters obtained in this work for DHE (black bar). Left panel – whole blood (a logarithm scale was used to allow comparison for all blood compartments, dominated by the erythrocytes if a linear scale was used); Right panel – lipoprotein fraction.

VIII.2.2 – Kinetics of Free Cholesterol Distribution among the Blood Compartments, Modeled as DHE

The rate constants obtained in this study and those previously reported by us for the interaction of DHE with lipid bilayers [139] allow the calculation of the rate of exchange of free cholesterol, modeled as DHE, among blood compartments. We have assessed this process by examining the temporal evolution of the concentration of free cholesterol in each blood compartment after addition of a bolus of 10% of total free cholesterol to a given compartment. Addition of the bolus to the aqueous phase (Figure VIII.2A) is the most biologically relevant situation as it reflects the entry of cholesterol into the blood, associated with cholesterol binding proteins or nascent HDL. It also presents the fastest exchange kinetics, generating transient increases in the cholesterol concentration of all blood compartments except erythrocytes (the slowest one).

The instantly imposed excess cholesterol in the aqueous compartment equilibrates among the various blood compartments to reach a new equilibrium, with 10% more cholesterol in each compartment, over several hours. The excess unesterified cholesterol first equilibrates with the binding agents with faster rate of association (HDL_3, HDL_2 and Alb) followed by a redistribution from those pools into the lipoproteins with slower exchange rates (LDL and VLDL). Finally, the excess cholesterol is redistributed between those binding agents and the erythrocytes, the binding agent with the slowest association kinetics (Figure VIII.2A, inset). The maximal excess cholesterol transiently accumulated is largest for the pools with the fastest kinetics (HDL3>HDL2>Alb>LDL>VLDL) and the time at which the concentration peak occurs follows the reverse order. No excess accumulation is observed for the pool with the slowest association kinetics (Ery). The amount of cholesterol in this pool undergoes a mono-exponential increase with a characteristic time of 150 min.

Importantly, these results indicate that the transient accumulation of cholesterol in HDL_2 and HDL_3 is much larger than that observed for LDL and VLDL. Thus, the amount of cholesterol in the small lipoproteins pool is more sensitive to variations in the rates of cholesterol entry into and removal from the blood, while LDL and VLDL are more robust regarding fluctuations in the total concentration of cholesterol.

Once the maximum concentration of cholesterol in a compartment is attained, it slowly decreases towards the value at the new equilibrium condition. For compartments with relatively slow exchange kinetics (LDL and VLDL) this decrease is approximately exponential with a characteristic time similar to that for equilibration with erythrocytes ($\tau \cong$ 150 min; corresponding to 100 to 130 min for 50% dissipation of the excess cholesterol, $t_{1/2}$). The situation is different for the compartments with fast kinetics (HDL_2, HDL_3 and Alb). These show two characteristic times, a faster process due to equilibration with the compartments with intermediate kinetics ($\tau \cong$ 5 min) followed by the final redistribution of cholesterol with the slowest compartment with a characteristic time constant around 150 min. This larger characteristic time is similar to that observed for the exchange of DHE between lipoproteins and cells [393].

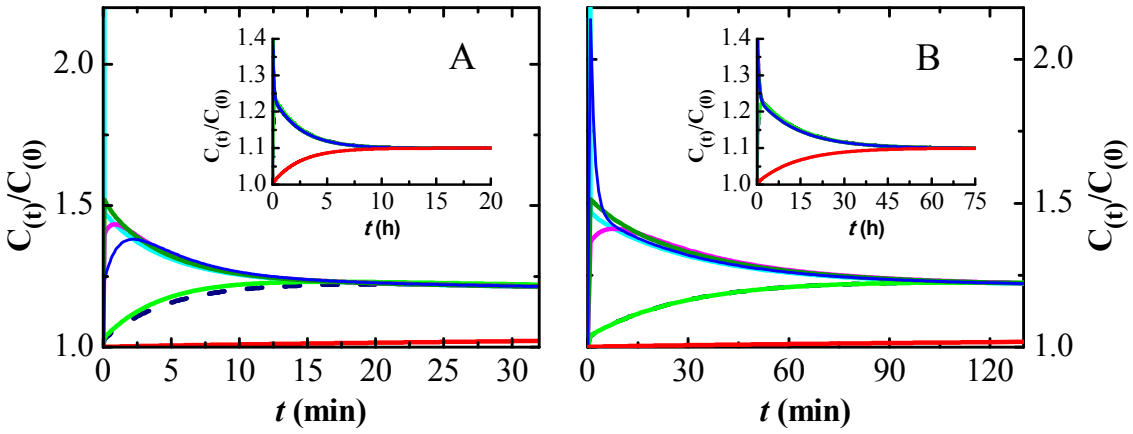

Figure VIII.2 – Simulation results for the kinetics of cholesterol redistribution in the blood at 37 °C after a bolus of 10% total unesterified cholesterol in the aqueous compartment. The rate constants used in the kinetic model were those obtained in this work for DHE (A) or taken from literature for cholesterol [385, 394] (B). Time evolution of the concentration of unesterified cholesterol in the distinct blood compartments: aqueous phase (light blue, □), HDL_3 (green, □), HDL_2 (pink, □), Alb (blue, □), LDL (light green, □), VLDL (dark blue, □) and Erythrocytes (red, □). The *y* axis is the concentration at time *t* , $C_{(t)}$, divided by the equilibrium concentration before the bolus, $C_{(0)}$. The insets show the results obtained at longer simulation times, with the transfer of cholesterol from the lipoproteins to the erythrocytes.

VIII.2.3 – Kinetics of Free Sterol Distribution among the Blood Compartments - Cholesterol *vs* DHE

In the section above we have modeled the temporal evolution of unesterified cholesterol among the blood compartments, after a bolus in a given compartment, using the parameters obtained for DHE. The structure of both sterols is very similar and DHE is commonly used as a model of cholesterol [140]. It can however be argued that the parameters obtained for DHE are not equal to those of cholesterol. In fact, the rates of dissociation of [^{3}H] or [4-^{14}C] cholesterol from lipoproteins and erythrocytes have been reported in the literature and are significantly different from those obtained in this work for DHE: $k_{-}^{HDL_3}$=4.1×10^{-3} s^{-1}, $k_{-}^{HDL_2}$=2.7×10^{-3} s^{-1}, k_{-}^{LDL}=2.7×10^{-4} s^{-1} [385] and k_{-}^{Ery} =1.3×10^{-5} s^{-1} [394]. To model cholesterol homeostasis the association rate constants are also needed (as well as the corresponding equilibrium association constants) but those parameters are not available. To overcome this difficulty we have assumed that the equilibrium association constants of cholesterol are equal to those obtained for DHE. This approximation is acceptable because the amphiphile's molecular properties tend to affect the rate constants of association and dissociation in the same direction [3-6], with

the effects in the equilibrium constants being much less sensitive to those properties. In particular, the relative equilibrium constants for association with different binding agents show very little dependence on the amphiphile's molecular properties for structurally related solutes [3-5, 139]. For this reason, in the following simulations we assumed that the equilibrium association of cholesterol is equal to that obtained for DHE and calculated the association rate constants from the relation $k_+ = K_{eq} k_-$. To further support this assumption, we have performed complementary simulations considering equilibrium constants up to 10 times larger and verified that the results obtained are not significantly affected (less than 1% variations in all output variables considered in this work).

No data is available in the literature for the interaction of cholesterol with the VLDL lipoproteins and with albumin. We have considered that the kinetic and equilibrium parameters for the interaction of cholesterol with the VLDL lipoproteins are equal to those observed for association with LDL, given that the results obtained with DHE are very similar for both lipoprotein classes, and that the parameters for association of cholesterol with albumin are equal to those obtained for DHE.

The results obtained for the temporal evolution of the concentration of free cholesterol in each blood compartment after addition of a bolus of 10% of total free cholesterol to the aqueous phase are given in Figure VIII.2B. As observed for DHE (Figure VIII.2A) the excess cholesterol in the aqueous phase is transiently accumulated in the compartments with fast exchange kinetics (Alb and HDL) followed by an equilibration with the compartments having intermediate kinetics (LDL and VLDL) and, at longer times, with the compartment showing the slowest exchange kinetics (Ery). A larger transient accumulation is now observed for cholesterol associated with Albumin because the kinetics considered for this pool is significantly faster than that of the remaining blood compartments.

In spite of the very good qualitative agreement between the results obtained for the distribution of DHE and cholesterol among the blood compartments, the results show that equilibration of cholesterol directly predicted from the available parameters (Figure VIII.2B) is significantly slower than that observed for DHE (Figure VIII.2A).

VIII.2.4 – Steady State Distribution of Cholesterol among the Blood Compartments – LCAT effect

The small deviations observed between the concentrations of cholesterol in the blood compartments predicted by the equilibrium parameters obtained in this study and those observed *in vivo* may have a physiological underpinning. In fact, the cholesterol distribution among blood components is not expected to be at equilibrium because there is entrance of cholesterol in the system as well as consumption by LCAT in HDL_2 and HDL_3 particles. The differential equations (VIII.4) were modified as follows so as to account for these processes: (a) a term accounting for entry of cholesterol through the aqueous phase was added ($\boldsymbol{v}_+$), representing any route not considered in the model that may release cholesterol with fast kinetics, such as cholesterol binding proteins or nascent HDL particles; and (b) terms accounting for cholesterol consumption in HDL_2 and HDL_3 ($\boldsymbol{k}_{\mathrm{LCAT}}$). The differential equations for HDL_2, HDL_3 and aqueous cholesterol in equations (VIII.4) were therefore substituted by:

$$\frac{d\left[\mathrm{Ch}_{\mathrm{HDL2}}\right]}{dt} = k_+^{\mathrm{HDL2}}\left[\mathrm{HDL2}\right]\left[\mathrm{Ch}\right]_{\mathrm{W}} - k_-^{\mathrm{HDL2}}\left[\mathrm{Ch}_{\mathrm{HDL2}}\right] - \boldsymbol{k}_{\mathrm{LCAT}}\left[\mathrm{Ch}_{\mathrm{HDL2}}\right]$$

$$\frac{d\left[\mathrm{Ch}_{\mathrm{HDL3}}\right]}{dt} = k_+^{\mathrm{HDL3}}\left[\mathrm{HDL3}\right]\left[\mathrm{Ch}\right]_{\mathrm{W}} - k_-^{\mathrm{HDL3}}\left[\mathrm{Ch}_{\mathrm{HDL3}}\right] - \boldsymbol{k}_{\mathrm{LCAT}}\left[\mathrm{Ch}_{\mathrm{HDL3}}\right]$$

$$\frac{d\left[\mathrm{Ch}_{\mathrm{W}}\right]}{dt} = \boldsymbol{v}_+ + \sum_i k_-^{x_i}\left[\mathrm{Ch}_{x_i}\right] - \sum_i k_+^{x_i}\left[x_i\right]\left[\mathrm{Ch}\right]_{\mathrm{W}} \qquad \text{(VIII.5).}$$

$$+\boldsymbol{\kappa}_-^{\mathrm{Ery^o}}\frac{A_{\mathrm{Ery}}^{\mathrm{o}}}{V_{\mathrm{L}}^{\mathrm{Ery^o}}}\left[\mathrm{Ch}_{\mathrm{Ery}}\right]f_{\mathrm{Ch^o}} - \boldsymbol{\kappa}_+^{\mathrm{Ery^o}}\frac{A_{\mathrm{Ery}}^{\mathrm{o}}}{V_{\mathrm{W}}}\left[\mathrm{Ch}\right]_{\mathrm{W}}$$

for x_i = Alb, HDL_2, HDL_3, LDL and VLDL

We solved the system for steady state and adjusted the rate of cholesterol influx ($\boldsymbol{v}_+$) such that the cholesterol concentration in LDL matched the experimental value. The agreement between the computed steady state cholesterol distribution and the experimentally found distribution is remarkable both when cholesterol distribution is modeled by DHE and when the literature data for the dissociation of cholesterol from the blood compartments is considered (Figure VIII.3).

In spite of the good agreement obtained, the rate of cholesterol turnover in the blood required to meet the imposed condition was unrealistically high: $v_+ = 7.5\times10^{-6}$ M s^{-1} and $k_{\mathrm{LCAT}} = 1.3\times10^{-2}$ s^{-1} when the kinetic parameters obtained with DHE are considered, and

v_+ =9.9×10^{-7} M s^{-1} and k_{LCAT}=1.8×10^{-3} s^{-1} considering the dissociation rate constants for cholesterol taken from literature [385, 394], whereas the usually accepted value is v_+ =1.1×10^{-8} M s^{-1} [395]. This indicates that this process cannot be the main explanation for the differences observed. The turnover of unesterified cholesterol in the blood at the physiological rate causes only modest (<10%) changes relative to the equilibrium distribution. It decreases the discrepancies observed between the predicted and experimentally found fractions of cholesterol in the various lipoproteins, but does not eliminate them.

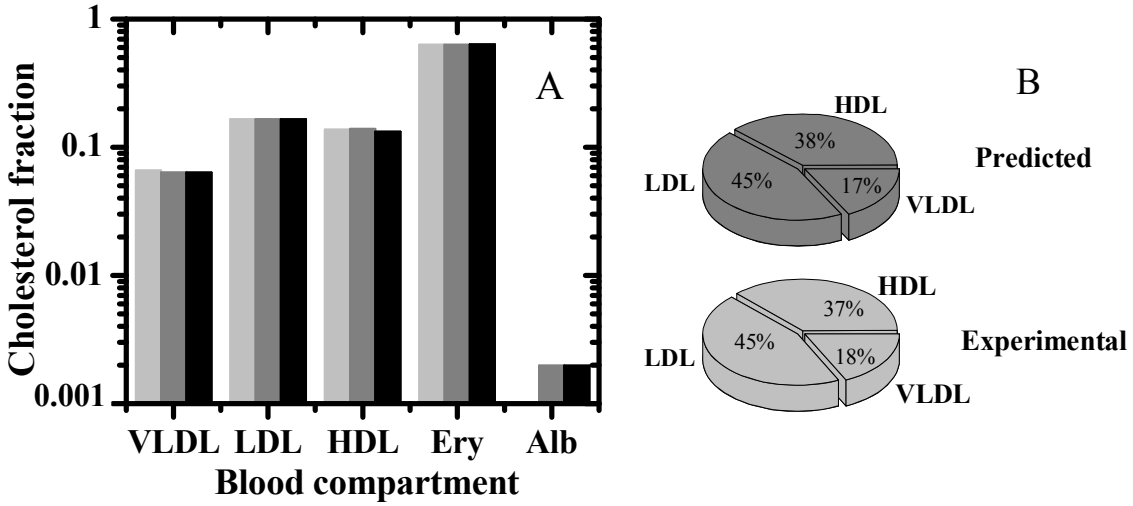

Figure VIII.3 – Distribution of unesterified cholesterol in the various blood compartments considered in the model. Reference values *in vivo* (light grey) and steady state values predicted from the model using equations (VIII.5) for cholesterol in the aqueous phase and in HDL, and equations in (VIII.4) for the remaining compartments, considering the rate constants obtained in this work for DHE (grey) and those taken from literature for cholesterol [385, 394] (black). The results for the whole blood are shown in the left panel and the distribution of cholesterol among the lipoproteins is given in the right panel. The steady-state distribution in the lipoproteins obtained from the kinetic data of Chol deviate less than 1% from those measured experimentally (lower panel) or calculated from DHE rate constants (upper panel). The steady state is attained with v_+ =7.5×10^{-6} M s^{-1}, k_{LCAT}=1.3×10^{-2} s^{-1} and v_+ =9.9×10^{-7} M s^{-1}, k_{LCAT} =1.8×10^{-3} s^{-1}, when the dissociation rate constants of DHE and cholesterol are used, respectively.

VIII.2.5 – Cholesterol Homeostasis in the Blood – Passive *vs* Active Transport

The homeostasis of unesterified cholesterol *in vivo* has been studied by Schwartz and co-workers [387] and the comparison between those results and the ones predicted by the kinetic model developed in this work may elucidate the relative importance of passive and active processes. The initial concentrations of cholesterol considered for each blood compartment were given by the steady state solution of the set of differential equations (VIII.5) with the physiologic rate of cholesterol entry in the system, $v_+ = 1.1\times10^{-8}$ M s^{-1} [395], and the corresponding rate constant for LCAT activity, $k_{LCAT} = 1.4\times10^{-5}$ s^{-1}. To simulate the conditions followed in the *in vivo* study, we have then defined three distinct subsets of unesterified cholesterol (Ch, Chα and Chβ, with Ch_T being the sum of all subsets of cholesterol). The cholesterol associated with HDL was identified as Chα, that of LDL *and* VLDL was identified as Chβ and the remaining cholesterol was maintained as Ch. The simulation was started and the exchange of Ch, Chα and Chβ among the distinct blood compartments was followed. The results obtained for the enrichment of Chα and Chβ in the distinct blood compartments are shown in Figure VIII.4, using the kinetic parameters obtained in this work for DHE (Figure VIII.4A and B) and those taken from literature for cholesterol (Figure VIII.4C and D).

As observed in the *in vivo* study [387], unesterified cholesterol associated with the lipoproteins equilibrates rapidly: after 90 minutes the enrichment of cholesterol within the lipoprotein classes is undistinguishable and independent on its location at the beginning of the simulation (Figure VIII.4C and D). This equilibration time is reduced to 15 minutes when the rate constants predicted from DHE are used (Figure VIII.4A and B). The equilibration time within the lipoproteins pool was estimated as 30 minutes in the *in vivo* study, clearly showing that passive processes have a very significant contribution for the overall rate of exchange.

A similar situation is observed for the exchange of cholesterol between the lipoproteins and the erythrocytes. The *in vivo* study shows that the enrichment of cholesterol in the erythrocytes and in the lipoproteins converges at around 400-600 minutes while the passive processes described by this kinetic model predict convergence at 1500 minutes (450 for predictions based on DHE, Figure VIII.4A and B). This kinetic model is also

able to distinguish between the sources of unesterified cholesterol in the beginning of the equilibration with the erythrocytes. The time at which 1 % enrichment of Chα (from HDL) in the erythrocytes is attained is half the time required for 1 % enrichment in Chβ (from LDL and VLDL). A faster partial equilibration between cholesterol from the HDL pool and the erythrocytes was also observed in the *in vivo* study, as well as when albumin is used as the cholesterol donor. This clearly indicates that passive exchange processes mediated by cholesterol in the aqueous phase (the enrichment of which depends directly on the dissociation rate constant from the donor pool) are significant even for the exchange between the lipoproteins and the erythrocytes.

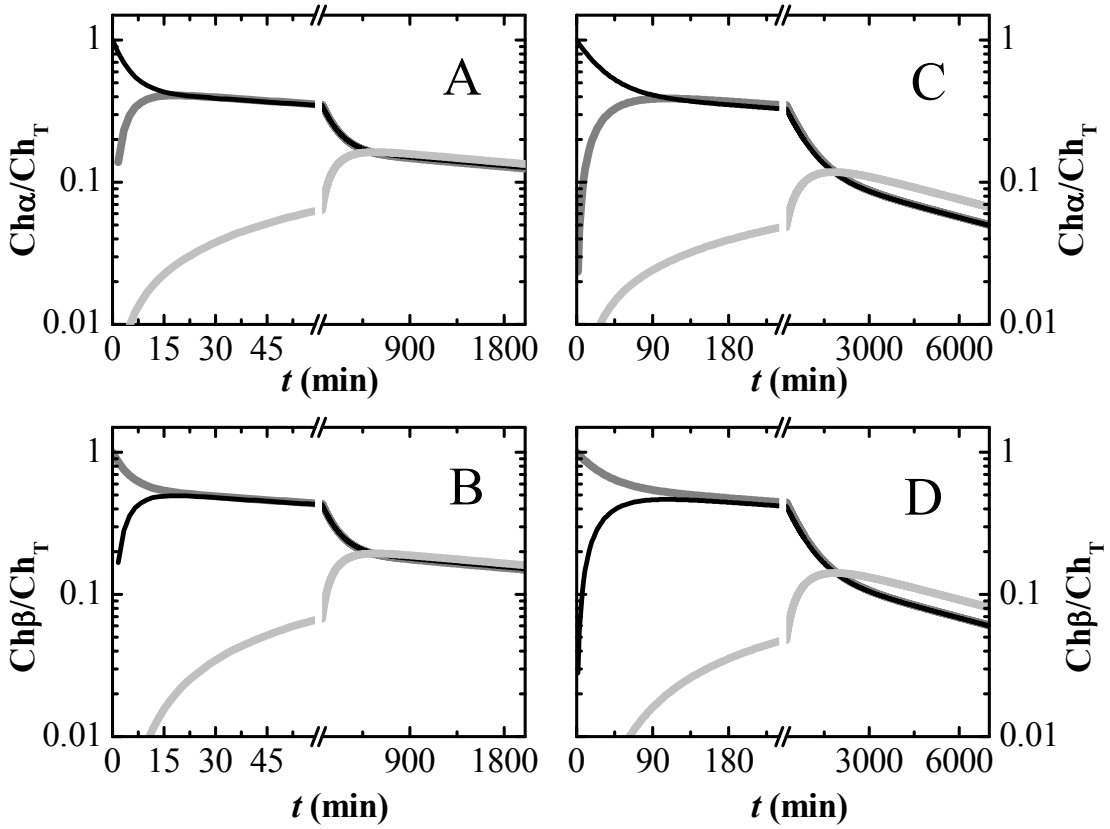

Figure VIII.4 – Simulation of the homeostasis of unesterified cholesterol in the blood at 37 °C due to passive processes. The rate constants obtained in this work for DHE are used in plot A and B, while desorption rate constants taken from literature for cholesterol [385, 394] are used in plot C and D. The concentrations of unesterified cholesterol in the distinct pools were obtained from the steady state solution of the kinetic scheme developed in this work, equations (VIII.4) and (VIII.5) for a rate of cholesterol entry in the blood equal to 1.1×10^{-8} M s^{-1}. At t=0 the unesterified cholesterol in the HDL fraction was replaced by Chα and that in LDL *and* VLDL fractions was replaced by Chβ. The relative enrichment in Chα (plot A and C) and Chβ (plot B and D) in the distinct blood compartments was followed over time for HDL (black, □), LDL and VLDL (grey, □) and the erythrocytes (light grey, □).

VIII.2.6 – Limitations of This Study

This work highlights important features of cholesterol homeostasis in the blood and is a significant contribution to this topic. It has however several limitations that should be understood to guide and improve future work. One should first consider the use of a single individual as donor of the lipoprotein fractions. This was a necessary condition in this work because the characteristics of the distinct lipoprotein fractions had to be maintained throughout the work. Further advancement in this subject should consider distinct donors and preferably individuals with distinct relative levels of high and low density lipoproteins as well as total cholesterol. It should be noted that all the kinetic and equilibrium parameters must be obtained for each donor to allow the establishment of eventual dependencies. Failure to do so will only increase the uncertainly associated with the parameters.

Another limitation is the use of DHE as a reporter of cholesterol. This was partially overcome with the use of kinetic data for cholesterol exchange taken from literature. However, the parameters were obtained with distinct methodologies and blood donors which reduces the precision and consistency of the parameters. Furthermore some of the required parameters could not be obtained from literature and those obtained in this work for DHE had to be used.

Future work on this subject should characterize quantitatively the exchange of cholesterol among the distinct blood compartments of a large number of individuals both with similar and distinct cholesterol and lipoprotein levels.

VIII.3 – Concluding Remarks

The blood homeostasis and distribution of cholesterol was modeled using experimental data for the interaction of DHE and cholesterol with major blood compartments, namely lipid bilayers mimicking the erythrocyte membrane, lipoproteins and albumin. The agreement between the simulated equilibrium distribution with the distribution expected from the literature is very good for all the compartments considered. The temporal evolution of the concentration of free cholesterol in each blood compartment was also followed after addition of a bolus of 10% of total free cholesterol in the aqueous compartment. The maximal excess cholesterol transiently accumulated is largest for the pools with the fastest kinetics (HDL3>HDL2>Alb>LDL>VLDL) and the time at which

the concentration peak occurs follows the reverse order. No excess accumulation is observed for the pool with the slowest association kinetics (Ery). Thus, the amount of cholesterol in the small lipoproteins pool is more sensitive to variations in the rates of cholesterol entry into and removal from the blood, while LDL and VLDL are more robust regarding fluctuations in the total concentration of cholesterol. DHE seems to be adequate to model the equilibrium distribution of cholesterol, which is structurally very similar. However, analysis of the temporal distribution of DHE vs Chol shows limitations on its use as a reporter of the kinetics of cholesterol interacting with biologic compartments. Equilibration of cholesterol in blood compartments directly predicted from the available parameters is significantly slower than that observed for DHE. Finally, the results of this work show the importance of the passive pathway for the overall rate of exchange of cholesterol in the blood.

Chapter IX

Beyond Overton's rule - Quantitative Modeling of Passive Permeation through a Cell Monolayer

This work was published as: Filipe, H. A. L.; Salvador, A.; Silvestre, J. M.; Vaz, W. L. C.; Moreno, M. J. Beyond Overton's Rule: Quantitative Modeling of Passive Permeation through Tight Cell Monolayers. Mol. Pharmaceutics 2014, 11, 3696-3706.

Hugo A. L. Filipe contributed to the development, execution and analysis of the simulations, and also contributed to the writing of the manuscript.

IX.1 – Introduction

Bioavailability of drugs at their active site is conditioned by their permeation through epithelial or endothelial cell monolayers such as the intestinal brush border or the blood-brain barrier [180, 187, 188, 396]. Permeation rates across these cellular barriers are usually predicted from results obtained using confluent cell cultures (*in vitro*) or from tissue drug distribution (*in vivo*) [152] and passive permeation through the lipid bilayer of cellular membranes is usually considered as a significant route [149]. Early stages of drug development require predictive knowledge of the drugs' molecular physic-chemical properties and their relation to permeation of cell membranes. As it is commonly used, "Overton's rule" [16], also known as the "Meyer-Overton rule" [150], to which we shall hereafter refer to as the solubility-diffusion model, does not explicitly consider the discrete, non-continuum nature of the lipid bilayer. Including kinetic and thermodynamic information relating the molecular properties of the drug as well as the membrane and their interactions with each other would significantly improve predictability.

Overton predicted a linear dependence between the permeability coefficient of a solute through a cell membrane and its solubility in non-polar solvents [12]. The rate-limiting step in the currently used solubility-diffusion model is solute diffusion across the bilayer and membrane/water partitioning of the solute is considered to be close to equilibrium. Most comparisons of the permeation of a large variety of solutes across membranes explicitly assume that membrane/water partition can be simulated by octanol/water partition. However, poor correlations and inadequate predictive values result for unrelated solutes even when structural properties of the solutes are considered in addition to organic solvent/water partition coefficients [151]. *In vivo* processes such as active transport (influx or efflux) and drug degradation and/or sequestration by the cell monolayer have been pointed as important determinants for the poor predictability of the current methods [151]. More importantly, inadequate evaluation of the passive routes due to an incorrect prediction of solute solubility in the biomembrane from its partition to organic solvents [155, 397], inaccurate description of the rate of diffusion through the membrane [398, 399], or breakdown of the assumption that the diffusion through the membrane is the rate limiting step in the overall permeation process [400] may be important factors. The present work addresses these three factors by focusing on

the rate of passive diffusion of a homologous series of amphiphiles through tight cell monolayers. We have previously studied the detailed kinetics and thermodynamics of interaction of these amphiphiles with membranes [5, 6, 280]. Similar data are scarce in the literature, and their need in the careful modeling of membrane permeation has been pointed out by several authors [398, 400].

The lipid bilayer of a biomembrane is a non-isotropic structured medium presenting regions with distinct polarity and density that affect the partition and the location of the solute in the membrane [156, 157]. Lipid anisotropy in membranes together with oriented water at the interface generates a dipole potential of several hundred mV with the negative pole oriented towards the bilayer/water interface [47]. The interaction of amphiphilic molecules with this strong local electric field (on the order of 10^9 V/m) leads to a specific orientation and/or affects their partition into and location in the membrane. Studies based on homogeneous media such as organic solvents fail to capture these properties. The prediction of solute transport across biomembranes must be based on quantitative information concerning solute partition into and translocation across the relevant lipid bilayers.

Modeling permeation across a tight cell monolayer must also consider that these systems have both an apical and a basolateral membrane, each with its own characteristics. Simple compartmental models that take this into consideration have substantially improved the quantitative interpretation of the observed permeability coefficients [401-403]. Detailed knowledge of the equilibrium and kinetic parameters for the interaction between a drug and each type of cell membrane would be desirable. We have been working towards filling this gap by studying the complete kinetic and thermodynamic characterization of interaction (insertion, desorption, and translocation) of several amphiphiles with serum albumin, lipoproteins and membranes of various lipid compositions [3-7, 9, 10, 74, 139, 280]. Some of these studies focus the dependence on the structure of the amphiphiles.

In this work we develop a detailed mechanistic model for permeation through a cell monolayer. We then apply it to predict the rate of passive permeation for a homologous series of amphiphiles with the same polar group (the fluorescent group NBD) and varying hydrophobic/hydrophilic ratio due to different alkyl chains (NBD-C_n with *n* equal to 2 to 16). This homologous series is structurally related to neuroactive N-acyldopamines [404] and some drugs against immunological diseases that have been

reported to cross the blood-brain barrier [362-364]. Additionally, the model includes the equilibrium distribution of the amphiphile between the aqueous medium and binding agents (serum albumin and lipoproteins) in blood plasma on one side of the cell monolayer. Inadequate consideration of the kinetic and thermodynamic parameters of drug binding by agents in the aqueous phase in *in vitro* studies of cell monolayer permeation [405, 406] may cause discrepancies in permeation studies of confluent cell monolayers [407, 408]. Finally, a sensitivity analysis is also performed to evaluate the dependence of the rate of the overall permeation process on the microscopic rate constants and equilibrium constants.

IX.2 – Results and Discussion

IX.2.1 – Kinetic Model for the Permeation through the Cell Monolayer

The kinetic scheme proposed for the passive permeation of a small amphiphilic molecule through a cell monolayer is illustrated in Figure IX.1. The amphiphile enters the system from the serum, where it is in equilibrium with serum albumin and lipoproteins with the equilibrium constants K_{B} and $K_{\mathrm{L_p}}$ respectively. It can insert into the outer leaflet of the apical side of the cell plasma membrane coming from the aqueous medium with the insertion rate constant $\kappa_{+}^{a^{\mathrm{o}}}$. The outer leaflet of the apical membrane is considered as laterally isolated due to the tight junctions (TJ), with no diffusion into the basolateral membrane or between adjacent cells. [17, 174] At this stage the amphiphile can have only the following two fates: 1) It can return to the serum with desorption rate constant $\kappa_{-}^{a^{\mathrm{o}}}$; or, 2) It can translocate into the inner leaflet of the apical side of the cell plasma membrane with the rate constant $k_{\mathrm{f}\,a}^{\mathrm{o}\to\mathrm{i}}$, from where it can return with the rate constant $k_{\mathrm{f}\,a}^{\mathrm{i}\to\mathrm{o}}$. Once in the inner leaflet of the cell plasma membrane the amphiphile can diffuse between the apical and basolateral sides with the diffusion coefficient D^{i} or desorb into the cytoplasm with the rate constant $\kappa_{-}^{a^{\mathrm{i}}}$. The amphiphile in the cytoplasm can re-insert into the inner leaflet of the apical ($\kappa_{+}^{a^{\mathrm{i}}}$) or basolateral ($\kappa_{+}^{b^{\mathrm{i}}}$) membrane. Translocation into the outer leaflet of the basolateral

membrane occurs with the rate constant $k_{\mathrm{f}\,b}^{\mathrm{i}\to\mathrm{o}}$ from where it can desorb into the tissue ($\kappa_{-}^{b^{\mathrm{o}}}$). The detailed definition of the parameters used to model each step is given in the Methods Chapter. All parameters and conversion factors are summarized in Tables A.3, A.4 and A.5 in the Appendix.

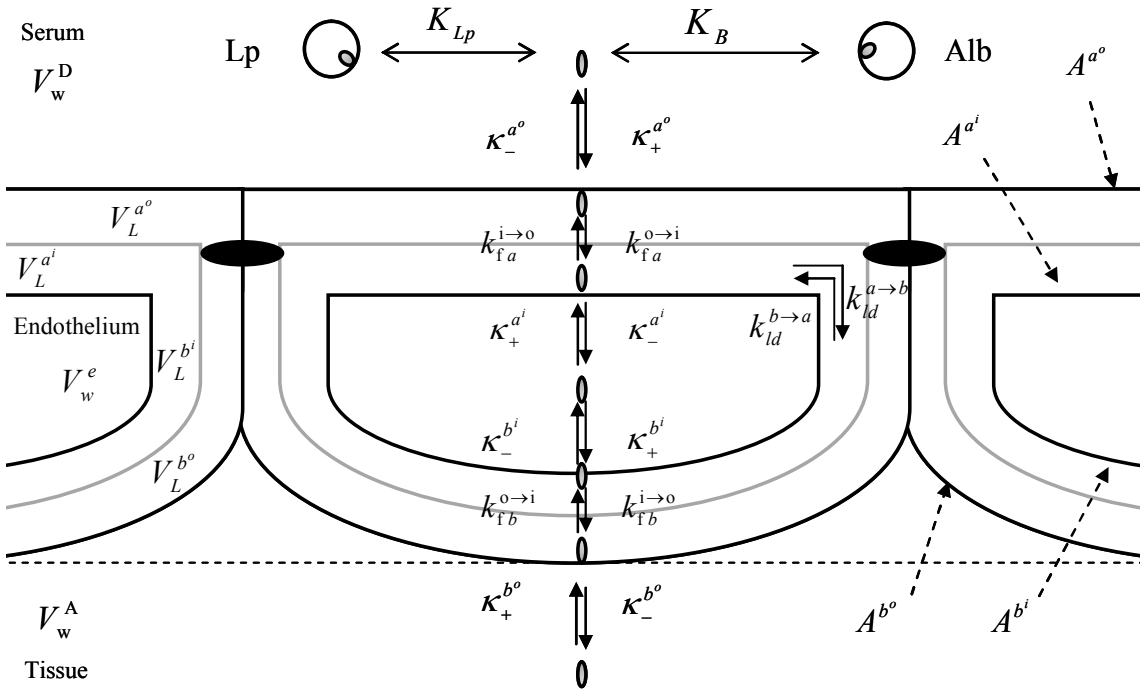

Figure IX.1 – Scheme describing the passive permeation through tight endothelia with the inclusion of the rate and equilibrium constants as well as structural data of the compartments considered. K_{B} and $K_{\mathrm{L_p}}$ are equilibrium binding constants to serum albumin (Alb) and Lipoproteins (L_P), respectively. The rate constants of insertion, desorption, translocation and diffusion are represented by $\kappa_{+}^{p^{\mathrm{q}}}$, $\kappa_{-}^{p^{\mathrm{q}}}$, $k_{\mathrm{f}\,x}^{q}$ and k_{ld}^{p} , where *p* represents the membrane compartment (apical, *a*, or basolateral, *b*); $a\to b$ indicating the direction from the apical to the basolateral membrane, and *q* the respective leaflet (inner, *i*, or outer, *o*); $o\to i$ indicating the direction from the outer to the inner leaflet. The surface areas of the cell membrane compartments are represented by A^{p^q} , the volumes of the lipid compartments by $V_L^{p^q}$ and the volumes of the aqueous compartments by V_{w}^{r} , where *p* and *q* are defined as above and *r* represents the donor (D), the cytoplasm (*e*) and the acceptor (A) compartments.

The differential equations, equations (IX.1), that describe the interaction of the amphiphiles with the serum components and their passive permeation through the cell

monolayer were obtained from the kinetic scheme presented in Figure IX.1 and were integrated numerically using the software *Mathematica*™ [409].

$$K_{x_i} = \frac{\left[\mathrm{S}_{x_i}\right]}{[\mathrm{S}][x_i]}$$

for x_i = Alb, VLDL, LDL, HDL_2, HDL_3

$$\frac{dS_{\mathrm{w}}^{\mathrm{D}}}{dt} = \frac{\kappa_{-}^{a^{\mathrm{o}}} \frac{A^{a^o}}{V_{\mathrm{L}}^{a^{\mathrm{o}}}} S^{a^o} - \kappa_{+}^{a^{\mathrm{o}}} \frac{A^{a^o}}{V_{\mathrm{w}}^{\mathrm{D}}} S_{\mathrm{w}}^{\mathrm{D}}}{1 + \sum_i K_{x_i}\left[x_i\right]}$$

for x_i = Alb, VLDL, LDL, HDL_2, HDL_3

$$\frac{dS^{a^o}}{dt} = \kappa_{+}^{a^{\mathrm{o}}} \frac{A^{a^o}}{V_{\mathrm{w}}^{\mathrm{D}}} S_{\mathrm{w}}^{\mathrm{D}} + k_{\mathrm{f}\,a}^{\mathrm{i}\to\mathrm{o}} S^{a^i} - \left(\kappa_{-}^{a^{\mathrm{o}}} \frac{A^{a^o}}{V_{\mathrm{L}}^{a^{\mathrm{o}}}} + k_{\mathrm{f}\,a}^{\mathrm{o}\to\mathrm{i}}\right) S^{a^o}$$

$$\frac{dS^{a^i}}{dt} = k_{\mathrm{f}\,a}^{\mathrm{o}\to\mathrm{i}} S^{a^o} + \kappa_{+}^{a^{\mathrm{i}}} \frac{A^{a^i}}{V_{\mathrm{w}}^{e}} S_{\mathrm{w}}^{e} + k_{ld}^{b\to a} S^{b^i} - \left(k_{\mathrm{f}\,a}^{\mathrm{i}\to\mathrm{o}} + \kappa_{-}^{a^{\mathrm{i}}} \frac{A^{a^i}}{V_{\mathrm{L}}^{a^{\mathrm{i}}}} + k_{ld}^{a\to b}\right) S^{a^i}$$

$$\frac{dS_{\mathrm{w}}^{e}}{dt} = \kappa_{-}^{a^{\mathrm{i}}} A^{a^i} \frac{S^{a^i}}{V_{\mathrm{L}}^{a^{\mathrm{i}}}} + \kappa_{-}^{b^{\mathrm{i}}} A^{b^i} \frac{S^{b^i}}{V_{\mathrm{L}}^{b^{\mathrm{i}}}} - \left(\kappa_{+}^{a^{\mathrm{i}}} \frac{A^{a^i}}{V_{\mathrm{w}}^{e}} + \kappa_{+}^{b^{\mathrm{i}}} \frac{A^{b^i}}{V_{\mathrm{w}}^{e}}\right) S_{\mathrm{w}}^{e}$$

$$\frac{dS^{b^i}}{dt} = \kappa_{+}^{b^{\mathrm{i}}} \frac{A^{b^i}}{V_{\mathrm{w}}^{e}} S_{\mathrm{w}}^{e} + k_{ld}^{a\to b} S^{a^i} + k_{\mathrm{f}\,b}^{o\to i} S^{b^o} - \left(\kappa_{-}^{b^{\mathrm{i}}} \frac{A^{b^i}}{V_{\mathrm{L}}^{b^{\mathrm{i}}}} + k_{ld}^{b\to a} + k_{\mathrm{f}\,b}^{\mathrm{i}\to\mathrm{o}}\right) S^{b^i}$$

$$\frac{dS^{b^o}}{dt} = k_{\mathrm{f}\,b}^{\mathrm{i}\to\mathrm{o}} S^{b^i} + \kappa_{+}^{b^{\mathrm{o}}} \frac{A^{b^o}}{V_{\mathrm{w}}^{\mathrm{A}}} S_T - \left(k_{\mathrm{f}\,b}^{\mathrm{o}\to\mathrm{i}} + k_{-}^{b^{\mathrm{o}}} \frac{A^{b^o}}{V_{\mathrm{L}}^{b^{\mathrm{o}}}}\right) S^{b^o}$$

$$\frac{dS_{\mathrm{w}}^{\mathrm{A}}}{dt} = \frac{\kappa_{-}^{b^{\mathrm{o}}} \frac{A^{b^o}}{V_{\mathrm{L}}^{b^{\mathrm{o}}}} S^{b^o} - \kappa_{+}^{b^{\mathrm{o}}} \frac{A^{b^o}}{V_{\mathrm{w}}^{\mathrm{A}}} S_{\mathrm{w}}^{\mathrm{A}}}{1 + \sum_i K_{\omega_i}\left[\omega_i\right]} \qquad \text{(IX.1)}$$

for ω_i = Alb, VLDL, LDL, HDL_2, HDL_3

In equations (IX.1) S^{p^q} (S_{w}^{r}) represents the moles of solute in a given membrane (aqueous) compartment, with *p*, *q* and *r* being defined as in Figure IX.1.

IX.2.2 – Simple Analysis from the Experimentally Obtained Values

The rate constants obtained for the interaction between NBD-C_n and POPC LUVs [5, 6] convey important information about the rate limiting step in the overall permeation process through a cell monolayer. To allow the comparison with the unimolecular steps (desorption and translocation), the bimolecular step (insertion) was converted into a pseudo-unimolecular step by multiplying the rate constant by the concentration of LUVs that would be obtained from the total lipid in the apical side of the cell membrane (≈78 μM of total lipid, see section A.IX.3 of the Appendix for details). The results are shown in Figure IX.2A. An equivalent analysis was performed regarding the equilibrium association with the various binding agents in the system (cell membranes, lipoproteins and albumin) and the predicted affinity (product of the equilibrium constant and the concentration of binding agent) is shown in Figure IX.2B.

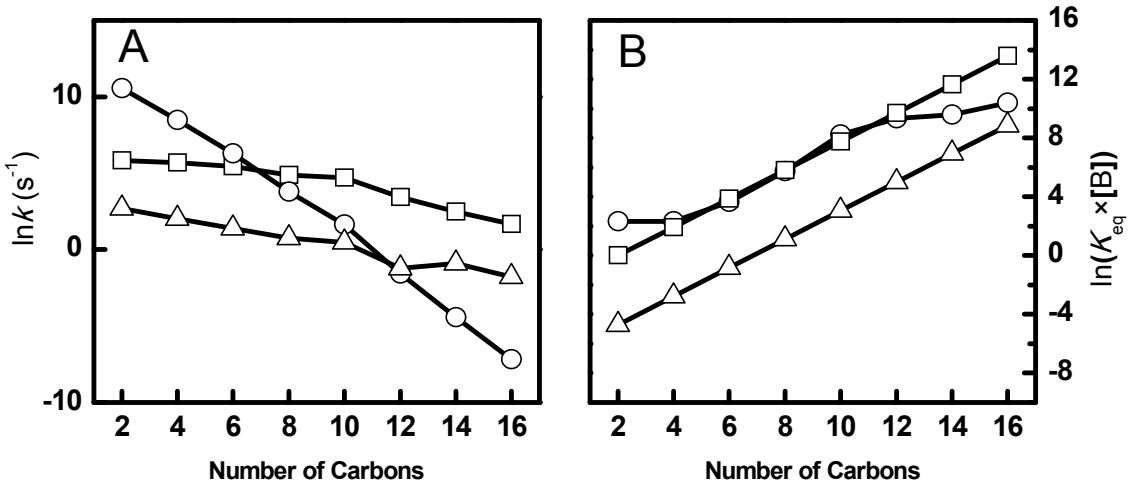

Figure IX.2 – Rate constants of insertion (□), desorption (○) and translocation (Δ) (A), and affinities of the amphiphiles for cell membranes (Δ), albumin (○) and all lipoproteins (□) (B), predicted from the parameters obtained for interaction with POPC LUVs, BSA and lipoproteins [5, 6] at 25 °C. The bimolecular steps, insertion and equilibrium association, were converted into pseudo-unimolecular steps multiplying the respective kinetic or equilibrium parameter by the amount of binding agent available ($k_+^{\mathrm{Lv}} \times [\mathrm{Lv}]$, $K_{\mathrm{L}} \times [\mathrm{Lv}]$, $K_{\mathrm{B}} \times [\mathrm{Alb}]$ and $K_{\mathrm{L_p}} \times [\mathrm{L_p}]$).

The results in Figure IX.2 indicate that at the lipid concentrations that characterize the human blood/tissue barrier, and considering the processes of desorption and translocation, the latter is the slowest process for $n \leq 8$, while desorption is the slowest process for $n \geq 14$. For $10 \leq n \leq 12$ the two rates are similar. Comparing insertion and

translocation, insertion is never the slower step for any of the amphiphiles examined. This suggests that for the most hydrophilic amphiphiles ($n < 10$) translocation is the rate limiting step in the overall process of permeation, in agreement with the assumptions considered in the solubility-diffusion model. But it also suggests that desorption becomes the rate limiting step for very hydrophobic amphiphiles. This is in agreement with the breakdown of the solubility-diffusion model reported for very hydrophobic solutes [400, 410].

The results shown in Figure IX.2B predict that NBD-C_n with $4 \leq n \leq 12$ have similar affinities for lipoproteins and serum albumin. The most hydrophobic amphiphiles have substantially higher affinities for lipoproteins, while the amphiphile with the shortest alkyl chain, NBD-C_2, has higher affinity for albumin. The predicted relative affinity for the cell membranes is smallest for all amphiphiles in the series.

In the next sections, the complete kinetic scheme, Figure IX.1 and equations (IX.1), will be solved and this analysis will be complemented with a detailed quantitative characterization of the overall permeation through the cell monolayer. The rate limiting step(s) will be clearly identified and the effect of sequestration by serum compartments on the overall permeation rate will be characterized.

IX.2.3 – Permeation of the Amphiphiles through the Cell Monolayer

The numerical integration of the differential equations obtained from Figure IX.1 (equations (IX.1)) gives the time evolution of the amount of amphiphile in each compartment considered in the model, from the serum, across the cell monolayer, and into the tissue.

The accumulation of each amphiphile in the tissue is shown in Figure IX.3A for the case of complete transfer of the amphiphiles into the tissue (model M1). The fractional deviation from equilibrium as a function of time is shown in Figure IX.3B. Both results were computed from the amount of amphiphile transferred into the tissue and from that remaining in the serum; the difference between the two giving the amount of amphiphile sequestered by the cell monolayer.

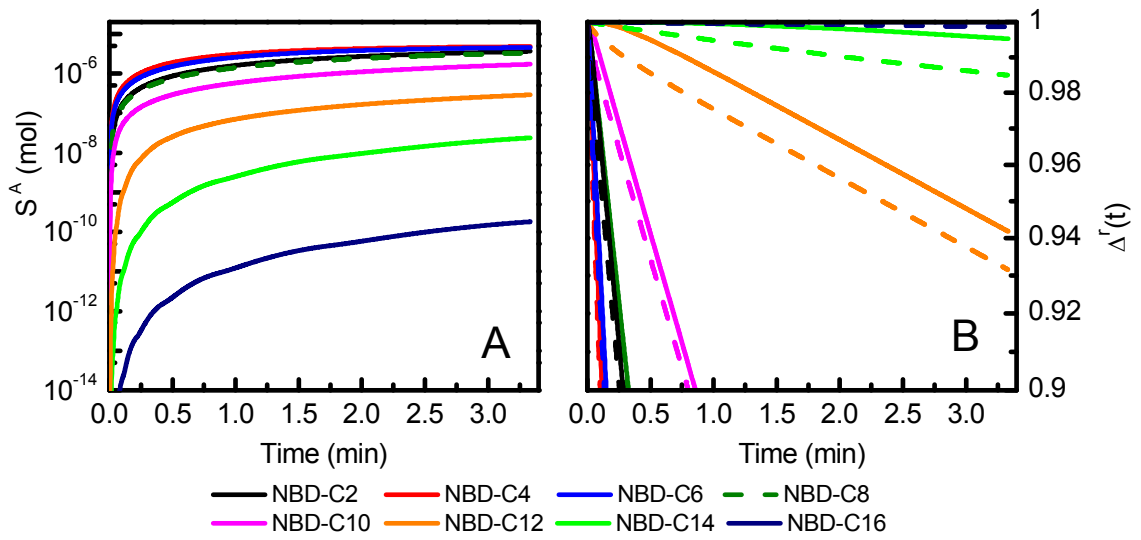

Figure IX.3 – A) Irreversible accumulation in the tissue for a total amount of 5×10^{-6} mol of amphiphile (see color code). The results obtained for NBD-C_8 are shown as a dashed line to permit the visualization of both -C_8 and -C_2, which show a very similar rate of accumulation in the tissue. B) Fractional deviation from the conditions at infinite time, equation IX.2, for the systems represented in the left plot: accumulation in the tissue (solid), and disappearance from the serum (dashed). Note that the logarithmic representation of the solute disappearance/accumulation is essentially linear as expected for a mono-exponential function.

The first important observation is that the rate of permeation increases with *n* for shorter alkyl chains, from 2 to 4 carbons, but decreases for $n \geq 6$. The time variation of the amphiphile concentration in the tissue is well described by a mono-exponential function from which a characteristic rate constant of transfer (β) can be obtained, equation (IX.2),

$$\Delta^r(t) = \frac{S^r(\infty) - S^r(t)}{S^r(\infty) - S^r(0)} = e^{-\beta t} \qquad \text{(IX.2)}$$

where $S^r(t)$, $S^r(0)$ and $S^r(\infty)$ is the amount of solute at time *t*, in the beginning and at equilibrium, for the amphiphile in the tissue (r = A) or in the donor compartment (r = D), respectively.

The characteristic rate constant for transfer is shown in Figure IX.4 highlighting the maximal permeation rate at intermediate alkyl chain lengths. The partition coefficient between the cell membrane and the aqueous phase increases with the chain length [5]. Therefore, for $n \geq 6$, the observed rate of accumulation into the tissue decreases as the

hydrophobicity of the amphiphile increases. This tendency contradicts the prediction of the solubility-diffusion model [16], which cannot therefore be applied to describe the relative permeation for the amphiphiles of this homologous series with $n \geq 4$ carbons. Regarding the discussion in the previous section, the result for amphiphiles with $n \geq 10$ carbons can be explained in part by the rate limiting step not being the one assumed in the derivation of the solubility-diffusion model. Additionally, as will be shown below, sequestration by serum compartments has an important role in the rate of overall permeation of the shorter amphiphiles. Our results agree qualitatively with the experimental work on the permeation of a homologous series of carboxylic acids [411], pyrrolopyrimidines [410] and also with simulations based on the results obtained for structurally unrelated carboxylic acids of different global hydrophobicity [412].

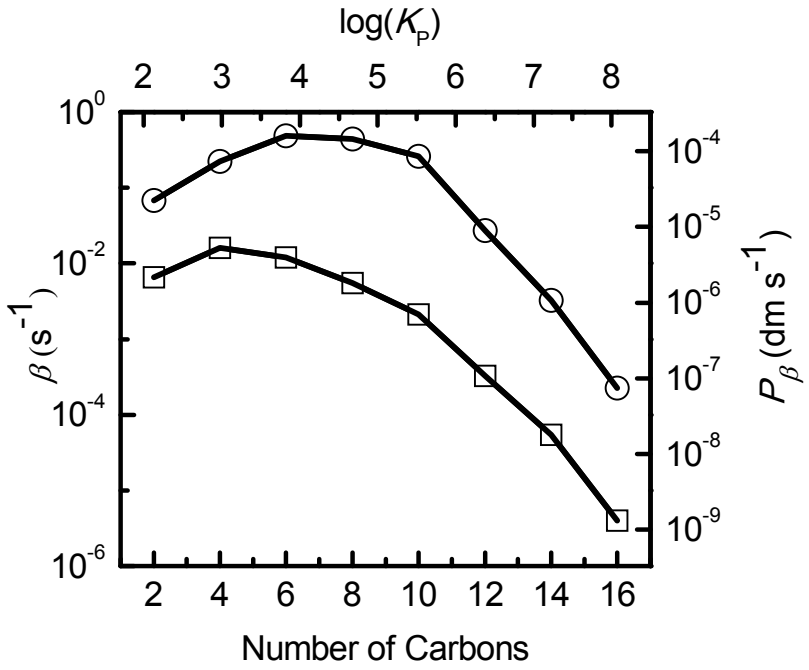

Figure IX.4 – Dependence of the characteristic rate constant for transfer, β, and permeability coefficient calculated from equation (IX.4), P_β, with the number of carbons for the NBD-C_n homologous series, for model M1 with (□) and without (○) binding agents in the donor compartment.

The permeability coefficient (P) is commonly calculated using the expression:

$$P = \frac{\frac{dS^{\mathrm{A}}(t)}{dt} V^{\mathrm{D}}}{A^{a^o} S^{\mathrm{D}}(0)} \qquad \text{(IX.3)}$$

where $S^{A}(t)$ is the total amount of solute (in the aqueous phase plus bound to binding agents when present) in the acceptor compartment (tissue) at time *t*, V^{D} is the total volume of the donor compartment, $A^{a^{o}}$ is the area of the barrier in contact with the donor compartment and $S^{D}(0)$ is the total amount of solute in the donor compartment at $t = 0$.

Equation (IX.3) is an approximate solution that is only valid at initial stages of the permeation process and relies on the following assumptions: i) negligible backflow of solute (irreversibility); ii) concomitant and simultaneous increase of solute in the acceptor compartment due to its disappearance in the donor compartment. The latter assumption requires that there is no significant mass imbalance due to solute decomposition or binding to the barrier or experimental apparatus. Under those conditions, the rate of solute accumulation in the acceptor compartment ($\frac{dS^{A}(t)}{dt}$) is maximal at very short times and remains nearly constant up to a few percent deviation from the initial conditions. The presence of a membrane barrier, which has the ability to retain the solute, always leads to the appearance of a delay between the increase in the amount of solute in the acceptor compartment and its corresponding disappearance in the donor compartment (Figure IX.3B and A.24). We have calculated the permeability coefficient considering the maximal rate of accumulation of solute in the acceptor compartment which in the models considered occurs at very short times, see Table A.6 (Appendix). In conditions of irreversibility, M1, the maximal rate of accumulation occurs always at less than 4% transfer to the tissue. When reversibility is considered, M2 to M4, the maximal rate is shifted to larger deviations from the initial conditions and can go up to 17% accumulation in the tissue, although it occurs typically at less than 10% (see Table A.7 in the Appendix).

The attainment of the maximal rate at small transfer fractions and the fact that $S^{A}(\infty)$ is equal to $S^{D}(0)$ in equation (IX.2) for the case of irreversible transfer, permits the calculation of the permeability coefficient directly from the characteristic transfer rate constant (β) using equation (IX.4) (see section A.IX.5 in the Appendix for details).

$$P_\beta = \frac{\beta V^{\mathrm{D}}}{A^{a^o}} \approx \frac{\beta V_{\mathrm{w}}^{D}}{A^{a^o}} \qquad \text{(IX.4)}$$

For situations of irreversible transfer of solute, the permeability coefficient is therefore proportional to the characteristic rate constant and the variation with the amphiphile hydrophobicity shows the same "parabolic like" dependence as observed for the characteristic rate constant (Figure IX.4). This behavior has been previously observed for the permeation and biological activity of drugs [213, 214, 410, 413-416]. This is expected for the combination of amphiphiles whose permeation is limited by translocation, in accordance with the solubility-diffusion model, with amphiphiles whose permeation is not translocation limited as is the case of very hydrophobic solutes.

The calculated P values range from 2.1×10^{-6} dm s^{-1} for NBD-C_2, to a maximum of 5.1×10^{-6} dm s^{-1} for NBD-C_4 and decrease to 1.3×10^{-9} dm s^{-1} for NBD-C_{16}. Particularly, P values for NBD-C_{10} and NBD-C_{12} of 6.9×10^{-7} dm s^{-1} and 1.1×10^{-7} dm s^{-1}, respectively, are of the same order of magnitude as P values experimentally determined for the passive permeation of drug molecules with similar hydrophobicity (assessed through $\mathrm{clogP_{Oct/w}}$, see values on Table A.8 in the Appendix) through confluent MDCK cell monolayers [410]. However, a quantitative comparison is not possible at this time due to differences in the properties of the system (membranes and aqueous compartments) and solutes (structure and rates of interaction with the membranes). In the next sections the influence of the properties of the aqueous compartments (sequestration) will be quantitatively evaluated and the contribution of each step to the overall rate of permeation will be quantitatively analyzed.

IX.2.4 – Drug Sequestration by Serum Components

There is a general consensus that drug sequestration in the serum reduces its rate of permeation through tight endothelia. However, a quantitative analysis of the effects on the observed permeability coefficient and its dependence on drug hydrophobicity has yet to be performed. Furthermore, *in vitro* studies of permeation through confluent cell monolayers often add albumin to the donor compartment to increase drug solubility [405, 410] without a systematic study of the effects of these additions on the measured permeability coefficient. Binding of the amphiphiles to the serum components reduces its free concentration in the aqueous medium due to more extensive sequestration, and

this decreases β. The increase in the characteristic transfer rate constant and on the permeability coefficient when the concentrations of the serum components albumin or lipoproteins are decreased is shown in Figure IX.5. Figure IX.5A shows the effect of total removal, while Figure IX.5B shows the effect of a progressive decrease/increase of the concentration by a factor *mf*.

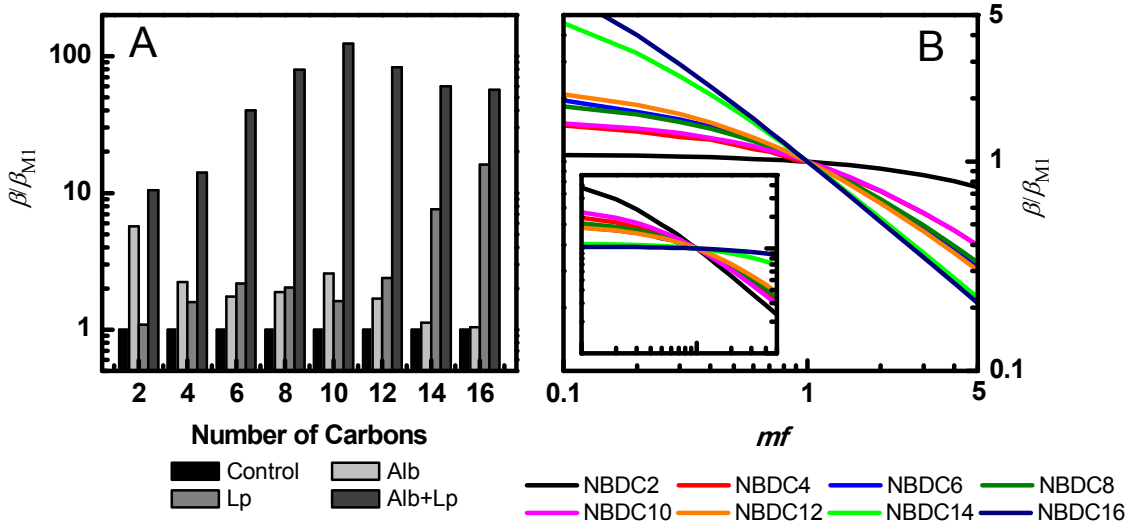

Figure IX.5 – Plot A - Effect of the total elimination of serum albumin, lipoproteins and serum albumin *plus* lipoproteins, in the characteristic transfer rate constant (β) (and consequently in the permeability coefficient (P)) for the irreversible transfer (M1) of amphiphiles from the serum to the tissue. Plot B – Sensitivity analysis (β/β_{M1}) with respect to the concentration of lipoproteins (main plot) or albumin (inset) in the donor compartment (see color code). The concentration of lipoproteins and albumin was varied through the multiplication of its reference value (Table A.5 in the Appendix) by a factor (*mf*). The axes in the inset of plot B are the same as in the main plot.

The total elimination of albumin in the donor compartment leads to a small increase in the observed characteristic transfer rate constant (or permeability coefficient), which is substantial for the less hydrophobic amphiphiles in the series ($n \leq 12$) and largest for NBD-C_2. In contrast, the removal of the lipoproteins from the donor compartment substantially affects β for amphiphiles with $n \geq 6$. This effect is especially pronounced for $n \geq 14$, where the observed permeability coefficient increases by nearly one order of magnitude. It reflects the relative association affinity of the amphiphiles to the lipoproteins compared to albumin, which increases with n (Figure IX.2B).

The sensitivity of the permeability coefficient of each amphiphile to the concentration of albumin and lipoproteins in the donor compartment is shown in Figure IX.5B. In

agreement with the results in Figure IX.5A, the highest sensitivities with respect to the concentration of lipoproteins are observed for the most hydrophobic amphiphiles. The reverse holds for the sensitivities with respect to the concentration of serum albumin, which are also lower (inset). The dependence on n is not monotonic. But nevertheless NBD-C_2 shows the highest sensitivity to the concentration of albumin, and the lowest to the concentration of Lp.

With the complete removal of all sequestrators, permeation becomes only dependent on the interaction with the permeation barrier. As shown in Figure IX.5A the total removal of sequestration has a non-monotonic effect, with higher influence for intermediate chain lengths. This result highlights a compromise between the affinity of the amphiphiles for the binding agents and their affinity and kinetics of interaction with the barrier. As a consequence, the removal of all sequestrators results in a stronger "parabolic like" dependence of β (and P) on the number of carbons (Figure IX.4). It should be noted here that even without sequestration β does not increase from NBD-C_6 to NBD-C_8, in contrast to what could be expected from the observation of Figure IX.2, which shows that the rate constant for translocation is significantly smaller than that of insertion/desorption up to n=8.

IX.2.5 – Rate Limiting Steps in the Permeation Process

In the last section it was shown that both the interaction with the barrier and the presence of binding agents can influence the permeation of molecules through cell membranes. Rational drug design requires that the rate limiting step(s) in the permeation process be clearly identified. We, therefore, performed a sensitivity analysis to identify the rate limiting steps for each amphiphile. The value of the kinetic parameter (reference value) being analyzed was multiplied by a factor (mf) and the resulting characteristic rate constant for the transfer from the serum to the tissue (β) was computed. All kinetic steps were analyzed independently and some combinations were also considered (insertion and desorption). The equilibrium constants for association with the lipoproteins and cell membranes were not varied directly but they were affected by variations in their respective insertion/desorption rate constants. The parameters were varied simultaneously for the lipoproteins and cell membranes because the solutes are expected to interact mainly with a lipidic phase in both systems. The

sensitivity analysis of the translocation between the leaflets of the apical and basolateral membranes was also modulated simultaneously. The results obtained are shown in Figure IX.6. The sensitivity is evaluated from the slopes in the log-log representation of the characteristic rate constant for transfer vs. *mf*, which are summarized in Table A.9 Appendix.

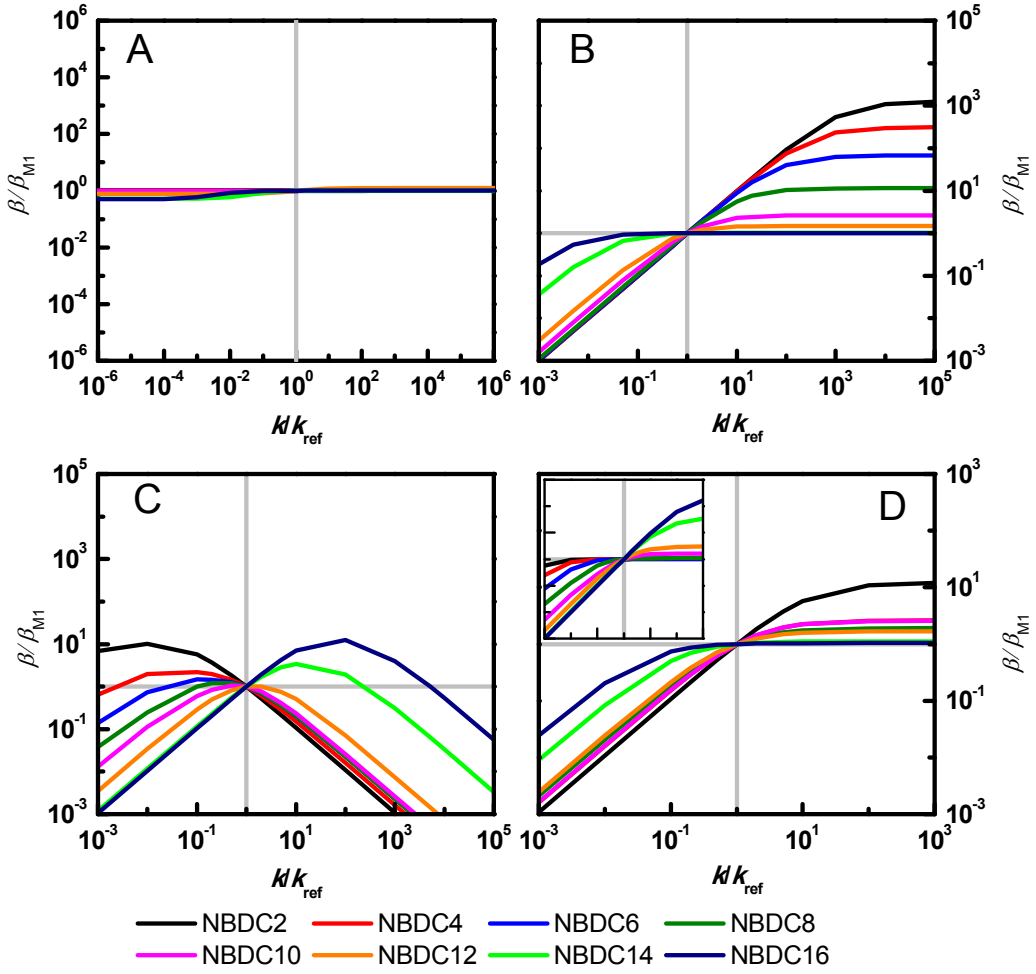

Figure IX.6 – Relative variation of β with the values of the rate constants for the lateral diffusion in the membrane (A), translocation across the bilayer leaflets (B), desorption from (C) and insertion into (D) the cell membranes, and variation of both desorption and insertion (inset of plot D), for the model considering irreversible transfer (M1). The axes in the inset of plot D are the same as in the main plot. Gray lines represent the reference values for the rate constants (k/k_{ref} = *mf*. equal to 1). Due to the kinetic details of the system, the maximal sensitivity expected with respect to each parameter is 1. In the log-log representation of the characteristic rate constant for transfer vs. a parameter, a line segment with slope 1 indicates that the parameter in point is the rate limiting step on the overall permeation over that range of parameter values. In turn, segments with slope 0 indicate that the parameter does not influence the overall permeation over that range of parameter values, as verified for the rate constants of the steps that are in fast equilibrium.

The results obtained for variations in the diffusion coefficient of the amphiphiles (altering the rate constant k_{ld}) are shown in Figure IX.6A. The sensitivity of the overall permeation rate to this parameter at the reference values is less than 0.11 for all amphiphiles, and β changes only about twofold when the parameter is changed by 12 orders of magnitude. This insensitivity is due to the presence of two alternative paths from the apical to the basolateral inner leaflets: *via* diffusion in the membrane or through desorption from the apical side of the membrane followed by diffusion in the cytoplasm and insertion into the basolateral membrane. The similar values obtained for the characteristic transfer rate constant at very small and very large diffusion coefficients indicates that the rate through both paths at the reference parameters is similar. However, we are not considering sequestration in the cytoplasm, and we assume fast diffusion in the cytoplasm. The sensitivity to the diffusion coefficient of inserted amphiphile would otherwise be higher because transfer through the cytoplasm would be slowed down. The results further indicate that at the reference conditions the most hydrophobic amphiphiles are transported mostly through the membrane while the less hydrophobic ones are transported through the cytoplasm.

Figure IX.6B shows the sensitivity of the rate of overall permeation to the rate constant of translocation through the cell membranes. This sensitivity decreases with increasing length of the acyl chain. Thus, translocation is the rate limiting step for the least hydrophobic amphiphile (NBD-C_2) but virtually does not influence the overall permeation of NBD-C_{16}. Independently of the hydrophobicity of the amphiphile in the series, the translocation rate constant can become the rate limiting step if its value is small enough.

To study the effect of the insertion and desorption rate constants three different situations were considered: *i*) changing only the desorption rate constant, which leads to an inverse variation of the partition coefficient (Figure IX.6C); *ii*) changing only the insertion rate constant, which leads to a proportional variation in the partition coefficient (Figure IX.6D); and *iii*) application of the multiplication factor to both, insertion and desorption rate constants, which leaves the partition coefficient unchanged (Figure IX.6D inset). In this last situation for $n \geq 14$ the rate of overall permeation strongly increases as the interaction with the lipid membranes becomes faster. Therefore, one or both of those steps is/are rate limiting for the most hydrophobic amphiphiles in the series. When only the desorption rate constant is increased from the

minimum value considered (Figure IX.6C), the overall permeability goes through a maximum, after which it decreases. The main reason for this negative sensitivity at high desorption rates is the decrease in the affinity for the cell membranes under conditions where translocation becomes rate limiting. At the reference values this is the case for amphiphiles with n = 2 to 10. In opposition, when desorption from the membrane is the rate limiting step, the overall permeation rate increases with the increase in this rate constant in spite of the accompanying decrease in the affinity for the cell membranes. This is in agreement with the simulation results presented by Thomae et al [412] and in clear contradiction to the solubility-diffusion model. At the reference values for the rate constants of this homologous series, this is observed for the most hydrophobic amphiphiles, NBD-C_{14} and NBD-C_{16}.

The sensitivity to the rate constant of insertion into the lipid membranes is shown in Figure IX.6D. For small rates of insertion, an increase in this rate constant leads to a faster permeation for all amphiphiles. However, values for this rate constant above a certain limit (dependent on the amphiphile) do not lead to further acceleration of the overall permeation. The following analysis shows that this is due to the effect of this parameter on the concentration of amphiphile in the aqueous phase, and consequently on the rate of insertion in the membrane.

The concentration of the amphiphile directly available for permeation from the aqueous compartment, depends on the presence of binding agents:

$$\left[S_w^D\right] = \frac{\left[S^D\right]}{1 + K_{Alb}\left[Alb\right] + \sum_{i=1}^{n} K_{x_i}\left[x_i\right]} \qquad \text{(IX.5).}$$

x_i = VLDL, LDL, HDL_2, HDL_3

An increase in the rate constant of insertion (k_+) leads to a corresponding increase in the equilibrium association with the cell membranes and with the lipoproteins. When $\sum_{i=1}^{n} K_{x_i}\left[x_i\right] \gg 1 + K_{Alb}\left[Alb\right]$, further increases in k_+ result in a nearly inversely proportional decrease in the aqueous concentration of amphiphile. In this situation, no variations are observed in the rate of insertion in the cell membranes, which is given by

$\kappa_+^{a^o} S_w^D \frac{A^{a^o}}{V_w^D}$. For sufficiently small values of k_+, the amount of solute in the aqueous phase and bound to albumin becomes significant ($\sum_{i=1}^{n} K_{x_i}[x_i] \leq 1 + K_{Alb}[Alb]$) and the solute concentration in the aqueous phase is not inversely proportional to k_+, leading to faster insertion as k_+ increases.

The sensitivity profile is similar for all amphiphiles, with a slope approaching zero for k_+ near to the reference values, with larger sensitivities for the amphiphiles with a higher relative efficiency of sequestration by albumin.

The sensitivity analysis shows that for $n \leq 8$ translocation through the lipid bilayer is the rate limiting step (slope higher than 0.91), while for $n \geq 14$ desorption from the membrane is the rate limiting step (slope higher than 0.82). For amphiphiles with intermediate hydrophobicity (NBD-C_{10} and NBD-C_{12}) there is not a clear rate limiting step. This is in good agreement with the simple analysis performed in Figure IX.2.

IX.2.6 – Effect of Reversibility in the Solute Transfer and Presence of Sequestrators in the Acceptor Compartment

The above discussion was based on the results obtained with the model considering irreversible transfer of solute (M1). Trying to more closely approach the most probable *in vivo* conditions, and to evaluate the dependence of the amount of solute transferred on the permeability coefficient, we have considered three additional models. In M2 the tissue is considered equivalent to water, leading to minimal transfer of solutes through the cell monolayer. The amount of solute that permeates the cell monolayer is progressively increased with the inclusion of albumin in the tissue (M3) and considering equal binding capacity in both the serum and tissue (M4). Figure IX.7A shows the amount of amphiphile in the acceptor compartment at equilibrium and Figure IX.7B shows the permeability coefficient calculated using equation (IX.3). As expected, introduction of reversibility in the system results in less amphiphile permeating to the acceptor compartment. However, the introduction of binding capacity in the acceptor compartment, experimentally mimicked by the addition of binding agents [406, 407,

417], results in an increasing amount of amphiphile permeating through the barrier. The amount of amphiphile accumulated in the tissue decreases with the solute hydrophobicity in the models with reversibility (Figure IX.7 and Table A.7 in the Appendix) reflecting the less efficient binding of the most hydrophobic solutes by the tissue as compared with plasma and cell barrier. This will not necessarily occur in vivo due to the presence of cell membranes in the tissue but is expected to occur in vitro where the binding capacity in the acceptor compartment is equal to or smaller than the binding capacity in the donor compartment.

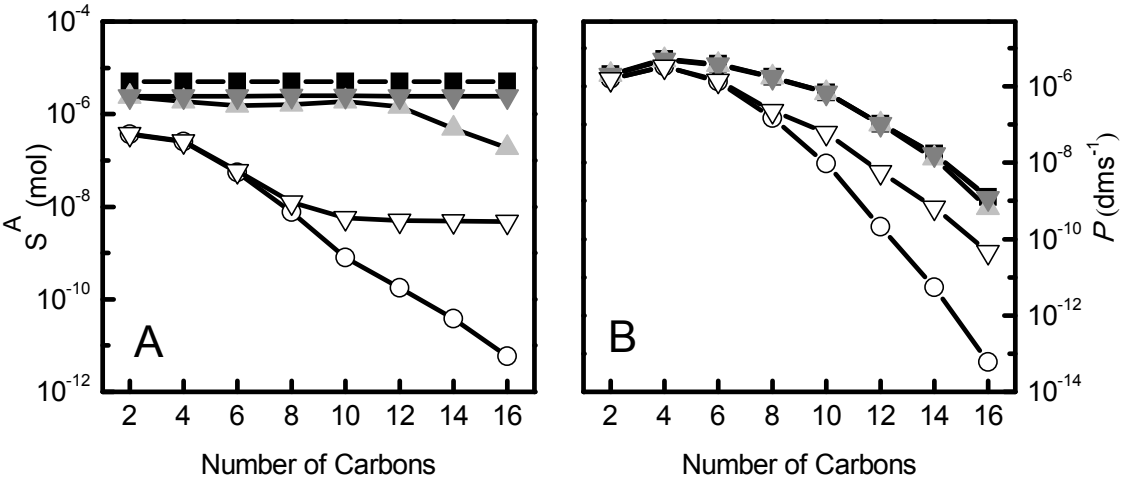

Figure IX.7 – Amount of amphiphile accumulated in the acceptor compartment (A), and permeability coefficient calculated from equation (IX.3) (B), for the transfer of the NBD-C_n homologous series from the serum to the tissue considering model M1 (black squares), M2 (white circles), M3 (light grey triangles), M4 (grey inverted triangles), and M4 with the amount of binding agents in the acceptor compartment decreased by a factor of 10^3 (white inverted triangles).

In all models considered the permeability coefficient increases from n = 2 to 4 and decreases with the increase in the amphiphile hydrophobicity for $n \geq 6$. The permeability coefficient obtained for the reversible models that consider a significant amount of solute binding in the acceptor compartment (M3 and M4) is very similar to that obtained for the irreversible system (M1). In contrast, in the absence of binding agents in the acceptor compartment (M2) the permeability coefficient is significantly smaller, particularly for the most hydrophobic solutes. Intermediate binding capacities lead to progressively smaller permeability coefficients. A reduction in the acceptor binding capacity in M4 by a factor of 10^3 reduces the permeability coeficients of NBD-C_2, NBD-C_4 and NBD-C_{16} to 77%, 68% and 4%.

This decrease in the permeability coefficient with decreasing binding capacity in the acceptor compartment is due to the establisment of significant backflow at earlier stages in the permeation leading to smaller net rates of solute permeation at the maximum (Figure A.24, in the Appendix).

IX.2.7 – Analytical Solutions to Predict the Rate of Permeation through the Cell Monolayer

The sensitivity analysis performed above allowed the identification of the rate limiting steps in the overall permeation. The existence of a single rate limiting step, in a localized transfer of the amphiphile from one compartment to another, implies that all the remaining steps are in equilibrium. Following this approach, two different situations can be considered for the reversible transfer: a) the rate limiting step is the interaction with the external leaflet of the apical membrane:

$$\begin{aligned} &S_{\mathrm{B}}^{\mathrm{D}} \xleftrightarrow[K_{\mathrm{B}}^{\mathrm{D}}]{} S_{\mathrm{W}}^{\mathrm{D}} \underset{\kappa_{-}^{a^o}}{\overset{\kappa_{+}^{a^o}}{\rightleftharpoons}} S^{a^o} \xleftrightarrow{K_{\mathrm{f}}^{a^{\mathrm{i}}/a^{\mathrm{o}}}} S^{a^i} \\ &S^{a^i} \xleftrightarrow{K_{\mathrm{P}}^{\mathrm{w}/a^{\mathrm{i}}}} S_{\mathrm{W}}^{e} \xleftrightarrow{K_{\mathrm{P}}^{b^{\mathrm{i}}/\mathrm{w}}} S^{b^i} \xleftrightarrow{K_{\mathrm{f}}^{b^{\mathrm{o}}/b^{\mathrm{i}}}} S^{b^o} \xleftrightarrow{K_{\mathrm{P}}^{\mathrm{w}/b^{\mathrm{o}}}} S_{\mathrm{W}}^{\mathrm{A}} \xleftrightarrow{K_{\mathrm{B}}^{\mathrm{A}}} S_{\mathrm{B}}^{\mathrm{A}} \end{aligned} \tag{IX.6}$$

and b) the rate limiting step is the translocation from the external leaflet to the internal leaflet of the apical membrane:

$$\begin{aligned} &S_{\mathrm{B}}^{\mathrm{D}} \xleftrightarrow[K_{\mathrm{B}}^{\mathrm{D}}]{} S_{\mathrm{W}}^{\mathrm{D}} \xleftrightarrow[K_{\mathrm{P}}^{\mathrm{w}/a^{\mathrm{o}}}]{} S^{a^o} \underset{k_{\mathrm{f}a}^{\mathrm{o}\to\mathrm{i}}}{\overset{k_{\mathrm{f}a}^{\mathrm{i}\to\mathrm{o}}}{\rightleftharpoons}} S^{a^i} \\ &S^{a^i} \xleftrightarrow{K_{\mathrm{P}}^{\mathrm{w}/a^{\mathrm{i}}}} S_{\mathrm{W}}^{e} \xleftrightarrow{K_{\mathrm{P}}^{b^{\mathrm{i}}/\mathrm{w}}} S^{b^i} \xleftrightarrow{K_{\mathrm{f}}^{b^{\mathrm{o}}/b^{\mathrm{i}}}} S^{b^o} \xleftrightarrow{K_{\mathrm{P}}^{\mathrm{w}/b^{\mathrm{o}}}} S_{\mathrm{W}}^{\mathrm{A}} \xleftrightarrow{K_{\mathrm{B}}^{\mathrm{A}}} S_{\mathrm{B}}^{\mathrm{A}} \end{aligned} \tag{IX.7}$$

where K_{B}^{r} refers to the equilibrium binding constant to the binding agents in the donor compartment (r=D) or acceptor (r=A), $K_{\mathrm{f}}^{\mathrm{x/y}}$ refers to the partition coefficient between the two leaflets (from y to x) of a given bilayer (being 1 for symmetric bilayers), and $K_{\mathrm{P}}^{x/y}$ is the partition coefficient between the membrane and the aqueous media (from y to x) and the other parameters are defined as in the legend of Figure IX.1. The analytical solution for a general system is presented in section A.IX.6 of the Appendix.

As expected from the sensitivity analysis, three distinct situations for accumulation of solute in the tissue were encountered. For the longer amphiphiles, the rate of

accumulation in the tissue is well described by the analytical solution obtained from equation (IX.6), while equation (IX.7) is not adequate (Figure IX.8A). For the shorter amphiphiles, the rate of accumulation in the tissue is best described by the analytical solution obtained from equation (IX.7), (Figure IX.8B). For the amphiphiles with intermediate hydrophobicity, NBD-C_{10} and NBD-C_{12}, none of the analytical solutions is able to describe adequately the rate of accumulation in the tissue, in agreement with the inexistence of a single rate limiting step in the overall permeation.

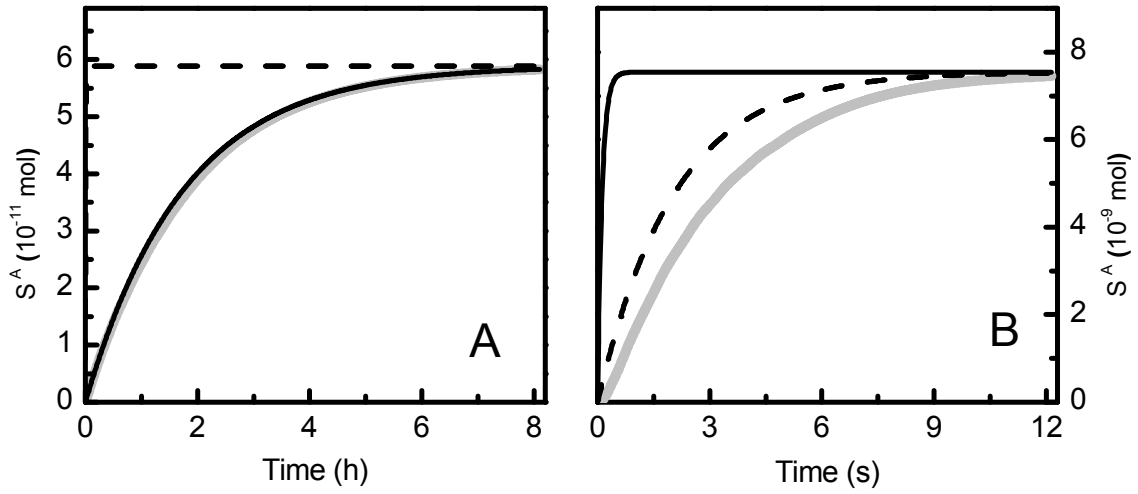

Figure IX.8 – Prediction of the accumulation of solute in the tissue according to the analytical solutions obtained from equation (IX.6) (solid black) or from equation (IX.7) (dashed black) and results obtained by integration of the complete kinetic scheme, equations (IX.1) (solid grey), for model M2. Plot A shows the results obtained for NBD-C_{16} (similar to NBD-C_{14}) and Plot B for NBD-C_8 (similar to NBD-C_n with n = 2, 4, 6). Note that in plot A the gray line is coincident with the predictions from equation (IX.6).

The analytical solutions for the irreversible transfer of solute into the tissue were obtained by considering that the solute interactions between the outer leaflet of the basolateral membrane and the aqueous media in the tissue can only occur in the direction membrane to tissue, $S^{b^o} \xrightarrow{\kappa_-^{b^o}} S_{\mathrm{W}}^{\mathrm{A}}$ instead of $S^{b^o} \xleftrightarrow{K_{\mathrm{P}}^{\mathrm{w}/b^{\mathrm{o}}}} S_{\mathrm{W}}^{\mathrm{A}}$ in equations (IX.6) and (IX.7), and that the intermediates are at steady state. The equations obtained are given in section A.IX.6 of the Appendix and the comparison between their predictions and the observed accumulation of solute in the tissue is shown in Figure IX.9. The results obtained are very similar to those described above for the models including reversibility.

It should be noted that while the rate of accumulation of the amphiphiles with the longer alkyl chain is very well described by equation (IX.6), Figure IX.8A and Figure IX.9A, the predictions from equation (IX.7) for the permeation of the amphiphiles with smaller alkyl chains is always somewhat faster than observed. This is due to the significant contribution of additional translocation steps in the pathway of the overall permeation. This discrepancy is expected to vanish when the lipid composition of the distinct cell membrane compartments is considered because the enrichment of the outer leaflet of the apical membrane in cholesterol and sphingomyelin leads to smaller rates of solute translocation [74]. The presence of additional steps of insertion/desorption does not lead to an incorrect prediction of the overall permeation because the rate of interaction with the membranes is dependent on the surface/volume ratio that is smallest for the case of the apical membrane/donor compartment.

The good agreement between the predictions from the analytical solutions and the observed overall permeation indicates that the overall rate of permeation can easily be predicted from the rate constants for the interaction of the permeating molecule with the membranes and that the rate limiting step can be identified. This can be achieved through the comparison between the predictions from both equations where the slowest permeation is the best predictor. Moreover, these equations can be used to perform a sensitivity analysis and guide molecular modifications in drug design in order to optimize the permeation process.

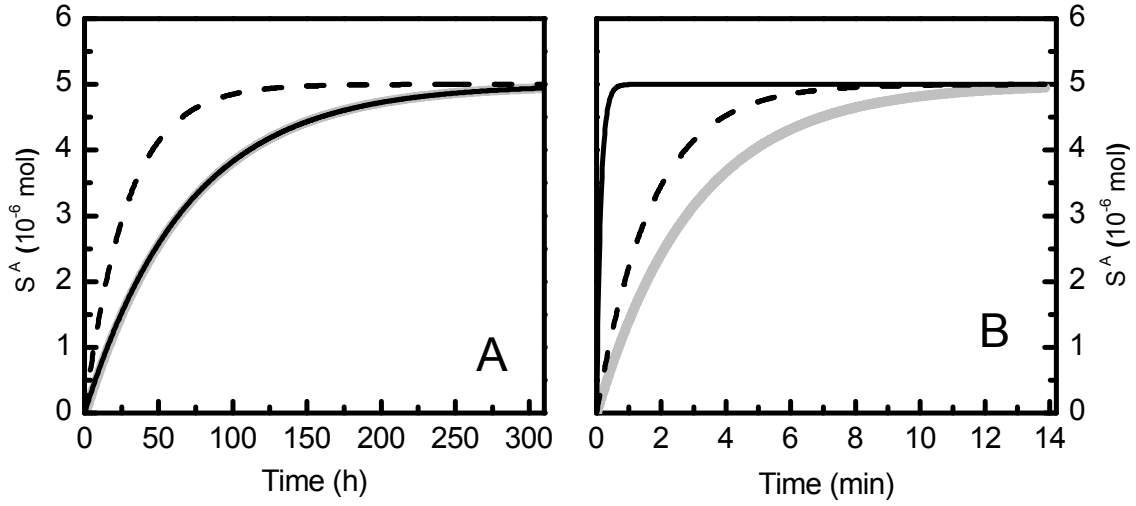

Figure IX.9 – Prediction of the accumulation of solute in the tissue according to the analytical solutions obtained from equation (IX.6) (solid black) or from equation (IX.7) (dashed black) and results obtained by integration of the complete kinetic scheme, equations (IX.1) (solid grey), for model M1. Plot A shows the results obtained for NBD-C_{16} (similar to NBD-C_{14}) and Plot B for NBD-C_8 (similar to NBD-Cn with n = 2, 4, 6). Note that in plot A the gray line is coincident with the predictions from equation (IX.6).

IX.3 – Concluding Remarks

A "master" kinetic scheme has been developed and applied to predict the rate of permeation across a cell monolayer, as an approximation to tight endothelia such as the blood-brain barrier. This mechanistic model can be applied to any molecule provided that the required experimental data are available.

From the solution of the kinetic scheme it was found that for some members of the homologous series of alkyl amphiphiles examined here, an increase in hydrophobicity leads to a decrease in the characteristic rate of accumulation in the tissue. This main result is the opposite of that predicted by the solubility-diffusion model.

The rate limiting step for overall permeation through the endothelium depends upon molecular characteristics of the amphiphile. For long chains it is the interaction (desorption rate constant) with the membrane of the endothelium, whereas for short chains it is translocation between bilayer leaflets. For intermediate chain lengths no single rate-limiting step can be defined. The inability of the solubility-diffusion model to describe the relative permeation of the entire homologous series is due to the violation of the assumption that trans-bilayer diffusion is always the rate limiting step.

In modeling membrane permeation, for most molecules of pharmacological interest, the membrane cannot be considered a canonic isotropic apolar fluid.

Solute sequestration by binding agents in the donor compartment substantially reduces the rate of overall permeation. Lipoproteins were found to affect the overall permeation of the most hydrophobic amphiphiles more significantly, whereas serum albumin dominates the sequestration of less hydrophobic solutes. Addition of binding agents to the acceptor compartment changes the permeability coefficient obtained in conditions of reversibility. This raises concerns about the adequate acceptor binding capacity to be considered in order to model the permeability of a concrete system.

Finally, we derived analytical equations that allow a simple characterization of the accumulation of amphiphiles in the tissue for the cases where a single limiting step was identified.

Chapter X

General Concluding Remarks

Understanding the interaction of amphiphiles with lipid bilayers is of fundamental importance to predict their bioavailability and permeation across tight endothelia such as the blood-brain barrier. In this work we have performed a detailed study, at diverse time and length scales, of the permeation of amphiphiles through lipid membranes, and their distribution among distinct biologic compartments. In this regard Chapters IV to VII referred to detailed atomistic MD simulations whereas Chapters VIII and IX referred to kinetic modeling simulations comprising experimental data and macroscopic information of biological systems. Following the work developed in the last years by this research group we characterized at atomic detail the interaction of the homologous series of fatty amines, NBD-Cn, with lipid bilayers of different compositions. The chosen lipid composition are POPC, the major constituent of biological membranes and, POPC:Chol (1:1) and SpM:Chol (6:4) which allow the emulation of the inner and outer leaflets, respectively, of erythrocytes and plasma membrane of endothelial cells. The chosen homologous series allows the systematic study of the effect of molecular structure, namely the hydrophobic/hydrophilic balance, on several properties, from the interaction with lipid bilayers to the permeation through cell monolayers.

For the first time, a complete series of homologous fluorescent membrane probes is studied using MD simulations. The atomistic description of these systems using unrestrained MD simulations has been a considerable contribution for the interpretation of experimental results obtained by this research group. We found that the NBD fluorophore locates near the glycerol backbone/carbonyl region of POPC for all derivatives. Location and orientation of the NBD fluorophore in this homologous series is similar to that determined for the acyl-chain labeled phospholipids C_6-NBD-PC and C_{12}-NBD-PC [264]. The perturbation of the lipid bilayer induced by moderate concentrations of NBD-C_n is relatively mild, as small, non-systematic variations were observed for parameters such as average area/lipid, bilayer thickness, POPC order parameters and lateral diffusion coefficient. The small variations of the transverse location of the fluorophore with probe chain length, agrees well with small variations measured in the photophysical properties of the various molecules. For example, the slightly deeper location of the fluorophore in NBD-C_{14} agrees with lower fluorescence quantum yield and anisotropy measured for this amphiphile [5]. The longer chained NBD-C_n amphiphiles show significant mass density near the bilayer midplane, and the chains of these derivatives interdigitate to some extent the opposite bilayer leaflet. This

phenomenon leads to a slower lateral diffusion for the longer-chained derivatives (n > 12). Amphiphiles with chain lengths inside the $8 \leq n \leq 12$ range have lateral diffusion coefficients similar to that of POPC, and, also taking into account their relatively mild perturbing effect, are useful fluorescent reporters of bilayer dynamics. This information allowed the interpretation of the maximal entropy variation obtained upon formation of the transition state in the desorption of NBD-C_{12} [6], which is due to the good structural matching between this amphiphile and the lipid bilayer, leading to the minimal entropy in the inserted state along the series.

The results obtained for the simulations in POPC:Chol (1:1) and SpM:Chol (6:4) bilayers also agree with both experimental and simulated published data. For all amphiphiles, and in both bilayers, the NBD fluorophore locates at the interface, in a more external position than observed in pure POPC bilayers. The more external position of the amphiphiles in the more ordered bilayers agrees with the low fluorescent quantum yield and higher ionization constants experimentally determined. Similarly to what was obtained in POPC bilayers, the longer-chained NBD-C_n amphiphiles show significant mass density near the bilayer midplane, and the chains of these derivatives, mainly NBD-C_{16}, interdigitate to some extent the opposite bilayer leaflet. As determined for the interaction with POPC, the effects of these amphiphiles on the structure and dynamics of the host lipid were also found to be relatively mild, in comparison with acyl-chain-labeled NBD probes [301]. As a matter of speculation, considering that biological membrane domains such as lipid rafts are rich in sphingomyelin and cholesterol, they are expected to exist in a relatively ordered state, not dissimilar to that of the systems addressed in this study. Therefore, for proteins which sit/locate in the head group region, with similar locations to that of the NBD group in our systems, the almost perfect fit of -C_{14} and -C_{16} chains attached to the protein and the host lipids' own chains in the same bilayer leaflet may be a reason why the acylation of proteins occurs mainly with myristoyl and palmitoyl acyl chains. Acyl chains that fit the thickness of a monolayer will allow the anchoring of proteins without perturbing the opposing membrane leaflet.

Further, the umbrella sampling technique was applied in order to compare calculated and experimental free energies of the insertion/desorption and translocation steps of the amphiphiles in lipid bilayers. We have determined the PMF profiles for a homologous series of amphiphiles, with the purpose of understanding the challenges and limitations

in related free energy calculations, and thereby to gain knowledge about appropriate criteria for convergence and sampling to avoid undesired artifacts. The present work provides an outlook of the issues that one has to deal with when free energy calculations of more and more complex molecules across membranes are being computed, and some pitfalls in free energy calculations were characterized. We found that the most challenging environment for free energy computations with long amphiphiles is the membrane-water interface. Despite quite extensive simulation times, when the amphiphiles in question were taken from the membrane to the water phase, and from water to the membrane, a substantial hysteresis at the membrane-water interface was observed. The analysis revealed that the cause of the hysteresis is the small frequency of insertion/desorption events of the amphiphile's alkyl chain in the membrane interface. As a second and related topic we observed lipids in a membrane to protrude towards the water phase, when an amphiphile around them was leaving the membrane, or approaching it from the water phase. With the PGD scheme, the alterations in membrane structure were observed to be larger than with the PGC method. The free energy results given by PGC were qualitatively consistent with experimental data, [5, 6], while the PGD results were not. Overall, it appears that the membrane-water interface is the region where the greatest care is required.

Following this methodological work, we proceed to the calculation and analysis of the PMF profiles of the homologous series of NBD-Cn amphiphiles with lipid bilayers of different composition, including an asymmetric bilayer. For all studied bilayers the PMF profiles have a minimum value when NBD is located at the head group region, which is more external in cholesterol-containing bilayers in agreement with other simulations and with unpublished experimental results from this research group. The quantitative comparison between simulation and experimental data is revealed as very complicated, precluding the determination of kinetic rate constants for systems that were not experimentally characterized. However, a qualitative description of the interaction of the amphiphiles at different bilayer depths was performed. This gives an enlightening illustration of the path of the amphiphiles during the permeation process through lipid membranes. Considering the bilayer, pure POPC in liquid disordered state is more prone to deformations than the cholesterol-containing membranes. Regarding the amphiphiles, the maximal value of the distance between the head group and the Cter is attained near the critical point before desorption, and correlates well with a situation

close to an *all-trans* conformation. However, regardless of the environment, the alkyl chains have preference for stretched confirmation. Concerning hydrogen bonding, as the NBD approaches/inserts into the bilayer, the probability of H-bonding with the lipid suddenly increases. According with the lower deformation of the cholesterol-containing membranes, the probability of the NBD establishing hydrogen bonds with the phospholipid, when deeply located inside the bilayer, is reduced. Inside the lipid bilayer, the NBD group tends to orient according with the membrane dipole potential. When deeply restrained in the membrane, it tends to orient the NO_2 towards the center of the bilayer. As the restraint distance increases, the hydrophobic chain serves as anchor and tends to orient the molecule along with the lipids in the bilayer, presenting angle distributions closer to 180º when the NBD is restrained near the desorption point. Overall, this analysis provides us with a complete illustration of the atomistic features related to the permeation of the amphiphiles through the lipid bilayers.

At larger time and length scales, the blood homeostasis and distribution of cholesterol was modeled using experimental data for the interaction of DHE and cholesterol with major blood compartments, namely lipid bilayers mimicking the erythrocyte membrane, lipoproteins and albumin. The model is able to reproduce the equilibrium distribution of cholesterol between blood compartments. DHE seems to be an adequate surrogate of cholesterol concerning its equilibrium distribution. However, its kinetics of interaction with biological compartments is significantly faster. The amount of cholesterol in the small lipoproteins pool (HDL) is more sensitive to variations in the rates of cholesterol entry into and removal from the blood, while LDL and VLDL are more robust regarding fluctuations in the total concentration of cholesterol. No excess accumulation is observed in erythrocytes, which have the slowest association kinetics. The results of this work show the importance of the passive pathway for the overall rate of exchange of cholesterol in the blood. Further, the results show that the application of experimental data for the interaction of amphiphilic molecules with biologic compartments can be used to assess their passive permeation through biological barriers.

In the last Chapter of this work this methodology was applied to build a mechanistic model for the passive permeation of amphiphilic molecules, like drugs, through a cell monolayer such as the tight endothelium of the BBB. It was found that for some members of the homologous series of alkyl amphiphiles examined here, an increase in hydrophobicity leads to a decrease in the characteristic rate of accumulation in the

tissue. This main result is the opposite of that predicted by the solubility-diffusion model, and consequently opposite to the inhomogeneous solubility-diffusion model applied in Chapter VII. The rate limiting step for overall permeation through the endothelium was found to depend upon molecular characteristics of the amphiphile. For long chains it is the interaction (desorption rate constant) with the membrane of the endothelium, whereas for short chains it is translocation between bilayer leaflets. For intermediate chain lengths no single rate-limiting step can be defined. This supports the idea that in modeling membrane permeation, for most molecules of pharmacological interest, the membrane cannot be considered a canonic isotropic apolar fluid. The mechanistic model allows the evaluation of the effect of binding agents, both from the blood side or from the tissue side. Solute sequestration by binding agents in the donor compartment substantially reduces the rate of overall permeation. Lipoproteins were found to affect the overall permeation of the most hydrophobic amphiphiles more significantly, whereas serum albumin dominates the sequestration of less hydrophobic solutes. Addition of binding agents to the acceptor compartment changes the permeability coefficient obtained in conditions of reversibility. This raises concerns about the adequate acceptor binding capacity to be considered in order to model the permeability of a concrete system. Finally, we derived analytical equations that allow a simple characterization of the accumulation of amphiphiles in the tissue for the cases where a single limiting step was identified. This work allowed the obtention of rules for permeation of drugs through the BBB. We believe that as the amount of data for the interaction of drugs with specific biological compartments increases, extensions or specific applications of the mechanistic model presented in this work can be very useful in drug design.

Appendix

This appendix section contains additional information that is mentioned through the text and usually is referred to as supplemental information accompanying published scientific papers.

Chapter IV – Interaction of NBD-labeled Fatty Amines with POPC Bilayers: A Molecular Dynamics Study

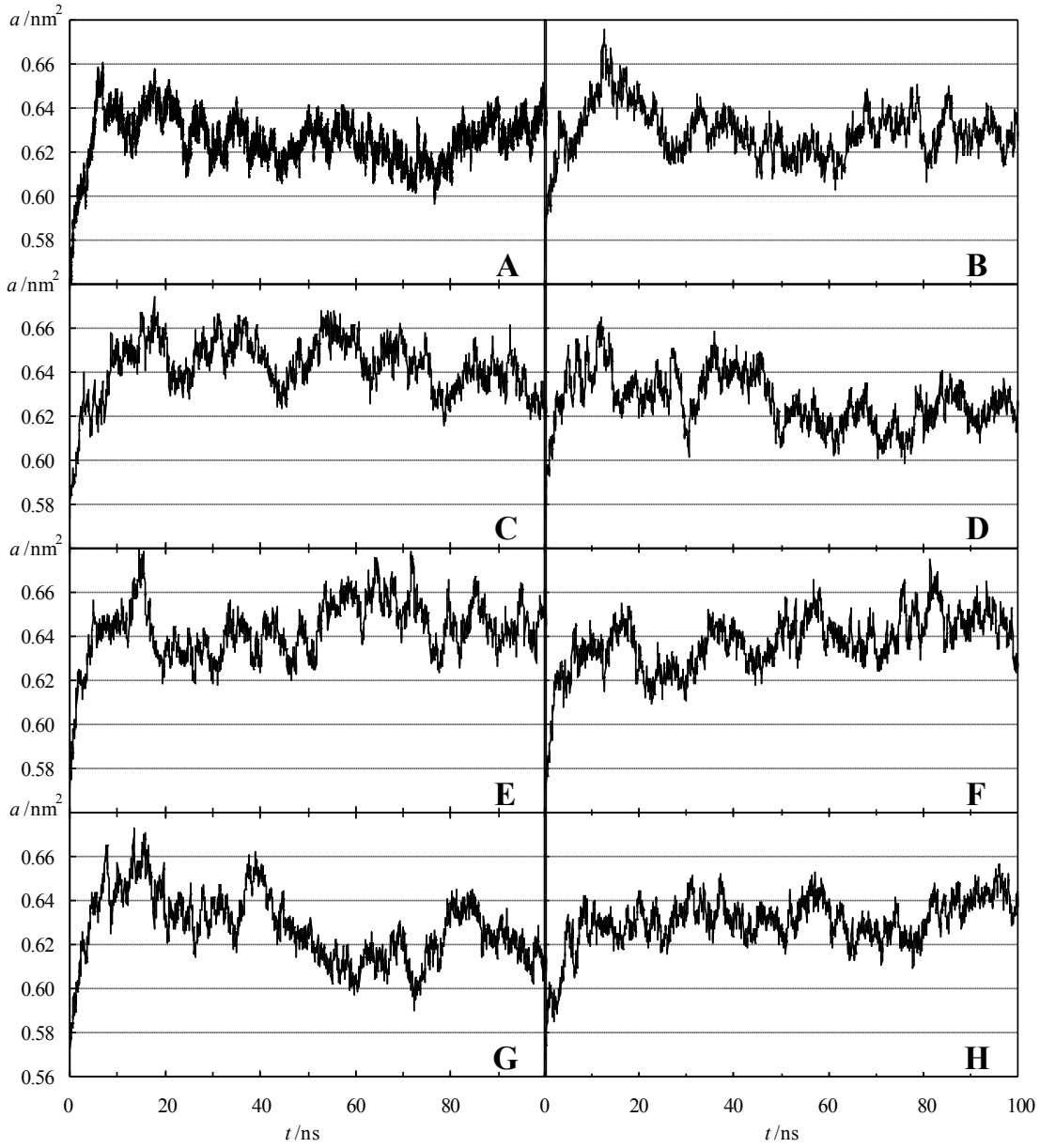

Figure A.1 - Instant area/lipid molecule (*a*) for (A) pure POPC and (B) 4 NBD-C_n/128 POPC bilayers. *n* = 4 (B), 6 (C), 8 (D), 10 (E), 12 (F), 14 (G) or 16 (H).

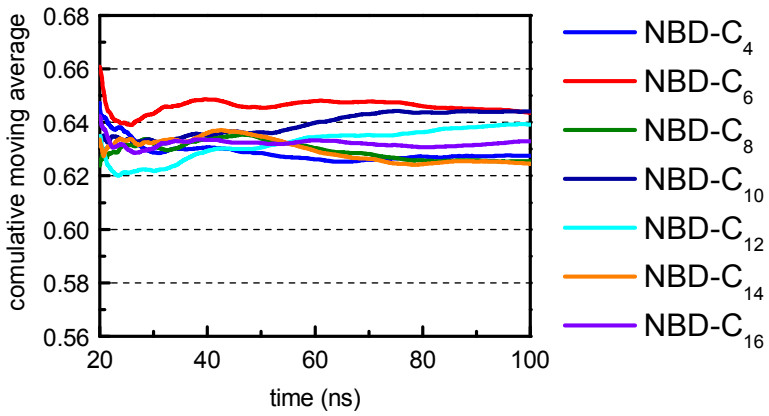

Figure A.2 – Cumulative moving averages of the area/lipid molecule for 4 NBD-C_n/128 POPC bilayers in the [20 ns, *t*] intervals. The vertical scale is the same used in Figure A.1.

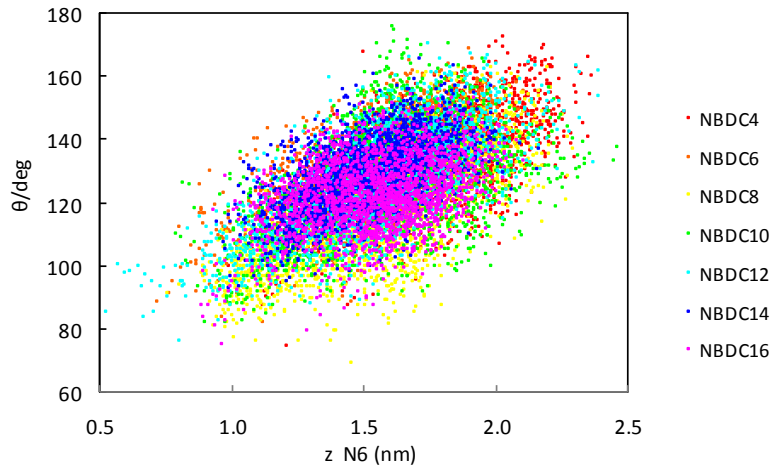

Figure A.3 – Correlation of the angle between the short axis, relative to the bilayer normal, and the position *z* of the N6 atom for a typical NBD-C_n molecule across the entire series.

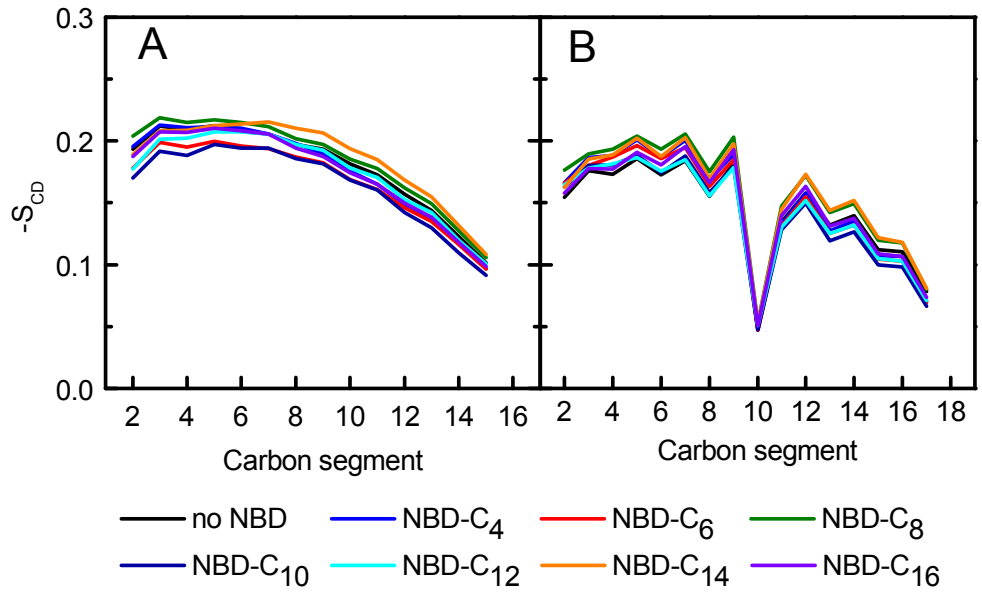

Figure A.4 – Deuterium order parameter of the POPC *sn*-1 (top) and *sn*-2 (bottom) carbon chains.

Chapter V – Interaction of NBD-labeled Fatty Amines with POPC:Chol and SpM:Chol Bilayers: A Molecular Dynamics Study

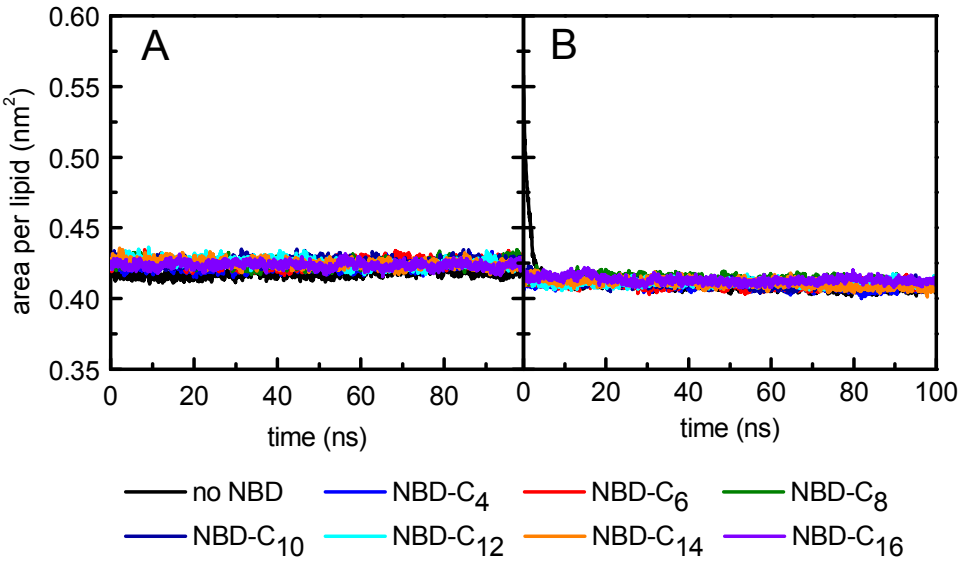

Figure A.5 – Time variation of the area per lipid for a) POPC:Chol and POPC:Chol:NBD systems, and for b) SpM:Chol and SpM:Chol:NBD systems.

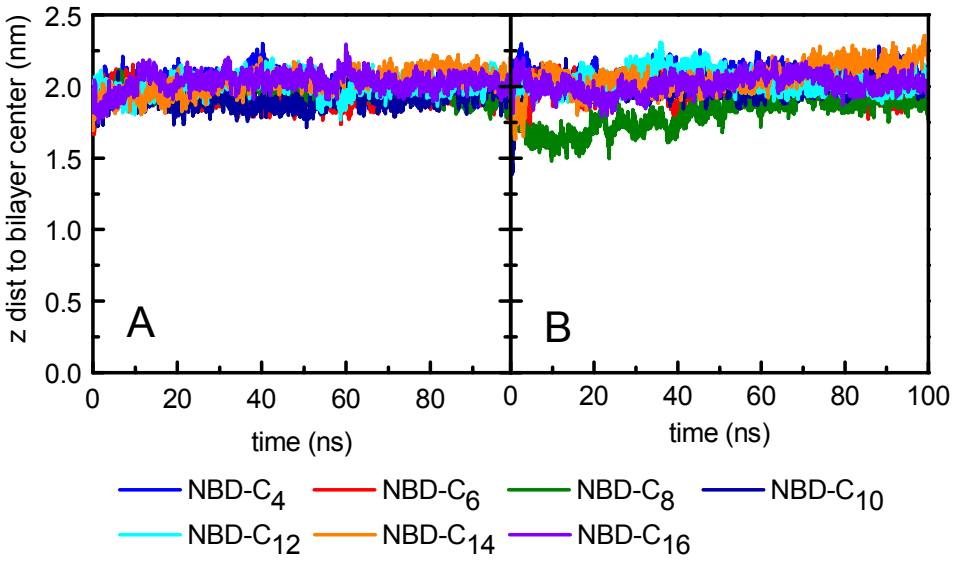

Figure A.6 – Time variation of the <z> distance of the NBD Center of mass to the center of the bilayer for: a) POPC:Chol:NBD systems, and for b) SpM:Chol:NBD systems.

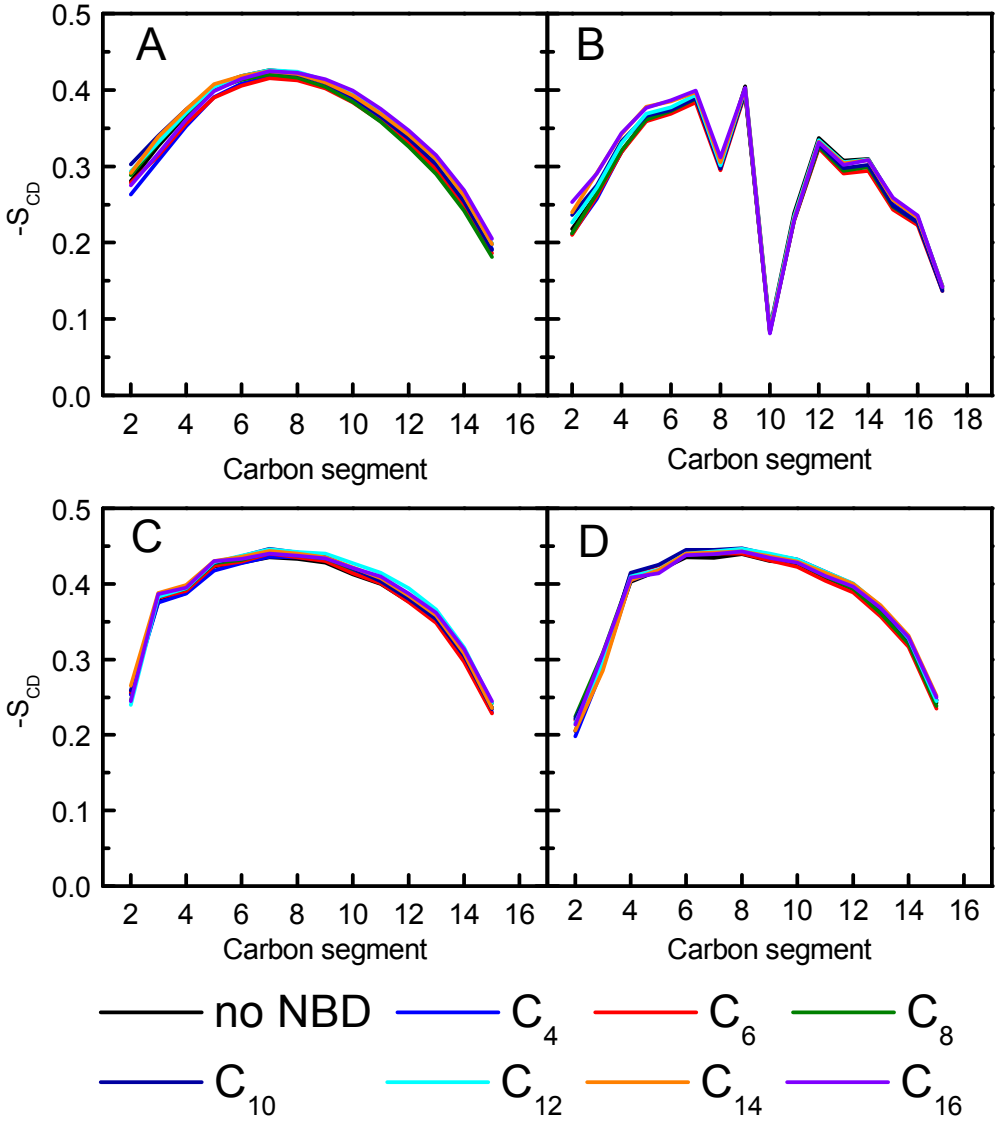

Figure A.7 – Deuterium order parameter of the POPC *sn*-1 (A) and *sn*-2 (B), and SpM acyl (C) and sphingosine (D) chains.

Chapter VI - How to Tackle the Issues in Free Energy Simulations of Long Amphiphiles Interacting with Lipid Membranes: Convergence and Local Membrane Deformations

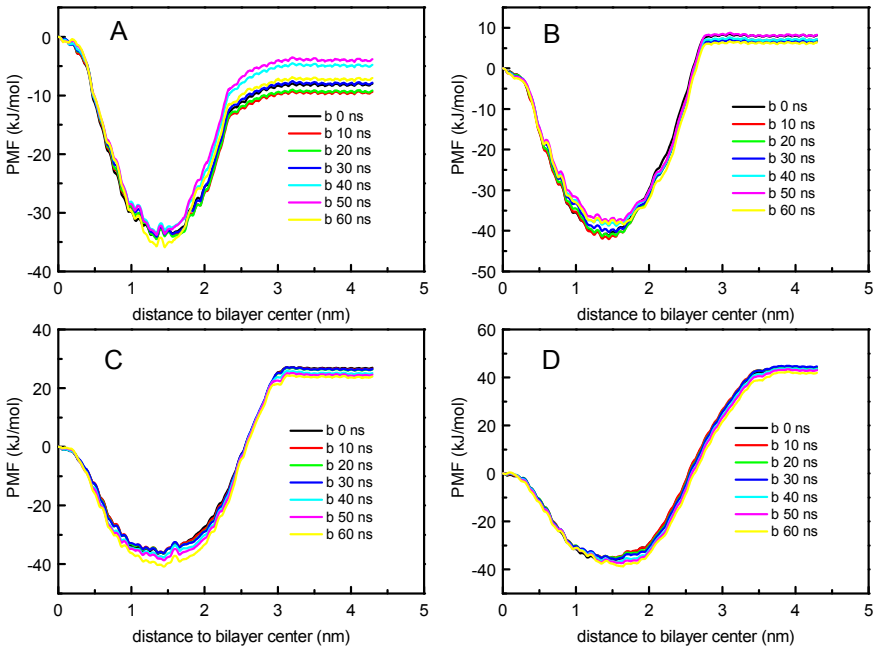

Figure A.8 – Convergence of the PMF profiles for the PGC method discarding initial simulation times. A) NBD-C_4; B) NBD-C_8; C) NBD-C_{12}; D) NBD-C_{16}. The maximum simulation time of each umbrella window is 100 ns.

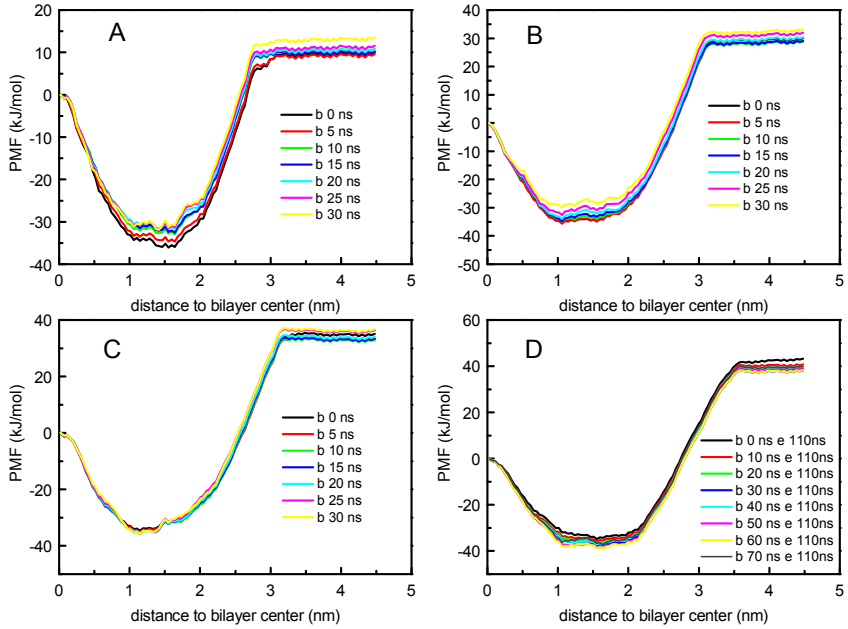

Figure A.9 – Convergence of the PMF profiles for the PGD method discarding initial simulation times. A) NBD-C_4; B) NBD-C_8; C) NBD-C_{12}; D) NBD-C_{16}. The maximum simulation time considered for each umbrella window of NBD-C_{16} is 110 ns. For NBD-C_4, NBD-C_8 and NBD-C_{12} the initial structures were equilibrated from that of NBD-C_{16}. That allows a maximal simulation time of each umbrella window of 50 ns.

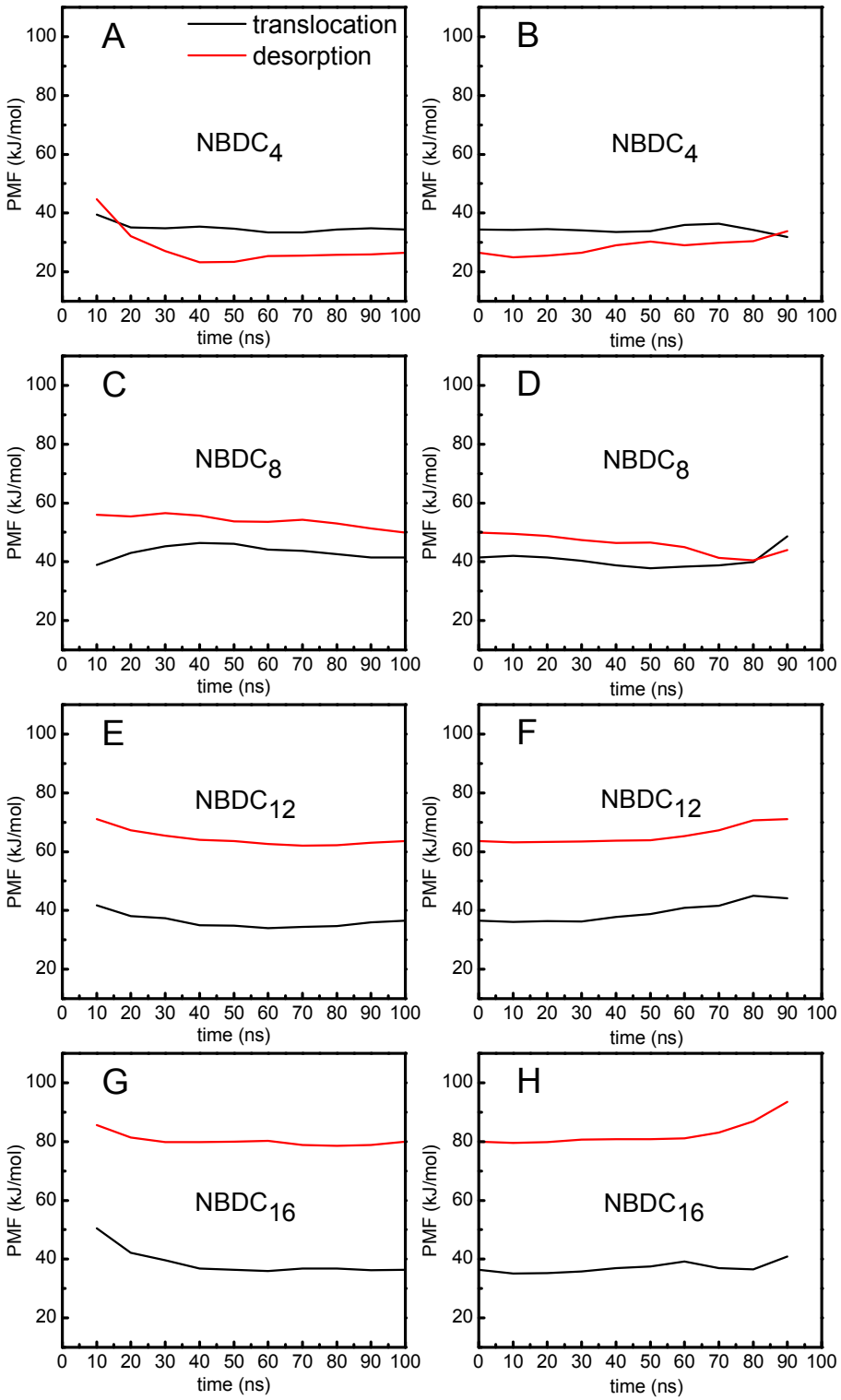

Figure A.10 – Convergence of the energy barriers for translocation and desorption, calculated from the PMF profiles for the PGC method increasing the total simulation time (A, C, E, G) and discarding initial simulation times (B, D, F, H) for NBD-C_4 (A, B), NBD-C_8 (C, D), NBD-C_{12} (E, F) and NBD-C_{16} (G, H). The maximal simulation time of each umbrella window is 100 ns.

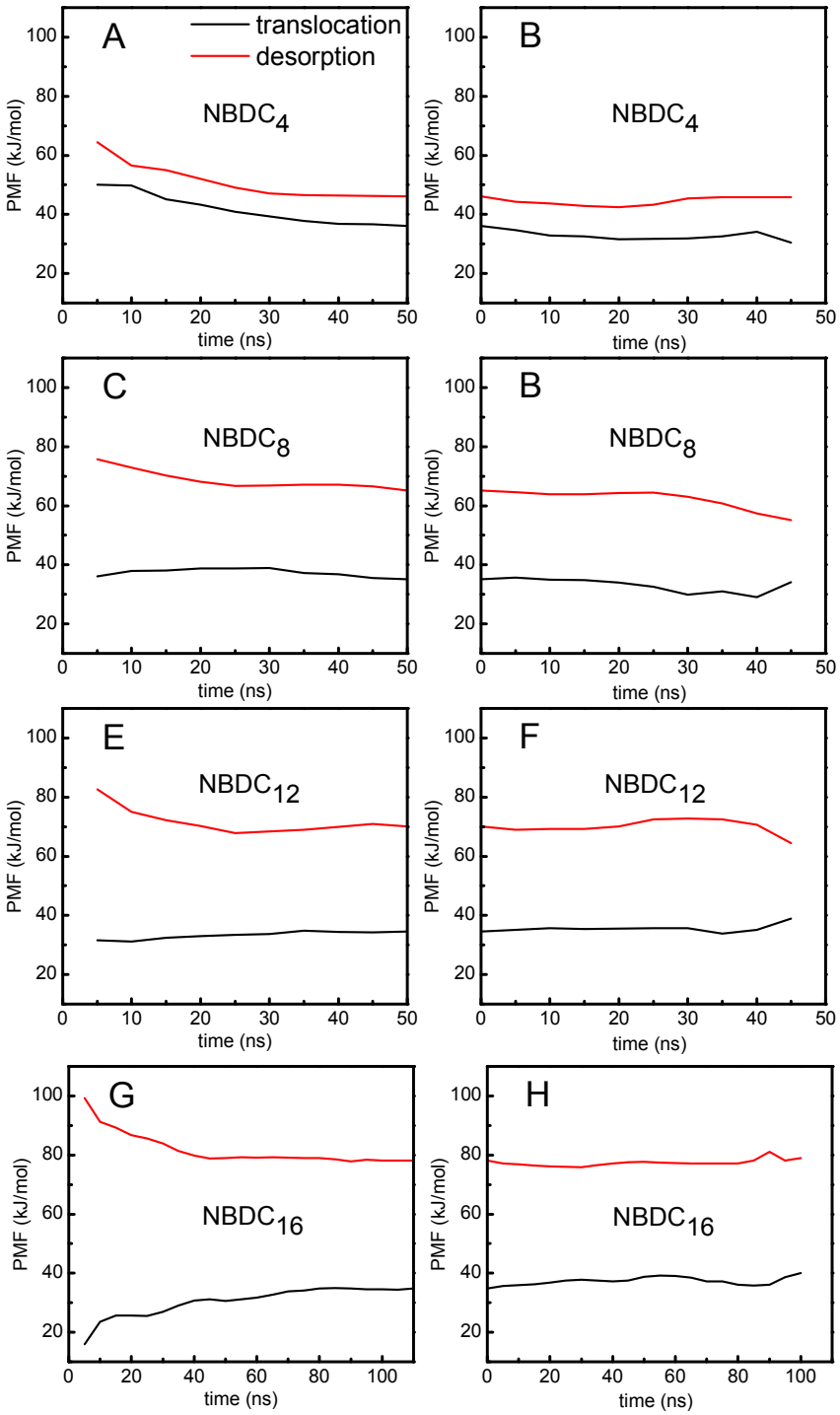

Figure A.11 – Convergence of the energy barriers for translocation and desorption, calculated from the PMF profiles for the PGD method increasing the total simulation time (A, C, E, G) and discarding initial simulation times (B, D, F, H) for NBD-C_4 (A, B), NBD-C_8 (C, D), NBD-C_{12} (E, F) and NBD-C_{16} (G, H). The maximal simulation time of each umbrella window is 110 ns for NBD-C_{16} and 50 ns for the remaining amphiphiles. The convergence analysis for NBD-C_{16} is shown in the main body of Chapter VI.

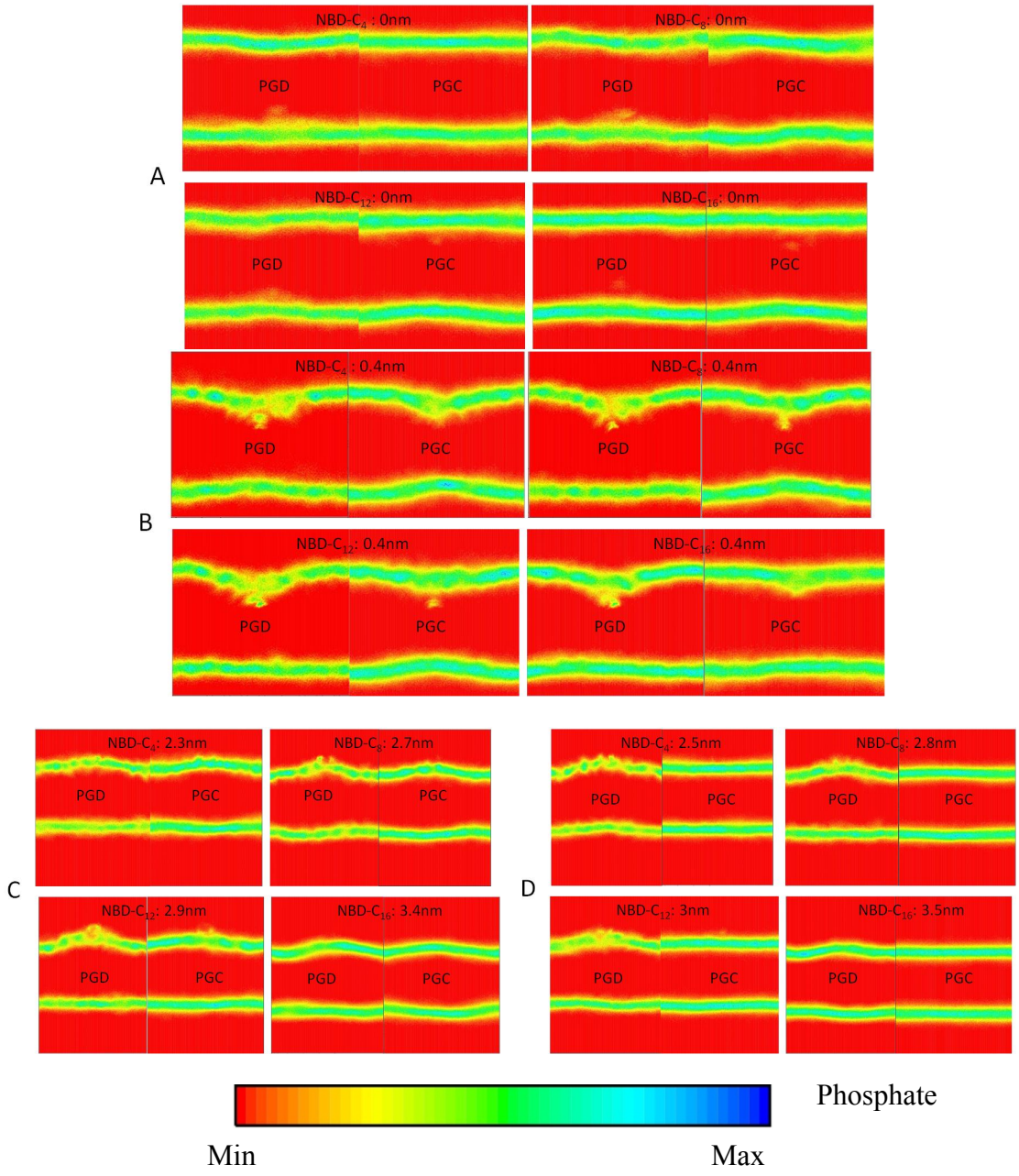

Figure A.12 – Density maps of POPC phosphate group for several systems at selected NBD distances from the bilayer center. In these maps, NBD is located in the *xy* center of the box, ordinate refers to the bilayer normal (*z*) direction, and abscissa is one of the directions along the bilayer plane (*y*). Density values, shown in color scale (see scale bar), are averaged along the *x* direction, for given *y* and *z*. A) NBD restrained at 0 nm from bilayer center; B) NBD restrained at 0.4 nm from bilayer center; C) NBD restrained at the desorption critical point with PGC (2.3, 2.7 2.9 and 3.4 nm, for NBD-C_4, NBD-C_8, NBD-C_{12}, NBD-C_{16}; respectively), D) NBD restrained at the desorption critical point with PGD (2.5, 2.8, 3.0 and 3.5 nm, for NBD-C_4, NBD-C_8, NBD-C_{12} and NBD-C_{16}; respectively).

Chapter VII - Free energy of Interaction of a Homologous Series of NBD-Labeled Fatty Amines with Lipid Bilayers

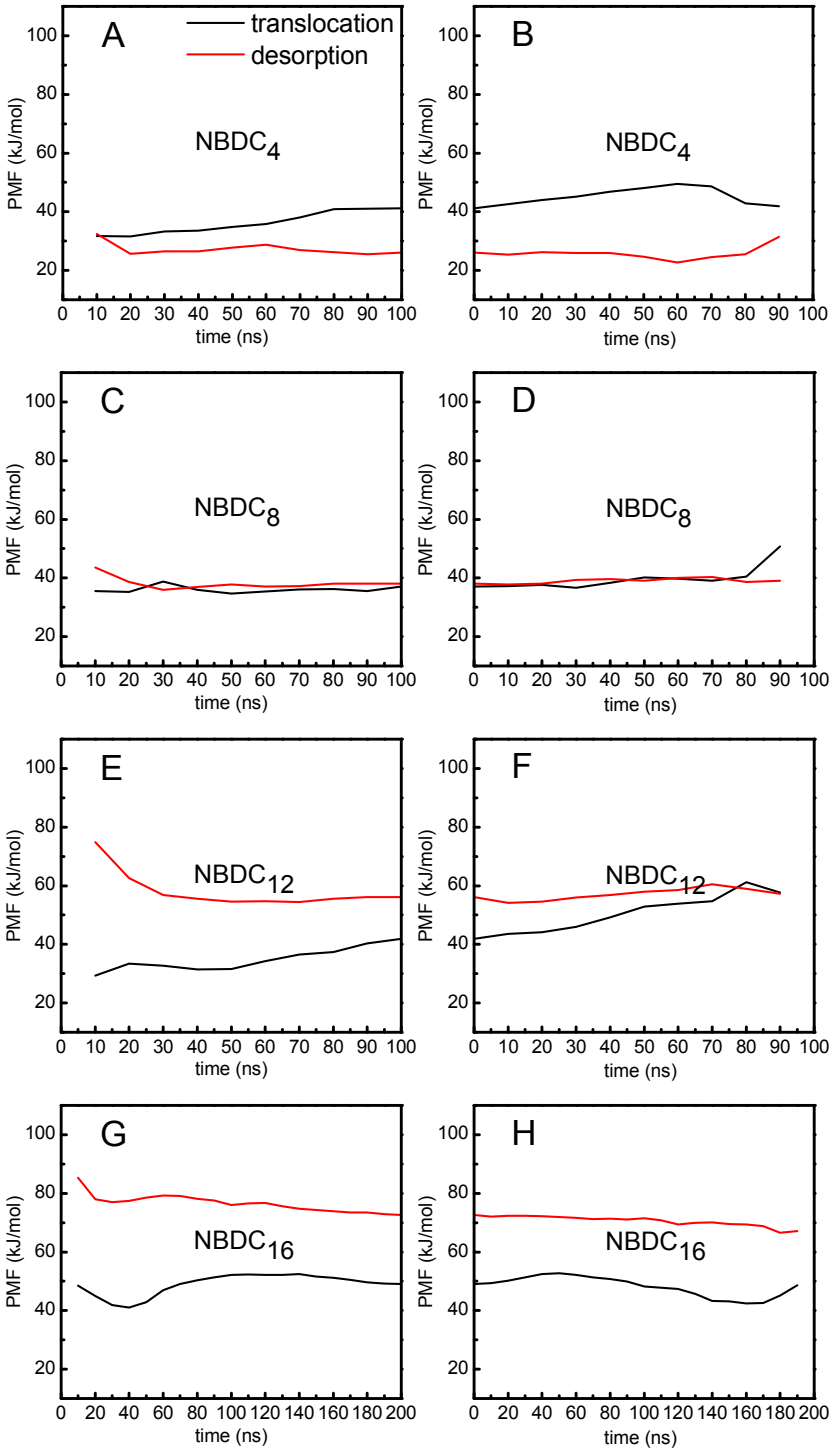

Figure A.13 – Convergence of the energy barriers for translocation (black) and desorption (red) of NBD-Cn in POPC:Chol (1:1) bilayers,, calculated from the PMF profiles increasing the total simulation time (A, C, E, G) and discarding initial simulation times (B, D, F, H) for NBD-C_4 (A, B), NBD-C_8 (C, D), NBD-C_{12} (E, F) and NBD-C_{16} (G, H). The maximal simulation time of each umbrella window is at least 100 ns.

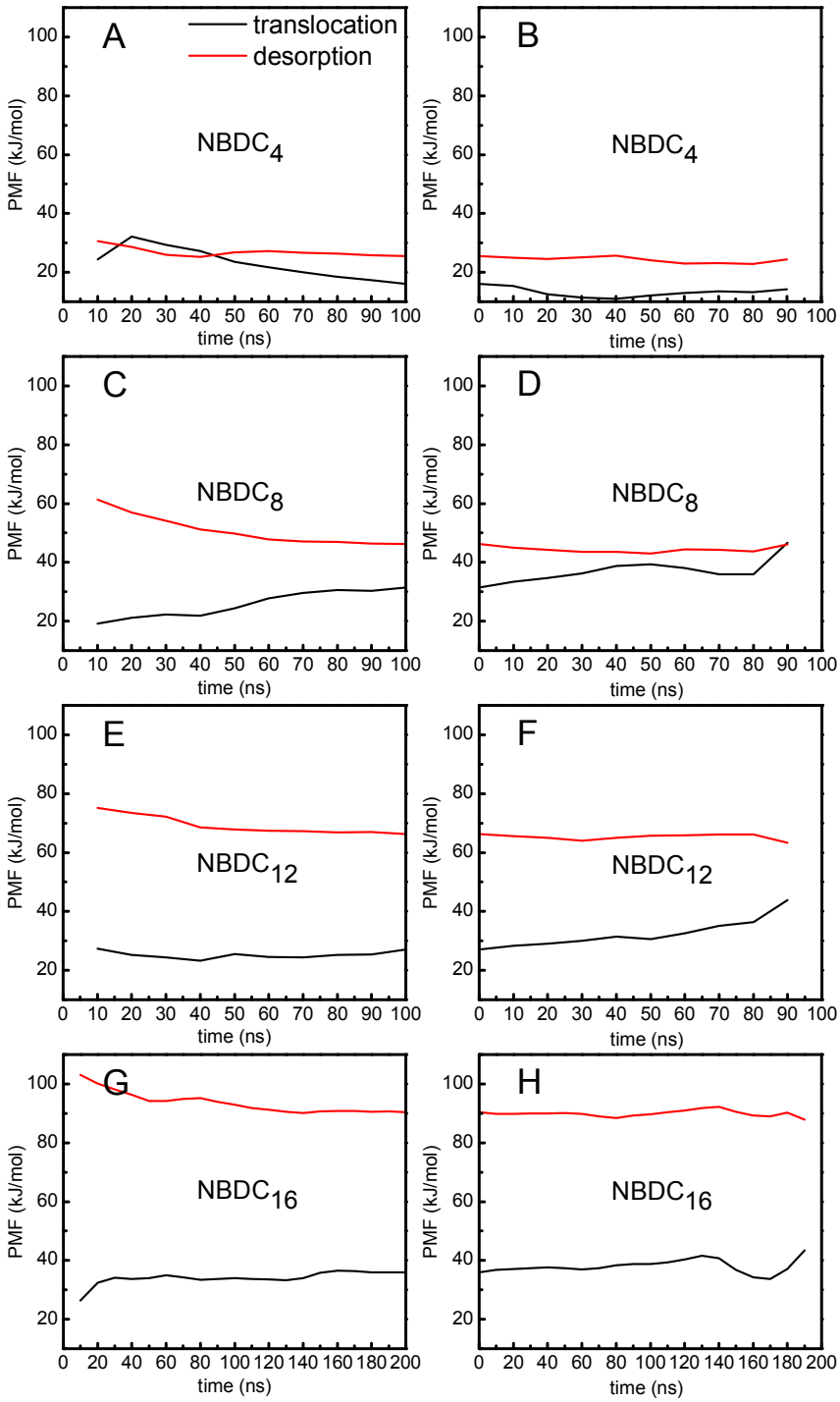

Figure A.14 – Convergence of the energy barriers for translocation (black) and desorption (red) of NBD-Cn in SpM:Chol (6:4) bilayers, calculated from the PMF profiles increasing the total simulation time (A, C, E, G) and discarding initial simulation times (B, D, F, H) for NBD-C_4 (A, B), NBD-C_8 (C, D), NBD-C_{12} (E, F) and NBD-C_{16} (G, H). The maximal simulation time of each umbrella window is at least 100 ns.

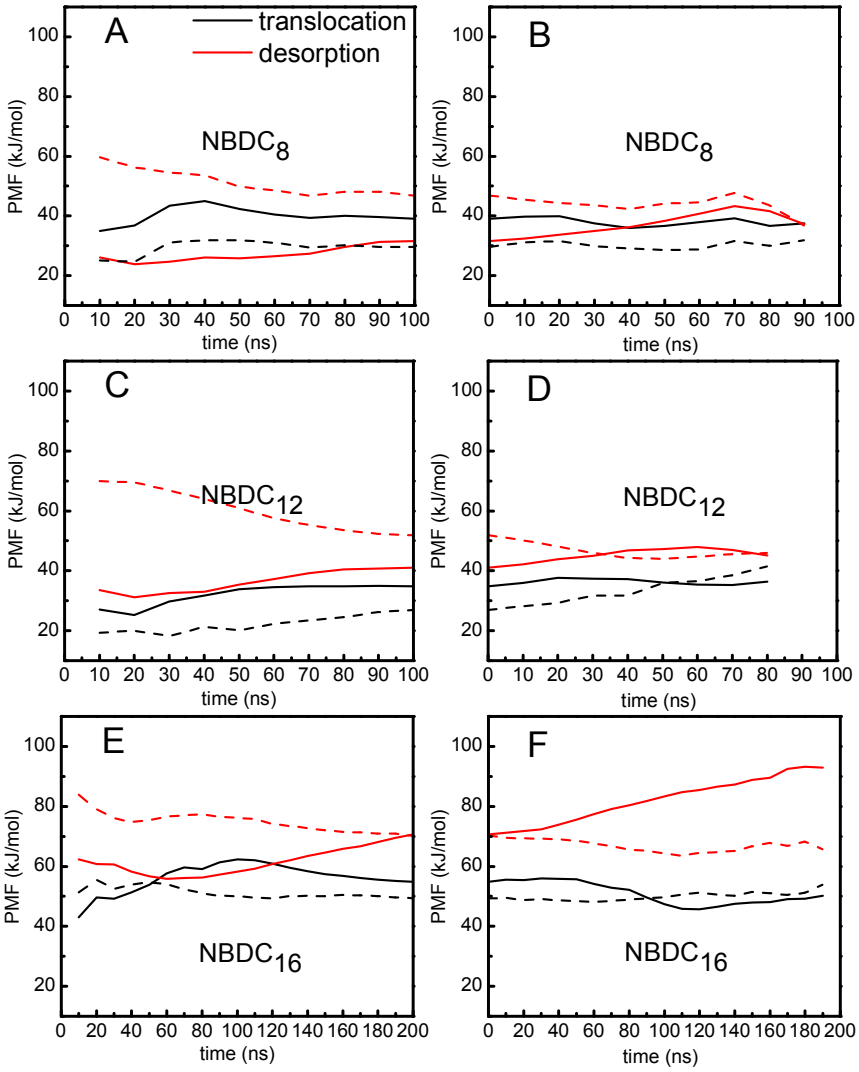

Figure A.15 – Convergence of the energy barriers for translocation (black) and desorption (red) of NBD-Cn in asymmetric bilayers for the POPC:Chol (1:1) leaflet (solid lines) and for SpM:Chol (6:4) leaflet (dashed), calculated from the PMF profiles increasing the total simulation time (A, C, E) and discarding initial simulation times (B, D, F), for NBD-C_8 (A, B), NBD-C_{12} (C, D) and NBD-C_{16} (E, F). The maximal simulation time of each umbrella window is at least 100 ns.

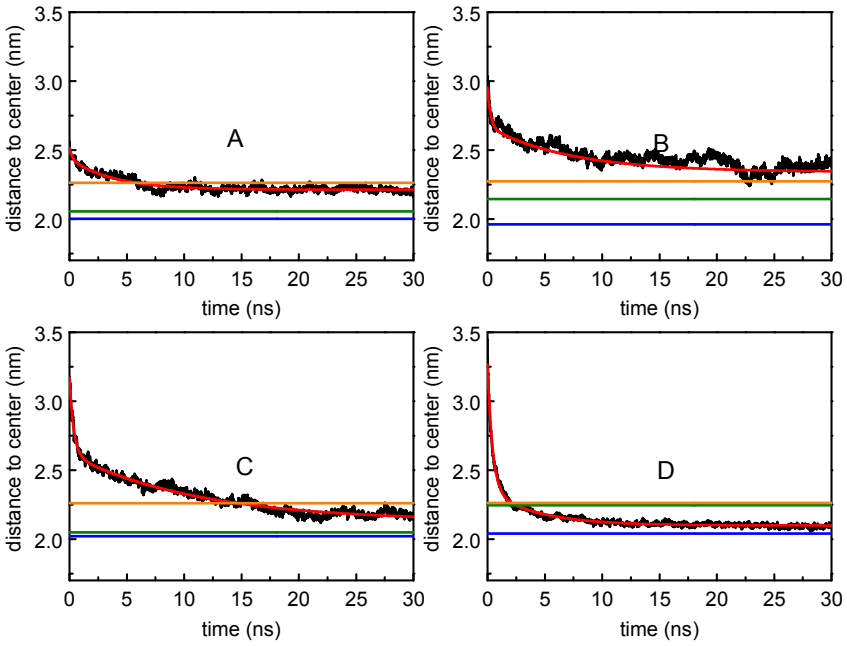

Figure A.16 – Relaxation of the amphiphiles, NBD-C_4 (A), NBD-C_8 (B), NBD-C_{12} (C) and NBD-C_{16} (D), from the desorption transition state until the equilibrium position in the POPC:Chol (1:1) bilayer. The average data of several simulations (black) was fitted with a biexponential function (red). Reference for P atoms (orange), and NBD equilibrium positions determined from unrestrained simulations (blue) and from PMF minima (green) are shown for comparison.

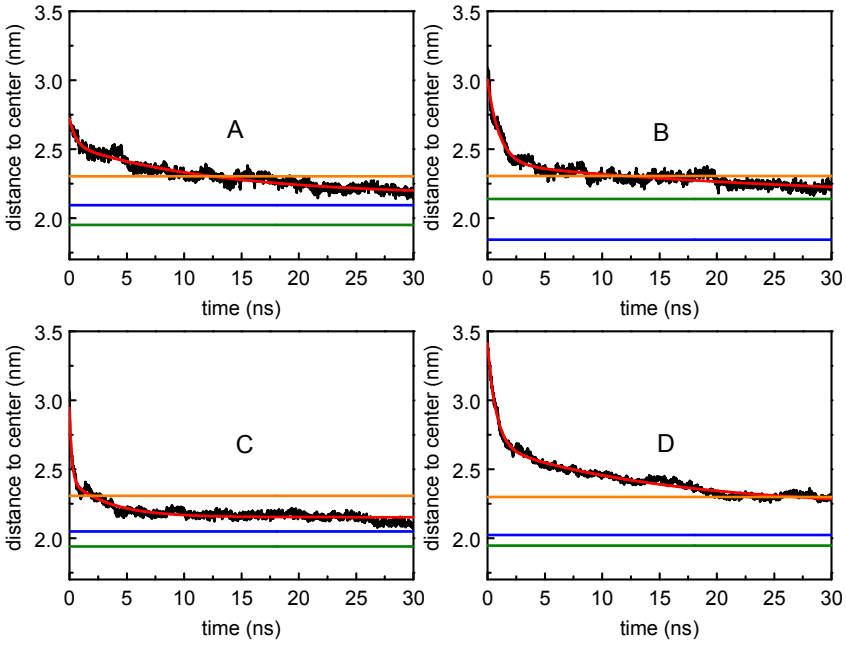

Figure A.17 – Relaxation of the amphiphiles, NBD-C_4 (A), NBD-C_8 (B), NBD-C_{12} (C) and NBD-C_{16} (D), from the desorption transition state until the equilibrium position in the SpM:Chol (6:4) bilayer. The average data of several simulations (black) was fitted with a biexponential function (red). Reference for P atoms (orange), and NBD equilibrium positions determined from unrestrained simulations (blue) and from PMF minima (green) are shown for comparison.

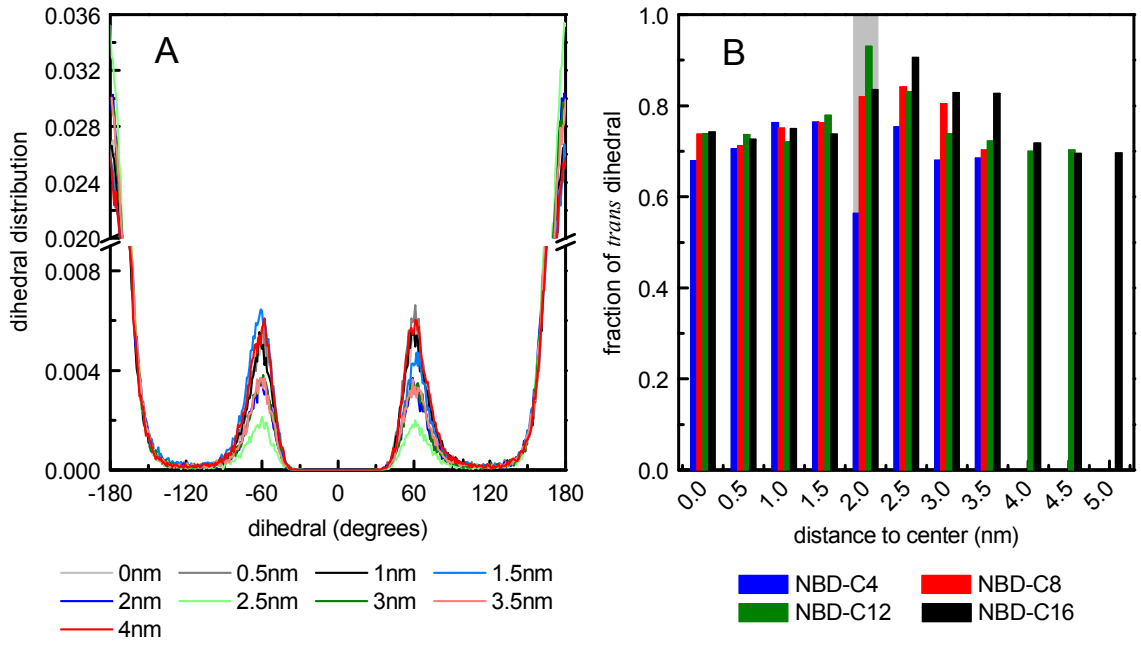

Figure A.18 – Chain dihedrals in POPC:Chol (1:1) bilayers. (A) distribution of the chain dihedrals of NBD-C_{16}, and (B) fraction of *trans* dihedrals of the alkyl chains of the NBD-C_n amphiphiles, as function of the distance of the NBD to the bilayer center. Gray bar indicates the equilibrium position of the NBD group.

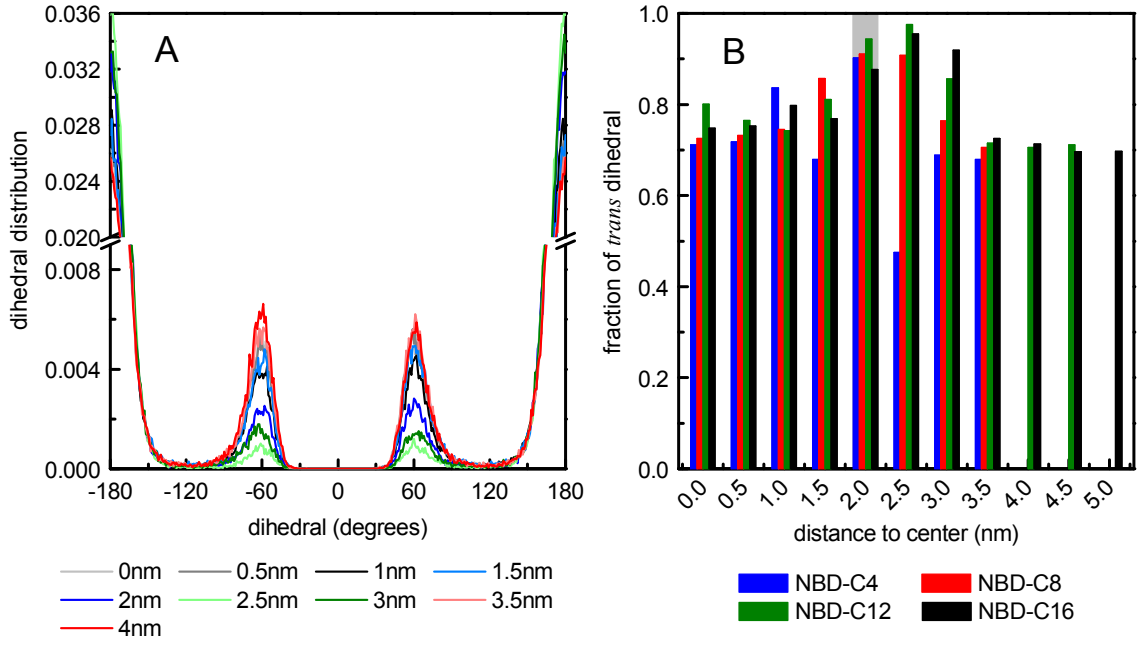

Figure A.19 – Chain dihedrals in SpM:Chol (6:4) bilayers. (A) distribution of the chain dihedrals of NBD-C_{16}, and (B) fraction of *trans* dihedrals of the alkyl chains of the NBD-C_n amphiphiles, as function of the distance of the NBD to the bilayer center. Gray bar indicates the equilibrium position of the NBD group.

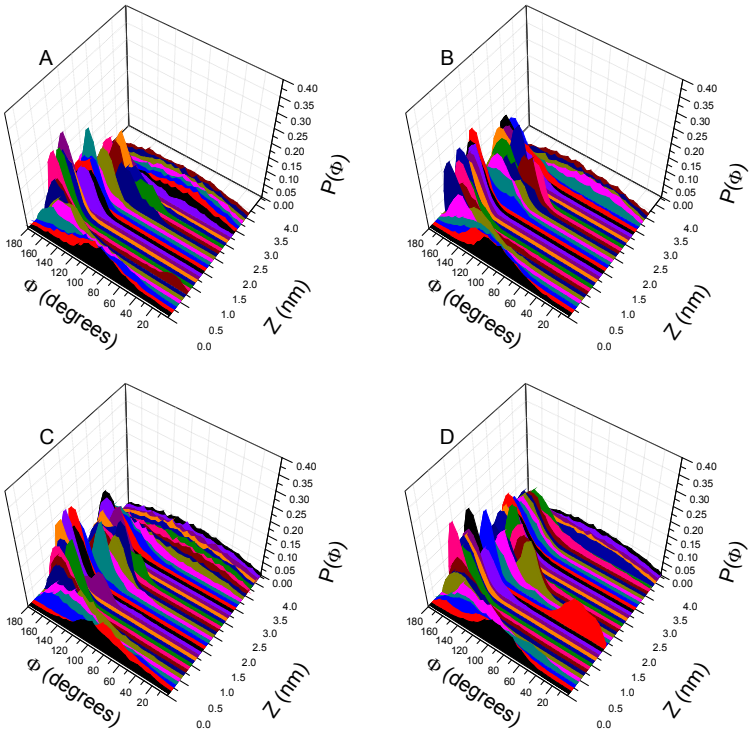

Figure A.20 – Orientation of the NBD group at different bilayer depths in POPC:Chol (1:1) bilayers for NBD-C_4 (A), NBD-C_8 (B), NBD-C_{12} (C) and NBD-C_{16} (D).

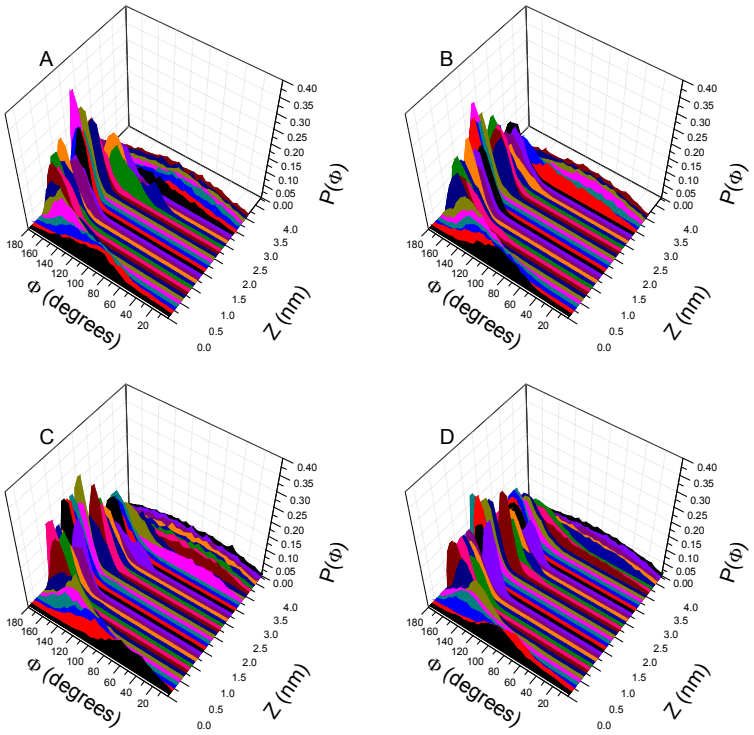

Figure A.21 – Orientation of the NBD group at different bilayer depths in SpM:Chol (6:4) bilayers for NBD-C_4 (A), NBD-C_8 (B), NBD-C_{12} (C) and NBD-C_{16} (D).

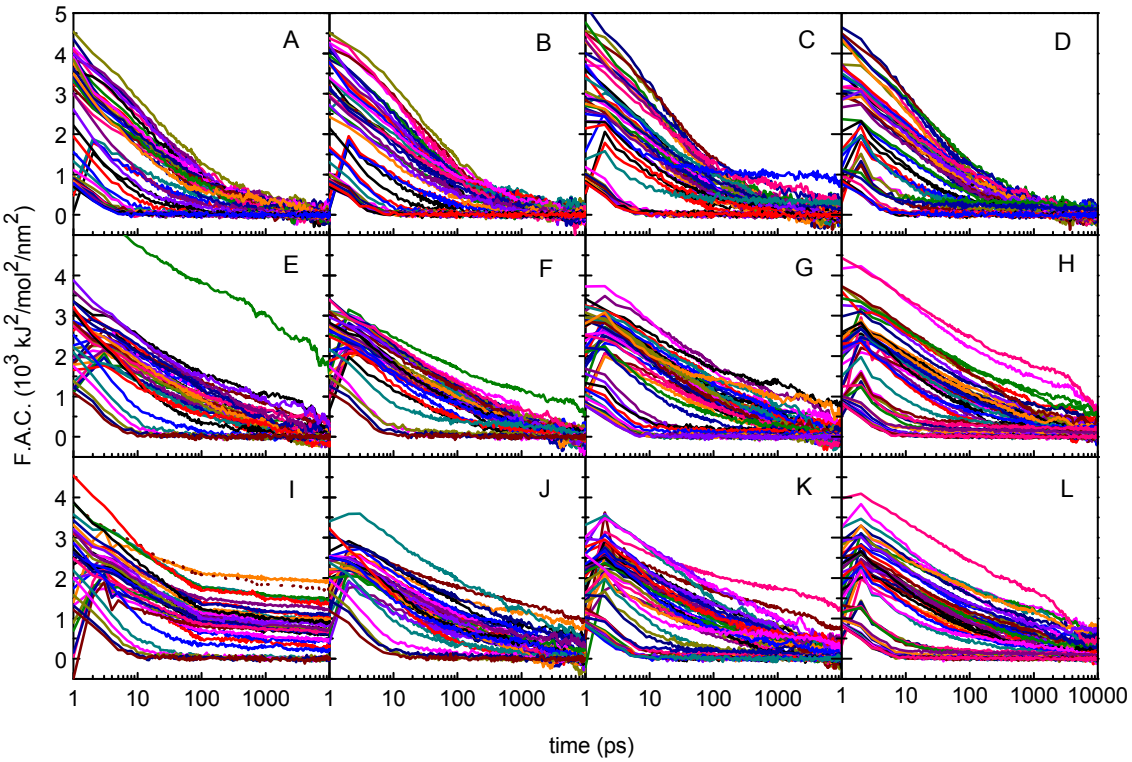

Figure A.22 – Force autocorrelation function of all trajectories with the NBD group at different bilayer depths, used for the calculation of *D*(z). Data are shown for NBD-C_4 (A, E, I), NBD-C_8 (B, F, J), NBD-C_{12} (C, G, K) and NBD-C_{16} (D, H, L) in POPC (A, B, C, D), POPC:Chol (1:1) (E, F, G, H) and SpM:Chol (6:4) (I, J, K, L) bilayers.

Chapter VIII – Homeostasis of Free Cholesterol in the Blood: a Preliminary Evaluation and Modeling of its Passive Transport

A.VIII.1 – Structural, equilibrium and kinetic and equilibrium parameters considered in the model

Table A.1 – Structural information and plasma concentration of lipoproteins.

	r [a] (nm)	M_W [a] (10^6 Da)	Protein [b] (w %)	nC [c]	$[L_P]$ [d] (μM)	mol % of surface lipids [f]		
						Chol	PC	SM
HDL_3	3.5	0.175	55	13	30 ±9	20	71	9
HDL_2	5.25	0.36	41	50	4 ±3			
LDL	10.8	2.3	23.9[e]	475	1.5 ±0.4	47	39	14
VLDL	27.5	45	7.7	3539	0.08 ±0.03	40	50	10

[a] values taken from [389]; [b] values taken from [388]; [c] number of unesterified cholesterol molecules *per* lipoprotein [197]; [d] values taken from [273]; [e] the w% of protein was calculated from the M_W of ApoB-100 and the overall M_W of LDL considering one ApoB-100 *per* LDL; [f] considering an average M_W of 775 for PC and SM, values taken from [390] and [389].

Table A.2– Rate and equilibrium constants, as well as thermodynamic parameters (in kJ mol^{-1}), for the interaction of DHE with the lipoproteins at 35 ºC. [10] The parameters for DHE interaction with lipid vesicles were taken from literature [139] and are also shown.

	HDL_3	HDL_2	LDL	VLDL	POPC:Chol (1:1)	SpM:Chol (6:4)
k_{diff} (10^{10} M^{-1} s^{-1})	2.1	2.9	5.6	14	25	25
k_{-diff} (10^{6} s^{-1})	143	66	16	2.5	0.77	0.77
k_{+} (10^{6} M^{-1} s^{-1})	3.4 ± 1.2	3.0 ± 1.5	4.1 ± 1.2	21 ± 8	64 ± 6	13 ± 1
k_{in} (10^{2} s^{-1})	234 ± 84	67 ± 34	12 ± 4	3.9 ± 1.5	2.0 ± 0.2	0.40 ± 0.03
k_{-} (10^{-3} s^{-1})	30 ± 8	25 ± 9	2.5 ± 1.1	1.7 ± 0.9	0.6 ± 0.2	0.07 ± 0.02
$K_P^{L_x/W}$ (10^5) [a]	11 ± 5	4.2 ± 0.9	11 ± 6	12 ± 10	25 ± 8	47 ± 15
$\Delta H^{o}_{(partition)}$	19 ± 9	4 ± 5	-42 ± 13	24 ± 30	-13 ± 10	53 ± 7
$T\Delta S^{o}_{(partition)}$	54 ± 10	37 ± 5	-6 ± 13	59 ± 30	23 ± 10 [b]	90 ± 7 [b]
$\Delta H^{\ddagger o}_{(insertion)}$	130 ± 10	116 ± 14	90 ± 7	95 ± 15	83 ± 7	110 ± 14
$T\Delta S^{\ddagger o}_{(insertion)}$	93 ± 10	79 ± 15	54 ± 7	63 ± 15	53 ± 7	77 ± 15
$\Delta H^{\ddagger o}_{(desorption)}$	111 ± 7	111 ± 10	132 ± 9	72 ± 21	95 ± 12	57 ± 16
$T\Delta S^{\ddagger o}_{(desorption)}$	27 ± 7	26 ± 11	41 ± 9	-20 ± 20	1 ± 12	-43 ± 16

[a] The partition coefficient between the aqueous phase and the lipid monolayer at the lipoproteins surface was calculated from the respective equilibrium binding constant as previously described [9].

[b] This entropy variation is different from the values given in the original reference because it is calculated from the temperature dependence of K_P (instead of K_{L_V}) to allow comparison between the parameters obtained for binding agents with very distinct sizes.

A.VIII.2 – Derivation of the equations used to model cholesterol homeostasis in the blood

Definition of the rate constants as moles *per* surface area *per* time

In the kinetic schemes for the interaction of solutes with binding agents, the binding agents were defined as individual particles and the corresponding insertion rate constants have units of M^{-1} s^{-1}. The rate constants obtained for the lipoproteins and BSA may be directly used to model cholesterol homeostasis in the blood because their structural properties in the blood and in the above model system are the same and their concentration in the blood is known. However, the rate constants obtained for the interaction of DHE with liposomes [139] cannot be used directly to model the

interaction of cholesterol with the erythrocyte membrane because the size and shape of the binding agents is different.

We have found that the association of DHE with the liposomes is not diffusion controlled; *i. e.* not all encounters between DHE and the liposomes lead to insertion of DHE into the lipid bilayer [139]. As a consequence, the association of DHE with lipid bilayers is not dependent on the state of division of this phase (size and shape of the lipidic phase) but simply on the surface area of the phase accessible to DHE. However, it is necessary to convert the rate constants obtained as a function of the liposome concentration into rate constants expressed in terms of lipid surface area accessible (A_L^o) and volume of each phase, as illustrated in Figure A.23. For simplification, in the derivation given below it is considered that only the outer monolayer of the LUVs is accessible to the solute (slow translocation).

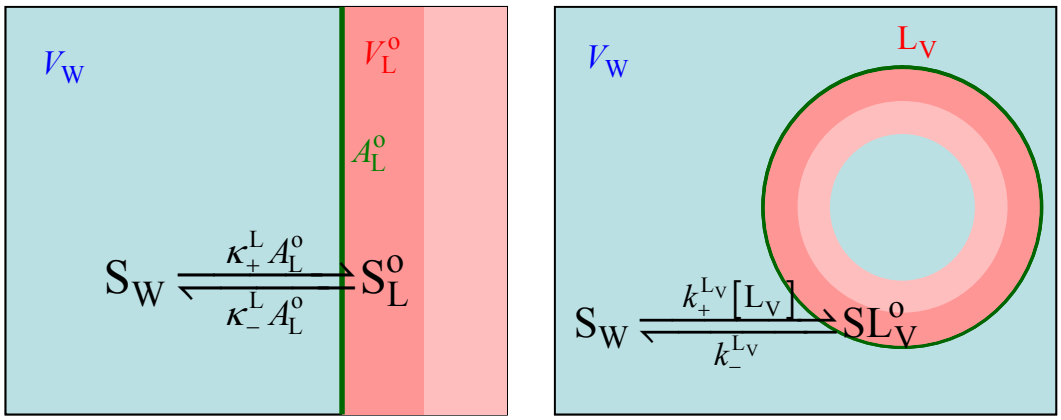

Figure A.23 – Schematic description for the association of the amphiphile with the lipid bilayer considered as a phase (left) and considering the fragmentation of the lipidic phase into LUVs (right).

The kinetic scheme shown in Figure A.23 for the lipid bilayer as a phase with the volume of the outer monolayer (V_L^o) in contact with the aqueous phase through the surface with the area A_L^o, leads to the following differential equation for the time dependence of the solute contents in the lipid phase (S_L^o):

$$\frac{dn_{S_L^o}}{dt} = \kappa_+^L A_L^o \frac{n_{S_W}}{V_W} - \kappa_-^L A_L^o \frac{n_{S_L^o}}{V_L^o} \qquad \text{A.1,}$$

from which the time dependence of the concentration of amphiphile in the lipid phase, with respect to the total volume, may be obtained:

$$\frac{d\left[\mathrm{S_L^o}\right]_\mathrm{T}}{dt} = \frac{d\left(n_{\mathrm{S_L^o}}/V_\mathrm{T}\right)}{dt} = \kappa_+^\mathrm{L} A_\mathrm{L}^\mathrm{o}\left[\mathrm{S_W}\right]_\mathrm{T}\frac{1}{V_\mathrm{W}} - \kappa_-^\mathrm{L} A_\mathrm{L}^\mathrm{o}\left[\mathrm{S_L^o}\right]_\mathrm{T}\frac{1}{V_\mathrm{L}^\mathrm{o}} \qquad \text{A.2.}$$

The differential equation that defines the temporal evolution of the concentration of solute in the outer monolayer of the LUVs when the fragmentation of the lipid bilayer is considered is given in equation A.3:

$$\frac{d\left[\mathrm{SL_V^o}\right]_\mathrm{T}}{dt} = k_+^{\mathrm{L_V}}\left[\mathrm{S_W}\right]_\mathrm{T}\left[\mathrm{L_V}\right]_\mathrm{T} - k_-^{\mathrm{L_V}}\left[\mathrm{SL_V^o}\right]_\mathrm{T} \qquad \text{A.3.}$$

The relation between the microscopic rate constants from both models may be obtained through the comparison of equations A.2 and A.3 and is shown in equations A.4 and A.5:

$$\kappa_+^\mathrm{L} = k_+^{\mathrm{L_V}}\frac{\left[\mathrm{L_V}\right]_\mathrm{T}}{\frac{A_\mathrm{L}^\mathrm{o}}{V_\mathrm{W}}} = k_+^{\mathrm{L_V}}\frac{\left[\mathrm{L_V}\right]_\mathrm{T}}{\frac{A_{\mathrm{L_V}}^\mathrm{o}\left[\mathrm{L_V}\right]_\mathrm{T}V_\mathrm{T}}{V_\mathrm{W}}} = k_+^{\mathrm{L_V}}\frac{1}{A_{\mathrm{L_V}}^\mathrm{o}}\frac{V_\mathrm{W}}{V_\mathrm{T}} \cong k_+^{\mathrm{L_V}}\frac{1}{A_{\mathrm{L_V}}^\mathrm{o}} \qquad \text{A.4}$$

$$\kappa_-^\mathrm{L} = k_-^{\mathrm{L_V}}\frac{\overline{V_{\mathrm{L_V}}^\mathrm{o}}}{A_{\mathrm{L_V}}^\mathrm{o}} = k_-^{\mathrm{L_V}}\ h \qquad \text{A.5}$$

where $\overline{A_{\mathrm{L_V}}^\mathrm{o}}$ is the molar surface area of lipidic phase accessible to the solute in the aqueous phase outside the liposomes (the total surface area accessible (A_L^o) is equal to the molar surface area ($\overline{A_{\mathrm{L_V}}^\mathrm{o}}$) multiplied by the concentration of liposomes ($[\mathrm{L_V}]_\mathrm{T}$) and the total volume of the solution (V_T)), $\overline{V_{\mathrm{L_V}}^\mathrm{o}}$ is the molar volume and *h* is the thickness of the liposomes outer monolayer (*h* was set to 2 nm for all lipid monolayers considered in this model).

When the solute is allowed to equilibrate between the outer and inner leaflets (fast translocation), the total amount associated with the lipid bilayer ($\mathrm{S_L}$ or $\mathrm{SL_V}$ depending on the model) is larger than the one in contact with the active surface for transfer between the aqueous and lipid phases (A_L^o) or directly accessible to the aqueous media outside the LUVs when the model with the fragmented lipid phase is considered ($\mathrm{SL_V^o}$). The differential equations for the time evolution of the solute inserted in the lipid bilayer are now given by A.6 for the case of symmetric liposomes and by A.7 for the case of asymmetric bilayers. These two situations correspond to equal or different rates

of translocation from the inner to the outer leaflet ($k_{\mathrm{f}}^{\mathrm{i}\to\mathrm{o}}$) and from the outer to the inner leaflet ($k_{\mathrm{f}}^{\mathrm{o}\to\mathrm{i}}$), respectively:

$$\frac{d\left[\mathrm{SL_V}\right]_{\mathrm{T}}}{dt} = k_{+}^{\mathrm{L_V}}\left[\mathrm{S_W}\right]_{\mathrm{T}}\left[\mathrm{L_V}\right]_{\mathrm{T}} - k_{-}^{\mathrm{L_V}}\left[\mathrm{SL_V}\right]_{\mathrm{T}}\frac{1}{2} \qquad \text{A.6}$$

$$\begin{aligned}\frac{d\left[\mathrm{S_L}\right]_{\mathrm{T}}}{dt} &= \kappa_{+}^{\mathrm{L}} A_{\mathrm{L}}^{\mathrm{o}}\left[\mathrm{S_W}\right]_{\mathrm{T}}\frac{1}{V_{\mathrm{W}}} - \kappa_{-}^{\mathrm{L}}\frac{A_{\mathrm{L}}^{\mathrm{o}}}{V_{\mathrm{L}}^{\mathrm{o}}}\left[\mathrm{S_L}\right]_{\mathrm{T}}\frac{k_{\mathrm{f}}^{\mathrm{i}\to\mathrm{o}}}{k_{\mathrm{f}}^{\mathrm{i}\to\mathrm{o}} + k_{\mathrm{f}}^{\mathrm{o}\to\mathrm{i}}} \\ &= \kappa_{+}^{\mathrm{L}} A_{\mathrm{L}}^{\mathrm{o}}\left[\mathrm{S_W}\right]_{\mathrm{T}}\frac{1}{V_{\mathrm{W}}} - \kappa_{-}^{\mathrm{L}}\frac{A_{\mathrm{L}}^{\mathrm{o}}}{V_{\mathrm{L}}^{\mathrm{o}}}\left[\mathrm{S_L}\right]_{\mathrm{T}}\frac{K_{\mathrm{P}}^{\mathrm{o}} V_{\mathrm{L}}^{\mathrm{o}}}{K_{\mathrm{P}}^{\mathrm{o}} V_{\mathrm{L}}^{\mathrm{o}} + K_{\mathrm{P}}^{\mathrm{i}} V_{\mathrm{L}}^{\mathrm{i}}}\end{aligned} \qquad \text{A.7.}$$

In this work, the outer leaflet of the erythrocyte was modeled by SpM:Chol (6:4) bilayers ($K_{\mathrm{P}}^{\mathrm{o}} = K_{\mathrm{P}}^{\mathrm{S:C}}$), the inner leaflet was modeled by POPC:Chol (1:1) bilayers ($K_{\mathrm{P}}^{\mathrm{i}} = K_{\mathrm{P}}^{\mathrm{P:C}}$) and the volumes of the outer and inner leaflets of the erythrocyte membrane were considered equal. The differential equations that describe the interaction of cholesterol with the blood compartments considered in this model, and the equations for the equilibrium distribution of cholesterol among the various compartments, may be obtained from those above and are given in the main text.

Chapter IX - Beyond Overton's rule - Quantitative Modeling of Passive Permeation through a Cell Monolayer

A.IX.1 – Structural, kinetic and equilibrium parameters considered in the model

Table A.3 – Kinetic and equilibrium parameters considered for the interaction of NBD-Cn with the lipid bilayers and with albumin.

Amphiphile	POPC					BSA
	k_+ ($M^{-1}s^{-1}$)	k_- (s^{-1})	k_f (s^{-1})	K_L (M^{-1})	K_P	K_B (M^{-1})
NBD-C_2	2.20×10^{11} [a]	3.79×10^{4} [a]	14.38 [b]	5.81×10^{6}	1.46×10^{2}	1.70×10^{4} [c]
NBD-C_4	1.91×10^{11} [a]	4.73×10^{3} [a]	7.59 [b]	4.04×10^{7}	1.02×10^{3}	1.70×10^{4}
NBD-C_6	1.50×10^{11} [a]	5.33×10^{2} [a]	4.00 [b]	2.81×10^{8}	7.07×10^{3}	6.30×10^{4}
NBD-C_8	8.55×10^{10}	44.0	2.11 [b]	1.94×10^{9}	4.89×10^{4}	5.20×10^{5}
NBD-C_{10}	6.98×10^{10}	5.10	1.59	1.37×10^{10}	3.44×10^{5}	6.30×10^{6}
NBD-C_{12}	1.96×10^{10}	2.07×10^{-1}	3.00×10^{-1}	9.47×10^{10}	2.38×10^{6}	1.90×10^{7}
NBD-C_{14}	7.80×10^{9}	1.18×10^{-2}	4.10×10^{-1}	6.61×10^{11}	1.66×10^{7}	2.40×10^{7}
NBD-C_{16}	3.46×10^{9}	7.61×10^{-4}	1.70×10^{-1}	4.55×10^{12}	1.14×10^{8}	5.50×10^{7}

[a] calculated from the results obtained experimentally for n=8 to 16 [6] considering the formation of an encounter complex of the amphiphile in the aqueous phase and the LUVs as an intermediate in insertion desorption (see [9] and references cited therein) and assuming linearity of the logarithm of the unimolecular rate constants of insertion and desorption with *n*.
[b] assuming linearity of $\ln(k_f)$ with *n* and considering the experimental values obtained for n=10 to 16 [6].
[c] same K_B as that of NBD-C_4 [418].

Table A.4 – Conversion factors used to calculate the rate and equilibrium parameters for the association of NBD-Cn with the lipoproteins from the experimental values obtained for their interaction with POPC membranes.

Conversion factor	Lipoprotein			
	VLDL	LDL	HDL_2	HDL_3
Insertion	3.48×10^{-1}	1.22×10^{-1}	3.35×10^{-2}	3.30×10^{-2}
Desorption	1.43	2.11	9.64	19.29
Equilibrium[a]	2.43×10^{-1}	5.78×10^{-2}	3.47×10^{-3}	1.71×10^{-3}

[a] ratio between insertion/desorption conversion factors.

Table A.5 – Concentration and structural parameters of the compartments considered in the model.

Compartment	Serum Concentration (M)	Compartment	Surface area (dm^2) [c]	Compartment	*Volume* (dm^3)
Alb	600×10^{-6} [a]	A^{a^o}	1.52×10^{4}	V_w^D	5.00 [d]
VLDL	8.00×10^{-8} [b]	A^{a^i}	1.52×10^{4}	V_w^T	5.00 [d]
LDL	1.50×10^{-6} [b]	A^{b^i}	2.28×10^{4}	$V_L^{a^i}$	3.03×10^{-4} [e]
HDL_2	4.00×10^{-6} [b]	A^{b^o}	2.28×10^{4}	$V_L^{a^o}$	3.03×10^{-4} [e]
HDL_3	30.0×10^{-6} [b]			V_w^e	1.52 [f]
				$V_L^{b^i}$	4.55×10^{-4} [e]
				$V_L^{b^o}$	4.55×10^{-4} [e]

[a] from [194].
[b] from [273].
[c] values adapted from [281]. The surface area of the basolateral membrane was defined as the area of the apical membrane multiplied by 1.5.
[d] V_w^D was taken from [281] and the same value was considered for V_w^T.
[e] area of the endothelial compartment (apical or basolateral) multiplied by the thickness of the lipid monolayer (2 nm).
[f] area of the apical membrane multiplied by 10 μm (thickness of the cell monolayer).

Table A.6 – Summary of the output data obtained with the kinetic model for the permeability coefficient (P), maximal rate of accumulation of solute in the tissue (V_{max}), time at which V_{max} is attained (t_{Vmax}) and time at which the system deviates 10% (50%) from the initial conditions considering that 100% variation is attained at equilibrium $t_{10\%}$ ($t_{50\%}$), for all the amphiphiles and models considered in this work.

	Model	C2	C4	C6	C8	C10	C12	C14	C16
P (dm^2/s)	M1	2.1×10^{-6}	5.1×10^{-6}	3.9×10^{-6}	1.8×10^{-6}	6.9×10^{-7}	1.1×10^{-7}	1.7×10^{-8}	1.3×10^{-9}
	M2	1.6×10^{-6}	3.3×10^{-6}	1.3×10^{-6}	1.5×10^{-7}	9.4×10^{-9}	2.1×10^{-10}	5.5×10^{-12}	6.0×10^{-14}
	M3	2.0×10^{-6}	4.8×10^{-6}	3.7×10^{-6}	1.7×10^{-6}	6.8×10^{-7}	9.9×10^{-8}	1.3×10^{-8}	6.6×10^{-10}
	M4	2.0×10^{-6}	4.9×10^{-6}	3.8×10^{-6}	1.8×10^{-6}	6.8×10^{-7}	1.0×10^{-7}	1.7×10^{-8}	1.2×10^{-9}
V_{max} (mol/s)	M1	3.2×10^{-8}	7.8×10^{-8}	6.0×10^{-8}	2.7×10^{-8}	1.0×10^{-8}	1.6×10^{-9}	2.6×10^{-10}	1.9×10^{-11}
	M2	2.4×10^{-8}	5.0×10^{-8}	2.0×10^{-8}	2.2×10^{-9}	1.4×10^{-10}	3.2×10^{-12}	8.0×10^{-14}	9.2×10^{-16}
	M3	3.1×10^{-8}	7.2×10^{-8}	5.4×10^{-8}	2.6×10^{-8}	1.0×10^{-8}	1.5×10^{-9}	2.0×10^{-10}	9.9×10^{-12}
	M4	3.1×10^{-8}	7.5×10^{-8}	5.8×10^{-8}	2.7×10^{-8}	1.0×10^{-8}	1.5×10^{-9}	2.5×10^{-10}	1.8×10^{-11}
t_{Vmax} (s)	M1	4.9	1.9	1.8	3.1	6.1	7.1×10^{1}	8.1×10^{2}	1.2×10^{4}
	M2	2.5	8.9×10^{-1}	5.8×10^{-1}	7.8×10^{-1}	1.4	1.3×10^{1}	3.2×10^{1}	1.2×10^{2}
	M3	4.2	1.6	1.4	2.5	5.2	5.6×10^{1}	4.3×10^{2}	4.2×10^{3}
	M4	4.3	1.7	1.6	2.7	5.4	6.3×10^{1}	6.9×10^{2}	1.0×10^{4}
$t_{10\%}$ (s)	M1	1.7×10^{1}	7.0	9.0	2.0×10^{1}	5.1×10^{1}	3.4×10^{2}	2.1×10^{3}	2.9×10^{4}
	M2	2.1	7.1×10^{-1}	4.1×10^{-1}	5.6×10^{-1}	1.1	1.0×10^{1}	5.5×10^{1}	6.9×10^{2}
	M3	8.7	2.9	3.0	6.9	2.1×10^{1}	1.1×10^{2}	3.6×10^{2}	$2.8\times10^{+3}$
	M4	9.0	3.7	4.7	1.0×10^{1}	2.6×10^{1}	1.8×10^{2}	1.1×10^{3}	1.6×10^{4}
$t_{50\%}$ (s)	M1	1.1×10^{2}	4.4×10^{1}	5.7×10^{1}	1.3×10^{2}	3.3×10^{2}	2.1×10^{3}	1.3×10^{4}	1.7×10^{5}
	M2	9.8	3.3	1.9	2.3	4.2	3.9×10^{1}	3.2×10^{2}	4.5×10^{3}
	M3	5.1×10^{1}	1.7×10^{1}	1.8×10^{1}	4.2×10^{1}	1.3×10^{2}	6.6×10^{2}	1.6×10^{3}	1.2×10^{4}
	M4	5.4×10^{1}	2.2×10^{1}	2.9×10^{1}	6.3×10^{1}	1.7×10^{2}	1.1×10^{3}	6.6×10^{3}	9.0×10^{4}

Table A.7 – Summary of system output data for the $\%S_T(\infty)$, $\%S_T(t_{Vmax})$, Max $\%S_{barrier}$ regarding S_{total} and Max $\%S_{barrier}$ regarding $S_T(\infty)$ for all amphiphiles of the NBD-C_n homologous series.

	Model	C2	C4	C6	C8	C10	C12	C14	C16
$\%S_T(\infty)$	M1	100.0	100.0	100.0	100.0	100.0	100.0	100.0	100.0
	M2	7.4	5.1	1.1	0.2	1.6×10^{-2}	3.5×10^{-3}	7.5×10^{-4}	1.2×10^{-4}
	M3	47.2	37.4	30.2	32.1	37.7	28.6	9.8	3.7
	M4	49.3	49.1	49.3	49.4	49.6	49.3	49.0	48.9
$\%S_T(t_{Vmax})$	M1	2.6	2.5	1.8	1.4	1.0	1.7	3.4	3.8
	M2	12.2	13.4	15.7	16.2	15.6	15.0	5.2	1.7
	M3	4.4	5.0	4.2	3.2	2.1	4.3	12.7	16.9
	M4	4.3	4.1	3.0	2.4	1.7	3.0	5.5	6.1
Max $\%S_{barrier}$ regarding S_{total}	M1	1.1	1.3	1.1	1.0	0.7	1.1	1.6	1.7
	M2	2.6	3.2	2.8	2.4	1.8	2.7	4.0	4.3
	M3	1.5	2.1	2.0	1.6	1.1	1.9	3.6	4.1
	M4	1.4	1.7	1.5	1.2	0.9	1.4	2.0	2.2
Max $\%S_{barrier}$ regarding $S_T(\infty)$	M1	1.1	1.3	1.1	1.0	0.7	1.1	1.6	1.7
	M2	35.0	62.6	254.6	1.6×10^{3}	1.1×10^{4}	7.6×10^{4}	5.3×10^{5}	3.7×10^{6}
	M3	3.1	5.6	6.6	5.1	2.9	6.7	36.9	110.6
	M4	2.9	3.5	2.9	2.4	1.8	2.8	4.2	4.5

Table A.8 – log(K_P) and clog($P_{Oct/w}$) for the NBD-C*n* homologous series at 298 K.

	Amphiphile (NBD-C*n*)							
	C_2	C_4	C_6	C_8	C_{10}	C_{12}	C_{14}	C_{16}
log(K_P)	2.2	3.0	3.8	4.7	5.5	6.4	7.2	8.1
clog$P_{Oct/w}$	2.0	3.0	3.9	4.9	5.9	6.9	7.9	8.8

Table A.9 – Sensitivity at the reference values to the different kinetic parameters.

	Amphiphile (NBD-C*n*)							
kinetic parameter	C_2	C_4	C_6	C_8	C_{10}	C_{12}	C_{14}	C_{16}
k_{ld}	0.00	0.00	0.00	0.00	0.01	0.11	0.03	0.00
k_f	1.00	1.00	0.98	0.91	0.62	0.34	0.03	0.00
k_+ and k_-	0.00	0.00	0.02	0.09	0.37	0.55	0.94	0.99
k_-	-0.91	-0.61	-0.43	-0.39	-0.24	0.14	0.82	0.95
k_+	0.91	0.62	0.44	0.48	0.60	0.41	0.12	0.04

A.IX.2 – Extrapolation of experimental parameters considering the encounter complex formalism.

The interaction of solutes with lipid membranes is usually and simply described by the equation A.8:

$$A+L_V \underset{k_-}{\overset{k_+}{\rightleftarrows}} AL_V \qquad K_L = \frac{k_+}{k_-} \tag{A.8}$$

where k_+ and k_- are insertion and desorption kinetic rate constants, respectively. However, when two entities collide with each other by random diffusion in condensed media, they stay some time in close proximity forming an encounter complex before random diffusion separates them apart. [381] During the lifetime of the encounter complex repeated collisions between the two entities occur and eventually a reaction takes place. The complete kinetic scheme considering the formation of the encounter complex is given by:

$$\begin{aligned} &\mathrm{A{+}L_V} \underset{k_{-diff}}{\overset{k_{diff}}{\rightleftarrows}} \mathrm{(A.L_V)} \qquad K_{(\mathrm{A.L_V})} = \frac{k_{\mathrm{diff}}}{k_{-\mathrm{diff}}} \\ &\mathrm{(A.L_V)} \underset{k_{out}}{\overset{k_{in}}{\rightleftarrows}} \mathrm{AL_V} \qquad\qquad K_{\mathrm{L}}^{'} = \frac{k_{\mathrm{in}}}{k_{\mathrm{out}}} \end{aligned} \tag{A.9}.$$

The encounter complex, ($A.L_V$), is formed from A and L_V with a diffusion-controlled rate constant, k_{diff}, and the two entities are held in close proximity by the solvent cage formed around them and by eventual interactions between their surfaces. This encounter complex is broken into the two free entities by diffusion with the rate constant k_{-diff}. The rate constants k_{diff} and k_{-diff} are given, respectively, as:

$$k_{\mathrm{diff}} = 4\pi a_{\mathrm{eff}} D_{\mathrm{eff}} \mathrm{N_A} \tag{A.10}$$

and

$$k_{\text{-diff}} = \frac{3D_{\mathrm{eff}}}{a_{\mathrm{eff}}^{\,2}} e^{-\frac{\Delta H_{(\mathrm{A.L_V})}}{\mathrm{R}T}} \tag{A.11}$$

where,

$$\begin{aligned} a_{\mathrm{eff}} &= a_{\mathrm{A}} + a_{\mathrm{L_V}} \\ D_{\mathrm{eff}} &= D_{\mathrm{A}} + D_{\mathrm{L_V}} = \frac{\mathrm{k_B}T}{6\pi\eta}\left(\frac{a_{\mathrm{A}} + a_{\mathrm{L_V}}}{a_{\mathrm{A}} a_{\mathrm{L_V}}}\right) \end{aligned} \tag{A.12}.$$

Here, a_{eff} is the sum of the radii of the amphiphile (calculated from the molecular volumes of the corresponding chemical groups [419] and the lipid aggregate (50 nm)), D_{eff} is the effective translational diffusion coefficient, N_A is the Avogadro constant, ΔH is the energy of interaction between the two entities in the encounter complex (here assumed to be zero), R is the ideal gas constant, T is the temperature, k_B is the Boltzmann constant, and η is the viscosity of the medium (water in this case). During the lifetime of the encounter complex a reaction between the two species, such as insertion of the amphiphile into the lipid aggregate, may occur with a rate constant k_{in}. The encounter complex is also formed when the amphiphile exits the lipid aggregate with the rate constant k_{out}. Assuming steady state for the amount of encounter complex, the analytical solution of equation A.9 may be obtained and k_+ and k_- may be related with k_{in} and k_{out}, respectively through equations A.13:

$$k_{+} = \frac{k_{in} k_{diff}}{k_{-diff} + k_{in}} \quad ; \quad k_{-} = \frac{k_{-diff} k_{out}}{k_{-diff} + k_{in}} \tag{A.13}.$$

Using equations A.13, k_+ and k_- for the amphiphiles with n = 2 to 6 were calculated from the corresponding k_{in} and k_{out}, which was obtained from the linear dependence of ln(k_{in}) and ln(k_{out}) (respectively) for the amphiphiles with n = 8 to 16.

A.IX.3 – Conversion of the bimolecular step for insertion into the cell membrane into a pseudo-unimolecular step

To allow the comparison with the unimolecular steps (desorption and translocation), the bimolecular step for insertion into the cell membrane was converted into a pseudo-unimolecular step. This was done through the multiplication of the rate constant by the LUVs concentration that would be obtained from the lipid in the apical side of the cell membrane corresponding to $A_a^o = 1.52\times10^4$ dm^2 [281] in V_D^w = 5 dm^3. The concentration of LUVs is obtained by:

$$[LUV] = \frac{A_a^o}{A_L N_A V_w n_L^{LUV^o}} \tag{A.14}$$

where A_L is the area per lipid molecule (equal to 64 Å^2 for POPC [326]), N_A is the Avogadro number and $n_L^{LUV^o}$ is the number of lipids in the outer leaflet of a LUV (~5×10^4 per LUV with 50 nm radii). The resulting [LUV] = 1.6 nM corresponds to a total lipid concentration of 78 μM.

A.IX.4 – Profile of the rate of permeation during the permeation process for different models

The presence of a membrane barrier that has the ability to retain the solute always leads to the appearance of a delay between the increase in the amount of solute in the acceptor compartment and its disappearance in the donor compartment. Therefore, the rate of solute accumulation at t=0 would in practice lead to a null permeability coefficient, Figure A24.

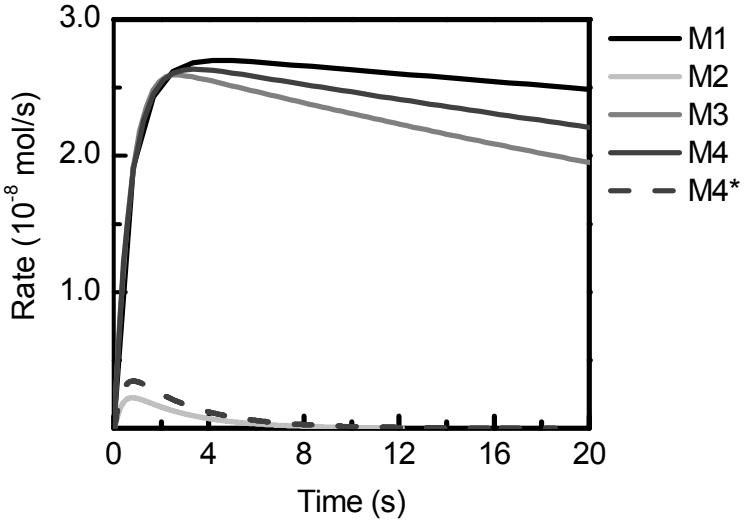

Figure A.24 – Rate of permeation profiles for NBD-C_8 during the permeation process for the different models considered, M1, M2, M3, M4 and M4* wich corresponds to M4 with the amount of acceptor binding agents reduced by a factor of 10^3.

A.IX.5 – Relationship between the characteristic rate constant for the monoexponential process (β) and the Permeability coefficient (P)

Since the permeation of solutes through cell membranes may be described by a monoexponential function, the characteristic rate constant of the monoexponential process (β) may be related to P. The simplest description of the permeation process of a solute from a donor side (S_D) to an acceptor side (S_A) through a cell monolayer may be described by equation A.15.

$$S_D \underset{k_-}{\overset{k_+}{\rightleftarrows}} S_A \tag{A.15}$$

Here k_+ and k_- are forward and reverse rate constants, respectively. The accumulation of S_A may be described by equation A.16,

$$S_A(t) = S_A(\infty) + \left(S_A(0) - S_A(\infty)\right) e^{-\beta t} \tag{A.16}.$$

The time derivative of equation A.16 at t=0, correspondent to the initial permeation times in experiments, is

$$\left[\frac{dS_A(t)}{dt}\right]_{t=0} = -\left(S_{A(0)} - S_{A(\infty)}\right)\beta \tag{A.17}.$$

Assuming that $S_{A(0)} = 0$, at t=0, β relates to the permeation rate through:

$$\beta = \frac{\left[\dfrac{dS_A(t)}{dt}\right]_{t=0}}{\left(S_{A(\infty)}\right)} \qquad \text{(A.18).}$$

For an irreversible process $S_{\mathrm{A}(\infty)} = S_{\mathrm{D}(0)}$, therefore considering equation IX.4 shown in the main text, β and P may be related by

$$P = \frac{\beta V_{\mathrm{D}}}{A_a^o} \qquad \text{(A.19).}$$

A.IX.6 – Derivation of the general analytical equations to describe the accumulation of amphiphile in the tissue

The existence of a single rate limiting step, in a localized transfer of the amphiphile from one compartment to another, implies that all the remaining steps are in equilibrium. Therefore analytical equations to describe the accumulation of the amphiphiles in the tissue may be derived. Let us first consider the case of reversible transfer. Considering an analogous situation where a reactant, S_1, forms a product, S_n, through a series of unimolecular processes with a unique rate limiting step (ℓ) and where x_i and ω_i are binding agents (in the donor and acceptor compartment, respectively):

$$S_{x_i} \xleftrightarrow[K_{x_i}]{} S_1 \xleftrightarrow[K_1]{} S_2 \xleftrightarrow[K_2]{} \ldots\ldots \xleftrightarrow[K_{\ell-1}]{} S_l \underset{k_{-\ell}}{\overset{k_\ell}{\rightleftharpoons}} S_{\ell+1}$$

$$S_{\ell+1} \xleftrightarrow[K_{\ell+1}]{} \ldots\ldots \xleftrightarrow[K_{\mathrm{n-1}}]{} S_{\mathrm{n}} \xleftrightarrow[K_{\omega_i}]{} S_{\omega_i} \qquad \text{(A.20).}$$

The total amount of amphiphile in this system is:

$$S_{\mathrm{T}} = \sum_{j=1}^{n} S_j + \sum_i S_{x_{\mathrm{i}}} + \sum_i S_{\omega_{\mathrm{i}}} \qquad \text{(A.21).}$$

According to equation A.20 all compartments situated before and after the limiting step are in equilibrium and the equilibrium constants between compartments may be defined as:

$$\frac{S_{\mathrm{j}}}{S_{\mathrm{j+1}}} = K_j \quad , \quad \mathrm{j} \in [1, \ell\text{-}1]; \qquad \frac{S_{\mathrm{j+1}}}{S_{\mathrm{j}}} = K_j \quad , \quad \mathrm{j} \in [\ell\text{+}1, \mathrm{n}\text{-}1]; \qquad \frac{k_\ell}{k_{-\ell}} = K_\ell ;$$

$$\frac{S_{x_i}}{S_1} = K_{x_i} \qquad ; \frac{S_{\omega_i}}{S_{\mathrm{n}}} = K_{\omega_i} \tag{A.22}.$$

The accumulation of amphiphile in the aqueous phase of the acceptor compartment, S_n, is given by:

$$S_{\mathrm{n}}(t) = \frac{S_{\mathrm{T}} \prod_{\mathrm{m}=\ell}^{\mathrm{n}-1} K_{\mathrm{m}}}{\sum_i K_{x_i} \prod_{\mathrm{m}=1}^{\ell-1} K_{\mathrm{m}} + \sum_{\mathrm{j}=1}^{\ell} \prod_{\mathrm{m}=j}^{\ell-1} K_{\mathrm{m}} + \sum_{\mathrm{j}=\ell+1}^{\mathrm{n}} \prod_{\mathrm{m}=\ell}^{\mathrm{j}-1} K_{\mathrm{m}} + \sum_i K_{\omega_i} \prod_{\mathrm{m}=\ell}^{\mathrm{n}-1} K_{\mathrm{m}}} \left(1 - e^{-\beta t}\right) \tag{A.23}$$

$$\beta = \frac{k_\ell \left(\sum_{\mathrm{j}=\ell+1}^{\mathrm{n}} \prod_{\mathrm{m}=\ell+1}^{\mathrm{j}-1} K_{\mathrm{m}} + \sum_i K_{\omega_i} \prod_{\mathrm{m}=\ell+1}^{\mathrm{n}-1} K_{\mathrm{m}} \right) + k_{-\ell} \left(\sum_{\mathrm{j}=1}^{\ell} \prod_{\mathrm{m}=j}^{\ell-1} K_{\mathrm{m}} + \sum_i K_{x_i} \prod_{\mathrm{m}=1}^{\ell-1} K_{\mathrm{m}} \right)}{\left(\sum_{\mathrm{j}=1}^{\ell} \prod_{\mathrm{m}=j}^{\ell-1} K_{\mathrm{m}} + \sum_i K_{x_i} \prod_{\mathrm{m}=1}^{\ell-1} K_{\mathrm{m}} \right) \left(\sum_{\mathrm{j}=\ell+1}^{\mathrm{n}} \prod_{\mathrm{m}=\ell+1}^{\mathrm{j}-1} K_{\mathrm{m}} + \sum_i K_{\omega_i} \prod_{\mathrm{m}=\ell+1}^{\mathrm{n}-1} K_{\mathrm{m}} \right)}$$

and the total amount of amphiphile in the acceptor compartment (free and associated with the binding agents) is given by:

$$S_{\mathrm{A}} = S_{\mathrm{n}} + \sum_i S_{\omega_i} = S_{\mathrm{n}} \left(1 + \sum_i K_{\omega_i} \right) \tag{A.24}.$$

The kinetic scheme for the irreversible accumulation of amphiphiles in the acceptor compartment is given in equation A.25. In this case, the last step of the transfer was not considered at equilibrium but rather as an irreversible step.

$$S_{x_i} \underset{K_{x_i}}{\longleftrightarrow} S_1 \underset{K_1}{\longleftrightarrow} S_2 \underset{K_2}{\longleftrightarrow} \ldots\ldots \underset{K_{l\text{-}1}}{\longleftrightarrow} S_\ell \underset{k_{-\ell}}{\overset{k_\ell}{\rightleftarrows}} S_{\ell+1}$$

$$S_{l+1} \underset{K_{l+1}}{\longleftrightarrow} \ldots\ldots \underset{K_{n\text{-}2}}{\longleftrightarrow} S_{n-1} \xrightarrow{k_{n\text{-}1}} S_{\mathrm{n}} \underset{K_{\omega_i}}{\longleftrightarrow} S_{\omega_i} \tag{A.25}$$

The relations shown in equations A.22 are also valid except between S_{n-1} and S_n which is now given by $\frac{dS_n}{dt} = \left(1 \Big/ \left(1 + \sum_i K_{\omega_i} \right) \right) k_{n-1} S_{n-1}$. The resulting set of differential equations and equilibrium relations may be solved, assuming steady-state for the intermediates (species $S_{\ell+1}$ to S_{n-1}), giving:

$$S_{\mathrm{n}}(t)=\frac{S_{\mathrm{T}}}{1+\sum_{i} K_{\omega_i}}\times\left(1-e^{-\beta t}\right)$$

$$\beta=\frac{k_{\ell}k_{n-1}\prod_{\mathrm{m}=\ell+1}^{\mathrm{n-2}}K_{\mathrm{m}}}{\left(\sum_{j=1}^{\ell}\prod_{\mathrm{m=j}}^{\ell\text{-}1}K_{\mathrm{m}}+\sum_{i}K_{x_i}\prod_{\mathrm{m}=1}^{\ell\text{-}1}K_{\mathrm{m}}\right)\left(k_{-\ell}+k_{n-1}\prod_{\mathrm{m}=\ell+1}^{\mathrm{n-2}}K_{\mathrm{m}}\right)+k_{\ell}\left(\sum_{\mathrm{j}=\ell+1}^{\mathrm{n-1}}\prod_{\mathrm{m}=\ell+1}^{\mathrm{j-1}}K_{\mathrm{m}}\right)}$$

(A.26).

References

1. Pokorny, A., P. F. F. Almeida, E. C. C. Melo, and W. L. C. Vaz. 2000. Kinetics of amphiphile association with two-phase lipid bilayer vesicles. Biophys. J. 78:267-280.
2. Estronca, L., M. J. Moreno, M. S. C. Abreu, E. Melo, and W. L. C. Vaz. 2002. Solubility of amphiphiles in membranes: influence of phase properties and amphiphile head group. Biochemical and Biophysical Research Communications 296:596-603.
3. Abreu, M. S. C., M. J. Moreno, and W. L. C. Vaz. 2004. Kinetics and thermodynamics of association of a phospholipid derivative with lipid bilayers in liquid-disordered and liquid-ordered phases. Biophys. J. 87:353-365.
4. Sampaio, J. L., M. J. Moreno, and W. L. C. Vaz. 2005. Kinetics and thermodynamics of association of a fluorescent lysophospholipid derivative with lipid bilayers in liquid-ordered and liquid-disordered phases. Biophys. J. 88:4064-4071.
5. Cardoso, R. M. S., H. A. L. Filipe, F. Gomes, N. D. Moreira, W. L. C. Vaz, and M. J. Moreno. 2010. Chain Length Effect on the Binding of Amphiphiles to Serum Albumin and to POPC Bilayers. J. Phys. Chem. B 114:16337-16346.
6. Cardoso, R. M. S., P. A. T. Martins, F. Gomes, S. Doktorovova, W. L. C. Vaz, and M. J. Moreno. 2011. Chain-Length Dependence of Insertion, Desorption, and Translocation of a Homologous Series of 7-Nitrobenz-2-oxa-1,3-diazol-4-yl-Labeled Aliphatic Amines in Membranes. J. Phys. Chem. B 115:10098-10108.
7. Martins, P. T., A. Velazquez-Campoy, W. L. C. Vaz, R. M. S. Cardoso, J. Valério, and M. J. Moreno. 2012. Kinetics and Thermodynamics of Chlorpromazine Interaction with Lipid Bilayers: Effect of Charge and Cholesterol. J. Am. Chem. Soc. 134:4184-4195.
8. Abreu, M. S. C., L. Estronca, M. J. Moreno, and W. L. C. Vaz. 2003. Binding of a fluorescent lipid amphiphile to albumin and its transfer to lipid bilayer membranes. Biophys. J. 84:386-399.
9. Estronca, L., M. J. Moreno, J. A. N. Laranjinha, L. M. Almeida, and W. L. C. Vaz. 2005. Kinetics and thermodynamics of lipid amphiphile exchange between lipoproteins and albumin in serum. Biophys. J. 88:557-565.
10. Estronca, L. M. B. B., H. A. L. Filipe, A. Salvador, M. J. Moreno, and W. L. C. Vaz. 2014. Homeostasis of free cholesterol in the blood: a preliminary evaluation and modeling of its passive transport. J. Lipid Res. 55:1033-1043.
11. Franklin, B., W. Brownrigg, and M. Farish. 1774. Of the stilling of waves by means of oil. extracted from sundry letters between Benjamin Franklin, LL. D. F. R. S. William Brownrigg, M. D. F. R. S. and the Reverend Mr. Farish. Philosophical Transactions (1683-1775):445-460.
12. Overton, E. 1899. Ueber die allgemeinen osmotischen Eigenschaften der Zelle, ihre vermutlichen Ursachen und ihre Bedeutung fur die Physiologie. Vierteljschr. d. Naturforsch. Ges. Zurich 44:88-135.
13. Gorter, E., and F. Grendel. 1925. On bimolecular layers of lipoids on the chromocytes of the blood. The Journal of Experimental Medicine 41:439-443.
14. Danielli, J. F., and H. Davson. 1935. A contribution to the theory of permeability of thin films. Journal of Cellular and Comparative Physiology 5:495-508.
15. Singer, S. J., and G. L. Nicolson. 1972. Fluid mosaic model of structure of cell membranes. Science 175:720-731.

16. Deamer, D. W., A. Kleinzeller, and D. M. Fambrough. 1999. Membrane permeability: 100 years since Ernest Overton. Curr. Top. Membr. 48.
17. Simons, K., and G. Vanmeer. 1988. Lipid sorting in epithelial-cells. Biochemistry 27:6197-6202.
18. Pike, L. J. 2006. Rafts defined: a report on the Keystone symposium on lipid rafts and cell function. J. Lipid Res. 47:1597-1598.
19. Simons, K., and E. Ikonen. 1997. Functional rafts in cell membranes. Nature 387:569-572.
20. Vereb, G., J. Szollosi, J. Matko, P. Nagy, T. Farkas, L. Vigh, L. Matyus, T. A. Waldmann, and S. Damjanovich. 2003. Dynamic, yet structured: The cell membrane three decades after the Singer-Nicolson model. P Natl Acad Sci USA 100:8053-8058.
21. Kox, A., J. Michels, and F. Wiegel. 1980. Simulation of a lipid monolayer using molecular dynamics. Nature 287:317-319.
22. van der Ploeg, P., and H. J. C. Berendsen. 1982. Molecular dynamics simulation of a bilayer membrane. J. Chem. Phys. 76:3271-3276.
23. Heller, H., M. Schaefer, and K. Schulten. 1993. Molecular dynamics simulation of a bilayer of 200 lipids in the gel and in the liquid crystal phase. The Journal of Physical Chemistry 97:8343-8360.
24. Marrink, S. J., and H. J. C. Berendsen. 1994. Simulation of water transport through a lipid membrane. Journal of Physical Chemistry 98:4155-4168.
25. Tieleman, D. P., and H. J. C. Berendsen. 1996. Molecular dynamics simulations of a fully hydrated dipalmitoylphosphatidylcholine bilayer with different macroscopic boundary conditions and parameters. J. Chem. Phys. 105:4871-4880.
26. Lyubartsev, A. P., and A. L. Rabinovich. 2011. Recent development in computer simulations of lipid bilayers. Soft Matter 7:25-39.
27. Bennett, W. F. D., and D. P. Tieleman. 2013. Computer simulations of lipid membrane domains. Biochim. Biophys. Acta, Biomembr. 1828:1765-1776.
28. Israelachvili, J. N., D. J. Mitchell, and B. W. Ninham. 1976. Theory of self-assembly of hydrocarbon amphiphiles into micelles and bilayers. Journal of the Chemical Society, Faraday Transactions 2: Molecular and Chemical Physics 72:1525-1568.
29. Israelachvili, J. N., D. J. Mitchell, and B. W. Ninham. 1977. Theory of self-assembly of lipid bilayers and vesicles. Biochim. Biophys. Acta, Biomembr. 470:185-201.
30. Ziegler, A. 2008. Thermodynamic studies and binding mechanisms of cell-penetrating peptides with lipids and glycosaminoglycans. Advanced Drug Delivery Reviews 60:580-597.
31. Leventis, P. A., and S. Grinstein. 2010. The Distribution and Function of Phosphatidylserine in Cellular Membranes. Annual Review of Biophysics 39:407-427.
32. Gennis, R. B., editor. 1989. Biomembranes: Molecular Structure and Function. Springer-Verlag, New York.
33. Voet, D., Judith G. Voet, editor. 2004. Biochemistry. John Wiley & Sons, Inc.
34. Delint-Ramirez, I., D. Willoughby, G. V. R. Hammond, L. J. Ayling, and D. M. F. Cooper. 2011. Palmitoylation Targets AKAP79 Protein to Lipid Rafts and Promotes Its Regulation of Calcium-sensitive Adenylyl Cyclase Type 8. Journal of Biological Chemistry 286:32962-32975.

35. Baumgart, T., A. T. Hammond, P. Sengupta, S. T. Hess, D. A. Holowka, B. A. Baird, and W. W. Webb. 2007. Large-scale fluid/fluid phase separation of proteins and lipids in giant plasma membrane vesicles. Proceedings of the National Academy of Sciences 104:3165-3170.
36. Schultz, A. M., L. E. Henderson, and S. Oroszlan. 1988. Fatty Acylation of Proteins. Annual Review of Cell Biology 4:611-647.
37. Bemporad, D., C. Luttmann, and J. W. Essex. 2004. Computer simulation of small molecule permeation across a lipid bilayer: Dependence on bilayer properties and solute volume, size, and cross-sectional area. Biophys. J. 87:1-13.
38. Xiang, T. X. 1993. A computer simulation of free volume distributions and related structural properties in a model lipid bilayer. Biophys. J. 65:1108-1120.
39. Mouritsen, O. G., editor. 2005. Life-As a Matter of Fat. Springer, Germany.
40. Cantor, R. S. 1997. The lateral pressure profile in membranes: A physical mechanism of general anesthesia. Biochemistry 36:2339-2344.
41. Cantor, R. S. 1998. The lateral pressure profile in membranes: A physical mechanism of general anesthesia. Toxicology Letters (Shannon) 100-101:451-458.
42. Griepernau, B., and R. A. Böckmann. 2008. The Influence of 1-Alkanols and External Pressure on the Lateral Pressure Profiles of Lipid Bilayers. Biophys. J. 95:5766-5778.
43. Terama, E., O. H. S. Ollila, E. Salonen, A. C. Rowat, C. Trandum, P. Westh, M. Patra, M. Karttunen, and I. Vattulainen. 2008. Influence of Ethanol on Lipid Membranes: From Lateral Pressure Profiles to Dynamics and Partitioning. J. Phys. Chem. B 112:4131-4139.
44. Flewelling, R. F., and W. L. Hubbell. 1986. Hydrophobic ion interactions with membranes. Thermodynamic analysis of tetraphenylphosphonium binding to vesicles. Biophys. J. 49:531-540.
45. Honig, B. H., W. L. Hubbell, and R. F. Flewelling. 1986. Electrostatic Interactions in Membranes and Proteins. Annual Review of Biophysics and Biophysical Chemistry 15:163-193.
46. Träuble, H., M. Teubner, P. Woolley, and H. Eibl. 1976. Electrostatic interactions at charged lipid membranes: I. Effects of ph and univalent cations on membrane structure. Biophysical Chemistry 4:319-342.
47. Brockman, H. 1994. Dipole potential of lipid membranes. Chemistry and Physics of Lipids 73:57-79.
48. Langner, M., and K. Kubica. 1999. The electrostatics of lipid surfaces. Chemistry and Physics of Lipids 101:3-35.
49. Cardoso, R. M. S. 2013. Kinetics and Thermodynamics of Interaction between Amphiphiles and Membranes: Interplay of Amphiphile Dipole Moment and Membrane Dipole Potential. Ph.D. Thesis, Coimbra, http://hdl.handle.net/10316/24273.
50. Luzzati, V., T. Gulik-Krzywicki, and A. Tardieu. 1968. Polymorphism of lecithins. Nature 218:1031-1034.
51. Kinnunen, P. K. J. 1996. On the molecular-level mechanisms of peripheral protein-membrane interactions induced by lipids forming inverted non-lamellar phases. Chemistry and Physics of Lipids 81:151-166.
52. Yeagle, P. L. 2010. The structure of biological membranes. CRC press.
53. Tieleman, D. P., S. J. Marrink, and H. J. C. Berendsen. 1997. A computer perspective of membranes: molecular dynamics studies of lipid bilayer systems. Biochimica Et Biophysica Acta-Reviews on Biomembranes 1331:235-270.

54. Gawrisch, K., and L. L. Holte. 1996. NMR investigations of non-lamellar phase promoters in the lamellar phase state. Chemistry and Physics of Lipids 81:105-116.
55. Seelig, J., and H. U. Gally. 1976. Investigation of phosphatidylethanolamine bilayers by deuterium and phosphorus-31 nuclear magnetic resonance. Biochemistry 15:5199-5204.
56. Yeagle, P. L., W. C. Hutton, C.-H. Huang, and R. B. Martin. 1976. Structure in the polar head region of phospholipid bilayers: a phosphorus-31 {proton} nuclear Overhauser effect study. Biochemistry 15:2121-2124.
57. Griffin, R. G., L. Powers, and P. S. Pershan. 1978. Head-group conformation in phospholipids: a 31P nuclear magnetic resonance study of oriented monodomain dipalmitoylphosphatidylcholine bilayers. Biochemistry 17:2718-2722.
58. Büldt, G., H. U. Gally, J. Seelig, and G. Zaccai. 1979. Neutron diffraction studies on phosphatidylcholine model membranes: I. Head group conformation. Journal of Molecular Biology 134:673-691.
59. Braach-Maksvytis, V. L., and B. A. Cornell. 1988. Chemical shift anisotropies obtained from aligned egg yolk phosphatidylcholine by solid-state 13C nuclear magnetic resonance. Biophys. J. 53:839-843.
60. Seelig, A., and J. Seelig. 1974. Dynamic structure of fatty acyl chains in a phospholipid bilayer measured by deuterium magnetic resonance. Biochemistry 13:4839-4845.
61. Seelig, A., and J. Seelig. 1977. Effect of a single cis double bond on the structure of a phospholipid bilayer. Biochemistry 16:45-50.
62. Seelig, J., and N. Waespe-Sarcevic. 1978. Molecular order in cis and trans unsaturated phospholipid bilayers. Biochemistry 17:3310-3315.
63. Seelig, A., and J. Seelig. 1975. Bilayers of dipalmitoyl-3-sn-phosphatidylcholine: Conformational differences between the fatty acyl chains. Biochim. Biophys. Acta, Biomembr. 406:1-5.
64. Ferreira, T. M., F. Coreta-Gomes, O. H. S. Ollila, M. J. Moreno, W. L. C. Vaz, and D. Topgaard. 2013. Cholesterol and POPC segmental order parameters in lipid membranes: solid state 1H-13C NMR and MD simulation studies. Physical Chemistry Chemical Physics 15:1976-1989.
65. Jendrasiak, G. L., and J. H. Hasty. 1974. The hydration of phospholipids. Biochimica et Biophysica Acta (BBA) - Lipids and Lipid Metabolism 337:79-91.
66. Holte, L. L., S. A. Peter, T. M. Sinnwell, and K. Gawrisch. 1995. 2H nuclear magnetic resonance order parameter profiles suggest a change of molecular shape for phosphatidylcholines containing a polyunsaturated acyl chain. Biophys. J. 68:2396-2403.
67. Niebylski, C. D., and N. Salem Jr. 1994. A calorimetric investigation of a series of mixed-chain polyunsaturated phosphatidylcholines: effect of sn-2 chain length and degree of unsaturation. Biophys. J. 67:2387-2393.
68. Lindblom, G., and G. Orädd. 1994. NMR Studies of translational diffusion in lyotropic liquid crystals and lipid membranes. Progress in Nuclear Magnetic Resonance Spectroscopy 26:483-515.
69. Almeida, P. F. F., W. L. C. Vaz, and T. E. Thompson. 1992. Lateral diffusion in the liquid phases of dimyristoylphosphatidylcholine/cholesterol lipid bilayers: a free volume analysis. Biochemistry 31:6739-6747.
70. Owicki, J. C., and H. M. McConnell. 1980. Lateral diffusion in inhomogeneous membranes. Model membranes containing cholesterol. Biophys. J. 30:383-397.

71. McConnell, H. M., and R. D. Kornberg. 1971. Inside-outside transitions of phospholipids in vesicle membranes. Biochemistry 10:1111-1120.
72. De Kruijff, B., and K. W. A. Wirtz. 1977. Induction of a relatively fast transbilayer movement of phosphatidylcholine in vesicles. A 13C NMR study. Biochim. Biophys. Acta, Biomembr. 468:318-326.
73. Doody, M. C., H. J. Pownall, Y. J. Kao, and L. C. Smith. 1980. Mechanism and kinetics of transfer of a fluorescent fatty acid between single-walled phosphatidylcholine vesicles. Biochemistry 19:108-116.
74. Moreno, M. J., L. Estronca, and W. L. C. Vaz. 2006. Translocation of phospholipids and dithionite permeability in liquid-ordered and liquid-disordered membranes. Biophys. J. 91:873-881.
75. Lange, Y., J. Dolde, and T. L. Steck. 1981. The rate of transmembrane movement of cholesterol in the human erythrocyte. Journal of Biological Chemistry 256:5321-5323.
76. Steck, T. L., J. Ye, and Y. Lange. 2002. Probing Red Cell Membrane Cholesterol Movement with Cyclodextrin. Biophys. J. 83:2118-2125.
77. Smith, R. J. M., and C. Green. 1974. The rate of cholesterol 'flip-flop' in lipid bilayers and its relation to membrane sterol pools. FEBS Letters 42:108-111.
78. Lange, Y., C. M. Cohen, and M. J. Poznansky. 1977. Transmembrane movement of cholesterol in human erythrocytes. Proceedings of the National Academy of Sciences 74:1538-1542.
79. Backer, J. M., and E. A. Dawidowicz. 1989. The rapid transmembrane movement of cholesterol in small unilamellar vesicles. Biochim. Biophys. Acta, Biomembr. 551:260-270.
80. Brasaemle, D. L., A. D. Robertson, and A. D. Attie. 1988. Transbilayer movement of cholesterol in the human erythrocyte membrane. J. Lipid Res. 29:481-489.
81. Devaux, P. F. 1992. Protein involvement in transmembrane lipid asymmetry. Annual Review of Biophysics and Biomolecular Structure 21:417-439.
82. Simons, K., and W. L. C. Vaz. 2004. Model systems, lipid rafts, and cell membranes. Annual Review of Biophysics and Biomolecular Structure 33:269-295.
83. Brown, D. A. 2001. Seeing is believing: Visualization of rafts in model membranes. Proceedings of the National Academy of Sciences 98:10517-10518.
84. Brown, D. A., and E. London. 1998. Structure and Origin of Ordered Lipid Domains in Biological Membranes. J Membrane Biol 164:103-114.
85. Sheets, E. D., G. M. Lee, R. Simson, and K. Jacobson. 1997. Transient Confinement of a Glycosylphosphatidylinositol-Anchored Protein in the Plasma Membrane†. Biochemistry 36:12449-12458.
86. Schütz, G. J., G. Kada, V. P. Pastushenko, and H. Schindler. 2000. Properties of lipid microdomains in a muscle cell membrane visualized by single molecule microscopy. The EMBO journal 19:892-901.
87. Pralle, A., P. Keller, E.-L. Florin, K. Simons, and J. K. H. Hörber. 2000. Sphingolipid–Cholesterol Rafts Diffuse as Small Entities in the Plasma Membrane of Mammalian Cells. The Journal of Cell Biology 148:997-1008.
88. Zajchowski, L. D., and S. M. Robbins. 2002. Lipid rafts and little caves. European Journal of Biochemistry 269:737-752.
89. Parton, R. G., B. Joggerst, and K. Simons. 1994. Regulated internalization of caveolae. The Journal of Cell Biology 127:1199-1215.

90. Fivaz, M., L. Abrami, and F. G. van der Goot. 1999. Landing on lipid rafts. Trends in cell biology 9:212-213.
91. Shin, J.-S., Z. Gao, and S. N. Abraham. 2000. Involvement of Cellular Caveolae in Bacterial Entry into Mast Cells. Science 289:785-788.
92. Oram, J. F., and S. Yokoyama. 1996. Apolipoprotein-mediated removal of cellular cholesterol and phospholipids. J. Lipid Res. 37:2473-2491.
93. Smart, E. J., Y.-s. Ying, W. C. Donzell, and R. G. W. Anderson. 1996. A Role for Caveolin in Transport of Cholesterol from Endoplasmic Reticulum to Plasma Membrane. Journal of Biological Chemistry 271:29427-29435.
94. Op den Kamp, J. A. F. 1979. Lipid Asymmetry in Membranes. Annual Review of Biochemistry 48:47-71.
95. Boesze-Battaglia, K., and R. Schimmel. 1997. Cell membrane lipid composition and distribution: implications for cell function and lessons learned from photoreceptors and platelets. The Journal of Experimental Biology 200:2927-2936.
96. Quinn, P. 2002. Plasma Membrane Phospholipid Asymmetry. In Phospholipid Metabolism in Apoptosis. P. Quinn, and V. Kagan, editors. Springer US. 39-60.
97. Dodge, J. T., and G. B. Phillips. 1967. Composition of phospholipids and of phospholipid fatty acids and aldehydes in human red cells. J. Lipid Res. 8:667-675.
98. Rothman, J. E., and J. Lenard. 1977. Membrane asymmetry. Science 195:743-753.
99. Owen, J. S., K. R. Bruckdorfer, R. C. Day, and N. McIntyre. 1982. Decreased Erythrocyte membrane fluidity and altered lipid composition in human liver disease. J. Lipid Res. 23:124-132.
100. Leidl, K., G. Liebisch, D. Richter, and G. Schmitz. 2008. Mass spectrometric analysis of lipid species of human circulating blood cells. Biochimica et Biophysica Acta (BBA) - Molecular and Cell Biology of Lipids 1781:655-664.
101. Barceló, F., J. S. Perona, J. Prades, S. S. Funari, E. Gomez-Gracia, M. Conde, R. Estruch, and V. Ruiz-Gutiérrez. 2009. Mediterranean-Style Diet Effect on the Structural Properties of the Erythrocyte Cell Membrane of Hypertensive Patients: The Prevencion con Dieta Mediterranea Study. Hypertension 54:1143-1150.
102. Fisher, K. A. 1976. Analysis of membrane halves: cholesterol. P Natl Acad Sci USA 73:173-177.
103. Yeagle, P. L. 1985. Cholesterol and the cell membrane. Biochimica et Biophysica Acta (BBA) - Reviews on Biomembranes 822:267-287.
104. Marrink, S. J., A. H. de Vries, T. A. Harroun, J. Katsaras, and S. R. Wassall. 2008. Cholesterol shows preference for the interior of polyunsaturated lipid. J. Am. Chem. Soc. 130:10-11.
105. Esteban-Martín, S., H. J. Risselada, J. s. Salgado, and S. J. Marrink. 2009. Stability of Asymmetric Lipid Bilayers Assessed by Molecular Dynamics Simulations. J. Am. Chem. Soc. 131:15194-15202.
106. Daleke, D. L. 2003. Regulation of transbilayer plasma membrane phospholipid asymmetry. J. Lipid Res. 44:233-242.
107. Zwaal, R. F. A., and A. J. Schroit. 1997. Pathophysiologic Implications of Membrane Phospholipid Asymmetry in Blood Cells. Blood 89:1121-1132.
108. Bevers, E. M., P. Comfurius, D. W. C. Dekkers, and R. F. A. Zwaal. 1999. Lipid translocation across the plasma membrane of mammalian cells. Biochimica et Biophysica Acta (BBA) - Molecular and Cell Biology of Lipids 1439:317-330.

109. Pomorski, T., S. Hrafnsdóttir, P. F. Devaux, and G. v. Meer. 2001. Lipid distribution and transport across cellular membranes. Seminars in Cell & Developmental Biology 12:139-148.
110. Gurtovenko, A. A. 2005. Asymmetry of lipid bilayers induced by monovalent salt: Atomistic molecular-dynamics study. J. Chem. Phys. 122:2244902.
111. Manno, S., Y. Takakuwa, and N. Mohandas. 2002. Identification of a functional role for lipid asymmetry in biological membranes: Phosphatidylserine-skeletal protein interactions modulate membrane stability. P Natl Acad Sci USA 99:1943-1948.
112. Schlegel, R. A., and P. Williamson. 2001. Phosphatidylserine, a death knell. Cell Death & Differentiation 8:551-563.
113. Maxfield, F. R., and I. Tabas. 2005. Role of cholesterol and lipid organization in disease. Nature 438:612-621.
114. Van Meer, G., D. R. Voelker, and G. W. Feigenson. 2008. Membrane lipids: where they are and how they behave. Nature Reviews Molecular Cell Biology 9:112-124.
115. Haberland, M. E., and J. A. Reynolds. 1973. Self-association of Cholesterol in Aqueous Solution. Proceedings of the National Academy of Sciences 70:2313-2316.
116. Franks, N. P. 1976. Structural analysis of hydrated egg lecithin and cholesterol bilayers I. X-ray diffraction. Journal of Molecular Biology 100:345-358.
117. Worcester, D. L., and N. P. Franks. 1976. Structural analysis of hydrated egg lecithin and cholesterol bilayers II. Neutron diffraction. Journal of Molecular Biology 100:359-378.
118. Huang, C.-H. 1976. Roles of carbonyl oxygens at the bilayer interface in phospholipid–sterol interaction. Nature 259:242-244.
119. Oldfield, E., and D. Chapman. 1972. Molecular dynamics of cerebroside—cholesterol and sphingomyelin—cholesterol interactions: Implications for myelin membrane structure. FEBS Letters 21:303-306.
120. Hjort Ipsen, J., G. Karlström, O. G. Mourtisen, H. Wennerström, and M. J. Zuckermann. 1987. Phase equilibria in the phosphatidylcholine-cholesterol system. Biochim. Biophys. Acta, Biomembr. 905:162-172.
121. Estep, T. N., D. B. Mountcastle, R. L. Biltonen, and T. E. Thompson. 1978. Studies on the anomalous thermotropic behavior of aqueous dispersions of dipalmitoylphosphatidylcholine-cholesterol mixtures. Biochemistry 17:1984-1989.
122. Mabrey, S., P. L. Mateo, and J. M. Sturtevant. 1978. High-sensitivity scanning calorimetric study of mixtures of cholesterol with dimyristoyl- and dipalmitoylphosphatidylcholines. Biochemistry 17:2464-2468.
123. Vist, M. R., and J. H. Davis. 1990. Phase equilibria of cholesterol/dipalmitoylphosphatidylcholine mixtures: deuterium nuclear magnetic resonance and differential scanning calorimetry. Biochemistry 29:451-464.
124. Reyes Mateo, C., A. Ulises Acuña, and J. C. Brochon. 1995. Liquid-crystalline phases of cholesterol/lipid bilayers as revealed by the fluorescence of trans-parinaric acid. Biophys. J. 68:978-987.
125. Smaby, J. M., M. M. Momsen, H. L. Brockman, and R. E. Brown. 1997. Phosphatidylcholine acyl unsaturation modulates the decrease in interfacial elasticity induced by cholesterol. Biophys. J. 73:1492-1505.

126. Lund-Katz, S., H. M. Laboda, L. R. McLean, and M. C. Phillips. 1988. Influence of molecular packing and phospholipid type on rates of cholesterol exchange. Biochemistry 27:3416-3423.
127. Falck, E., M. Patra, M. Karttunen, M. T. Hyvönen, and I. Vattulainen. 2004. Impact of cholesterol on voids in phospholipid membranes. J. Chem. Phys. 121:12676-12689.
128. McIntosh, T. J. 1978. The effect of cholesterol on the structure of phosphatidylcholine bilayers. Biochim. Biophys. Acta, Biomembr. 513:43-58.
129. Butler, K. W., K. G. Johnson, and I. C. P. Smith. 1978. Acholeplasma laidlawii membranes: An electron spin resonance study of the influence on molecular order of fatty acid composition and cholesterol. Archives of Biochemistry and Biophysics 191:289-297.
130. Rintoul, D. A., S. M. Chou, and D. F. Silbert. 1979. Physical characterization of sterol-depleted LM-cell plasma membranes. Journal of Biological Chemistry 254:10070-10077.
131. Brzustowicz, M. R., W. Stillwell, and S. R. Wassall. 1999. Molecular organization of cholesterol in polyunsaturated phospholipid membranes: a solid state 2H NMR investigation. FEBS Letters 451:197-202.
132. Yeagle, P. L., W. C. Hutton, C. H. Huang, and R. B. Martin. 1975. Headgroup conformation and lipid--cholesterol association in phosphatidylcholine vesicles: a 31P(1H) nuclear Overhauser effect study. Proceedings of the National Academy of Sciences 72:3477-3481.
133. Yeagle, P. L., W. C. Hutton, C.-H. Huang, and R. B. Martin. 1977. Phospholipid head-group conformations; intermolecular interactions and cholesterol effects. Biochemistry 16:4344-4349.
134. Goldstein, J. L., and M. S. Brown. 2001. The Cholesterol Quartet. Science 292:1310-1312.
135. Phillips, M. C., W. J. Johnson, and G. H. Rothblat. 1987. Mechanisms and consequences of cellular cholesterol exchange and transfer. Biochimica et Biophysica Acta (BBA) - Reviews on Biomembranes 906:223-276.
136. McLean, L. R., and M. C. Phillips. 1981. Mechanism of cholesterol and phosphatidylcholine exchange or transfer between unilamellar vesicles. Biochemistry 20:2893-2900.
137. Backer, J. M., and E. A. Dawidowicz. 1981. Mechanism of cholesterol exchange between phospholipid vesicles. Biochemistry 20:3805-3810.
138. Yeagle, P. L., and J. E. Young. 1986. Factors contributing to the distribution of cholesterol among phospholipid vesicles. Journal of Biological Chemistry 261:8175-8181.
139. Estronca, L., M. J. Moreno, and W. L. C. Vaz. 2007. Kinetics and thermodynamics of the association of dehydroergosterol with lipid bilayer membranes. Biophys. J. 93:4244-4253.
140. McIntosh, A., B. Atshaves, H. Huang, A. Gallegos, A. Kier, and F. Schroeder. 2008. Fluorescence Techniques Using Dehydroergosterol to Study Cholesterol Trafficking. Lipids 43:1185-1208.
141. Robalo, J. R., A. M. T. M. do Canto, A. J. P. Carvalho, J. P. P. Ramalho, and L. M. S. Loura. 2013. Behavior of Fluorescent Cholesterol Analogues Dehydroergosterol and Cholestatrienol in Lipid Bilayers: A Molecular Dynamics Study. J. Phys. Chem. B 117:5806-5819.
142. Pourmousa, M., T. Róg, R. Mikkeli, l. Vattulainen, L. M. Solanko, D. Wüstner, N. H. List, J. Kongsted, and M. Karttunen. 2014. Dehydroergosterol as an

Analogue for Cholesterol: Why It Mimics Cholesterol So Well—or Does It? J. Phys. Chem. B 118:7345-7357.
143. Demel, R. A., K. R. Bruckdorfer, and L. L. M. Van Deenen. 1972. The effect of sterol structure on the permeability of lipomes to glucose, glycerol and Rb+. Biochim. Biophys. Acta, Biomembr. 255:321-330.
144. Papahadjopoulos, D., S. Nir, and S. Ohki. 1972. Permeability properties of phospholipid membranes: Effect of cholesterol and temperature. Biochim. Biophys. Acta, Biomembr. 266:561-583.
145. Hediger, M., M. Romero, J.-B. Peng, A. Rolfs, H. Takanaga, and E. Bruford. 2004. The ABCs of solute carriers: physiological, pathological and therapeutic implications of human membrane transport proteins. Pflugers Arch - Eur J Physiol 447:465-468.
146. Sugano, K., M. Kansy, P. Artursson, A. Avdeef, S. Bendels, L. Di, G. F. Ecker, B. Faller, H. Fischer, G. Gerebtzoff, H. Lennernaes, and F. Senner. 2010. Coexistence of passive and carrier-mediated processes in drug transport. Nat. Rev. Drug Discovery 9:597-614.
147. Kell, D. B., P. D. Dobson, and S. G. Oliver. 2011. Pharmaceutical drug transport: the issues and the implications that it is essentially carrier-mediated only. Drug Discovery Today 16:704-714.
148. Di, L., P. Artursson, A. Avdeef, G. F. Ecker, B. Faller, H. Fischer, J. B. Houston, M. Kansy, E. H. Kerns, S. D. Krämer, H. Lennernäs, and K. Sugano. 2012. Evidence-based approach to assess passive diffusion and carrier-mediated drug transport. Drug Discovery Today 17:905-912.
149. Smith, D., P. Artursson, A. Avdeef, L. Di, G. F. Ecker, B. Faller, J. B. Houston, M. Kansy, E. H. Kerns, S. D. Krämer, H. Lennernäs, H. van de Waterbeemd, K. Sugano, and B. Testa. 2014. Passive Lipoidal Diffusion and Carrier-Mediated Cell Uptake Are Both Important Mechanisms of Membrane Permeation in Drug Disposition. Molecular Pharmaceutics 11:1727-1738.
150. Missner, A., and P. Pohl. 2009. 110 Years of the Meyer-Overton Rule: Predicting Membrane Permeability of Gases and Other Small Compounds. Chemphyschem 10:1405-1414.
151. Testa, B., G. F. Waterbeemb, and R. Guy. 2001. Pharmacokinetic Optimization in Drug Research: Biological, Physicochemical, and Computational Strategies. Verlag Helvetica Chimica Acta, Zurich.
152. Mensch, J., J. Oyarzabal, C. Mackie, and P. Augustijns. 2009. In Vivo, In Vitro and In Silico Methods for Small Molecule Transfer Across the BBB. Journal of Pharmaceutical Sciences 98:4429-4468.
153. Kwon, J.-H., H. M. Liljestrand, and L. E. Katz. 2006. Partitioning of moderately hydrophobic endocrine disruptors between water and synthetic membrane vesicles. Environmental Toxicology and Chemistry 25:1984-1992.
154. De Young, L. R., and K. A. Dill. 1988. Solute partitioning into lipid bilayer membranes. Biochemistry 27:5281-5289.
155. Jain, M. K., and L. V. Wray Jr. 1978. Partition coefficients of alkanols in lipid bilayer/water. Biochemical Pharmacology 27:1294-1295.
156. Mouritsen, O., and K. Jørgensen. 1998. A New Look at Lipid-Membrane Structure in Relation to Drug Research. Pharm Res-Dordr 15:1507-1519.
157. Bemporad, D., J. W. Essex, and C. Luttmann. 2004. Permeation of small molecules through a lipid bilayer: A computer simulation study. J. Phys. Chem. B 108:4875-4884.

158. Paula, S., A. G. Volkov, A. N. VanHoek, T. H. Haines, and D. W. Deamer. 1996. Permeation of protons, potassium ions, and small polar molecules through phospholipid bilayers as a function of membrane thickness. Biophys. J. 70:339-348.
159. Deamer, D. W., and J. W. Nichols. 1989. Proton flux mechanisms in model and biological membranes. Journal of Membrane Biology 107:91-103.
160. Sapay, N., W. F. D. Bennett, and D. P. Tieleman. 2009. Thermodynamics of flip-flop and desorption for a systematic series of phosphatidylcholine lipids. Soft Matter 5:3295-3302.
161. Loura, L. S., and J. P. Prates Ramalho. 2009. Fluorescent membrane probes' behavior in lipid bilayers: insights from molecular dynamics simulations. Biophys Rev 1:141-148.
162. Loura, L. M. S., and J. P. P. Ramalho. 2011. Recent Developments in Molecular Dynamics Simulations of Fluorescent Membrane Probes. Molecules 16:5437-5452.
163. MacCallum, J. L., and D. P. Tieleman. 2008. Chapter 8 Interactions between Small Molecules and Lipid Bilayers. In Curr. Top. Membr. E. F. Scott, editor. Academic Press. 227-256.
164. Gumbart, J. C., B. Roux, and C. Chipot. 2012. Standard Binding Free Energies from Computer Simulations: What Is the Best Strategy? J. Chem. Theory Comput. 9:794-802.
165. Kirkwood, J. G. 1935. Statistical Mechanics of Fluid Mixtures. J. Chem. Phys. 3:300-313.
166. Torrie, G. M., and J. P. Valleau. 1977. Nonphysical sampling distributions in Monte Carlo free-energy estimation: Umbrella sampling. J. Comput. Phys. 23:187-199.
167. Kästner, J. 2011. Umbrella sampling. Wiley Interdiscip. Rev.: Comput. Mol. Sci. 1:932-942.
168. Roux, B. 1995. The calculation of the potential of mean force using computer simulations. Comput. Phys. Commun. 91:275-282.
169. Kumar, S., J. M. Rosenberg, D. Bouzida, R. H. Swendsen, and P. A. Kollman. 1992. THE weighted histogram analysis method for free-energy calculations on biomolecules. I. The method. J. Comput. Chem. 13:1011-1021.
170. Hub, J. S., B. L. de Groot, and D. van der Spoel. 2010. g_wham—A Free Weighted Histogram Analysis Implementation Including Robust Error and Autocorrelation Estimates. J. Chem. Theory Comput. 6:3713-3720.
171. Gustavsson, A., M. Svensson, F. Jacobi, C. Allgulander, J. Alonso, E. Beghi, R. Dodel, M. Ekman, C. Faravelli, L. Fratiglioni, B. Gannon, D. H. Jones, P. Jennum, A. Jordanova, L. Jönsson, K. Karampampa, M. Knapp, G. Kobelt, T. Kurth, R. Lieb, M. Linde, C. Ljungcrantz, A. Maercker, B. Melin, M. Moscarelli, A. Musayev, F. Norwood, M. Preisig, M. Pugliatti, J. Rehm, L. Salvador-Carulla, B. Schlehofer, R. Simon, H.-C. Steinhausen, L. J. Stovner, J.-M. Vallat, P. V. den Bergh, J. van Os, P. Vos, W. Xu, H.-U. Wittchen, B. Jönsson, and J. Olesen. 2011. Cost of disorders of the brain in Europe 2010. Eur Neuropsychopharm 21:718-779.
172. Abbott, A. 2011. Novartis to shut brain research facility. Nature 480:161-162.
173. Kola, I., and J. Landis. 2004. Opinion: Can the pharmaceutical industry reduce attrition rates? Nat. Rev. Drug Discovery 3:711-716.

174. Gloor, S. M., M. Wachtel, M. F. Bolliger, H. Ishihara, R. Landmann, and K. Frei. 2001. Molecular and cellular permeability control at the blood–brain barrier. Brain Research Reviews 36:258-264.
175. Ballabh, P., A. Braun, and M. Nedergaard. 2004. The blood–brain barrier: an overview: Structure, regulation, and clinical implications. Neurobiology of Disease 16:1-13.
176. Hawkins, R. A., R. L. O'Kane, I. A. Simpson, and J. R. Viña. 2006. Structure of the Blood–Brain Barrier and Its Role in the Transport of Amino Acids. The Journal of Nutrition 136:218S-226S.
177. Butt, A. M., H. C. Jones, and N. J. Abbott. 1990. Electrical resistance across the blood-brain barrier in anaesthetized rats: a developmental study. The Journal of Physiology 429:47-62.
178. Smith, Q. R., and S. I. Rapoport. 1986. Cerebrovascular Permeability Coefficients to Sodium, Potassium, and Chloride. J Neurochem 46:1732-1742.
179. van Meer, G., and K. Simons. 1986. The function of tight junctions in maintaining differences in lipid composition between the apical and the basolateral cell surface domains of MDCK cells. The EMBO journal 5:1455.
180. Abbott, N. J. 2004. Prediction of blood-brain barrier permeation in drug discovery from in vivo, in vitro and in silico models. Drug Discovery Today: Technologies 1:407-416.
181. Tamai, I., and A. Tsuji. 2000. Transporter-mediated permeation of drugs across the blood–brain barrier. Journal of Pharmaceutical Sciences 89:1371-1388.
182. Demeule, M., A. Régina, J. Jodoin, A. Laplante, C. Dagenais, F. Berthelet, A. Moghrabi, and R. Béliveau. 2002. Drug transport to the brain: key roles for the efflux pump P-glycoprotein in the blood–brain barrier. Vascular Pharmacology 38:339-348.
183. Eisenblätter, T., S. Hüwel, and H.-J. Galla. 2003. Characterisation of the brain multidrug resistance protein (BMDP/ABCG2/BCRP) expressed at the blood–brain barrier. Brain Res 971:221-231.
184. Ambudkar, S. V., I.-W. Kim, and Z. E. Sauna. 2006. The power of the pump: Mechanisms of action of P-glycoprotein (ABCB1). European Journal of Pharmaceutical Sciences 27:392-400.
185. Eytan, G. D. 2005. Mechanism of multidrug resistance in relation to passive membrane permeation. Biomedicine & Pharmacotherapy 59:90-97.
186. Seelig, A. 2007. The Role of Size and Charge for Blood–Brain Barrier Permeation of Drugs and Fatty Acids. J Mol Neurosci 33:32-41.
187. Habgood, M. D., D. J. Begley, and N. J. Abbott. 2000. Determinants of passive drug entry into the central nervous system. Cellular and Molecular Neurobiology 20:231-253.
188. Pardridge, W. M. 1998. CNS drug design based on principles of blood-brain barrier transport. J Neurochem 70:1781-1792.
189. Abbott, N. J., L. Ronnback, and E. Hansson. 2006. Astrocyte-endothelial interactions at the blood-brain barrier. Nature Reviews Neuroscience 7:41-53.
190. Leung, S. S. F., J. Mijalkovic, K. Borrelli, and M. P. Jacobson. 2012. Testing Physical Models of Passive Membrane Permeation. Journal of Chemical Information and Modeling 52:1621-1636.
191. Di, L., E. H. Kerns, K. Fan, O. J. McConnell, and G. T. Carter. 2003. High throughput artificial membrane permeability assay for blood–brain barrier. European Journal of Medicinal Chemistry 38:223-232.

192. Ong, S., H. Liu, and C. Pidgeon. 1996. Immobilized-artificial-membrane chromatography: measurements of membrane partition coefficient and predicting drug membrane permeability. Journal of Chromatography A 728:113-128.
193. Hervé, F., S. Urien, E. Albengres, J.-C. Duché, and J.-P. Tillement. 1994. Drug Binding in Plasma. Clin. Pharmacokinet. 26:44-58.
194. Peters, T. 1996. All about Albumin: Biochemistry, Genetics and Medical Applications. Academic Press.
195. He, X. M., and D. C. Carter. 1992. Atomic structure and chemistry of human serum albumin. Nature 358:209-215.
196. Bos, O. J. M., J. F. A. Labro, M. J. E. Fischer, J. Wilting, and L. H. M. Janssen. 1989. The Molecular mechanism of the neutral-to-base transition of human serum albumin - acid/base titration and proton nuclear magnetic-resonance studies on a large peptic and a large tryptic fragment of albumin. Journal of Biological Chemistry 264:953-959.
197. Shen, B. W., A. M. Scanu, and F. J. Kézdy. 1977. Structure of human serum lipoproteins inferred from compositional analysis. Proceedings of the National Academy of Sciences 74:837-841.
198. Vieira, O. V., J. A. Laranjinha, V. M. Madeira, and L. M. Almeida. 1996. Rapid isolation of low density lipoproteins in a concentrated fraction free from water-soluble plasma antioxidants. J. Lipid Res. 37:2715-2721.
199. Shepherd, J. 2003. Combined lipid lowering drug therapy for the effective treatment of hypercholesterolaemia. European Heart Journal 24:685-689.
200. Brown, M., P. Kovanen, and J. Goldstein. 1981. Regulation of plasma cholesterol by lipoprotein receptors. Science 212:628-635.
201. Langer, T., R. I. Levy, and W. Strober. 1972. Metabolism of low density lipoprotein in familial type II hyperlipoproteinemia. Journal of Clinical Investigation 51:1528-1536.
202. Assmann, G., and J. R. Nofer. 2003. Atheroprotective effects of high-density lipoproteins. Annual Review of Medicine-Selected Topics in the Clinical Sciences 54:321-341.
203. Fielding, C. J., and P. E. Fielding. 1995. Molecular physiology of reverse cholesterol transport. J. Lipid Res. 36:211-228.
204. Steck, T. L. 1974. Organization of proteins in human red blood-cell membrane - a review. Journal of Cell Biology 62:1-19.
205. Artursson, P., and J. Karlsson. 1991. Correlation between oral drug absorption in humans and apparent drug permeability coefficients in human intestinal epithelial (Caco-2) cells. Biochemical and Biophysical Research Communications 175:880-885.
206. Clark, D. E., and P. D. J. Grootenhuis. 2003. Predicting passive transport in silico - History, hype, hope. Current Topics in Medicinal Chemistry 3:1193-1203.
207. Lipinski, C. A., F. Lombardo, B. W. Dominy, and P. J. Feeney. 1997. Experimental and computational approaches to estimate solubility and permeability in drug discovery and development settings. Advanced Drug Delivery Reviews 23:3-25.
208. Palm, K., K. Luthman, A. L. Ungell, G. Strandlund, and P. Artursson. 1996. Correlation of drug absorption with molecular surface properties. Journal of Pharmaceutical Sciences 85:32-39.

209. Palm, K., P. Stenberg, K. Luthman, and P. Artursson. 1997. Polar Molecular Surface Properties Predict the Intestinal Absorption of Drugs in Humans. Pharm Res-Dordr 14:568-571.
210. Abraham, M. H., H. S. Chadha, and R. C. Mitchell. 1994. Hydrogen bonding. 33. Factors that influence the distribution of solutes between blood and brain. Journal of Pharmaceutical Sciences 83:1257-1268.
211. Platts, J. A., M. H. Abraham, Y. H. Zhao, A. Hersey, L. Ijaz, and D. Butina. 2001. Correlation and prediction of a large blood–brain distribution data set—an LFER study. European Journal of Medicinal Chemistry 36:719-730.
212. Crivori, P., G. Cruciani, P.-A. Carrupt, and B. Testa. 2000. Predicting Blood−Brain Barrier Permeation from Three-Dimensional Molecular Structure. Journal of Medicinal Chemistry 43:2204-2216.
213. Kubinyi, H. 1977. Quantitative structure-activity relations. 7. The bilinear model, a new model for nonlinear dependence of biological activity on hydrophobic character. Journal of Medicinal Chemistry 20:625-629.
214. Hansch, C., and J. M. Clayton. 1973. Lipophilic character and biological activity of drugs II: The parabolic case. Journal of Pharmaceutical Sciences 62:1-21.
215. Frenkel, D., and B. Smit. 2001. Understanding molecular simulation: from algorithms to applications. Academic press.
216. van Gunsteren, W. F., and H. J. C. Berendsen. 1990. Computer Simulation of Molecular Dynamics: Methodology, Applications, and Perspectives in Chemistry. Angewandte Chemie International Edition in English 29:992-1023.
217. Jönsson, B., O. Edholm, and O. Teleman. 1986. Molecular dynamics simulations of a sodium octanoate micelle in aqueous solution. J. Chem. Phys. 85:2259-2271.
218. Egberts, E., and H. J. C. Berendsen. 1988. Molecular dynamics simulation of a smectic liquid crystal with atomic detail. J. Chem. Phys. 89:3718-3732.
219. Berendsen, H. J. C., D. van der Spoel, and R. van Drunen. 1995. GROMACS: A message-passing parallel molecular dynamics implementation. Comput. Phys. Commun. 91:43-56.
220. Pronk, S., S. Páll, R. Schulz, P. Larsson, P. Bjelkmar, R. Apostolov, M. R. Shirts, J. C. Smith, P. M. Kasson, D. van der Spoel, B. Hess, and E. Lindahl. 2013. GROMACS 4.5: a high-throughput and highly parallel open source molecular simulation toolkit. Bioinformatics 29:845-854.
221. Kalé, L., R. Skeel, M. Bhandarkar, R. Brunner, A. Gursoy, N. Krawetz, J. Phillips, A. Shinozaki, K. Varadarajan, and K. Schulten. 1999. NAMD2: Greater Scalability for Parallel Molecular Dynamics. J. Comput. Phys. 151:283-312.
222. Phillips, J. C., R. Braun, W. Wang, J. Gumbart, E. Tajkhorshid, E. Villa, C. Chipot, R. D. Skeel, L. Kalé, and K. Schulten. 2005. Scalable molecular dynamics with NAMD. J. Comput. Chem. 26:1781-1802.
223. Case, D. A., T. E. Cheatham, T. Darden, H. Gohlke, R. Luo, K. M. Merz, A. Onufriev, C. Simmerling, B. Wang, and R. J. Woods. 2005. The Amber biomolecular simulation programs. J. Comput. Chem. 26:1668-1688.
224. Brooks, B. R., R. E. Bruccoleri, B. D. Olafson, D. J. States, S. Swaminathan, and M. Karplus. 1983. CHARMM: A program for macromolecular energy, minimization, and dynamics calculations. J. Comput. Chem. 4:187-217.
225. Plimpton, S. 1995. Fast Parallel Algorithms for Short-Range Molecular Dynamics. J. Comput. Phys. 117:1-19.

226. Limbach, H. J., A. Arnold, B. A. Mann, and C. Holm. 2006. ESPResSo—an extensible simulation package for research on soft matter systems. Comput. Phys. Commun. 174:704-727.
227. Hess, B., H. Bekker, H. J. C. Berendsen, and J. Fraaije. 1997. LINCS: A linear constraint solver for molecular simulations. J. Comput. Chem. 18:1463-1472.
228. Hess, B. 2007. P-LINCS: A Parallel Linear Constraint Solver for Molecular Simulation. J. Chem. Theory Comput. 4:116-122.
229. Notman, R., and J. Anwar. 2013. Breaching the skin barrier — Insights from molecular simulation of model membranes. Advanced Drug Delivery Reviews 65:237-250.
230. van Buuren, A. R., S. J. Marrink, and H. J. C. Berendsen. 1993. A molecular dynamics study of the decane/water interface. The Journal of Physical Chemistry 97:9206-9212.
231. Marrink, S. J., A. H. de Vries, and D. P. Tieleman. 2009. Lipids on the move: Simulations of membrane pores, domains, stalks and curves. Biochim. Biophys. Acta, Biomembr. 1788:149-168.
232. Marrink, S. J., A. H. de Vries, and A. E. Mark. 2003. Coarse Grained Model for Semiquantitative Lipid Simulations. J. Phys. Chem. B 108:750-760.
233. Marrink, S. J., H. J. Risselada, S. Yefimov, D. P. Tieleman, and A. H. de Vries. 2007. The MARTINI Force Field: Coarse Grained Model for Biomolecular Simulations. J. Phys. Chem. B 111:7812-7824.
234. Miyamoto, S., and P. A. Kollman. 1992. Settle: An analytical version of the SHAKE and RATTLE algorithm for rigid water models. J. Comput. Chem. 13:952-962.
235. Malde, A. K., L. Zuo, M. Breeze, M. Stroet, D. Poger, P. C. Nair, C. Oostenbrink, and A. E. Mark. 2011. An Automated Force Field Topology Builder (ATB) and Repository: Version 1.0. J. Chem. Theory Comput. 7:4026-4037.
236. Domański, J., P. Stansfeld, M. P. Sansom, and O. Beckstein. 2010. Lipidbook: A Public Repository for Force-Field Parameters Used in Membrane Simulations. J Membrane Biol 236:255-258.
237. Poger, D., and A. E. Mark. 2009. On the Validation of Molecular Dynamics Simulations of Saturated and cis-Monounsaturated Phosphatidylcholine Lipid Bilayers: A Comparison with Experiment. J. Chem. Theory Comput. 6:325-336.
238. Benz, R. W., F. Castro-Román, D. J. Tobias, and S. H. White. 2005. Experimental Validation of Molecular Dynamics Simulations of Lipid Bilayers: A New Approach. Biophys. J. 88:805-817.
239. Chiu, S. W., M. Clark, V. Balaji, S. Subramaniam, H. L. Scott, and E. Jakobsson. 1995. Incorporation of surface tension into molecular dynamics simulation of an interface: a fluid phase lipid bilayer membrane. Biophys. J. 69:1230-1245.
240. Feller, S. E., and R. W. Pastor. 1996. On simulating lipid bilayers with an applied surface tension: periodic boundary conditions and undulations. Biophys. J. 71:1350-1355.
241. Jähnig, F. 1996. What is the surface tension of a lipid bilayer membrane? Biophys. J. 71:1348.
242. Marsh, D. 1996. Lateral pressure in membranes. Biochimica et Biophysica Acta (BBA) - Reviews on Biomembranes 1286:183-223.

243. Berendsen, H. J. C., J. P. M. Postma, W. F. van Gunsteren, A. DiNola, and J. R. Haak. 1984. Molecular dynamics with coupling to an external bath. J. Chem. Phys. 81:3684-3690.
244. Nosé, S. 1984. A molecular dynamics method for simulations in the canonical ensemble. Mol. Phys. 52:255-268.
245. Hoover, W. G. 1985. Canonical dynamics: Equilibrium phase-space distributions. Physical Review A 31:1695-1697.
246. Bussi, G., D. Donadio, and M. Parrinello. 2007. Canonical sampling through velocity rescaling. J. Chem. Phys. 126:014101.
247. van der Spoel, D., E. Lindahl, B. Hess, A. R. van Buuren, E. Apol, P. J. Meulenhoff, D. P. Tieleman, A. L. T. M. Sijbers, K. A. Feenstra, R. van Drunen, and H. J. C. Berendsen. 2010. Gromacs User Manual version 4.5.4, www.gromacs.org.
248. Parrinello, M., and A. Rahman. 1981. Polymorphic transitions in single crystals: A new molecular dynamics method. Journal of Applied Physics 52:7182-7190.
249. Nosé, S., and M. L. Klein. 1983. Constant pressure molecular dynamics for molecular systems. Mol. Phys. 50:1055-1076.
250. Martyna, G. J., M. E. Tuckerman, D. J. Tobias, and M. L. Klein. 1996. Explicit reversible integrators for extended systems dynamics. Mol. Phys. 87:1117-1157.
251. Darden, T., D. York, and L. Pedersen. 1993. Particle mesh Ewald: An N·log(N) method for Ewald sums in large systems. J. Chem. Phys. 98:10089-10092.
252. Essmann, U., L. Perera, M. L. Berkowitz, T. Darden, H. Lee, and L. G. Pedersen. 1995. A smooth particle mesh Ewald method. J. Chem. Phys. 103:8577-8593.
253. Lindahl, E., B. Hess, and D. van der Spoel. 2001. GROMACS 3.0: a package for molecular simulation and trajectory analysis. Journal of Molecular Modeling 7:306-317.
254. Hess, B., C. Kutzner, D. van der Spoel, and E. Lindahl. 2008. GROMACS 4: Algorithms for Highly Efficient, Load-Balanced, and Scalable Molecular Simulation. J. Chem. Theory Comput. 4:435-447.
255. Berendsen, H. J. C., J. P. M. Postma, W. F. Gunsteren, and J. Hermans. 1981. Interaction Models for Water in Relation to Protein Hydration. In Intermolecular Forces. B. Pullman, editor. Springer Netherlands. 331-342.
256. Berger, O., O. Edholm, and F. Jahnig. 1997. Molecular dynamics simulations of a fluid bilayer of dipalmitoylphosphatidylcholine at full hydration, constant pressure, and constant temperature. Biophys. J. 72:2002-2013.
257. Hoff, B., E. Strandberg, A. S. Ulrich, D. P. Tieleman, and C. Posten. 2005. H-2-NMR study and molecular dynamics simulation of the location, alignment, and mobility of pyrene in POPC bilayers. Biophys. J. 88:1818-1827.
258. Loura, L. M. S., A. J. P. Carvalho, and J. P. P. Ramalho. 2010. Direct calculation of Forster orientation factor of membrane probes by molecular simulation. J. Mol. Struct.: THEOCHEM 946:107-112.
259. Schuttelkopf, A. W., and D. M. F. van Aalten. 2004. PRODRG: a tool for high-throughput crystallography of protein-ligand complexes. Acta Crystallographica Section D 60:1355-1363.
260. Schmidt, M. W., K. K. Baldridge, J. A. Boatz, S. T. Elbert, M. S. Gordon, J. H. Jensen, S. Koseki, N. Matsunaga, K. A. Nguyen, S. Su, T. L. Windus, M. Dupuis, and J. A. Montgomery. 1993. General atomic and molecular electronic structure system. J. Comput. Chem. 14:1347-1363.

261. Gordon, M. S., and M. W. Schmidt. 2005. Advances in electronic structure theory: GAMESS a decade later. Theory and Applications of Computational Chemistry: the first forty years:1167-1189.
262. Jorgensen, W. L., D. S. Maxwell, and J. Tirado-Rives. 1996. Development and Testing of the OPLS All-Atom Force Field on Conformational Energetics and Properties of Organic Liquids. J. Am. Chem. Soc. 118:11225-11236.
263. Besler, B. H., K. M. Merz, and P. A. Kollman. 1990. Atomic charges derived from semiempirical methods. J. Comput. Chem. 11:431-439.
264. Loura, L. M. S., and J. P. P. Ramalho. 2007. Location and dynamics of acyl chain NBD-labeled phosphatidylcholine (NBD-PQ in DPPC bilayers. A molecular dynamics and time-resolved fluorescence anisotropy study. Biochim. Biophys. Acta, Biomembr. 1768:467-478.
265. Niemelä, P., M. T. Hyvönen, and I. Vattulainen. 2004. Structure and Dynamics of Sphingomyelin Bilayer: Insight Gained through Systematic Comparison to Phosphatidylcholine. Biophys. J. 87:2976-2989.
266. Martins do Canto, A. M. T., A. J. Palace Carvalho, J. P. Prates Ramalho, and L. M. S. Loura. 2010. Structure and conformation of HIV fusion inhibitor peptide T-1249 in presence of model membranes: A molecular dynamics study. Journal of Molecular Structure: THEOCHEM 946:119-124.
267. Loura, L. M. S., A. M. T. M. do Canto, and J. Martins. 2013. Sensing hydration and behavior of pyrene in POPC and POPC/cholesterol bilayers: A molecular dynamics study. Biochim. Biophys. Acta, Biomembr. 1828:1094-1101.
268. Feenstra, K. A., B. Hess, and H. J. C. Berendsen. 1999. Improving efficiency of large time-scale molecular dynamics simulations of hydrogen-rich systems. J. Comput. Chem. 20:786-798.
269. Anézo, C., A. H. de Vries, H.-D. Höltje, D. P. Tieleman, and S.-J. Marrink. 2003. Methodological Issues in Lipid Bilayer Simulations. J. Phys. Chem. B 107:9424-9433.
270. Flyvbjerg, H., and H. G. Petersen. 1989. Error estimates on averages of correlated data. J. Chem. Phys. 91:461-466.
271. Martinez-Seara, H., T. Róg, M. Karttunen, R. Reigada, and I. Vattulainen. 2008. Influence of cis double-bond parametrization on lipid membrane properties: How seemingly insignificant details in force-field change even qualitative trends. J. Chem. Phys. 129:105103.
272. Höltje, M., T. Förster, B. Brandt, T. Engels, W. von Rybinski, and H.-D. Höltje. 2001. Molecular dynamics simulations of stratum corneum lipid models: fatty acids and cholesterol. Biochim. Biophys. Acta, Biomembr. 1511:156-167.
273. Freedman, D. S., J. D. Otvos, E. J. Jeyarajah, I. Shalaurova, L. A. Cupples, H. Parise, R. B. D'Agostino, P. W. F. Wilson, and E. J. Schaefer. 2004. Sex and age differences in lipoprotein subclasses measured by nuclear magnetic resonance spectroscopy: The Framingham study. Clinical Chemistry 50:1189-1200.
274. Löfgren, L., M. Ståhlman, G.-B. Forsberg, S. Saarinen, R. Nilsson, and G. I. Hansson. 2012. The BUME method: a novel automated chloroform-free 96-well total lipid extraction method for blood plasma. J. Lipid Res. 53:1690-1700.
275. Bagdade, J. D., M. C. Ritter, M. Davidson, and P. V. Subbaiah. 1992. Effect of marine lipids on cholesteryl ester transfer and lipoprotein composition in patients with hypercholesterolemia. Arteriosclerosis, Thrombosis, and Vascular Biology 12:1146-1152.
276. Evans, E., and Y.-C. Fung. 1972. Improved measurements of the erythrocyte geometry. Microvascular Research 4:335-347.

277. Smaby, J. M., H. L. Brockman, and R. E. Brown. 1994. Cholesterol's Interfacial Interactions with Sphingomyelins and-Phosphatidylcholines: Hydrocarbon Chain Structure Determines the Magnitude of Condensation. Biochemistry 33:9135-9142.
278. Kalvodova, L., J. L. Sampaio, S. Cordo, C. S. Ejsing, A. Shevchenko, and K. Simons. 2009. The Lipidomes of Vesicular Stomatitis Virus, Semliki Forest Virus, and the Host Plasma Membrane Analyzed by Quantitative Shotgun Mass Spectrometry. Journal of Virology 83:7996-8003.
279. Moreno, M. J., and E. Melo. 1999. Diffusion-controlled photochemical reactions in membranes. Photodimerization of 6-(9-anthroyloxy) stearic acid in POPC bilayers under steady-state irradiation. J. Phys. Chem. B 103:10711-10717.
280. Filipe, H. A. L., M. J. Moreno, T. Róg, I. Vattulainen, and L. M. S. Loura. 2014. How To Tackle the Issues in Free Energy Simulations of Long Amphiphiles Interacting with Lipid Membranes: Convergence and Local Membrane Deformations. J. Phys. Chem. B 118:3572-3581.
281. Wolinsky, H. 1980. A proposal linking clearance of circulating lipoproteins to tissue metabolic-activity as a basis for understanding atherogenesis. Circulation Research 47:301-311.
282. Butor, C., and J. Davoust. 1992. Apical to basolateral surface area ratio and polarity of MDCK cells grown on different supports. Experimental cell research 203:115-127.
283. Pownall, H. J., D. L. Hickson, and L. C. Smith. 1983. Transport of biological lipophiles: effect of lipophile structure. J. Am. Chem. Soc. 105:2440-2445.
284. Kleinfeld, A. M., and J. Storch. 1993. Transfer of long-chain fluorescent fatty acids between small and large unilamellar vesicles. Biochemistry 32:2053-2061.
285. Peitzsch, R. M., and S. McLaughlin. 1993. Binding of acylated peptides and fatty acids to phospholipid vesicles: Pertinence to myristoylated proteins. Biochemistry 32:10436-10443.
286. Zhang, F. L., F. Kamp, and J. A. Hamilton. 1996. Dissociation of long and very long chain fatty acids from phospholipid bilayers. Biochemistry 35:16055-16060.
287. Massey, J. B., D. H. Bick, and H. J. Pownall. 1997. Spontaneous transfer of monoacyl amphiphiles between lipid and protein surfaces. Biophys. J. 72:1732-1743.
288. Pool, C. T., and T. E. Thompson. 1998. Chain length and temperature dependence of the reversible association of model acylated proteins with lipid bilayers. Biochemistry 37:10246-10255.
289. Hoyrup, P., J. Davidsen, and K. Jorgensen. 2001. Lipid membrane partitioning of lysolipids and fatty acids: Effects of membrane phase structure and detergent chain length. J. Phys. Chem. B 105:2649-2657.
290. Thomas, R. M., A. Baici, M. Werder, G. Schulthess, and H. Hauser. 2002. Kinetics and mechanism of long-chain fatty acid transport into phosphatidylcholine vesicles from various donor systems. Biochemistry 41:1591-1601.
291. Fujikawa, M., R. Ano, K. Nakao, R. Shimizu, and M. Akamatsu. 2005. Relationships between structure and high-throughput screening permeability of diverse drugs with artificial membranes: Application to prediction of Caco-2 cell permeability. Bioorganic & Medicinal Chemistry 13:4721-4732.

292. Resh, M. D. 1999. Fatty acylation of proteins: new insights into membrane targeting of myristoylated and palmitoylated proteins. Biochimica Et Biophysica Acta-Molecular Cell Research 1451:1-16.
293. Nadolski, M. J., and M. E. Linder. 2007. Protein lipidation. Febs J 274:5202-5210.
294. Vogler, O., J. M. Barcelo, C. Ribas, and P. V. Escriba. 2008. Membrane interactions of G proteins and other related proteins. Biochim. Biophys. Acta, Biomembr. 1778:1640-1652.
295. Martins, P. A. T., F. Gomes, W. L. C. Vaz, and M. J. Moreno. 2008. Binding of phospholipids to beta-Lactoglobulin and their transfer to lipid bilayers. Biochim. Biophys. Acta, Biomembr. 1778:1308-1315.
296. Chattopadhyay, A. 1990. Chemistry and biology of N-(7-nitrobenz-2-oxa-1,3-diazol-4-yl)-labeled lipids: fluorescent probes of biological and model membranes. Chemistry and Physics of Lipids 53:1-15.
297. Lakowicz, J. R. 2006. Principles of Fluorescence Spectroscopy. New York, Springer.
298. Kyrychenko, A. 2010. A molecular dynamics model of rhodamine-labeled phospholipid incorporated into a lipid bilayer. Chemical Physics Letters 485:95-99.
299. Franova, M., J. Repakova, P. Capkova, J. M. Holopainen, and I. Vattulainen. 2010. Effects of DPH on DPPC-Cholesterol Membranes with Varying Concentrations of Cholesterol: From Local Perturbations to Limitations in Fluorescence Anisotropy Experiments. J. Phys. Chem. B 114:2704-2711.
300. Skaug, M. J., M. L. Longo, and R. Faller. 2009. Computational Studies of Texas Red−1,2-Dihexadecanoyl-sn-glycero-3-phosphoethanolamine—Model Building and Applications. J. Phys. Chem. B 113:8758-8766.
301. Loura, L. M. S., F. Fernandes, A. C. Fernandes, and J. P. P. Ramalho. 2008. Effects of fluorescent probe NBD-PC on the structure, dynamics and phase transition of DPPC. A molecular dynamics and differential scanning calorimetry study. Biochim. Biophys. Acta, Biomembr. 1778:491-501.
302. Holtta-Vuori, M., R. L. Uronen, J. Repakova, E. Salonen, I. Vattulainen, P. Panula, Z. G. Li, R. Bittman, and E. Ikonen. 2008. BODIPY-Cholesterol: A New Tool to Visualize Sterol Trafficking in Living Cells and Organisms. Traffic 9:1839-1849.
303. Gullapalli, R. R., M. C. Demirel, and P. J. Butler. 2008. Molecular dynamics simulations of DiI-C-18(3) in a DPPC lipid bilayer. Physical Chemistry Chemical Physics 10:3548-3560.
304. Curdova, J., P. Capkova, J. Plasek, J. Repakova, and I. Vattulainen. 2007. Free pyrene probes in gel and fluid membranes: Perspective through atomistic simulations. J. Phys. Chem. B 111:3640-3650.
305. Repakova, J., J. M. Holopainen, M. Karttunen, and I. Vattulainen. 2006. Influence of pyrene-labeling on fluid lipid membranes. J. Phys. Chem. B 110:15403-15410.
306. Repakova, J., J. M. Holopainen, M. R. Morrow, M. C. McDonald, P. Capkova, and I. Vattulainen. 2005. Influence of DPH on the structure and dynamics of a DPPC bilayer. Biophys. J. 88:3398-3410.
307. Repakova, J., P. Capkova, J. M. Holopainen, and I. Vattulainen. 2004. Distribution, orientation, and dynamics of DPH probes in DPPC bilayer. J. Phys. Chem. B 108:13438-13448.

308. Lantzsch, G., H. Binder, H. Heerklotz, M. Wendling, and G. Klose. 1996. Surface areas and packing constraints in POPC/C(12)EO(n) membranes. A time-resolved fluorescence study. Biophysical Chemistry 58:289-302.
309. Konig, B., U. Dietrich, and G. Klose. 1997. Hydration and structural properties of mixed lipid/surfactant model membranes. Langmuir 13:525-532.
310. Bockmann, R. A., A. Hac, T. Heimburg, and H. Grubmuller. 2003. Effect of sodium chloride on a lipid bilayer. Biophys. J. 85:1647-1655.
311. Mukhopadhyay, P., H. J. Vogel, and D. P. Tieleman. 2004. Distribution of pentachlorophenol in phospholipid bilayers: A molecular dynamics study. Biophys. J. 86:337-345.
312. Gurtovenko, A. A., and J. Anwar. 2009. Interaction of Ethanol with Biological Membranes: The Formation of Non-bilayer Structures within the Membrane Interior and their Significance. J. Phys. Chem. B 113:1983-1992.
313. Pandit, S. A., S.-W. Chiu, E. Jakobsson, A. Grama, and H. L. Scott. 2008. Cholesterol Packing around Lipids with Saturated and Unsaturated Chains: A Simulation Study. Langmuir 24:6858-6865.
314. Raghuraman, H., S. Shrivastava, and A. Chattopadhyay. 2007. Monitoring the looping up of acyl chain labeled NBD lipids in membranes as a function of membrane phase state. Biochim. Biophys. Acta, Biomembr. 1768:1258-1267.
315. Huster, D., P. Müller, K. Arnold, and A. Herrmann. 2001. Dynamics of Membrane Penetration of the Fluorescent 7-Nitrobenz-2-Oxa-1,3-Diazol-4-yl (NBD) Group Attached to an Acyl Chain of Phosphatidylcholine. Biophys. J. 80:822-831.
316. Cevc, G., and D. Marsh. 1987. Phospholipid Bilayers. Physical Principles and Models. John Wiley & Sons: New York.
317. Douliez, J. P., A. Leonard, and E. J. Dufourc. 1995. Restatement of order parameters in biomembranes: calculation of C-C bond order parameters from C-D quadrupolar splitings. Biophys. J. 68:1727-1739.
318. Klose, G., B. Madler, H. Schafer, and K. P. Schneider. 1999. Structural characterization of POPC, and C12E4 in their mixed membranes at reduced hydration by solid state H-2 NMR. J. Phys. Chem. B 103:3022-3029.
319. Klauda, J. B., R. M. Venable, J. A. Freites, J. W. O'Connor, D. J. Tobias, C. Mondragon-Ramirez, I. Vorobyov, A. D. MacKerell, and R. W. Pastor. 2010. Update of the CHARMM All-Atom Additive Force Field for Lipids: Validation on Six Lipid Types. J. Phys. Chem. B 114:7830-7843.
320. Patra, M., E. Salonen, E. Terama, I. Vattulainen, R. Faller, B. W. Lee, J. Holopainen, and M. Karttunen. 2006. Under the influence of alcohol: The effect of ethanol and methanol on lipid bilayers. Biophys. J. 90:1121-1135.
321. Gurtovenko, A. A., and I. Vattulainen. 2009. Calculation of the electrostatic potential of lipid bilayers from molecular dynamics simulations: Methodological issues. J. Chem. Phys. 130:215107.
322. Lindahl, E., and O. Edholm. 2001. Molecular dynamics simulation of NMR relaxation rates and slow dynamics in lipid bilayers. J. Chem. Phys. 115:4938-4950.
323. Febo-Ayala, W., D. P. Holland, S. A. Bradley, and D. H. Thompson. 2007. Lateral diffusion coefficients of an eicosanyl-based bisglycerophosphocholine determined by PFG-NMR and FRAP. Langmuir 23:6276-6280.
324. Köchy, T., and T. M. Bayerl. 1993. Lateral diffusion coefficients of phospholipids in spherical bilayers on a solid support measured by resonance 2 relaxation. Physical Review E 47:2109-2116.

325. Robalo, J. R., J. P. P. Ramalho, and L. M. S. Loura. 2013. NBD-Labeled Cholesterol Analogues in Phospholipid Bilayers: Insights from Molecular Dynamics. J. Phys. Chem. B 117:13731-13742.
326. Filipe, H. A. L., M. J. Moreno, and L. M. S. Loura. 2011. Interaction of 7-Nitrobenz-2-oxa-1,3-diazol-4-yl-Labeled Fatty Amines with 1-Palmitoyl, 2-Oleoyl-sn-glycero-3-phosphocholine Bilayers: A Molecular Dynamics Study. J. Phys. Chem. B 115:10109-10119.
327. Yalovsky, S., M. Rodríguez-Concepción, and W. Gruissem. 1999. Lipid modifications of proteins – slipping in and out of membranes. Trends in Plant Science 4:439-445.
328. Greaves, J., and L. H. Chamberlain. 2007. Palmitoylation-dependent protein sorting. J Cell Biol 176:249-254.
329. Anania, V. G., and L. Coscoy. 2011. Palmitoylation of MIR2 Is Required for Its Function. Journal of Virology 85:2288-2295.
330. Dunphy, J. T., and M. E. Linder. 1998. Signalling functions of protein palmitoylation. Biochimica et Biophysica Acta (BBA) - Molecular and Cell Biology of Lipids 1436:245-261.
331. Shenoy-Scaria, A. M., D. J. Dietzen, J. Kwong, D. C. Link, and D. M. Lublin. 1994. Cysteine3 of Src family protein tyrosine kinase determines palmitoylation and localization in caveolae. J Cell Biol 126:353-363.
332. Levental, I., D. Lingwood, M. Grzybek, Ü. Coskun, and K. Simons. 2010. Palmitoylation regulates raft affinity for the majority of integral raft proteins. Proceedings of the National Academy of Sciences 107:22050-22054.
333. Pike, L. J. 2009. The challenge of lipid rafts. J. Lipid Res. 50:S323-S328.
334. Simons, M., P. Keller, B. De Strooper, K. Beyreuther, C. G. Dotti, and K. Simons. 1998. Cholesterol depletion inhibits the generation of β-amyloid in hippocampal neurons. Proceedings of the National Academy of Sciences 95:6460-6464.
335. Mumby, S. M. 1997. Reversible palmitoylation of signaling proteins. Current Opinion in Cell Biology 9:148-154.
336. Hofsass, C., E. Lindahl, and O. Edholm. 2003. Molecular dynamics simulations of phospholipid bilayers with cholesterol. Biophys. J. 84:2192-2206.
337. Zhang, Z., S. Y. Bhide, and M. L. Berkowitz. 2007. Molecular Dynamics Simulations of Bilayers Containing Mixtures of Sphingomyelin with Cholesterol and Phosphatidylcholine with Cholesterol. J. Phys. Chem. B 111:12888-12897.
338. Saito, H., and W. Shinoda. 2011. Cholesterol Effect on Water Permeability through DPPC and PSM Lipid Bilayers: A Molecular Dynamics Study. J. Phys. Chem. B 115:15241-15250.
339. Khelashvili, G. A., and H. L. Scott. 2004. Combined Monte Carlo and molecular dynamics simulation of hydrated 18:0 sphingomyelin--cholesterol lipid bilayers. J. Chem. Phys. 120:9841-9847.
340. Niemela, P. S., S. Ollila, M. T. Hyvonen, M. Karttunen, and I. Vattulainen. 2007. Assessing the nature of lipid raft membranes. PLoS Comput. Biol. 3:304-312.
341. Zidar, J., F. Merzel, M. Hodošček, K. Rebolj, K. Sepčić, P. Maček, and D. a. Janežič. 2009. Liquid-Ordered Phase Formation in Cholesterol/Sphingomyelin Bilayers: All-Atom Molecular Dynamics Simulations. J. Phys. Chem. B 113:15795-15802.

342. McIntosh, T. J., S. A. Simon, D. Needham, and C. H. Huang. 1992. Interbilayer interactions between sphingomyelin and sphingomyelin/cholesterol bilayers. Biochemistry 31:2020-2024.
343. Javanainen, M., H. Hammaren, L. Monticelli, J.-H. Jeon, M. S. Miettinen, H. Martinez-Seara, R. Metzler, and I. Vattulainen. 2013. Anomalous and normal diffusion of proteins and lipids in crowded lipid membranes. Faraday Discuss. 161:397-417.
344. Laidler, K. J., and K. E. Shuler. 1949. The Kinetics of Membrane Processes. I. The Mechanism and the Kinetic Laws for Diffusion through Membranes. J. Chem. Phys. 17:851-855.
345. Zwolinski, B. J., H. Eyring, and C. E. Reese. 1948. Diffusion and Membrane Permeability. J. Phys. Colloid Chem. 53:1426-1453.
346. Wennberg, C. L., D. van der Spoel, and J. S. Hub. 2012. Large Influence of Cholesterol on Solute Partitioning into Lipid Membranes. J. Am. Chem. Soc. 134:5351-5361.
347. MacCallum, J. L., W. F. D. Bennett, and D. P. Tieleman. 2008. Distribution of Amino Acids in a Lipid Bilayer from Computer Simulations. Biophys. J. 94:3393-3404.
348. Sapay, N., W. F. D. Bennett, and D. P. Tieleman. 2010. Molecular Simulations of Lipid Flip-Flop in the Presence of Model Transmembrane Helices. Biochemistry 49:7665-7673.
349. Hinner, M. J., S. J. Marrink, and A. H. de Vries. 2009. Location, Tilt, and Binding: A Molecular Dynamics Study of Voltage-Sensitive Dyes in Biomembranes. J. Phys. Chem. B 113:15807-15819.
350. Tieleman, D. P., and S.-J. Marrink. 2006. Lipids Out of Equilibrium: Energetics of Desorption and Pore Mediated Flip-Flop. J. Am. Chem. Soc. 128:12462-12467.
351. Bennett, W. F. D., and D. P. Tieleman. 2012. Molecular simulation of rapid translocation of cholesterol, diacylglycerol, and ceramide in model raft and nonraft membranes. J. Lipid Res. 53:421-429.
352. Bennett, W. F. D., J. L. MacCallum, and D. P. Tieleman. 2009. Thermodynamic Analysis of the Effect of Cholesterol on Dipalmitoylphosphatidylcholine Lipid Membranes. J. Am. Chem. Soc. 131:1972-1978.
353. MacCallum, J. L., and D. P. Tieleman. 2006. Computer simulation of the distribution of hexane in a lipid bilayer: Spatially resolved free energy, entropy, and enthalpy profiles. J. Am. Chem. Soc. 128:125-130.
354. Neale, C., W. F. D. Bennett, D. P. Tieleman, and R. Pomès. 2011. Statistical Convergence of Equilibrium Properties in Simulations of Molecular Solutes Embedded in Lipid Bilayers. J. Chem. Theory Comput. 7:4175-4188.
355. Neale, C., C. Madill, S. Rauscher, and R. Pomès. 2013. Accelerating Convergence in Molecular Dynamics Simulations of Solutes in Lipid Membranes by Conducting a Random Walk along the Bilayer Normal. J. Chem. Theory Comput. 9:3686-3703.
356. Paloncýová, M., K. Berka, and M. Otyepka. 2012. Convergence of Free Energy Profile of Coumarin in Lipid Bilayer. J. Chem. Theory Comput. 8:1200-1211.
357. Jo, S., H. Rui, J. B. Lim, J. B. Klauda, and W. Im. 2010. Cholesterol Flip-Flop: Insights from Free Energy Simulation Studies. J. Phys. Chem. B 114:13342-13348.

358. Ghaemi, Z., M. Minozzi, P. Carloni, and A. Laio. 2012. A Novel Approach to the Investigation of Passive Molecular Permeation through Lipid Bilayers from Atomistic Simulations. J. Phys. Chem. B 116:8714-8721.
359. Parisio, G., M. M. Sperotto, and A. Ferrarini. 2012. Flip-Flop of Steroids in Phospholipid Bilayers: Effects of the Chemical Structure on Transbilayer Diffusion. J. Am. Chem. Soc. 134:12198-12208.
360. Jämbeck, J. P. M., and A. P. Lyubartsev. 2013. Exploring the Free Energy Landscape of Solutes Embedded in Lipid Bilayers. J. Phys. Chem. Lett. 4:1781-1787.
361. Cardenas, A. E., and R. Elber. 2013. Computational study of peptide permeation through membrane: searching for hidden slow variables. Mol. Phys. 111:3565-3578.
362. Meno-Tetang, G. M. L., H. Li, S. Mis, N. Pyszczynski, P. Heining, P. Lowe, and W. J. Jusko. 2006. Physiologically Based Pharmacokinetic Modeling of FTY720 (2-Amino-2[2-(-4-octylphenyl)ethyl]propane-1,3-diol hydrochloride) in Rats After Oral and Intravenous Doses. Drug Metab. Dispos. 34:1480-1487.
363. Brinkmann, V. 2009. FTY720 (fingolimod) in Multiple Sclerosis: therapeutic effects in the immune and the central nervous system. Br. J. Pharmacol. 158:1173-1182.
364. Brinkmann, V., A. Billich, T. Baumruker, P. Heining, R. Schmouder, G. Francis, S. Aradhye, and P. Burtin. 2010. Fingolimod (FTY720): discovery and development of an oral drug to treat multiple sclerosis. Nat. Rev. Drug Discovery 9:883-897.
365. Sharma, P., B. Dube, and K. Sawant. 2012. Synthesis of Cytarabine Lipid Drug Conjugate for Treatment of Meningeal Leukemia: Development, Characterization and *In Vitro* Cell Line Studies. J. Biomed. Nanotechnol. 8:928-937.
366. Testa, B., and J. M. Mayer. 2001. Concepts in Prodrug Design to Overcome Pharmacokinetic Problems. In Pharmacokinetic Optimization in Drug Research: Biological, Physicochemical, and Computational Strategies. B. Testa, G. F. Waterbeemb, and R. Guy, editors. Verlag Helvetica Chimica Acta, Zurich. 85-95.
367. Eyring, H. 1935. The Activated Complex and the Absolute Rate of Chemical Reactions. Chem. Rev. (Washington, DC, U. S.) 17:65-77.
368. Roux, B. 1999. Theories of ion permeation: a chaser. J. Gen. Physiol. 114:605-608.
369. Paloncýová, M., R. DeVane, B. Murch, K. Berka, and M. Otyepka. 2014. Amphiphilic Drug-Like Molecules Accumulate in a Membrane below the Head Group Region. J. Phys. Chem. B 118:1030-1039.
370. Berka, K., T. Hendrychová, P. Anzenbacher, and M. Otyepka. 2011. Membrane Position of Ibuprofen Agrees with Suggested Access Path Entrance to Cytochrome P450 2C9 Active Site. The Journal of Physical Chemistry A 115:11248-11255.
371. Košinová, P., K. Berka, M. Wykes, M. Otyepka, and P. Trouillas. 2011. Positioning of Antioxidant Quercetin and Its Metabolites in Lipid Bilayer Membranes: Implication for Their Lipid-Peroxidation Inhibition. J. Phys. Chem. B 116:1309-1318.
372. Bhide, S. Y., Z. Zhang, and M. L. Berkowitz. 2007. Molecular Dynamics Simulations of SOPS and Sphingomyelin Bilayers Containing Cholesterol. Biophys. J. 92:1284-1295.

373. Gurtovenko, A. A., and I. Vattulainen. 2007. Lipid Transmembrane Asymmetry and Intrinsic Membrane Potential: Two Sides of the Same Coin. J. Am. Chem. Soc. 129:5358-5359.
374. Gurtovenko, A. A., and I. Vattulainen. 2008. Membrane Potential and Electrostatics of Phospholipid Bilayers with Asymmetric Transmembrane Distribution of Anionic Lipids. J. Phys. Chem. B 112:4629-4634.
375. Bennett, W. F. D., J. L. MacCallum, M. J. Hinner, S. J. Marrink, and D. P. Tieleman. 2009. Molecular View of Cholesterol Flip-Flop and Chemical Potential in Different Membrane Environments. J. Am. Chem. Soc. 131:12714-12720.
376. Harroun, T. A., J. Katsaras, and S. R. Wassall. 2006. Cholesterol Hydroxyl Group Is Found To Reside in the Center of a Polyunsaturated Lipid Membrane. Biochemistry 45:1227-1233.
377. Harroun, T. A., J. Katsaras, and S. R. Wassall. 2008. Cholesterol Is Found To Reside in the Center of a Polyunsaturated Lipid Membrane. Biochemistry 47:7090-7096.
378. Homan, R., and H. J. Pownall. 1988. Transbilayer diffusion of phospholipids: dependence on headgroup structure and acyl chain length. Biochim. Biophys. Acta, Biomembr. 938:155-166.
379. Wynne-Jones, W. F. K., and H. Eyring. 1935. The Absolute Rate of Reactions in Condensed Phases. J. Chem. Phys. 3:492-502.
380. Evans, M. G., and M. Polanyi. 1935. Some applications of the transition state method to the calculation of reaction velocities, especially in solution. Transactions of the Faraday Society 31:875-894.
381. Steinfeld, J. I., Francisco, S., Hase, W. L., editor. 1999. Chemical kinetics and Dynamics. Prentice Hall, Upper Saddle River, NJ, 300-302.
382. Bedrov, D., G. D. Smith, H. Davande, and L. Li. 2008. Passive Transport of C60 Fullerenes through a Lipid Membrane: A Molecular Dynamics Simulation Study. J. Phys. Chem. B 112:2078-2084.
383. Rothblat, G. H., and M. C. Phillips. 2010. High-density lipoprotein heterogeneity and function in reverse cholesterol transport. Current opinion in lipidology 21:229.
384. von Eckardstein, A., J.-R. Nofer, and G. Assmann. 2001. High Density Lipoproteins and Arteriosclerosis: Role of Cholesterol Efflux and Reverse Cholesterol Transport. Arteriosclerosis, Thrombosis, and Vascular Biology 21:13-27.
385. Lund-Katz, S., B. Hammerschlag, and M. C. Phillips. 1982. Kinetics and mechanism of free cholesterol exchange between human serum high- and low-density lipoproteins. Biochemistry 21:2964-2969.
386. Lange, Y., A. L. Molinaro, T. R. Chauncey, and T. L. Steck. 1983. On the mechanism of transfer of cholesterol between human erythrocytes and plasma. Journal of Biological Chemistry 258:6920-6926.
387. Schwartz, C. C., L. A. Zech, J. M. VandenBroek, and P. S. Cooper. 1993. Cholesterol kinetics in subjects with bile fistula. Positive relationship between size of the bile acid precursor pool and bile acid synthetic rate. The Journal of Clinical Investigation 91:923-938.
388. Chapman, M. 1986. Comparative analysis of mammalian plasma lipoproteins. Methods in enzymology 128:70-143.
389. Gotto, A. M., H. J. Pownall, and R. J. Havel. 1986. Introduction to the plasma lipoproteins. Methods in enzymology 128:3-41.

390. Kuksis, A., J. J. Myher, K. Geher, G. J. L. Jones, J. Shepherd, C. J. Packard, J. D. Morrisett, O. D. Taunton, and A. M. Gotto. 1982. Effect of saturated and unsaturated fat diets on lipid profiles of plasma lipoproteins. Atherosclerosis 41:221-240.
391. Colhoun, H. M., J. D. Otvos, M. B. Rubens, M. R. Taskinen, S. R. Underwood, and J. H. Fuller. 2002. Lipoprotein Subclasses and Particle Sizes and Their Relationship With Coronary Artery Calcification in Men and Women With and Without Type 1 Diabetes. Diabetes 51:1949-1956.
392. de Grooth, G. J., J. A. Kuivenhoven, A. F. H. Stalenhoef, J. de Graaf, A. H. Zwinderman, J. L. Posma, A. van Tol, and J. J. P. Kastelein. 2002. Efficacy and Safety of a Novel Cholesteryl Ester Transfer Protein Inhibitor, JTT-705, in Humans: A Randomized Phase II Dose-Response Study. Circulation 105:2159-2165.
393. Storey, S. M., A. M. Gallegos, B. P. Atshaves, A. L. McIntosh, G. G. Martin, R. D. Parr, K. K. Landrock, A. B. Kier, J. M. Ball, and F. Schroeder. 2007. Selective Cholesterol Dynamics between Lipoproteins and Caveolae/Lipid Rafts†. Biochemistry 46:13891-13906.
394. Lange, Y., J. S. D'Alessandro, and D. M. Small. 1979. The affinity of cholesterol for phosphatidylcholine and sphingomyelin. Biochim. Biophys. Acta, Biomembr. 556:388-398.
395. Nestel, P. J., H. M. Whyte, and D. S. Goodman. 1969. Distribution and turnover of cholesterol in humans. Journal of Clinical Investigation 48:982-991.
396. Artursson, P., K. Palm, and K. Luthman. 2012. Caco-2 monolayers in experimental and theoretical predictions of drug transport. Advanced Drug Delivery Reviews 64, Supplement:280-289.
397. Ribeiro, M. M. B., M. N. Melo, I. D. Serrano, N. C. Santos, and M. A. R. B. Castanho. 2010. Drug–lipid interaction evaluation: why a 19th century solution? Trends Pharmacol Sci 31:449-454.
398. Krämer, S. D., D. Lombardi, A. Primorac, A. V. Thomae, and H. Wunderli-Allenspach. 2009. Lipid-Bilayer Permeation of Drug-Like Compounds. Chemistry & Biodiversity 6:1900-1916.
399. Tejwani, R. W., M. E. Davis, B. D. Anderson, and T. R. Stouch. 2011. Functional group dependence of solute partitioning to various locations within a DOPC bilayer: A comparison of molecular dynamics simulations with experiment. Journal of Pharmaceutical Sciences 100:2136-2146.
400. Jing, P., P. J. Rodgers, and S. Amemiya. 2009. High Lipophilicity of Perfluoroalkyl Carboxylate and Sulfonate: Implications for Their Membrane Permeability. J. Am. Chem. Soc. 131:2290-2296.
401. Ambudkar, S. V., C. O. Cardarelli, I. Pashinsky, and W. D. Stein. 1997. Relation Between the Turnover Number for Vinblastine Transport and for Vinblastine-stimulated ATP Hydrolysis by Human P-glycoprotein. Journal of Biological Chemistry 272:21160-21166.
402. Sun, H. D., and K. S. Pang. 2008. Permeability, transport, and metabolism of solutes in caco-2 cell monolayers: A theoretical study. Drug Metab. Dispos. 36:102-123.
403. Yu, L. X., and G. L. Amidon. 1999. A compartmental absorption and transit model for estimating oral drug absorption. International Journal of Pharmaceutics 186:119-125.

404. Connor, M., C. W. Vaughan, and R. J. Vandenberg. 2010. N-Acyl amino acids and N-acyl neurotransmitter conjugates: neuromodulators and probes for new drug targets. Br. J. Pharmacol. 160:1857-1871.
405. Sawada, G. A., N. F. H. Ho, L. R. Williams, C. L. Barsuhn, and T. J. Raub. 1994. Transcellular permeability of chlorpromazine demonstrating the roles of protein-binding and membrane partitioning. Pharm Res-Dordr 11:665-673.
406. Aungst, B. J., N. H. Nguyen, J. P. Bulgarelli, and K. Oates-Lenz. 2000. The influence of donor and reservoir additives on Caco-2 permeability and secretory transport of HIV protease inhibitors and other lipophilic compounds. Pharm Res-Dordr 17:1175-1180.
407. Yamashita, S., T. Furubayashi, M. Kataoka, T. Sakane, H. Sezaki, and H. Tokuda. 2000. Optimized conditions for prediction of intestinal drug permeability using Caco-2 cells. European Journal of Pharmaceutical Sciences 10:195-204.
408. Youdim, K. A., A. Avdeef, and N. J. Abbott. 2003. In vitro trans-monolayer permeability calculations: often forgotten assumptions. Drug Discovery Today 8:997-1003.
409. Wolfram Research, I. 2012. Mathematica. Wolfram Research, Inc., Champaign, Illinois.
410. Sawada, G. A., C. L. Barsuhn, B. S. Lutzke, M. E. Houghton, G. E. Padbury, N. F. H. Ho, and T. J. Raub. 1999. Increased lipophilicity and subsequent cell partitioning decrease passive transcellular diffusion of novel, highly lipophilic antioxidants. J Pharmacol Exp Ther 288:1317-1326.
411. Grime, J. M. A., M. A. Edwards, N. C. Rudd, and P. R. Unwin. 2008. Quantitative visualization of passive transport across bilayer lipid membranes. P Natl Acad Sci USA 105:14277-14282.
412. Thomae, A. V., T. Koch, C. Panse, H. Wunderli-Allenspach, and S. D. Kramer. 2007. Comparing the lipid membrane affinity and permeation of drug-like acids: The intriguing effects of cholesterol and charged lipids. Pharm Res-Dordr 24:1457-1472.
413. Hansch, C., A. R. Steward, S. M. Anderson, and D. L. Bentley. 1968. Parabolic dependence of drug action upon lipophilic character as revealed by a study of hypnotics. Journal of Medicinal Chemistry 11:1-11.
414. McKeage, M. J., S. J. Berners-Price, P. Galettis, R. J. Bowen, W. Brouwer, L. Ding, L. Zhuang, and B. C. Baguley. 2000. Role of lipophilicity in determining cellular uptake and antitumour activity of gold phosphine complexes. Cancer Chemother Pharmacol 46:343-350.
415. Jeppsson, R. 1975. Parabolic Relationship between Lipophilicity and Biological Activity of Aliphatic Hydrocarbons, Ethers and Ketones after Intravenous Injections of Emulsion Formulations into Mice. Acta Pharmacologica et Toxicologica 37:56-64.
416. Wils, P., A. Warnery, V. Phung-Ba, S. Legrain, and D. Scherman. 1994. High lipophilicity decreases drug transport across intestinal epithelial cells. J Pharmacol Exp Ther 269:654-658.
417. Krishna, G., K. W. J. Chen, C. C. Lin, and A. A. Nomeir. 2001. Permeability of lipophilic compounds in drug discovery using in-vitro human absorption model, Caco-2. International Journal of Pharmaceutics 222:77-89.
418. Matsushita, Y., M. Takahashi, and I. Moriguchi. 1986. Binding of fluorescent 7-amino-4-nitrobenzoxadiazole derivatives to bovine serum albumin. Chemical & pharmaceutical bulletin 34:333-339.

419. Edward, J. T. 1970. Molecular volumes and the Stokes-Einstein equation. Journal of Chemical Education 47:261-271.